upna
Universidad Pública de Navarra
Nafarroako Unibertsitate Publikoa

PUBLIC UNIVERSITY OF NAVARRE
Electrical, Electronic, and Communication
Engineering Department

NEW FILTER DESIGN METHODS AND TOPOLOGIES FOR THE FUTURE MICROWAVE AND MILLIMETER-WAVE HIGH-CAPACITY SATELLITES

Doctoral Thesis by
Fernando Teberio Berdún

Supervised by
Miguel Ángel Gómez Laso
José María Lopetegui Beregaña

Pamplona, June 2018

upna
Universidad Pública de Navarra
Nafarroako Unibertsitate Publikoa

NEW FILTER DESIGN METHODS AND TOPOLOGIES FOR THE FUTURE MICROWAVE AND MILLIMETER-WAVE HIGH-CAPACITY SATELLITES

PhD Dissertation

Fernando Teberio
Public University of Navarre

upna
Universidad Pública de Navarra
Nafarroako Unibertsitate Publikoa

To my wife Maite

F. T.

Contents

ABSTRACT

In this Thesis, several novel design techniques for waveguide low-pass filters (LPFs) and band-pass filters (BPFs) are proposed. Firstly, a quasi-analytical technique for classical corrugated waveguide LPFs is presented. It allows to reduce the design-times and its associated costs, since the final dimensions of the final prototype are computed by closed-form expressions. This technique has been extended to include the inherent rounded corners due to the fabrication by conventional milling techniques. In this case, the novel method is based on very simple equations which can be easily computed by an EM solver tool in a negligible CPU time. Additionally, a new method to embed routing capability in the classical corrugated LPF avoiding subsequent bending structures is also proposed. It permits to reduce the insertion loss, volume/weight, and PIM. The previous filters are the classical solution when the suppression of only the fundamental mode is needed. However, if the suppression of the higher-order modes is also a requirement, the classical solution is the waffle-iron filter. This filter has a cumbersome time-consuming design method mainly based on approximations and optimizations. In this Thesis, an accurate and simple design procedure for classical waffle-iron filters is also proposed. With this technique, waffle-iron filters with and without transmission zeros can be designed in a matter of minutes. Besides, a new type of waffle-iron filter is also presented. This novel structure is more compact and has lower insertion loss than its classical counterpart.

The main issue of the previous classical filters is that it is not possible to achieve a wide rejected band and a high-power behavior simultaneously. This issue has been surpassed with the novel LPFs with smooth profile presented in this Thesis. Specifically, a synthesis technique has been developed, which permits to obtain larger gaps and very wide rejected bands at the same time. These new structures allow their use in high-power applications such as the output stage of satellite payloads. However, although their fabrication following space-compatible procedures has been demonstrated, it is quite difficult and expensive to be utilized in mass-production. Therefore, a new design method which accomplishes easy-to-manufacture LPFs with the same performance in terms of frequency and high-power behavior has been proposed. In this case, the objective is to reduce the fabrication costs and to develop a fully-customized technique that opens the range of potential applications of these devices. Indeed, its feasibility to be utilized as output filter in broadband satellite payloads, between the amplifiers and the diplexers in multi-beam payloads, and in high-performance diplexers is demonstrated. Furthermore, a combination between the latter low-pass filtering structure and a classical high-pass filtering function is utilized to develop a new class of BPF which can be used in high-performance compact satellite diplexers.

Finally, a different BPFs with reduced sensitivity to manufacturing tolerances is also proposed. This structure finds its niche market in the upcoming Q/V-band satellite payloads. Indeed, the fabrication yield of a novel BPF intended for Q-band payloads has been dramatically improved in comparison with the one obtained from its classical counterpart. Last but not least, the size of the previous structures can be reduced with the new meandered topology developed in this Thesis. This technique permits to reduce the size of the previous BPFs (and also in classical LPFs) along with embedding routing capabilities, opening the door to more complex and compact terminals due to their adaptable and flexible layout. Additionally, it also allows to include several transmission zeros to enhance the out-of-band rejection of the LPFs.

Low-power and high-power measurements have been performed in several manufactured prototypes to validate the frequency behavior and the power-handling capability of the designed devices, respectively.

RESUMEN

En esta Tesis se han propuesto diversos métodos de diseño para filtros paso bajo y paso banda en guía de onda rectangular. En primer lugar, se presenta un método de diseño cuasi-analítico para filtros corrugados clásicos, cuya nueva metodología permite calcular las dimensiones finales del filtro sin utilizar el simulador electromagnético, así como prescindiendo también de optimizaciones. Además, se presenta la posibilidad de incluir capacidad de enrutado en este tipo de estructuras por medio de un nuevo método de diseño. Posteriormente, también se propone un nuevo método simple y rápido para el diseño de filtros waffle-iron, el cual evita la utilización de los métodos clásicos basados en aproximaciones y optimización, cuestión por la cual los hace difíciles de utilizar y muy costosos en lo que a tiempos de diseño se refiere.

El siguiente punto que se aborda en esta Tesis es el diseño de filtros paso bajo con perfil suave. Este tipo de filtros permite obtener simultáneamente grandes anchos de banda de rechazo y manejo de alta potencia, cuyas características los hace ser especialmente interesantes en la parte de salida de un satélite de comunicaciones. A continuación, se propone un nuevo tipo de filtro paso bajo con las mismas características de anchos de banda de rechazo y alta potencia pero cuya fabricación es mucho más sencilla. En este caso, el objetivo es desarrollar un método de diseño que abra el abanico de aplicación de estas estructuras como filtros de salida, filtros intermedios en satélites multi-haz o diplexores. Asimismo, también se presenta un nuevo filtro paso banda como combinación de las estructuras anteriores con una respuesta

tipo paso alto. Este nuevo tipo de estructuras son muy convenientes para ser utilizadas en diplexores de altas prestaciones de bajo coste debido a su fácil fabricación y su tamaño compacto.

Finalmente, también se ha desarrollado un nuevo método de diseño de filtros paso banda con fuerte resistencia a las tolerancias de fabricación, especialmente enfocado en las nuevas bandas Q y V. Por último, se propone una nueva topología en forma de meandros que permite reducir el tamaño de las anteriores estructuras (así como de los filtros clásicos paso-bajo), además de dotar de enrutabilidad a la estructura e incluir ceros de transmisión para mejorar su respuesta fuera de banda.

ACKNOWLEDGMENTS

Now that the elaboration of this Thesis is coming to the end, I would like to acknowledge all the people that has made this possible. First of all, I would like to show my sincere gratitude to my supervisors Mikel Gómez Laso and Txema Lopetegi. All their guidance, support, and smart advice during these years have been fundamental to accomplish this work. A very special mention deserves Nilo Martín-Iglesias: not only has he opened the doors of ESA-ESTEC for me, but also the one of his home and family. Thank you Nilo for your supervision and suggestions and, above all, for your positive attitude and disposition. A great thanks goes to Israel Arnedo and Iván Arregui, who patiently helped me during all those years, and without whom I would have been unable to reach all the objectives of this work. I would also like to thank all the members of the MCG group (David Benito, Jon Percaz, Magdalena Chudzik, Aintzane Lujambio, Verónica Urrea, Esteban Menargues, Adrian Gómez…) with whom I have shared my research activities. This list of names should be extended even more to include all the people that belong to the Electrical and Electronic Department of the Public University of Navarre and specifically the Antenna Group (Jorge Teniente, etc.).

I am also indebted to Vicente E. Boria and Marco Guglielmi, from the Universidad Politécnica de Valencia, for sparing no effort to offer me invaluable advice and guidelines for my research work. I sincerely acknowledge also to Pablo Soto and Santiago Cogollos for their smart suggestions.

I really appreciate the support provided by all the people I was working with in the different projects, Franz J. Görtz and Michael Zedler from Tesat-Spacecom GmbH & Co. and Antonio Oñoro from Thales Alenia Space (Spain). I kindly thank Ángel Alonso, Idelfonso López y Ángel Patús from Novalti S.A., for the fabrication of some prototypes and for giving me the opportunity to work within your company. I would also like to extend my acknowledgements to all the people of INTOR, Iñaki, Javi, Mendoza, ESA/ESTEC Petar, César, Jaione, Gergely, and friends.

I cannot finish without saying how grateful I am to my Mother and Sister, who have been my support in each and every moment of my life. My deepest thanks to my Father and Grandfather, who encouraged me to believe in dreams. Last but not least, my warmest and grateful acknowledge to Maite Iriarte. You are the shadow co-author of this work for many different reasons, such as your trust, sensitivity, patience, devotion, and infinite support, but one stands out from the others: you are my inspiration. Finally, the greatest thanks to the smallest person, Ariane, my smile.

F. T.

ACRONYMS

AM	Additive Manufacturing
BPF	Band-Pass Filter
BSS	Broadcast Satellite Services
CCM	Computer-Controlled Milling
COTS	Commercial Off-The-Shelf
CS	Consumer Services
CST MWS	CST Microwave Studio
CTE	Coefficient of Thermal Expansion
DBS	Direct Broadcast Services
DUT	Device Under Test
ECSS	European Cooperation for Space Standardization
EDM	Electro-Discharge Machining
EM	Electromagnetic
EOS	Earth Observation Services
ESA	European Space Agency

FSS	Fixed Satellite Services
GEO	Geostationary Orbit
IMUX	Input Multiplexer
LEO	Low-Earth Orbit
MEMS	Microelectromechanical Systems
MSS	Mobile Satellite Services
LPF	Low-Pass Filter
LSB	Lower Stopband
OMUX	Output Multiplexer
PIC	Particle-In-Cell
PIM	Passive Intermodulation
RF	Radio Frecuency
Rx	Reception
SEY	Secondary Emission Yield
SW	Software
TE	Transversal Electric
TEM	Transversal Electromagnetic
TE	Transversal Magnetic
TTC	Tracking, Telemetry and Command
Tx	Transmission
UE	Unit Element
USB	Upper Stopband
VHTS	Very High Throughput Satellites
VSAT	Very Small Aperture Terminal
VSC	Val-Space Consortium

CHAPTER 1

INTRODUCTION

This Chapter describes the purpose of this Thesis and the characteristics of microwave filters concerned with satellite communications, giving the reader an overview of the work that is collected herein. The chapter begins with a brief introduction that places the research within the broad field that encompasses microwave filter technology. Then, an overview over classical filters leads the reader to a perspective over the state-of-the-art of the most significant filters that will be treated in this work. Afterwards, a short description of multipactor effect and SEY (Secondary Emission Yield) materials have been done since they are of paramount importance for satellite communication applications, which demand for higher number of channels operating at high power levels. Finally, a deeper study over different fabrication methods has been done to cope with the satellite communications industry requirements.

1.1 Satellite Communications

Satellite communications, in the telecommunications field, can be defined as the use of artificial satellites to provide global communication links between various points on Earth (relay analog and digital signals carrying voice, video, and data) [1]. The history of the satellite communications begins with the launch of the Intelsat series in the late 1960s. Intelsat 1, previously known as Early Bird, was built by the Boeing Satellite Systems for COMSAT. It was launched in 1965 and was the first commercial geostationary communications satellite. Intelsat 1 carried 240 telephone lines and was also capable of transmitting one television signal. In those days, only a few countries started with the space race. Fifty years later, more than 50 countries have started to invest in satellite communications (see Figure 1.2), which demonstrates the key advantages that satellite communications provide the society [2]. Firstly, the allowance of wireless communications between two points on Earth which are separated through large distance. Moreover, not only allow they the communication between two terrestrial points, but also maritime and aeronautical ones, since their coverage has global availability and high reliability. Additionally, satellite communications can be considered as a very cost-effective solution, where neither the number of users nor the distance between them have influence in the final cost. Furthermore, over the last years, the satellite services have been diversified to:

Figure 1.1: The RCA Satcom K-2 communications satellite is photographed as it spins from the cargo bay of the Earth-orbiting Atlantis. A TV camera at right records the deployment for a later playback to Earth. This frame was photographed with a handheld Hasselblad camera inside the spacecraft.

- **Consumer Services (CS)**: satellite television, radio or broadband communications.
- **Fixed Satellite Services (FSS)**: where the signals are transmitted in a limited number of fixed locations on the Earth. It includes transponder agreements and managed network services.
- **Broadcast Satellite Services (BSS) or Direct Broadcast Service (DBS)**: where the signals are transmitted directly to the specific customer.
- **Mobile Satellite Services (MSS)**: where the signals are transmitted from/to mobile terminals and/or fixed gateways.
- **Earth Observation Services (EOS)**.

Basically, satellite communications are composed of: the space segment, the ground segment, and the control segment [1].

- The **space segment** contains one or several satellites organized into a constellation.
- The **ground segment** contains all the traffic of the earth stations.
- The **control segment** contains all ground facilities for the control and monitoring of the satellites, also named TTC (Tracking, Telemetry and Command) stations. It also allows the management of the traffic and the on-board resources of the satellite.

The type of links (shown in Figure 1.3) are the following:

- The **uplink** from the earth stations to the satellites.
- The **downlink** from the satellites to the earth stations.
- The **intersatellite link** between satellites.

Uplinks and downlinks consist of RF modulated carriers while intersatellite links can be either RF or optical. These links are determined by several parameters such as the bandwidth occupied by the signals. This bandwidth depends on the information data rate, the channel coding rate (forward error correction), and the type of modulation used to modulate the carrier. For satellite links, the trade-off between required carrier power and occupied bandwidth is paramount to the cost-effective design of the link (see Table 1.1).

Regarding the allocation of these links, generally, Ku- and Ka-bands and those below them are the most popular because of the relative low cost of available equipment and the more favorable propagation characteristics. The Q-, V-, and W-bands employ millimeter wavelengths and are potentially useful for very high bandwidth transmissions into small receiving antennas.

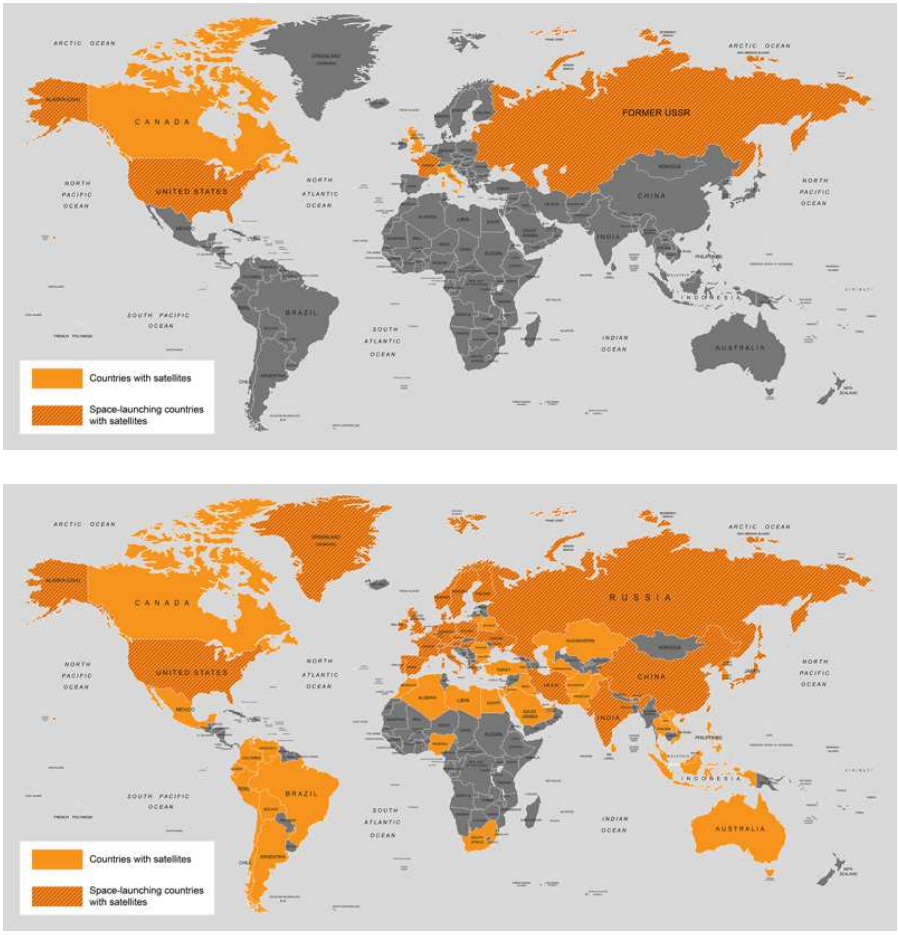

Figure 1.2: Evolution of the countries with satellites between (a) 1966 and (b) 2016, [2].

Table 1.1: Satellite Frequency Bands

Band	Downlink (GHz)	Uplink (GHz)
C band	3.7 - 4.2	5.925 - 6.425
Ku band	10.7 - 12.7	14 - 14.5
Ka band	17.7 - 21.2	27.5 - 30
Q band	37.5 - 42.5	47.2 - 51.4

The ground segment is composed of all the earth stations: those connected to the end-user's terminal by a terrestrial network and, in the case of small stations (Very Small Aperture Terminal (VSAT)), directly connected to the end-user's terminal. There are stations which both transmit and receive and others which receive only. The latter is the case, e. g., of the home receiving stations for broadcasting satellite systems for television or data signals.

Regarding the space segment, the satellite can be subdivided into the *payload* and the *platform*. The payload basically consists of the receiving and transmitting antennas and the electronic equipment which supports the transmission of the carriers. For this reason, the payload is the most significant part, in view of microwave filters, as it is shown in Figure 1.4 [3]–[7].

The main functions of the payload are the following (see Figure 1.4):

- to capture as little interference as possible the signal transmitted by the earth stations in the antenna;
- to amplify the received carriers while limiting noise and distortion as much as possible in the receiver block;
- to change the frequency of the carriers received on the uplink to the downlink;
- to separate in frequency the carriers of the downlink;
- to amplify individually each channel;
- to combine the carriers on a manifold;
- to radiate the carriers the amplified signal.

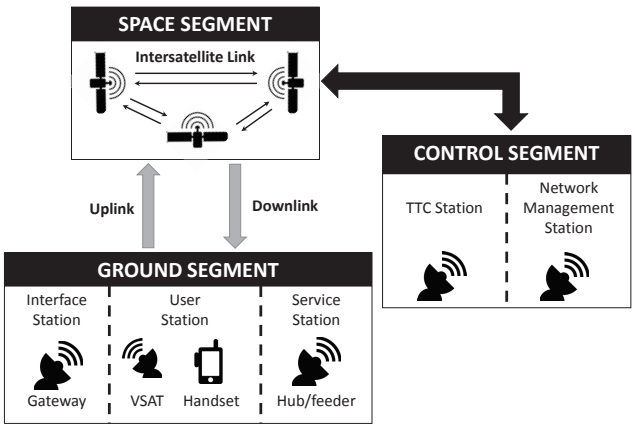

Figure 1.3: Block diagram of the satellite communications.

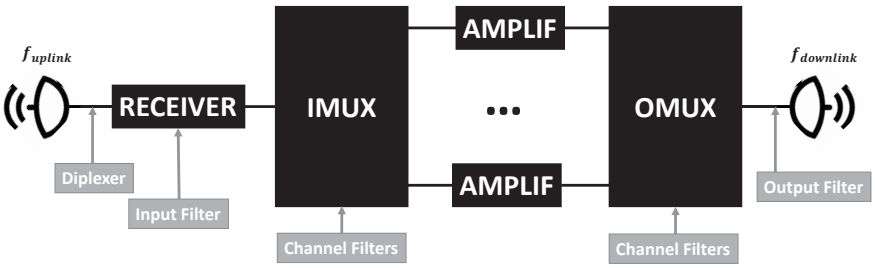

Figure 1.4: Block diagram of a typical payload of a communication satellite.

The conventional payload resembles a *bent-pipe* in the sky, more appropriately called a *repeater*. However, other advanced payload functions include digital-signal processing which are accomplished with on-board processors. There are different types of payload configurations which depend on the demanded service (i.e. FSS, BSS, MSS, Earth Observation, etc.).

The space environment and the limitations of RF and baseband hardware impose some constraints to the payload [8]:

- **Mass**. The payload mass reduction is perhaps the most crucial design criterion. Any decrease in the payload mass will have a direct consequence in the launch costs.
- **Power consumption**. Each piece of equipment in the payload is designed to minimize its power consumption. Moreover, it is important to note that any power not emitted as RF is converted to heat, complicating the thermal management. It will be related to the insertion loss in the case of microwave filters.
- **Thermal control**. The electrical performance of most components of a payload are temperature dependent. Thus, it must be controlled and carried away to prevent temperature rise.
- **Transmission requirements**. Passive equipment (such as filters) relies on resonance or electrical path-length effects which are both frequency dependent. Furthermore, imperfect matching between microwave elements causes reflections, resulting in interferences across the bandwidth.Then, the group-delay must be also controlled. Payloads typically require a maximum group-delay variation of few nanoseconds across the required bandwidth.

- **Noise**. Noise sources in payloads are generally divided into phase-noise and thermal-noise, although both types are, in fact, thermal in origin. The phenomenon of multipaction is also mentioned here as it results in a high level of broadband noise. This effect will be explained in detail in Section 1.4. Payload noise will directly add noise into the overall satellite link so it is usually rigorously controlled.

- **Spurious signals**. The ideal payload would simply amplify and translate the frequency of the uplink signal. As well as the previous noise, there are spurious signals which are introduced into the transmission path. PIM products are usually associated with active equipment, but passive devices such as connectors and filters can generate them, particularly when high power is involved. PIM products can be caused by any non-linear process, but oxide layers on metal-to-metal interfaces or saturated ferromagnetic materials are frequent causes. Another major source of spurious signals in a payload is the local oscillator. The frequency-conversion process will produce the input frequencies plus or minus the local oscillator frequency. Finally, the non-linear operation of the amplifiers also introduces unwanted harmonics to the RF chain.

The *satcom* market is experiencing profound technical transformations with the introduction of Very High Throughput Satellites (VHTS), flexible payloads, and large satellite constellations. It has resulted in significantly system capacity increase and higher bandwidth to end users at a reduced cost per bit. For example, OneWeb satellite constellation will have more than 650 low-Earth orbit (LEO) satellites delivering a total throughput of more than 5 Terabits, providing a global coverage of high-speed Internet connectivity equivalent to terrestrial fiber-optic networks (see Figure 1.5) [9]. In the case of GEO systems, a high number of identical high power filters (band and low pass filters) is required with the consequent accommodation restrictions. Similar constrains regarding accommodation are envisaged in the case of small LEO satellites. In both cases, satellite manufactured have begun to reformulate the satellite design, testing and production to cope with the new requirements in terms of time and costs. Efficient EM design could allow the manufacturers of RF/Microwave parts to go directly from a digital design to the final product reducing as much as possible any cost associated with manufacturing and testing of breadboards to validate the designs. Furthermore, the use of COTS (Commercial off-the-shelf) components, miniaturization, remote testing and integration of subsystems (i.e. by additive manufacturing) can be applied for potential reduce costs in satellite production. Besides, mass production is a key issue in the large satellite constellations and multi-beam payloads.

Therefore, the growing development of modern communication systems, such as Internet and television broadcasting, military applications, and cellular communications services, have triggered the need of a huge development of more complex payloads where microwave passive components and, specifically, microwave filters are key elements to improve the aforementioned constraints in these systems. To fix the scope of this Thesis, different parts of the payload of a satellite system, where

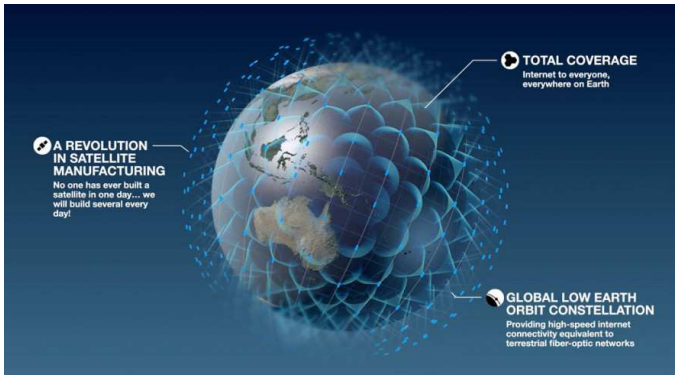

Figure 1.5: OneWeb's constellation will consist of 648 LEO satellites plus spares. Credit: Airbus/OneWeb.

microwave filters are typically inserted will be considered: the input filter, the output filter, and the diplexer (see Figure 1.4).

Based on the need of each application, as it is detailed in [5], [10], filters are required to have different electrical specifications, and are implemented in the most suitable transmission technology. There are several technologies to implement microwave filters: acoustic, MEMS, planar, coaxial, dielectric or waveguide. The selection of the technology is a trade-off between: in-band and out-of-band performance, thermal and mechanical performances, power handling or cost [11]. For instance, in spite of the recent trend toward miniaturization and integration, if low loss and high-power handling capability are a requirement, rectangular waveguide will be the selected technology [12]. Indeed, it is widely utilized in a large amount of filters in the payload of a communication satellite, and will be the technology utilized in the developments of this Thesis.

1.2 Rectangular Waveguide

In order to contextualize the technology which is used along this Thesis to implement filters, a brief background about rectangular waveguide technology is presented. Rectangular waveguide was one of the earliest types of transmission lines used to transport microwave signals [12].

The rectangular waveguide with a cross section, as illustrated in Figure 1.6, is a single conductor device that can propagate TE (transversal electric) and TM (transversal magnetic) modes, but not TEM (transversal EM) waves. Moreover, the TE and TM modes of a rectangular waveguide have cutoff frequencies where below which the propagation is not possible since its phase constant β must be real .

The TE and TM waves, or modes, may be labeled by two identifying integer subscripts n and m, for example TE_{nm}. The integers n and m pertain to the number

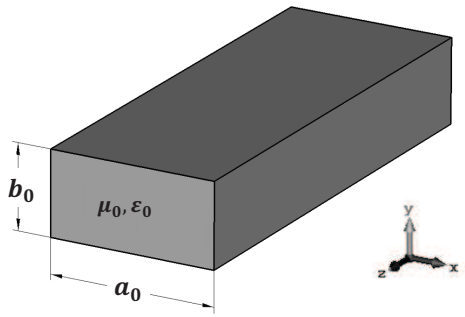

Figure 1.6: Geometry of a rectangular waveguide.

of standing-wave interference maxima occurring in the field solutions that describe the variation of the fields along two transverse coordinates [13].

At a given operating frequency f, only those modes TE_{nm} and TM_{nm} having $f_{co,nm} < f$ will propagate; modes with $f_{co,nm} > f$ will lead to an imaginary β, meaning that all field components will decay exponentially away from the source of excitation. Thus, each mode (combination of n and m) will have a cutoff frequency $f_{co,nm}$ given by equation (1.1).

$$f_{co,nm} = \frac{1}{2\pi\sqrt{\mu\epsilon}}\sqrt{\left(\frac{n\pi}{a_0}\right)^2 + \left(\frac{m\pi}{b_0}\right)^2} \tag{1.1}$$

Assuming $a_0 > b_0$, the mode with the lowest cutoff frequency, which is called the fundamental mode, is the TE_{10}.

In the vast majority of applications the operating frequency and guide dimensions are chosen so that the fundamental TE_{10} mode will only propagate (single-mode operation). If more than the first mode is propagating, the waveguide is said to be in multi-mode operation. Given the importance of the fundamental TE_{10} mode, the attenuation due to conductor loss will be defined by equation (1.2),

$$\alpha_c = \frac{2\pi^2 \cdot R_s \cdot \left(b_0 + a_0/2 + \beta^2 \cdot a_0^3/2\pi^2\right)}{\omega \cdot \mu \cdot a_0^3 \cdot b_0 \cdot \beta} \tag{1.2}$$

where R_s is the wall surface resistance and ω is the operating frequency.

1.3 Classical Design Methods for Rectangular Waveguide Filters

A first approach to define a microwave filter is that it is a passive component which has the property of the transmission of selective frequencies, allowing to transmit and attenuate energy in the passband and the stopband respectively. A very deep review of many different filter topologies and corresponding electrical performances are described in [14]–[17]. Moreover, over the last years, some overviews about the design and development of microwave filters have been also published in the literature [10], [18], [19]. In spite of the complexity of the design procedure for microwave filters, it can be summarized in three steps as it is mentioned in [20]: i) mathematical filter synthesis by means of lumped and / or distributed elements [14]; ii) physical dimensions estimation that are related with the elements of the prototype [15], [16], and iii) final optimization of the dimensions of the filter [21], [22].

Classical theories and techniques for filter design are: the image parameter method and the insertion loss method [14]. The image parameter method is a simple method that involves the specification of passband and stopband characteristics for a cascade of two-port networks. However, with this method it is not possible to incorporate an arbitrary frequency response. Instead, the insertion loss method allows a high degree of control over the passband, the stopband and the phase performance by means of a desired rational filtering function such as Butterworth, Chebyshev, Zolotarev, and Chained Function. Both methods provide lumped elements, but for microwave frequencies such designs must be modified to use distributed elements consisting of transmission line sections (see Figure 1.7). This is due to the fact that the equivalence between microwave structures used and their lumped element models will hold for a certain bandwidth but will quickly degrade as the frequency moves away from it. Therefore, these problems may be of little importance for narrowband applications, but they will become more troublesome when wideband applications are demanded [12].

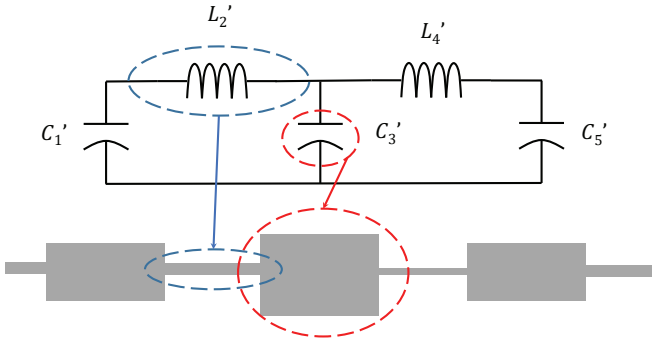

Figure 1.7: Example of distributed elements which correspond to lumped elements.

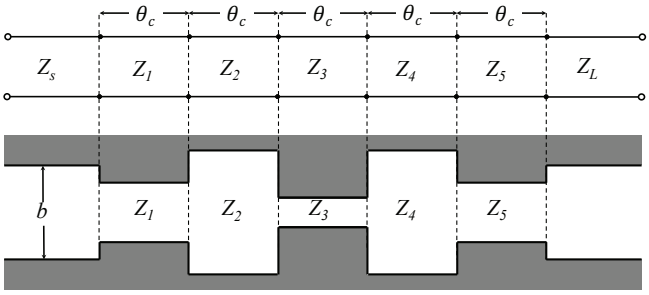

Figure 1.8: Fifth-order stepped impedance LPF prototype circuit and direct rectangular waveguide realization.

In order to provide this step for the insertion loss method, some techniques such as *Richards' transformation* or *Kuroda's identities* are perfectly described in well-known text books like [12], [13], [15], [16]. *Richards' transformation* is used to convert lumped-elements to transmission line sections, while *Kuroda's identities* are able to separate filter elements with transmission lines, transform series stubs into shunt stubs or change unworkable characteristic impedances into realizable ones.

It is interesting to describe briefly the *Richards' transformation* published in [23]. This establishes a simple relationship between lumped and distributed elements using a simple transformation, where an inductor would become a short-circuited stub, while a capacitor can be replaced by an open-circuited stub of identical electrical length. It maps the frequency response of the microwave distributed network between $-f_0 \leq f \leq f_0$, into the frequency response of the equivalent lumped-element network defined between $-\infty \leq f \leq \infty$, where at f_0 the transmission lines will be $\lambda/4$ and an attenuation pole will occur. One of the most significant characteristics of this transformation is that the response will be periodically repeated for higher frequencies [24], [25].

A relatively easy way to implement LPFs utilizing the technique previously described is to use alternating sections of high and low characteristic impedance lines. Such filters are referred as stepped-impedance (corrugated) filters and are perfectly described in the literature [15], [16], [26], [27].

The classical corrugated waveguide filter was firstly proposed by Cohn [26], who estimated the physical dimensions of the filter after relating the prototype of lumped / distributed elements (previously calculated by a mathematical method) to the components of the real structure. In [28], Levy presented an insightful method based on a set of commensurate transmission lines of different impedances, which are implemented in rectangular waveguide by means of a cascade of waveguide sections of different heights (see Figure 1.8). However, the straightforward application of these techniques produces some errors (mainly due to the excitation of higher-order modes), which are typically compensated by a final optimization.

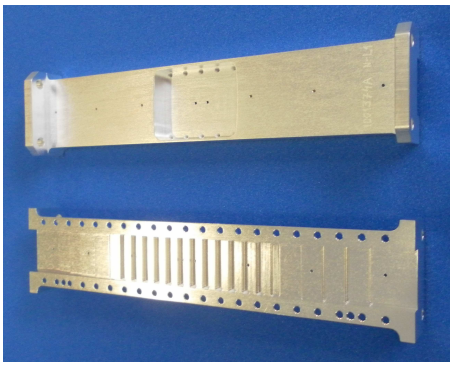

Figure 1.9: Photograph of a classical corrugated low pass filter.

Classical corrugated LPFs exhibit low-loss, wide passband, and a compact size, although it is sometimes necessary the use of transformers at the input and output ports in order to match the filter with the standard ports [15]. However, a trade-off exists between a wide spurious-free stopband and the minimum mechanical gap of the device. This gap size will define the high power handling capability of the filter. Moreover, since the main function of the classical E-plane corrugated filter is to reject the noise and interfering signals up to several times the cutoff frequency, a degradation of the stopband may occur for the following reasons: i) the repeat passbands of the commensurate line network, ii) the mode conversion within the filter structure, and iii) propagation of the higher-order TE_{n0} modes. The first issue is an inherent feature of the design technique and cannot be avoided. The second problem can be considerably reduced by ensuring that the heights are not greater than the incoming waveguide [15]. Ideally, there should be no higher-order TE_{n0} modes at the input of the filter, but they might be generated by certain coaxial-to-waveguide transitions, waveguide bends, and / or misalignments between sections of waveguide (H-plane discontinuities) [12]. Therefore, these spurious bands may appear and ruin the out-of-band measurements of the device under test [27].

When the rejection of the higher-order TE_{n0} modes is also a requirement in a waveguide LPF, the widely-employed classical solution is the waffle-iron filter, which provides very wide stopband (up to several harmonics) attenuating all the propagating modes in the required frequency band. Invented by S. B. Cohn [29], its physical structure (see Figure 1.10) is based on the aforementioned classical corrugated low-pass filters, where longitudinal slots are added to conform the waffle-iron structure and to achieve the suppression of the higher-order TE_{n0} modes. The attenuation of these modes can be explained considering that the waffle-iron structure is designed to be roughly isotropic, having the same characteristics, at a given frequency, for plane waves propagating through it in any direction. Thus, knowing that any TE_{n0} mode can be decomposed into two plane waves propagating at different angles, all of them are affected similarly at a given frequency [13].

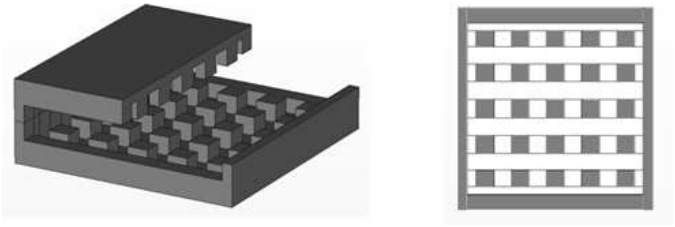

Figure 1.10: Classical uniform waffle-iron filter; a) cut-away perspective view, b) top view.

1.4 Multipactor: Simulation and Test

Nowadays, the satellite industry demands a prior assessment of the power-handling capability of the devices since most of them, such as the output LPFs or the diplexers proposed in this Thesis, operate in high-power conditions. When designing a filter for high-power operation, it is usually taken into account the multipactor effect. In fact, this phenomenon sets one of the main limits to the working power of RF devices in space [30].

The multipactor phenomenon is a RF resonant avalanche of free electrons between two surfaces of a microwave device in vacuum sustained by the secondary electron yield (SEY) of the materials involved [31], [32] (the SEY of the materials will be explained in detail in the next Section 1.5). If the free electrons enter in resonance with the EM field, they will be accelerated and will collide with the metallic walls of the device. Then, if its energy is high enough, more electrons will be striped from the surface (SEE). Then, the electron cloud will be accelerated towards by the EM field, repeating the process. This results in the disturbance of the signal, additive noise, high reflections, and finally it may destroy the device [6].

Multipactor effect depends on number of factors, including the size of the gap across the electrons are accelerated, the vacuum condition, the frequency, the strength and duration of the EM field, the SEY of the material, and the initial energy and number of electrons present [33].

Multipactor experiments and tests are relatively expensive, time, and resource consuming. Thus, with appropriate models of the phenomena and different materials characterization, simulation will be the key to prevent possible failures in the device before they may occur. Over the last years, multipactor models and simulation tools have made much progress. In order to estimate the multipactor threshold in waveguide filters, two approaches are usually used: the parallel-plate model and the particle-in-cell (PIC) tool.

1.4.1 Parallel-Plate Theory: ECSS Multipactor Tool

The parallel-plate model was developed at the European Space Agency [34]. Some experiments were performed with different gap sizes and waveguide geometries, showing different susceptibility zones where each boundary zone is given by a co-

efficient (which depends on the material) and the product between frequency and gap. Although in theory this model only applied to infinite parallel-plate geometries, it is used to predict multipactor in many different waveguide structures [30]. In fact, within the framework of some projects sponsored by ESA, some SW tools to predict the occurrence of multipactor discharge modeled as parallel plate have been developed [35], and methods to determine the breakdown voltage in real waveguide components have been proposed [36]–[38]. However, parallel-plate model provides a too restrictive estimation of the threshold input power since the infinite parallel-plate theory is, in many occasions, the worst possible scenario. In fact, over the last years, the theory has been enhanced in the case of a parallel-plate waveguide partially filled with dielectrics or magnetized ferrite [39], [40]. Moreover, the multipactor effect has been also investigated in a waveguide iris [41], between curved metal surfaces [42], and narrow gaps [43].

Following [44], the threshold input power, P_{thr}, can be estimated as:

$$P_{thr}(f) = \frac{1}{[VMF_{max}(f)]^2} \cdot \frac{V_{multi}^2(f)}{2 \cdot Z_0} \tag{1.3}$$

where the multipactor breakdown voltage (V_{multi}) in the mechanical gap of height b_{gap} is calculated as:

$$V_{multi}[V] = 62.4 \cdot f[GHz] \cdot b_{gap}[mm] \tag{1.4}$$

considering that silver is used as the conductor material. In equation (1.3), Z_0 is the input impedance defined by the following equation:

$$Z_0 = \eta_0 \cdot \frac{2b_0}{a_0} \cdot \frac{\lambda_{gD}}{\lambda} \tag{1.5}$$

where a_0 and b_0 are the width and height of the port, λ_{gD} is the wavelength in the input guide, λ is the wavelength in free space, and $\eta_0 = \sqrt{\mu_0/\epsilon_0}$ is the vacuum intrinsic impedance. Finally, in equation (1.6), the Voltage Magnification Factor (VMF) is defined as the ratio between the voltage along the mechanical gap (V_{gap}) and the input voltage (V_{in}) at a fixed frequency.

$$VMF = \frac{V_{gap}}{V_{in}} \tag{1.6}$$

In this Thesis, the VMF is calculated at the critical frequency from the electric field distribution in the minimum mechanical gap of the devices (where the maximum field is achieved) obtained with CST MWS.

The ECSS Multipactor Tool provides similar results (almost equal) to the ones obtained following the previous formulas since they use the same equations to calculate this value. The only difference is due to the fact that, in this case, the voltage obtained with CST MWS at the minimum gap of the device can be considered, but not the one at the input port because it can be known a priori if a power equal to 1 W is used as the input signal. The difference between this voltage value and the one obtained with CST MWS at the input port produces the slight difference between both power estimations.

1.4.2 PIC Tools: CST Particle Studio and SPARK3D

Recently, numerical simulation methods based on PIC codes have been developed achieving a more accurate multipactor analysis [45]–[49]. To do this, the EM field distribution inside the microwave device is utilized. Once the EM field distribution is known for any point of the device, some electrons are generated (the initial angle and energy are the main parameters) and electron trackers are used to estimate the threshold input power of the multipactor, taking into account the SEY of the material, the operation frequency, and the geometry.

In this Thesis, two different SW will be used: CST Particle Studio (CST PS) [49] and SPARK3D [47]. The procedure to perform high-power simulations with both SW is detailed in Chapter 4, where simulations will be also compared with high-power tests.

1.4.3 Multi-carrier

Classical multipactor theory only covers the single-carrier case (only one carrier is transmitted). However, in such cases as satellite applications, the normal case is to operate with a high number of channels, each of which operating at a single carrier frequency. So, this produces a higher power level in the multi-carrier-path of the payload. Therefore, a typical multi-carrier signal is a complex signal composed of several very-closed modulated signals. Hence, the resulting multi-carrier signal is a modulated RF signal whose envelope varies periodically. The study of this kind of signals and, specifically, their behavior in a multipactor context is not theoretically well understood yet. Indeed most of the published works are based on experimental results or PIC codes. In this framework, it is important to highlight the recently published PhD thesis, [50], where multi-carrier theory and the different detection methods are very well reviewed.

There are several multi-carrier prediction methods used by the industry. The most restrictive one, which will be applied in this Thesis to obtain the worst case, is the N^2 rule. This method forces the in-phase maximum peak power to be below the single-carrier breakdown level, where N is the number of carriers. For example, if a multi-carrier system of 2 carriers of 125 W each is assumed, the peak power that the device needs to withstand will be 500 W (125 W x 2^2). This rule does not allow the multi-carrier envelope to be above the threshold at all, and therefore no electron production exists.

Another method is also utilized for the multipactor estimation in a multi-carrier scenario. The standard *20-gap-crossing rule* was proposed by ESA [44] [51], [52]. The *20-gap-crossing rule* states that multipactor occurs only if the multi-carrier signal envelope exceeds the breakdown voltage for a time equal or higher than the time that an electron takes to cross the gap 20 times. This rule produces more relaxed predictions in comparison with the N^2 rule. However, it is important to stress that this rule is extracted from several simulations and experiments and does not have a theoretical basis. Then, for both rules, large design margins are applied to be even more conservative (typically +3 dB or + 6 dB).

Recently, a non-stationary multi-carrier theory has been published as the first theory which is able to fully characterize the multipactor phenomenon for a completely arbitrarily multi-carrier signal [50], [53], [54].

1.4.4 Test

Multipactor detection methods fall into two categories: local and global. Local methods are used close to the point of the actual discharge, and global methods show that a discharge is present somewhere in the high power assembly [33]. In order to detect the multipactor discharge, the set-up should include at least two detection methods and at least one of these methods shall be a global method [55].

The typical local detection method is the electron probe, which is utilized nearby the discharge point. It is a very small positively charged probe which attracts the free electrons generated as a result of a multipactor discharge. In order to measure it, a high impedance amplifier is connected to the probe to provide an impedance transformation to 50 Ω. Then, an oscilloscope or voltmeter may be used to monitor the probe current.

Two different global methods are usually utilized. The nulling of the forward/reverse power is used to indicate if a discharge is present somewhere inside the DUT. It is implemented by superposing the input and reflected signals with a directional coupler. The sample of the input power is connected to a variable attenuator and the reflected to a phase shifter. Then, both signals are combined with a 3 dB hybrid and the resulting signal is measured in a spectrum analyzer. This method is very sensitive, making it very appropriate to detect a possible discharge. The second global method is the harmonic detection. When a multipactor discharge occurs, it can be observed in the spectrum since the different harmonics increase their power. Therefore, by filtering the signal of the different harmonics (the second and the third are usually observed) and amplifying it with low-noise amplifiers, it can be measured with a spectrum analyzer.

A schematic of the RF breakdown test set-up, where the previous detection methods can be observed, is depicted in Figures 1.11 and 1.12. In order to initiate the multipactor discharge, it is important to have enough free electrons in the vicinity of the theoretical area of discharge inside the DUT. To do so, two different methods are utilized. The first one is to use beta emitting radioactive source placed near the DUT. Indeed, in the ESA-VSC High-Power Laboratory of Valencia (where the multipactor tests presented in this Thesis took place), a ^{90}Sr beta emitting radioactive was utilized. To increase the efficiency of the radioactive source and generate enough electrons inside the DUT, the walls of the structure in the vicinity of the theoretical area of discharge must be of around 1 mm-thickness. The second method to seed the DUT is an optical fiber connected one end to an ultraviolet lamp and the other inside the DUT, introduced through a venting hole placed in the critical area of discharge. A detail of the RF breakdown set-up configuration with the optical fiber and the radioactive source is shown in Figure 1.13.

Last but not least, the real operation of the DUT in the space conditions are mimicked in the vacuum chamber. To do so, the pressure inside the chamber is set with a

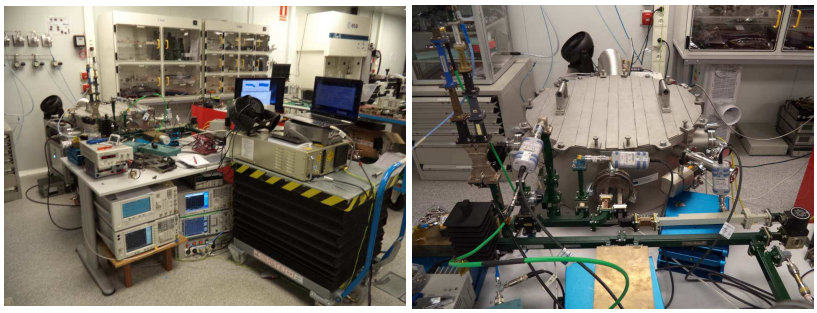

Figure 1.11: General view of the Ku-band test bed.

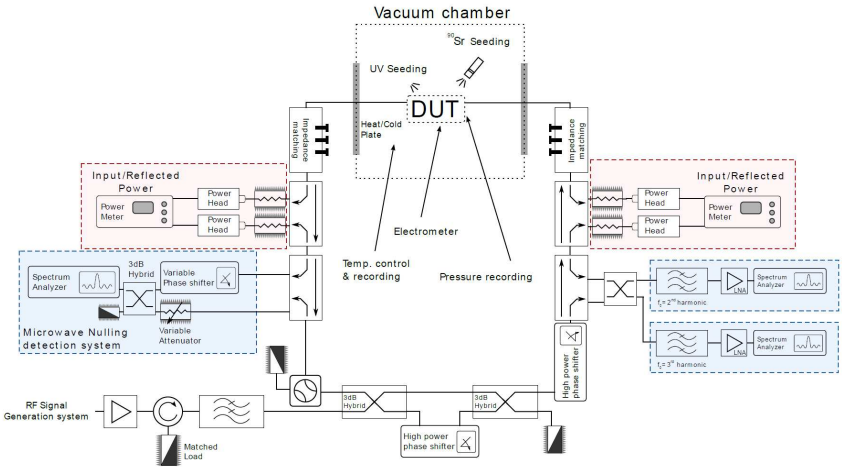

Figure 1.12: Schematic of the multipactor test bed configuration.

value of less than $5 \cdot 10^{-5}$ mbar. Moreover, ambient temperature (22°C) and a pulse duty cycle of 2% and width of 20 μs is used.

Finally, it is important to highlight that in the space industry, a margin between 3-4 dB (depending on the component) over the multipactor threshold level is required for tested devices and only components with a theoretical margin between 6-12 dB are exempt from testing [44].

1.5 Materials

Traditionally, for space applications, the materials used to fabricate filters must be stable, structurally stiff, lightweight, highly conductive, thermally stable and, taking into account the multipactor issues explained in the previous Section 1.4, with a good performance in SEY.

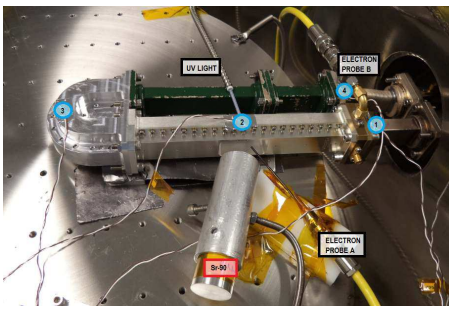

Figure 1.13: DUT installed inside the TVAC for high power tests: radioactive source, UV lamp, thermocouples and local detection systems.

For instance, Invar (Fe-Ni alloy) shows a very low temperature coefficient of thermal expansion (CTE), so it will ensure that the intended passband of the filter does not shift significantly with changes in temperature [56]. Iron-Nickel alloys of 36 weight percent nickel and 64 weight percent iron is generally regarded as having the lowest CTE among all alloys in the range from room temperature (about 20° C.) up to approximately 230° C. Invar has low coefficients of expansion over only a rather narrow range of temperature. Nevertheless, it is extremely heavy and has poor electrical conductivity, so all parts fabricated with this material need to be silver-plated to minimize the insertion loss and it should be only reserved to the irises of the BPFs.

Aluminum is lightweight and easy to mechanize, and that is why it is the preferred material for the hardware manufacturing in the payload of a satellite. However, there are several negative points such as, easy oxidation, low conductivity, or SEY. Therefore, gold and silver are quite frequently utilized as coating to improve the conductivity and the high-power handling capability [57]. Recently, aluminum-silicon (Al-Si) alloys have been proven to be exceptional due to corrosion resistance, low wear rates, and low thermal expansion [58]. Silicon is one of the elements which when added to aluminum has minimum weight increment. Increase the silicon percentage in Al-Si alloys results in the increase in the wear resistance and mechanical properties. When increasing silicon proportion beyond 17% in conventional casting processes, a deterioration on the material toughness happens. This problem has been effectively overcome by the use of rapid solidification processing (RSP). RSP was initially developed approximately 35 years ago by Dewez and his colleagues at California Institute of Technology. They chilled a thin layer of liquid metal on to a very conductive substrate. RS is defined as the transformation of liquid to solid by removing superheat and latent heat at a cooling rate of 102-106 Ks^{-1} [59]–[62]. Indeed, by changing the alloy composition of the aluminum-silicon system, the CTE of the substrate material can be adjusted and by raising the silicon content, the physical properties density and thermal expansion decrease while the specific stiffness increases without impacting density or thermal conductivity.

Lighter materials, such as Kevlar (composed of light plastic fibers), graphite, carbon fiber technology, and magnesium have been also considered [5], [6], [63]. Nev-

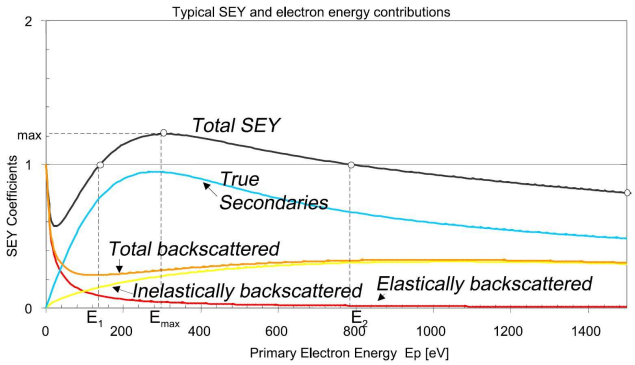

Figure 1.14: Typical SEY curve [35].

ertheless, when using these light materials a coating of silver or gold onto them is typically required to achieve the good conductor properties required in the waveguide walls.

The multipactor discharge is highly dependent on the surface material as it was mentioned in the previous Section 1.4. In fact, depending on the impact energy and angle, the electrons can be:

- deflected;
- can enter inside the material, loose some energy, and then being deflected backwards, or;
- can penetrate in the material and transfer part of its energy to secondary electrons which are released backwards from the material surface.

The SEY is the ratio between emitted and impacting electrons on a material surface, being a characteristic of each material. It is typically modeled as a function depending on the energy of the impacted electron. Figure 1.14 shows a typical SEY curve, where E_1 and E_2 are the energy values in which the SEY is equal to 1. E_{max} is the energy in which the SEY reaches its maximum value (σ_{max}). These parameters are typical in the literature [32] for characterizing the SEY of a material.

A studied way to avoid multipactor discharge is to use materials with maximum SEY coefficient, σ_{max}, less than one. Unfortunately, good conductors used in space filters (such as copper or silver) have σ_{max} greater than one and are dependent on the surface oxidation and contamination. Metals with σ_{max} lower than one, like titanium or stainless steel, usually have a poor conductivity leading to high insertion loss. For that reason, it exists a promising investigation in new materials and coatings of low secondary electron emission to prevent the multipactor effect in high-power RF devices in space [64].

As it has been mentioned previously, typical SEY parameters for the most relevant materials come from the fitting of the multipactor breakdown results to a particular

test campaign done in [34]. However, there are no *universal* SEY curves since, for example, the SEY of the silver coating of a company may differ from the SEY of the silver coating of another company [65]. Moreover, the SEY properties of a material may change with time in a process that is called aging. Therefore, with all of this in mind, it is important to do a SEY measurement with the coating of the material used in the device under test.

1.6 Fabrication Methods

The most frequent manufacturing technique for waveguide filters for space applications is the computer-controlled milling (CCM or CNC) [57], which is a machining process that uses rotary cutters to remove material from a work-piece. This technique leads to very efficient low-cost designs and short manufacturing time. Nevertheless, in many microwave applications, it is necessary the use of ultra-precision machining to meet the performance requirements of the final product, particularly at very high-frequency ranges such as Q, V, W or even higher bands, where the advantages of CCM seem less obvious due to the manufacturing tolerances [66]. Furthermore, when CCM is employed, the structure needs to be divided into several subsections which must be assembled together later on. This fact leads to misalignments between the different subsections that worsen the RF performance. Moreover, some of the corners of the device need to be rounded (this is the so-called rounded-corner effect over the frequency response, that has been widely studied in the literature [67]).

In the last years, additive manufacturing (AM) has been proposed as a very promising solution, particularly for structures of very complex geometries [68]. However, the accuracy provided by this manufacturing method, together with the difficulties when silver plating needs to be applied, suppose a drawback for nowadays demanded solutions.

Electroforming process is an old but still interesting alternative for manufacturing complex designs which require low insertion loss and high geometrical accuracy [57]. Electroforming can be simply summarized into three steps: i) mandrel preparation, ii) electro-deposition, and iii) mandrel removal. A range of fabrication methods are used to produce mandrels such as CCM or EDM (electro-discharge machining). Nevertheless, at frequencies above the G band ($\lambda_0 < 2.1$mm), this technique starts to be difficult to perform and it does not provide the required precision due to the small size of the devices [69], [70]. At this point, it is noticeable the need to develop new and advanced alternative machining techniques; more precise, more efficient, and with a low cost.

Although, of course, CCM is currently the most used fabrication technique and, probably, its advantages surpass the disadvantages in most cases, there are also some cases where electroforming behave better, in particular for intricate geometries, as orthomode transducers [71].

1.6.1 Computer-Controlled Milling (CCM)

The most important machining processes for mechanical microwave engineering are of course computer-controlled milling (CCM). In many microwave applications, such as space applications, waveguide filters [5] are usually manufactured by CCM.

CCM creates the piece by removing unwanted material by means of rotatory cutters from a blank. The milling process requires a milling machine, work-piece, fixture, and tools. The work-piece is a piece of material that is secured to the fixture, which itself is attached to a platform inside the milling machine. The cutter is a cutting tool with sharp teeth that is also secured in the milling machine and rotates at high speeds. By feeding the work-piece into the rotating cutter, material is cut away from this work-piece in the form of small chips to create the desired shape (see Figure 1.15). The most important characteristics of a machining process are: feed, depth of cut, cutting speed, tool geometry, tool angles, material and coating type of the tool and the nose radius [72].

The basic design rules to make the milling process of microwave filters low-cost and easier are as follows:

- To try to minimize the material removed.
- To try to reduce the workpiece in order to minimize the manufacturing stages.
- To avoid long, thin or flexible areas where the workpiece could be damaged due to machining forces.
- To select geometries suitable for common standardized tools.
- To minimize the number of tools for the different machining processes.
- To aim at symmetrical geometries.
- The radius of the tools should be selected as bigger as the final device permits, taking into account that the length of the tool should not surpassed four times the diameter of the tool in order to avoid harmful vibrations.

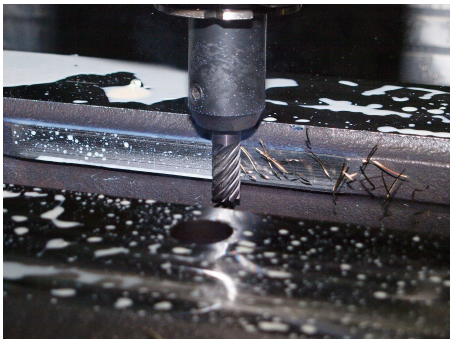

Figure 1.15: Milling example.

The cutter in a CCM machine is able to move along multiple axes (there are now 5-axis machines), and can create a rich variety of shapes [73]. By means of large cutters, the process makes the production more cost-effective and efficient. However it implies that the radius of the tool will be wider to avoid harmful vibrations. These vibrations often result in an increase of the machining forces that could damage the work-piece [57]. In fact, depending on the radius of the tool used, some detrimental effects can appear in the frequency response of the final device. This question has been extensively studied in the literature [67], [74].

In order to mechanize by CCM, it is necessary to split the device into different subsections (which might increase the level of passive intermodulation [66]). The most advisable solution is to divide it into two symmetrical structures. This will contribute to make the manufacturing process easier, and to simplify the assembly of the different pieces later on. It is important to note that misalignments between the different pieces will result in a degradation of the frequency response. Moreover, the different pieces must be assembled by screws with the consequent mass and footprint increase. Another point to take into account in this fabrication procedure is then the maximum allowed distance between the mounting screws since it will determine the quality of the enclosure of the device. A worse enclosure could lead to an increase of the ohmic losses or EM leakage. The tolerances of the CCM fabrication method are typically around 10-20 μm.

1.6.2 Electro-Discharge Machining (EDM)

EDM (Electro-Discharge Machining) is a typical fabrication method based on an electro-thermal production process in which a high voltage in an electrode is used to melt away metal, rather than mechanically removing metal with CCM [75]. EDM manufacturing is quite affordable when low counts or high accuracy is required. There are two basic types of EDM: sinker EDM and wire EDM. Sinker EDM uses an electrically charged electrode that is made with a specific geometry to burn this geometry into a metal component. Wire EDM uses a thin wire to cut through metal by the use of heat from electrical sparks. Both machining methods can easily fabricate very complex parts with very high precision (less than 5 μm for wire EDM). Moreover, EDM allows to copy the shape of the final devices without rounded corners. The surface roughness obtained is very good (mirror finish can be obtained). However, as it occurs with CCM, it is not possible to mechanize a filter in a single piece. Therefore, we will have the same problems as in CCM when the final filter is assembled.

1.6.3 Electroforming

Electroforming was first observed by Jacobi during the electro-deposition of copper onto a printing plate in 1837, and the ASTM (American Society for Testing and Materials) describes it as follows: *Electroforming is the production or reproduction of articles by electro-deposition upon a mandrel or mold that is subsequently separated from the deposit*, [76]. Therefore, based on the previous definition, electroform-

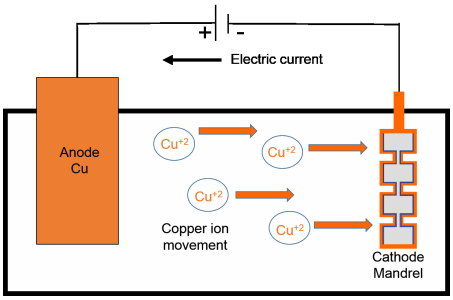

Figure 1.16: Detail of the electroforming process

ing process can be simply summarized into three stages: i) mandrel preparation, ii) electro-deposition, and ii) separation between the mandrel and the deposit [77].

Electroless plating, physical vapor deposition or spray forming are used as well as electroforming to produce components by means of deposition of metals on a mandrel [78]. Nevertheless, ”classical” electroforming will be explained in this Subsection.

A wide range of materials can be used to produce mandrels. The range can be classified as conductors (pure metals or alloys) or non-conductors (which must made it conductive to allow electro-deposition by means of thin metallic film) of electricity. Hence, within this classification, mandrels can be expendable or permanent and its choice depends on the particular design and the volume production. If there are not concave shapes in the device (shapes with interior angles greater than 180 degrees), it is possible to use permanent mandrels. However, if concave shapes are involved, the mandrel must be expendable. It is important to note that the success of an electroforming process is largely dependent on making a good choice of mandrel type and the dimensions and tolerance of the manufacturing process selected to fabricate the mandrel (EDM, CCM, etc.). The fastest and cheapest way to produce the mandrel in aluminum is by using EDM with a very thin wire. The use of other techniques such as CCM can be also employed if the geometry of the mandrel favors and demands the usage of the milling tools. The fabrication of the mandrel is critical in the whole electroforming process since it determines the accuracy of the final dimensions of the device and the roughness of its inner surface.

The prototypes fabricated by electroforming of this Thesis will be expendables and the mandrel will be manufactured by wire-EDM (fabrication method with the best tolerances and minimum radius) in aluminum (Aluminum alloy EN-AW6082).

Once the mandrel is manufactured, the next step is the electro-deposition. The basic principle of the process is shown in Figure 1.16. The process requires an electric current that passes between two electrodes (an anode and a cathode) immersed in a conducting electrolyte containing metallic salts. The anode is usually a bar of the metal being plated and the cathode is the mandrel. Therefore, the metallic ions contained in the solution are converted in atoms on the cathode surface, and these build up micron upon micron to produce an exact replica of the shape of the mandrel. Elec-

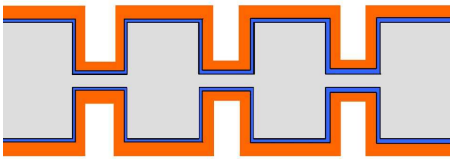

Figure 1.17: Detail of the electroforming process showing the different materials. Grey: Aluminum, Blue: Silver (15 μm thickness), Orange: Copper (1 mm thickness)..

troforming can fabricate a device in just one piece if the component includes a single mandrel. Moreover, the thickness of the deposit can be easily controlled, and different materials, such as nickel, copper or silver, can be used to grow the deposit (see Figure 1.17). The material thickness can typically vary between 0.01 to 0.5 mm with a shape deposition rate defined around 10 μm per hour [78]. For thicker devices, the shape deposition rate is increased. Additionally, in order to control the deposition upon the mandrel, it is important to define correctly the location of the anode and the cathode (as illustrated in Figure 1.16).

Finally, after the desired electro-deposition has taken place, the final electroformed component is separated from the mandrel. To do this, the mandrel is dissolved with a chemical solution leaving behind the finished device.

Therefore, electroforming appears as a technique able to: a) fabricate exactly the ideal theoretical profile (this includes the silver plating), even complex ones; b) fabricate the filter in just one piece, avoiding the use of screws and the misalignment problems appearing when the filter consists of two or more parts; and c) avoid the need to include the rounding effect which, in the end, depends on each particular fabrication facility, in the design process. Some other limitations arise from the materials that can be employed or the dependence on the electroformed component on the quality of the mandrel (in the end made by other traditional means like EDM or milling).

Some issues have been observed while doing the electroforming of microwave devices [71], [79], [80]. Firstly, a lack of material deposition of enough thickness in critical areas (with difficult access or very narrow gaps) of the work-piece was sometimes detected. It might occur as a result of the anodes location [81] and some constraints due to the support geometry. Hence, additional internal anodes were placed in an adjusted support to ensure the minimum thickness needed in the critical areas. Moreover, the deposition time was increased and the power supply was separated with different voltages for secondary anodes to draw less current.

Secondly, several imperfections due to the bubbles were observed which may affect the stiffness of the structure and the frequency response of the final device. The root causes for this issue might be: mandrel surface contamination, lack of agitation in the bath, gas generated during the electro-deposition, and fluids flaw being blocked by the electrodes. In order to avoid the previous issues, it is recommended to guarantee contamination-free surfaces on the mandrel using cleaning processes (firstly, grease and oil removal with a basic degrease to obtain a complete cleaned

surface and, secondly, a neutralization procedure and acid washing to neutralizing basic layers and removing oxidant layers on the surface [82]) and minimize the storing time between the mandrel fabrication and the electroforming process. In fact, a proper handling, packaging and storage of the mandrel is essential in all phases. Furthermore, the rotation of the mandrel in the bath (boosting the fluids flow) plays an important role to avoid a deficient agitation (besides, recent studies revealed that a copper deposit speed can be raised by cathode agitation [83]).

Finally, after the washing out, some pieces of the mandrel may remain fixed on the final structure. This is mainly due to a limited time of exposition inside the chemical bath. Therefore, the exposition time must ensure the complete removal of the mandrel and an additional step including an ultrasonic bath cleaning using the caustic solution could be performed. In order to cope with the risk of over-exposition to the chemical bath and to assure a low impact over the electrical parameters of the plating, a thicker coating could be done.

1.6.4 Additive Manufacturing (AM)

Additive manufacturing (AM) [84] is a promising fabrication technique that builds a device by adding ultra-thin layers of material one by one. The strengths of AM permit highly complex structures which can be extremely light and low-cost [85]. Moreover, AM allows customize and / or change the product whenever it is needed very easily, since the design model and the fabrication process are directly connected (unlike CCM where programming of the machines is necessary) [86]. However, the tolerances of this fabrication method are sometimes quite high when high accuracy is demanded. Typical tolerances are around 100 μm for the conventional AM processes and they have strong dependency on the size of the part. Other important issues are porosity and the finish surface (roughness) of the final prototype. Note that the surface roughness will be different in the different axis planes.

1.6.5 Coatings

Regardless of the fabrication method used (CCM, EDM or AM), the coating of the inner surface with a good conductor (with no modifications in the intended dimensions of the device) is typically required to reduce the ohmic losses. The inside surfaces of waveguides are often silver plated since silver has the best conductivity of all metals at a reasonable price. This property is crucial, for example, if very low insertion loss or very low levels of passive intermodulation are desired. Moreover, silver has a good high-power behavior. If aluminum is used as base material, the silver plating process may be critical, since silver does not adhere directly on aluminum alloys. Thus, several intermediate layers need to be applied between silver and aluminum. Firstly, a chemical etching is done to create an adequate roughness to improve the adherence; secondly, a zinc amalgam is used to adherence nickel to aluminum; and finally chemical nickel to assure the adherence of the electrolytic silver. It is essential to stress that the silver coating process itself usually has a tolerance around 5-10 μm (additional to manufacturing tolerance). Some tests have been tried

on electroless silver as final coat, but the minimum required thickness has not been achieved. Whereas the silver-plating of components made by CCM is currently very well controlled, silver plating of pieces made by AM is not so obvious.

1.7 Scope of the Thesis

In order to compete with terrestrial networks and to cope with the economical and technical demands of the telecommunications market, the satellite industry needs to upgrade its systems and services with new developments. RF and, specifically, microwave filters are one of the best candidates to be enhanced by reducing their design times and manufacturing costs. The choice of the waveguide technology depends on the concrete application and the specific needs in terms of insertion loss, weight, or power handling. Rectangular waveguide technology is widely used in satellite communication payloads when low insertion loss and high-power behavior are required despite of its mass and volume. Therefore, the reduction of both troublesome characteristics in any applications, but specifically in the satellite ones, is seen as highly advantageous.

Modern satellite payloads are operated with an increasing number of communication channels and still increasing power level per channel. In fact, the peak power due to multiple carriers operating simultaneously compromises the output multiplexer and, more precisely, the output low-pass filter (LPF). Specifically, with the growing development of high-power payloads in the 12 to 20 kW range, the power at the output of the OMUX can now reach several kW. In the classical scheme, a channelized approach with a LPF for each channel is utilized. However, this is not optimum in terms of mass and volume. Then, one objective of this Thesis will be to develop a new high-power LPF able to support high power levels without showing multipactor breakdown. Furthermore, the requirements imposed in terms of power handling might make very difficult and costly to fully assess multipactor experimentally in these filters due to the high power levels involved at high frequencies. Therefore, it would be very useful for the space industry to develop a method to design filters which could handle at least 6 dB above the equivalent multi-carrier peak power to avoid testing the devices.

Similarly, the industry is demanding reductions in manufacturing costs (by eliminating tuning screws and guaranteeing first-shot fabrications). Hence, to develop more compact high-performance filters and diplexers with reduced sensitivity to manufacturing tolerances is in the spotlight, and will be a key aspect in this Thesis.

Additionally, the currently utilized frequency bands (Ku- and Ka-bands) are becoming crowded and the capacity is limited to service the new broadband services. Thus, there are some studies in the industry focused on the exploration of the higher-frequencies for future payload applications. In fact, it supports the trend to use the Q-, V-, and W-bands in the near and far future for commercial telecommunications programs. At these frequencies, the accuracy of the usual manufacturing tools (e.g. the standard computer-controlled milling (CCM)) becomes more significant, due to

the reduced physical dimensions of the filters. This means preciseness fabrications, which urge the need of high-precision CCM and / or the use of tuning screws which unfortunately lead to time-consuming and expensive manufacturing processes. Then, to develop low-cost filters for these bands will be also a key point addressed in this Thesis.

Finally, in such applications, waveguide bends can be often found after the filters producing a waste of volume / mass and increasing the insertion loss. Moreover, when two different structures (screwed by its flanges) are utilized, an additional negative impact in the PIM is produced. Therefore, it is also in the spotlight to develop new BPFs and LPFs along with accurate and robust design techniques to allow the designers to obtain: i) tuning-free, ii) compact structures, and iii) with routing capabilities.

1.8 Thesis Outline

The Thesis is organized in nine Chapters. This **first Chapter** has presented a brief overview of satellite communications, focusing on the main application of the devices developed in this Thesis, the payload of a communication satellite. Then, the classical methods to design rectangular waveguide filters have been reviewed. These methods rely on an equivalent circuit prototype based on lumped and/or distributed elements, which are usually implemented by cascading waveguide sections whose discontinuities strongly influence the frequency response of the filter, making use of final EM optimizations to compensate them, which is not efficient in terms of design-times.

In **Chapter 2**, the design of classical corrugated LPFs will be approached from a different perspective, proposing a new synthesis procedure where neither EM simulations nor optimizations are needed to obtain the final dimensions of the final prototype. Unlike in the methods previously published in the literature, it provides an exact solution by means of closed-form expressions, being possible to design a classical corrugated LPF in a negligible CPU time. Additionally, the technique will be extended to consider rounded corners (inherent of conventional milling fabrications) and also to embed routing capability in the device. In this case, an EM tool is needed to obtain the physical parameters, although its simple methodology (based on a divide-and-rule strategy) allows the designers to design a classical corrugated LPF with rounded corners and/or embedded bends in a matter of minutes. Additionally, this technique can be easily integrated in a EM design tool (such as FEST3D or CST MWS).

The corrugated waveguide LPF is the classical solution when the suppression of only the fundamental mode is needed. However, if the suppression of the higher-order modes is also a requirement, the waffle-iron filter is usually utilized. The design methods for this kind of filter are quite complex and time-consuming, since they are based on approximations and further optimizations. As in the previous case, a new design technique for waffle-iron filters will be proposed in **Chapter 3** to reduce design-times and subsequent design-costs. It is based on a modular design which,

instead of paying attention on the whole structure, their constituent substructures are designed consecutively and independently to eventually assemble the filter afterwards. With the novel design technique, waffle-iron filters without transmission zeros and with transmission zeros at a single frequency can be designed. Moreover, a new waffle-iron filter with multiple transmission zeros at multiple frequencies will be also proposed. This filter allows to obtain lower insertion loss and around a 40%-length reduction in comparison with the classical structures. Additionally, its high-power behavior will be also enhanced, though not sufficiently, to be utilized as output filter in modern satellite payloads.

The latter application will be covered with the novel filters with smooth profile presented in **Chapter 4**. These LPFs mark an important breakthrough, since it is possible to achieve a very wide rejected band (up to the third harmonic) and very high-power operation in a single structure. This technique, which leads to filters with smooth profile, achieves the suppression of all higher-order modes if desired. Compared to the classical waffle-iron solution, the novel proposals have highly increased power-handling capability for the same frequency specifications. In this Chapter, prototypes fabricated by electroforming and by CCM will be also included, showing the possibility of manufacturing these filters with space-compatible fabrication procedures. Besides, their power-handling capability will be simulated and tested with measurements. Indeed, multipactor measurements have been carried out in the European High Power RF Space Laboratory (ESA-VSC), showing an excellent behavior.

Even though the fabrication following space-compatible procedures of the filters in Chapter 4 has been demonstrated, it is rather difficult and expensive to be done. In order to overcome these issues and to obtain a LPF able to be fabricated in mass-production with minimum costs, a fully-customized design technique for a novel easy-to-fabricate LPF will be presented in **Chapter 5**. The novel filter is based on step-shaped bandstop elements which can be easily manufactured by CCM as well as achieve very wide stopbands (up to the third harmonic) and high-power operation as in the previous case. Additionally, the size and insertion loss will be reduced. To demonstrate the feasibility of the technique, several examples will be proposed with simulations and measurements of different prototypes. Furthermore, to demonstrate that very high-power multipactor levels can be also achieved, an output filter for Ku-band payloads, whose multipactor input power is better than 100 kW will be presented. Besides, a LPF intended for mass-production in Ka-band multi-beam payloads will be also designed. This filter is 40% smaller, has almost half insertion loss, and handles 10 dB more power than its classical counterpart. Its multipactor threshold level has been also tested obtaining excellent results. Finally, the flexibility of the proposed technique to be utilized in different applications will be demonstrated through the design of a diplexer with a novel LPF and a classical inductive iris filter.

Chapter 6 is devoted to propose a method for the design of BPFs in rectangular waveguide technology. The novel design method is based on a combination of a low-pass structure (as the one presented in the previous Chapter) and a classical high-pass filtering structure. This kind of structures are perfect to be utilized in high-performance compact diplexers for Ku-K-band applications since the novel BPF are compact, easy-to-fabricate, and provides much wider spurious-free stopbands

in comparison with the classical solution. Moreover, it has also a large minimum mechanical gap, which allows high-power operation. To prove the feasibility of the easy integration of the proposed BPF in high-performance diplexers, two different examples will be proposed in simulation and one of them will be also fabricated by CCM obtaining a remarkable accordance between simulations and measurements.

A new type of BPF with reduced sensitivity to manufacturing tolerances intended for the new Q/V-band payloads will be proposed in **Chapter 7**. This filter is based on the first inherent passband replica of the classical stepped-impedance LPF with a continuous width reduction. The novel technique has been proved through the design of a BPF for Q-band payloads. The manufacturing yield of the novel filter is 92% while only 8%-yield is obtained for its classical counterpart the inductive-iris filter.

Chapter 8 describes the new meandered waveguide LPFs and BPFs. This topology permits to reduce the size of the BPFs presented in the previous Chapter and to embed routing capabilities. It also applies to classical LPFs where, additionally, several transmission zeros can be also achieved to enhance the out-of-band performance. The novel filters allow to design systems with adaptable physical layout, which would improve the industrys freedom to boost design more complex and compact terminals and payloads. The novel technique has been validated through the design, simulation, and fabrication of a BPF for Q-band payloads and a LPF intended for Ku-band applications, obtaining excellent results.

Chapter 9 summarizes the conclusions of the Thesis. Likewise, it describes future research and development lines associated with the work performed in the framework of this Thesis.

Finally, it is important to emphasize that all Chapters in this Thesis are interrelated, but independent from each other and self-contained, allowing the reader to have a background of the state-of-the-art as well as giving them the necessary tools to design the proposed new structures. Moreover, the high potential of these techniques is endorsed by publications and contracts with the European Space Agency and reference companies of the satellite industry such as TESAT Spacecom and Thales Alenia Space.

REFERENCES

[1] G. Maral and M. Bousquet, *Satellite Communications Systems: Systems, Techniques and Technology*. Wiley, 2002.

[2] *Ucs satellite database*, (Online: accessed 1-April-2018). [Online]. Available: `https://www.ucsusa.org`.

[3] A. Atia, "The role of passive components in satellite payloads," in *2008 6th ESA International Workshop on Multipactor, Corona and Passive Intermodulation (MULCOPIM)*, Sep. 2008.

[4] V. E. Boria, "Recent achievements in filters for space communications," in *2009 EuMC Workshop on Advanced Topics in Design and Realization of Microwave Filters*, Sep. 2009.

[5] V. Boria and B. Gimeno, "Waveguide filters for satellites," *Microwave Magazine, IEEE*, vol. 8, no. 5, pp. 60–70, Oct. 2007.

[6] C. Kudsia, R. Cameron, and W.-C. Tang, "Innovations in microwave filters and multiplexing networks for communications satellite systems," *IEEE Transactions on Microwave Theory and Techniques*, vol. 40, no. 6, pp. 1133–1149, Jun. 1992.

[7] K. Zaki, "Microwave filters and multiplexers for space applications," in *2008 6th ESA International Workshop on Multipactor, Corona and Passive Intermodulation (MULCOPIM)*, Sep. 2008.

[8] B. G. Evans, Ed., *Satellite Communication Systems*, ser. Telecommunications. Institution of Engineering and Technology, 1999.

[9] *SPARK3D*, Available: http://www.oneweb.world/.

[10] I. Hunter, L. Billonet, B. Jarry, and P. Guillon, "Microwave filters-applications and technology," *IEEE Transactions on Microwave Theory and Techniques*, vol. 50, no. 3, pp. 794–805, Mar. 2002.

[11] C. Ernst and L. Rigaudeau, "ESA-CNES keynote presentation," in *2010 International Workshop on Microwave Filters (IWMF)*, Nov. 2010.

[12] D. M. Pozar, *Microwave Engineering Fourth Edition*. Wiley, 2011.

[13] R. E. Collin, *Foundations for Microwave Engineering*. McGraw Hill, 1992.

[14] G. Matthaei, L. Young, and E. M. T. Jones, *Microwave filters, impedance-matching networks and coupling structures*. Artech House, 1980.

[15] R. Cameron, C. Kudsia, and R. Mansour, *Microwave Filters for Communication Systems: Fundamentals, Design and Applications*. Wiley-Interscience, 2007.

[16] I. Hunter, *Theory and Design of Microwave Filters*. Artech House, 2006.

[17] J. Uher, J. Bornemann, and U. Rosenberg, *Waveguide Components for Antenna Feed Systems: Theory and CAD*. Artech House, 1993.

[18] R. Levy and S. B. Cohn, "A history of microwave filter research, design, and development," *IEEE Transactions on Microwave Theory and Techniques*, vol. 32, no. 9, pp. 1055–1067, Sep. 1984.

[19] R. Levy, R. Snyder, and G. Matthaei, "Design of microwave filters," *IEEE Transactions on Microwave Theory and Techniques*, vol. 50, no. 3, pp. 783–793, Mar. 2002.

[20] V. Boria, P. Soto, and S. Cogollos, "Distributed models for filter synthesis," *Microwave Magazine, IEEE*, vol. 12, no. 6, pp. 87–100, Oct. 2011.

[21] A. Garcia-Lamperez, S. Llorente-Romano, M. Salazar-Palma, and T. Sarkar, "Efficient electromagnetic optimization of microwave filters and multiplexers using rational models," *IEEE Transactions on Microwave Theory and Techniques*, vol. 52, no. 2, pp. 508–521, Feb. 2004.

[22] J. Ros, P. Pacheco, H. Gonzalez, V. Esbert, C. Martin, M. Calduch, S. Borras, and B. Martinez, "Fast automated design of waveguide filters using aggressive space mapping with a new segmentation strategy and a hybrid optimization algorithm," *IEEE Transactions on Microwave Theory and Techniques*, vol. 53, no. 4, pp. 1130–1142, Apr. 2005.

[23] P. Richards, "Resistor-transmission-line circuits," *Proceedings of the IRE*, vol. 36, no. 2, pp. 217–220, Feb. 1948.

[24] B. J. Minnis, *Designing Microwave Circuits by Exact Synthesis*. Artech House, 1996.

[25] R. Levy and I. Whiteley, “Synthesis of distributed elliptic-function filters from lumped-constant prototypes,” *IEEE Transactions on Microwave Theory and Techniques*, vol. 14, no. 11, pp. 506–517, Nov. 1966.

[26] S. B. Cohn, “A theoretical and experimental study of a waveguide filter structure,” *Office Naval Res.*, vol. 39, no. 11, Apr. 1948.

[27] R. Levy, “Tapered corrugated waveguide low-pass filters,” *IEEE Transactions on Microwave Theory and Techniques*, vol. 21, no. 8, pp. 526–532, Aug. 1973.

[28] ——, “A generalized design technique for practical distributed reciprocal ladder networks,” *IEEE Transactions on Microwave Theory and Techniques*, vol. 21, no. 8, pp. 518–526, Aug. 1973.

[29] S. B. Cohn, “Design relations for the wide-band waveguide filter,” *Proceedings of the IRE*, vol. 38, no. 7, pp. 799–803, Jul. 1950.

[30] M. Yu, “Power-handling capability for rf filters,” *Microwave Magazine, IEEE*, vol. 8, no. 5, pp. 88–97, Oct. 2007.

[31] A. J. Hatch and H. Williams, “The secondary electron resonance mechanism of low 2010;pressure high 2010;frequency gas breakdown,” *Journal of Applied Physics*, vol. 25, no. 4, pp. 417–423, Apr. 1954.

[32] J. Vaughan, “Multipactor,” *IEEE Transactions on Electron Devices*, vol. 35, no. 7, pp. 1172–1180, Jul. 1988.

[33] W.-C. Tang and C. Kudsia, “Multipactor breakdown and passive intermodulation in microwave equipment for stellite applications,” in *Military Communications Conference, 1990. MILCOM ’90, Conference Record, A New Era. 1990 IEEE*, Sep. 1990, 181–187 vol.1.

[34] J. Woode A. Petit, *Diagnostic investigations into the multipactor effect, susceptibility zone measurements and parameters affecting a discharge*. Noordwijk, The Neederlands: Technical report, ESTEC working paper No. 1556, Nov. 1989.

[35] J. de Lara, F. Perez, M. Alfonseca, L. Galan, I. Montero, E. Roman, and D. Garcia-Baquero, “Multipactor prediction for on-board spacecraft rf equipment with the mest software tool,” *IEEE Transactions on Plasma Science*, vol. 34, no. 2, pp. 476–484, Apr. 2006.

[36] M. Ludovico, L. Accatino, G. Zarba, and M. Mongiardo, “CAD of multipactor-free waveguide components for communication satellites,” in *2002 IEEE MTT-S International Microwave Symposium Digest (IMS)*, vol. 3, Jun. 2002, 2077–2080 vol.3.

[37] P. Sarasa, A. González, H. Esteban, P. Mader, K. Tossou, and P. Lepeltier, “Comparative study of the power handling capability of space broadband antenna filters in ku-band,” in *2005 5th ESA International Workshop on Multipactor, Corona and Passive Intermodulation in Space RF Hardware (MULCOPIM)*, Sep. 2005.

[38] I. Arregui, S. Anza, I. Arnedo, C. Vicente, A. Lujambio, J. Gil, M. Chudzik, B. Gimeno, T. Lopetegi, M. Laso, and V. Boria, "Multipactor prediction in novel high-power low-pass filters with wide rejection band," in *2009 39th European Microwave Conference (EuMC)*, Sep. 2009, pp. 675–678.

[39] A. Coves, G. Torregrosa-Penalva, C. Vicente, B. Gimeno, and V. Boria, "Multipactor discharges in parallel-plate dielectric-loaded waveguides including space-charge effects," *IEEE Transactions on Electron Devices*, vol. 55, no. 9, pp. 2505–2511, Sep. 2008.

[40] D. Gonzalez-Iglesias, B. Gimeno, V. Boria, A. Gomez, and A. Vegas, "Multipactor effect in a parallel plate waveguide partially filled with magnetized ferrite," *IEEE Transactions on Electron Devices*, vol. 61, no. 7, pp. 2552–2557, Jul. 2014.

[41] R. Udiljak, D. Anderson, M. Lisak, J. Puech, and V. Semenov, "Multipactor in a waveguide iris," *IEEE Transactions on Plasma Science*, vol. 35, no. 2, pp. 388–395, Apr. 2007.

[42] V. Semenov, J. Rasch, E. Rakova, and J. Johansson, "General study of multipactor between curved metal surfaces," *IEEE Transactions on Plasma Science*, vol. 42, no. 3, pp. 721–728, Mar. 2014.

[43] V. Semenov, E. Rakova, D. Anderson, M. Lisak, and J. Puech, "Importance of reflection of low-energy electrons on multipactor susceptibility diagrams for narrow gaps," *IEEE Transactions on Plasma Science*, vol. 37, no. 9, pp. 1774–1781, Sep. 2009.

[44] ESA, *ECSS Space engineering, multipactor design, and test*. Noordwijk, The Neederlands: ESA Publications Division, Apr. 2000, vol. ECSS-E-20-01.

[45] C. Vicente, M. Mattes, D. Wolk, B. Mottet, H. .-.-L. Hartnagel, J. Mosig, and D. Raboso, "Multipactor breakdown prediction in rectangular waveguide based components," in *2005 IEEE MTT-S International Microwave Symposium Digest (IMS)*, Jun. 2005.

[46] S. Anza, C. Vicente, D. Raboso, J. Gil, B. Gimeno, and V. Boria, "Enhanced prediction of multipaction breakdown in passive waveguide components including space charge effects," in *2008 IEEE MTT-S International Microwave Symposium Digest (IMS)*, Jun. 2008, pp. 1095–1098.

[47] *SPARK3D*, Available: https://www.cst.com/products/spark3d.

[48] A. Al-Mudhafar, J. Puech, C. Miquel-Espanya, D. Raboso, H. Hartnagel, and E. Consortium, "EVEREST simulation campaign results on multipactor effect using CST particle studioTM," in *2014 8th European Conference on Antennas and Propagation (EuCAP)*, Apr. 2014, pp. 1464–1468.

[49] *CST PS*, Available: https://www.cst.com/products/cstps.

[50] S. Anza, *Multipactor in multicarrier systems: theory and prediction*. PhD dissertation, Univesidad Politécnica de Valencia, 2017.

[51] S. Anza, C. Vicente, J. Gil, M. Mattes, D. Wolk, U. Wochner, V. E. Boria, B. Gimeno, and D. Raboso, "Multipactor prediction with multi-carrier signals: Experimental results and discussions on the 20-gap-crossing rule," in *2014 8th European Conference on Antennas and Propagation (EuCAP)*, Apr. 2014, pp. 1638–1642.

[52] S. Anza, C. Vicente, J. Gil, V. E. Boria, and D. Raboso, "Experimental verification of multipactor prediction methods in multicarrier systems," in *2016 46th European Microwave Conference (EuMC)*, Oct. 2016, pp. 226–229.

[53] S. Anza, C. Vicente, J. Gil, M. Mattes, D. Wolk, U. Wochner, V. Boria, B. Gimeno, and D. Raboso, "Prediction of multipactor breakdown for multicarrier applications: The quasi-stationary method," *IEEE Transactions on Microwave Theory and Techniques*, vol. 60, no. 7, pp. 2093–2105, Jul. 2012.

[54] S. Anza, C. Vicente, J. Gil, V. E. Boria, B. Gimeno, and D. Raboso, "Nonstationary statistical theory for multipactor," *Physics of Plasmas*, vol. 17, no. 6, p. 062 110, 2010.

[55] R. Udiljak, D. Anderson, P. Ingvarson, U. Jordan, U. Jostell, L. Lapierre, G. Li, M. Lisak, J. Puech, and J. Sombrin, "New method for detection of multipaction," *IEEE Transactions on Plasma Science*, vol. 31, no. 3, pp. 396–404, Jun. 2003.

[56] M. Kunes, "Microwave multiplexers for space applications," *Electronics Communication Engineering Journal*, vol. 10, no. 1, pp. 29–35, Feb. 1998.

[57] H. Eskelinen and P. Eskelinen, *Microwave component mechanics*. Noordwood MA: Artech House, 2003.

[58] P. Martin-Iglesias, F. Teberio, S. Martin-Iglesias, I. Arregui, M. A. G. Laso, I. Arnedo, and L. Accatino, "Thermal stability variation for alsi(40)," in *2018 International Workshop on Microwave Filters (IWMF)*, Apr. 2018.

[59] E. J. Lavernia, J. D. Ayers, and T. S. Srivatsan, "Rapid solidification processing with specific application to aluminium alloys," *International Materials Reviews*, vol. 37, no. 1, pp. 1–44, 1992.

[60] H. Jones, *Rapid Solidification of Metals and Alloys*. The Institution of Metallurgists, 1982.

[61] H. H. Liebermann, *Rapid Solidified Alloys*. Marcel Dekker, 1993.

[62] R. Rohloff, *A novel athermal approach for high performance cryogenic metal optics*. Marcel Dekker, 1993.

[63] J. V. Morro, H. Esteban, V. E. Boria, C. Bachiller, and A. Belenguer, "Optimization techniques for the efficient design of low-cost satellite filters considering new light materials," *Int. Journal of RF and Microwave Computer-Aided Egineering*, vol. 18, no. 2, pp. 168–175, Feb. 2008.

[64] I. Montero, L. Aguilera, L. Olano, M. Vazquez, M. E. Davila, V. Nistor, L. A. Gonzalez, L. Galan, U. Wochner, and D. Raboso, "Anti-multipactor coatings for ku band rf filters using chemical methods," in *2014 ESA International Workshop on Multipactor, Corona and Passive Intermodulation (MULCOPIM)*, Sep. 2014.

[65] J. Puech, C. E. Miquel-Espana, D. Raboso, and Everest consortium, "Synthesis of the results of the EVEREST project," in *2014 ESA International Workshop on Multipactor, Corona and Passive Intermodulation (MULCOPIM)*, Sep. 2014.

[66] C. Lee-Yow, J. Scupin, P. Venezia, and T. Califf, "Compact high-performance reflector-antenna feeds and feed networks for space applications [antenna applications]," *Antennas and Propagation Magazine, IEEE*, vol. 52, no. 4, pp. 210–217, Aug. 2010.

[67] S. Cogollos, V. Boria, P. Soto, B. Gimeno, and M. Guglielmi, "Efficient CAD tool for inductively coupled rectangular waveguide filters with rounded corners," in *2001 31st European Microwave Conference (EuMC)*, Sep. 2001, pp. 1–4.

[68] J. Lorente, M. Mendoza, A. Petersson, L. Pambaguian, A. Melcon, and C. Ernst, "Single part microwave filters made from selective laser melting," in *2009 39th European Microwave Conference (EuMC)*, Sep. 2009, pp. 1421–1424.

[69] V. Furtula, H. Zirath, and M. Salewski, "Waveguide band-pass filters for millimeter-wave radiometers," *Journal of Infrared, Millimeter, and Terahertz Waves*, vol. 34, no. 12, pp. 824–836, 2013.

[70] P. Bruneau, H. Janzen, and J. Ward, "Machining of terahertz split-block waveguides with micrometer precision," in *Infrared, Millimeter and Terahertz Waves, 2008. IRMMW-THz 2008. 33rd International Conference on*, Sep. 2008, pp. 1–2.

[71] F. Teberio, I. Arregui, A. Gomez-Torrent, E. Menargues, M. A. G. Laso, C. Vicente, J. Gil, A. Alonso, N. Sidiropoulos, P. Martin-Iglesias, and M. Diaz-Martin, "Assessment of electroforming for complex rf/microwave components," in *2015 International Workshop on Microwave Filters (IWMF)*, Mar. 2015, pp. 1–8.

[72] S. Kalpakjian and S. Schmid, *Manufacturing Engineering and Technology*. New Jersey: Prentice-Hall Inc., 2000.

[73] ——, *Manufacturing Engineering and Technology*. Pearson Education, 2006.

[74] E. Diaz Caballero, J. Morro, A. Belenguer, H. Esteban, and V. Boria, "CAD technique for designing H-plane waveguide filters considering rounded corners," in *2013 IEEE MTT-S International Microwave Symposium Digest (IMS)*, Jun. 2013, pp. 1–3.

[75] E. C. Jameson, *Electrical discharge machining*. Dearborn: Society of Manufacturing Engineers, 2001.

[76] ASTM International, *ASTM B832-93, Standard Guide for Electroforming with Nickel and Copper*. West Conshohocken, 2013.

[77] S. M. Silimani and S. John, "Review on recent advances in electroforming during the last decade," *Bulletin of electrochemistry*, vol. 17, no. 12, pp. 553–556, Dec. 2001.

[78] C. Coddet, *Materials processing technology by additive approaches*. Xi'an Jiaotong University Master courses, 2012-2013.

[79] Public University of Navarre (UPNA), Novalti S.A., Aurorasat S.L., Customer: TESAT, "Compact high-power spurious-free low-pass waveguide filters," ESA, ITI-B project EIN-RP-1401, Oct. 2014.

[80] SPACE ENGINEERING, "Ku-band high power feed components," ESA, Artes 5.1 project SPG-RP-KHP-013, Dec. 2014.

[81] Z.-W. Zhu, D. Zhu, N.-S. Qu, K. Wang, and J.-M. Yang, "Electroforming of revolving parts with near-polished surface and uniform thickness," *Int. J. Adv. Manuf. Technol.*, vol. 39, no. 11-12, pp. 1164–1170, Dec. 2008.

[82] C. Y. Hsu, D. Y. Chen, M. Y. Lai, and G. J. Tzou, "Edm electrode manufacturing using rp combining electroless plating with electroforming," *Int. J. Adv. Manuf. Technol.*, vol. 38, no. 9-10, pp. 915–924, Sep. 2007.

[83] F.-T. Weng, "A study of cathode agitation in ultrasonic-aided microelectroforming," *Int. J. Adv. Manuf. Technol.*, vol. 25, no. 9-10, pp. 909–912, May 2005.

[84] ASTM International, *ASTM F2792-12a, Standard Terminology for Additive Manufacturing Technologies*. West Conshohocken, 2012.

[85] N. Guo and M. C. Leu, "Additive manufacturing: Technology, applications and research needs," *Frontiers of Mechanical Engineering*, vol. 8, no. 3, pp. 215–243, May 2013.

[86] M. C. Bourell D. L. Leu and D. W. Rosen, *Roadmap for additive manufacturing: identifying the future of freeform processing*. Austin: University of Texas, 2009.

CHAPTER 2

QUASI-ANALYTICAL SYNTHESIS PROCEDURE FOR CLASSICAL CORRUGATED LPFs

This Chapter firstly describes a simple, quasi-analytical, and accurate method to design classical corrugated rectangular waveguide LPFs [1]. Unlike other published techniques, the dimensions of the final filter are directly obtained in a quasi-analytical manner following exclusively closed-form expressions and, in particular, using neither EM simulation nor optimization. Thus, this novel method is amenable to be implemented by using an off-the-self mathematical SW tool, such as Matlab or Python [2]. Secondly, a modular design procedure to take into account the rounded of the corners (for CCM manufacturing) is also presented [3]. Finally, this technique is extended to embed routing capability in the classical device [4]. The novel method has been validated with three design examples, which show a remarkable accordance between the ideal, simulated, and measured frequency responses.
It is important to note that the techniques developed in this Chapter have been done within the framework of a NPI activity with the European Space Agency [5].

2.1 Background

Stepped-impedance filters have been widely used in countless applications, such as satellite communications or ground stations. Indeed, the corrugated waveguide filter is a classical low-pass solution when low-loss, high-power, and easy manufacturing are required [6], [7], [8]. Depending on the target application, different requirements are imposed in the frequency specifications of the LPF such as: maximum frequency of the passband, minimum in-band return loss, maximum insertion loss, minimum frequency of the rejection band, and minimum out-of-band rejection level. For this reason, a significant effort has been made over the years to develop different sophisticated design strategies in order to cope with all those requirements [9].

The classical corrugated waveguide filter was firstly proposed by Cohn [10], who estimated the physical dimensions of the filter after relating the prototype of lumped / distributed elements (previously calculated by a mathematical method) to the components of the real structure. In [11], Levy presented an insightful method based on a set of commensurate transmission lines of different impedances, which are implemented in rectangular waveguide by means of a cascade of waveguide sections of different heights. However, the straightforward application of these techniques produces some errors (mainly due to the excitation of higher-order modes), which are typically compensated by a final optimization.

Over the last years, some techniques have been published in the literature with the aim of compensating for the errors in the lengths of the waveguide sections. In [12], the authors proposed this length correction by means of an EM simulation evaluating the phase contribution of the frequency response of the waveguide junction. Although it is a fast method, the technique cannot be implemented using just closed-form expressions and off-the-self mathematical SW tools, such as Matlab, as in the technique proposed in this Thesis. Besides, the performance of this synthesis method decreases if the maximum heights of the waveguide filter grow, as it was pointed out in [13]. Indeed, in [13], a more accurate circuit design procedure was proposed. This method is based on a succession of transmission lines and ABCD matrices which model each junction between two adjacent waveguides of different heights. These matrices are characterized using EM simulations. Finally, the resulting prototype is optimized to obtain a suitable frequency response. In this Chapter, a simple, quasi-analytical, and accurate synthesis method based on closed-form expressions is presented [1], [2]. Unlike [12] and [13], neither EM simulations nor optimizations are needed to obtain the physical dimensions of the final device.

When computer-controlled-milling (CCM) is assumed as fabrication technique, it is not possible to mechanize perfect square corners or cavities with dimensions smaller than the tool [14]. This limitation must be considered before the fabrication to avoid deviations between the predicted and the measured frequency response. However, with the previous design techniques it cannot be accomplished. Therefore, in this case, EM simulations must be used to take into account the rounded of the corners [3].

Finally, the physical configuration of numerous applications (such as ground terminals or multi-beam satellite payloads) has become very intricate in order to allo-

cate different RF/microwave components which are put together trying to make the best use of the volume available [15], [16]. There, it can be found waveguide bends after LPFs. Both are different components which are obliged to be connected together. This issue produces a negative impact to the insertion loss, volume/weight, and PIM products. Therefore, developing a novel design technique for waveguide filters with adaptable physical layout will improve the industrys' freedom to trade-off all these variables, as well as it will also boost the flexibility to design more complex and compact terminals and payloads. As far as the author knowledge, all efforts to fold waveguide filters have kept focused on BPFs [17], [18]. In the case of LPFs, all of them follow the same in-line topology, and a design procedure for an arbitrarily folded corrugated LPF would be very practical for the satellite community to avoid additional bending structures and the connection between them [4].

2.2 Objective

In order to reduce costs and cope with the economic and technical demands of the telecommunications market, the main objective of the proposed techniques is to reduce design times by means of developing an automated synthesis technique, which give the designers the final dimensions of the desired structure.

Moreover, the technique should allow the designers to obtain a filter ready to be fabricated (including rounded corners for conventional CCM) and/or with a specific topology (by embedding bends in the structure) with the aim of enhance the flexibility of the device to design more complex and compact terminals and payloads.

2.3 Design Method

The physical structure of a classical E-plane corrugated LPF featuring any all-pole frequency response of order N (e.g. Butterworth, Chebyshev, Zolotarev, Chained function, etc.) is composed of a cascade of N+2 rectangular waveguide sections, all of them with the same width, a, and different heights, b_i. This type of filter is theoretically modeled by connecting commensurate transmission lines, i.e., transmission lines with the same electrical length - also called Unit Elements - and different characteristic impedances, Z_i, see Figure 2.1. The electrical length, θ, is related to the physical length, l, through the phase constant, β, or the wavelength, λ_g, as follows:

$$\theta = \beta \cdot l = \frac{2 \cdot \pi}{\lambda_g} \cdot l \tag{2.1}$$

The frequency of maximum rejection, f_0, is attained when $\theta = \pi/2$ rad. For the design of LPFs it is very useful to define also the maximum frequency of the passband, f_c, and its associated θ_c [8].

The synthesis procedure begins by calculating the Z_i of each Unit Element once the all-pole frequency response is selected. These are obtained by applying the well-known *Richards' transformation* and the Unit Element extraction procedure that is

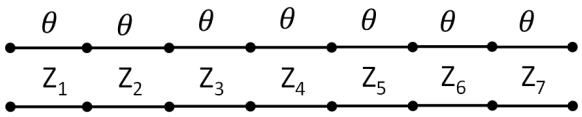

Figure 2.1: Example of a 5th-order commensurate-line filter prototype.

fully detailed in Annex A and [8], see Figure 2.2(a) for a typical Chebyshev response. Hence, in each connection between two Unit Elements a local reflection coefficient, Γ_i, is produced by the characteristic impedance mismatch, whose value is given by:

$$\Gamma_i = \frac{Z_i - Z_{i-1}}{Z_i + Z_{i-1}} \tag{2.2}$$

The combination of all these local reflections placed θ rad apart produces the aimed frequency response of the filter.

Then, the novel method continues by computing the b_i values of the final structure. First, b_0 has to be fixed. This value is usually set in accordance to the requirements of power handling and stopband performance. As it is explained in [12] and [13], b_i is directly proportional to the impedance Z_i and, consequently, equation (2.2) can be used interchanging Z_i with b_i, thus obtaining:

$$\Gamma_i^{aprox} = \frac{b_i - b_{i-1}}{b_i + b_{i-1}} \tag{2.3}$$

However, this simple relationship between Z_i and b_i neglects the effect of the higher-order mode excitation at the discontinuity. This effect can be modeled by a shunt capacitance related to the reactive energy stored around the discontinuity between the adjacent waveguides of different heights. The presence of the shunt capacitance modifies the local Γ_i magnitude, considered here for the first time to the knowledge of the authors, as follows:

$$|\Gamma_i'| = \sqrt{\frac{(b_i - b_{i-1})^2 + (b_i \cdot B)^2}{(b_i + b_{i-1})^2 + (b_i \cdot B)^2}} \tag{2.4}$$

where B is the parasitic shunt capacitance that can be directly computed by the approximate expressions available in [19] and included here for the sake of completeness:

$$\begin{aligned} B = \frac{2 \cdot b_{i-1}}{\lambda_{g,f_c}} \Bigg\{ & ln\left[\left(\frac{1-\alpha^2}{4\alpha}\right)\left(\frac{1+\alpha}{1-\alpha}\right)^{0.5(\alpha+\frac{1}{\alpha})}\right] \\ & + 2 \cdot \frac{A + D + 2C}{A \cdot D - C^2} \\ & + \left(\frac{b_{i-1}}{4\lambda_{g,f_c}}\right)^2 \left(\frac{1-\alpha}{1+\alpha}\right)^{4\cdot\alpha} \left(\frac{5\alpha^2 - 1}{1-\alpha^2} + \frac{4}{3}\frac{\alpha^2 \cdot C}{A}\right)^2 \Bigg\} \end{aligned} \tag{2.5}$$

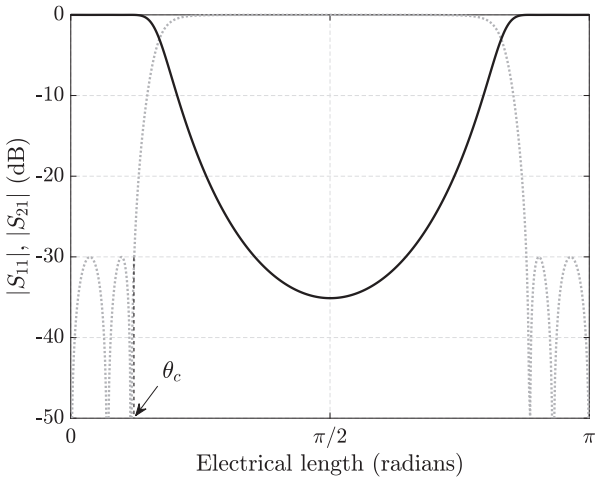

(a)

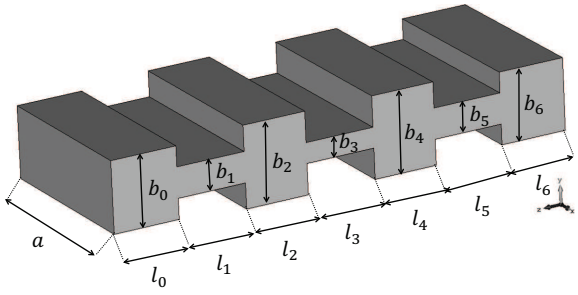

(b)

Figure 2.2: Example of a 5th order commensurate-line stepped-impedance filter prototype (a) $|S_{11}|$ (dotted line) and $|S_{21}|$ (solid line) parameters and (b) 3D view of the filter with its design parameters.

where

$$A = \left(\frac{1+\alpha}{1-\alpha}\right)^{2\alpha} \cdot \frac{1+\sqrt{1-\left(\frac{b_{i-1}}{\lambda_{g,f_c}}\right)^2}}{1-\sqrt{1-\left(\frac{b_{i-1}}{\lambda_{g,f_c}}\right)^2}} - \frac{1+3\alpha^2}{1-\alpha^2}$$

$$D = \left(\frac{1+\alpha}{1-\alpha}\right)^{\frac{2}{\alpha}} \cdot \frac{1+\sqrt{1-\left(\frac{b_i}{\lambda_{g,f_c}}\right)^2}}{1-\sqrt{1-\left(\frac{b_i}{\lambda_{g,f_c}}\right)^2}} + \frac{3+\alpha^2}{1-\alpha^2}$$

$$C = \left(\frac{4\alpha}{1-\alpha^2}\right)^2$$

$$\alpha = \frac{b_i}{b_{i-1}}$$

Therefore, once b_0 is fixed, the next height, b_1, is calculated to satisfy that $|\Gamma_1'| = |\Gamma_1|$. Then, proceeding iteratively, once a certain b_{i-1} is known, b_i is calculated to assure that equation (2.4) provides the reflection value prescribed by equation (2.2), i.e., $|\Gamma_i'| = |\Gamma_i|$. When $i = N+1$, all b_i in the final structure will have been calculated without involving any EM simulations (see Figure 2.2(b)). It is important to highlight that the new dimensions of the filter will provide less height excursion than in other previously reported methods. This can be clearly seen when equation (2.4) and equation (2.3) are compared. Certainly, equation (2.4) always produces higher local reflection values and, thus, when they are forced to fulfill equation (2.2), b_i keeps close to b_{i-1}. Besides, this behavior makes the calculation of b_i using equation (2.4) pretty simple, i.e. the process can start from the b_i inaccurately estimated by equation (2.3) and then reduce (or increase) its value, to make it closer to b_{i-1}, until equation (2.4) equals equation (2.2). Finally, it should be taken into account that B is frequency dependent, see equation (2.5). This implies that a specific frequency should be picked to ideally adjust the value of the reflection coefficient equation (2.4) at that frequency (for instance, f_c can be selected).

Now, the proposed synthesis method continues with the calculation of the lengths of each waveguide section, l_i. As it was aforementioned, since the structure is commensurate all the Unit Elements have the same electrical length. Therefore, in principle, each section should have the same physical length, l, given by:

$$l = \frac{\theta_c}{\beta_{10,f_c}} \tag{2.6}$$

However, the phase of the local Γ_i is also affected by the high-order mode excitation produced in the vicinity of each junction, and it needs to be considered by

modeling the shunt capacitance with subsceptance B. Therefore, l_i must be compensated taking into account this reactive load. This correction was firstly published in [12], it was also utilized in [13], and it is based on previous works of Levy [20], as it is pointed out in [9]. However, unlike [12] and [13], which utilize EM simulations to calculate the correcting factors, the value of B obtained with equation (2.5) will be used in the height calculation, but applied to the phase. Therefore, l_i will have two correcting factors obtained from:

$$\delta_i^{(1)} = \frac{\lambda_{g,f_c}}{2\pi} \cdot \frac{\phi_i^{(2)}}{2} \tag{2.7}$$

$$\delta_i^{(2)} = \frac{\lambda_{g,f_c}}{2\pi} \cdot \frac{\phi_i^{(2)}}{2} \tag{2.8}$$

where $\phi_i^{(1)}$ and $\phi_i^{(2)}$ are the phases of the local Γ_i from the right and from the left, respectively, in the ith waveguide junction. These phases can be calculated using the following expressions:

$$\phi_i^{(1)} = \tan^{-1}\left(\frac{-2 \cdot b_i^2 \cdot B}{b_i^2 - b_{i-1}^2 - b_i^2 \cdot B^2}\right) \tag{2.9}$$

$$\phi_i^{(2)} = \tan^{-1}\left(\frac{-2 \cdot b_{i-1} \cdot b_i \cdot B}{b_{i-1}^2 - b_i^2 - b_i^2 \cdot B^2}\right) \tag{2.10}$$

Therefore, the final l_i, is calculated as:

$$l_i = l + \delta_{i-1}^{(2)} + \delta_i^{(1)} \tag{2.11}$$

To summarize, the novel quasi-analytic synthesis method allows the designer to obtain a very accurate physical structure whose simulated frequency response will be very close to the ideal one. Moreover, unlike [12] and [13], neither EM simulations nor optimizations are needed, since the physical dimensions of the filter are directly obtained from closed-form expressions. Additionally, the novel synthesis method provides accurate attenuation levels and accurate values for f_c, f_0, and the maximum frequency of the stopband.

2.4 Design Method Considering Rounded Corners

The most utilized fabrication technique in the space industry, CCM, introduces internal rounded corners when applied to the low-cost production of classical corrugated LPFs. If this mechanization effect is taken into account during the design stage, the production of the aforementioned devices will be more accurate, reducing costs and development times. However, the design technique in the previous Section does not consider this effect. For the synthesis of these devices, a novel design technique

which utilizes a divide-and-rule strategy has been developed. Instead of paying attention to the whole structure, their constituent Design Building Blocks (DBBs) will be calculated separately and consecutively, to eventually assemble the filter afterwards. The ith-DBB is composed of the second half of the $(i-1)$th-waveguide section, the first half of the ith-section, and the junction between them, with the desired rounded corner (to be manufactured cut by the H-plane as in Figure 2.3 (a) or cut by the E-plane as in Figure 2.3 (b)). In particular, the DBB should behave as its electrical model prototype composed of one-half transmission line, an impedance step, and another one-half transmission line.

The design procedure will be identical to the previous synthesis method. Firstly, b_0 is set. Then, b_1, is computed to satisfy that $|S_{11,1}(f_c)| = |\Gamma_1|$, where $|S_{11,1}(f_c)|$ is the magnitude of the S_{11}-parameter of the 1st-DBB at the passband upper frequency, f_c. This magnitude value only depends on the heights b_0 and b_1 and, since b_0 has already been fixed, b_1 can be easily obtained by means of an EM SW tool (where high-order modes are taken into account). Notice that if $\Gamma_i > 0$ then $b_{i-1} < b_i$, and if $\Gamma_i < 0$ then $b_{i-1} > b_i$. Then, proceeding consecutively with the rest of the DBBs, once a certain b_{i-1} is known, b_i is calculated to assure that $|S_{11,i}(f_c)|$ provides the reflection value prescribed by $|\Gamma_i|$. When $i = N+1$, all b_i's in the final structure have been calculated.

$$|S_{11,i}(f_c)| = |\Gamma_i| \tag{2.12}$$

The design process continues with the calculation of the lengths l_i of each waveguide section. As it was aforementioned, and can be observed in Fig. 2.3, both halves of two consecutive waveguide sections are considered as the DBB. Hence, in the ith-DBB, two different lengths will be computed, i.e. $l_{i,1}$ and $l_{i,2}$. Both lengths will be calculated taking into account the phase of the ith-DBB, in transmission, $\phi_{i,S_{21}}$, and in reflection, $\phi_{i,S_{11}}$, to resemble the target. On the one hand, the phase of the ith-DBB in transmission should satisfy:

$$\phi_{i,S_{21}}(f_c) = -\theta_c \tag{2.13}$$

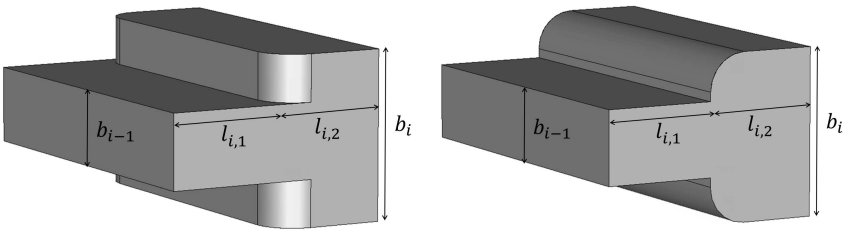

Figure 2.3: Detailed notation of the ith-DBB and their associated constituent parameters. (a) H-plane cut. (b) E-plane cut.

where θ_c is the target electrical length at the passband upper frequency, f_c. On the other hand, depending on the sign of the targeted Γ_i, the ith-DBB reflection phase should satisfy:

$$\phi_{i,S_{11}}(f_c) = 180 - \theta_c \quad \text{for} \quad b_{i-1} < b_i \tag{2.14}$$

$$\phi_{i,S_{11}}(f_c) = -\theta_c \quad \text{for} \quad b_{i-1} > b_i \tag{2.15}$$

Notice that those phases are affected by the high-order modes excited in the vicinity of each junction, but $l_{i,1}$ and $l_{i,2}$ can be computed using again an EM simulator, as it was done in the b_i calculations.

As an alternative to EM solvers for the calculus, quasi-analytical models can be found in [19]. The advantage of employing an EM solver for the calculus is that it opens the door to routing filters. All in all, the novel design method allows designers to obtain the filter's physical structure with the aimed rounded corners whose frequency response will be very close to the desired one in a negligible CPU time. A minor adjustment might be needed only in the lengths of the final prototype, accounting for the effect of high-order modes excited in the junctions, which are evanescently present in the intersections of the DBBs, and the slight frequency dependence of the reflection coefficient of the junction. Then, the final structure ready to be fabricated is accomplished.

2.5 Design Method to Embed Routing Capability in Classical Corrugated LPFs

Following the same modular strategy utilized in the previous Section to include rounded corners in the final structure, routing capability (understood as the possibility of embedding bends to boost the flexibility to design more complex and compact terminals and payloads) can be achieved in classical corrugated LPFs. In this case, two different DBBs will be considered: the straight DBB (Figure 2.4 (a)) and the folded DBB (Figure 2.4 (b)). The procedure to obtain the dimensions of each DBB will be the same, regardless of the type of junction between the contiguous sections (straight, folded up- or down-wards). Indeed, the heights, b_i, of the novel filter will be computed by satisfying equation (2.12) and the lengths, l_i, satisfying equations (2.13), (2.14), and (2.15). Therefore, it could then connect two waveguide sections using an in-line or a folded configuration, depending on the desired final layout, while the response is preserved. Finally, as in the previous case, minor adjustments might be needed only in the lengths of the final prototype, accounting for the effect of high-order modes excited in the junctions. It is important to note that this structure opens the door of more complex ones, utilizing E-plane mitered bends as it will be shown in Chapter 8.

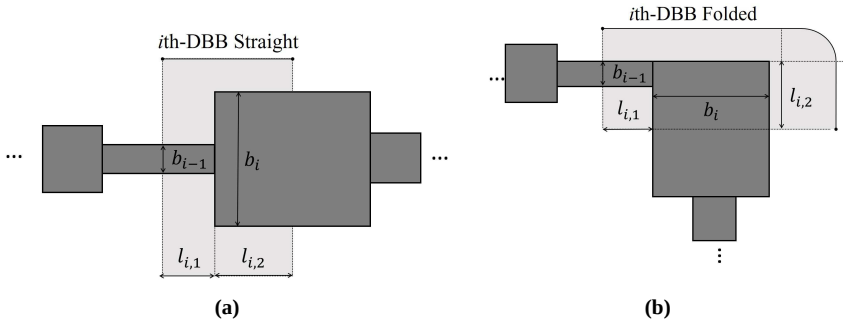

Figure 2.4: Detailed notation of the ith-DBB and their associated constituent parameters. (a) Sketch of the in-line topology where the second waveguide section is connected straight. (b) Sketch of the folded topology where the second waveguide section is connected downwards.

Design Examples

According to the design methodologies proposed, three different examples will be presented in this Chapter. Firstly, in Section 2.6, the novel accurate synthesis procedure based on closed-form expressions detailed in Section 2.6 will be assessed with the state-of-the-art techniques, [1], [2]. The second example (Section 2.7) will demonstrate the feasibility of designing classical corrugated LPFs taking into account the inherent rounded corners of conventional CCM fabrication techniques following the novel design technique described in Section 2.4, [3]. The third example (Section 2.8) includes a novel corrugated LPF with embedded bends will be designed following the novel technique described in Section 2.5, [4]. Besides, a prototype of the last two examples will be also fabricated and measured.

2.6 Design Example 1: Assessment with State-of-the-Art Synthesis Techniques

2.6.1 Specifications

In order to demonstrate the feasibility of the novel direct synthesis method, a classical Chebyshev corrugated LPF will be designed. The filter will fulfill the same frequency specifications as in [13] (see Table 2.1) to perform a fair comparison between the the technique presented in Section 2.3 and the latest reported technique [13].

2.6.2 Design and Simulation

The physical dimensions of both, the filter (see Figure 2.5) extracted using the technique in [13] and the structure obtained with the novel method in this Chapter are given in Table 2.2 (the filter obtained applying the length corrections as in [12] is not given since it was later surpassed by [13]). As it can be observed in Table 2.2, the low

Table 2.1: Summary of design parameters of the example in Section 2.6.

Filtering function type	Chebyshev
Order, N	31
In-band return loss	25 dB
Passband upper frequency, f_c	11 GHz
Maximum rejection frequency, f_0	13.29 GHz
Waveguide width, a	19.05 mm

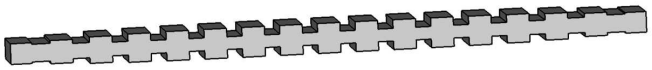

Figure 2.5: 3D view of the synthesized filter in Section 2.6.

Z_i values produce higher b_i values in comparison with [13] and the high Z_i values produce shorter b_i values. Finally, the lengths are slightly longer in the novel filter. It is important to note that, although the correction length utilized in this Chapter and in [13] is the same, the length values obtained are different since the height values utilized to calculate them are also different.

The FEST3D frequency responses of the previous filters along with the ideal response are compared in Figure 2.6 and Figure 2.7. The maximum attenuation of the filter synthesized following the technique described in Section 2.3 is closer to the target compared to [13]. Furthermore, the shift of the maximum frequency of the stopband has been significantly reduced, 70 MHz in this example vs. 210 MHz in [13]. All these results are summarized in Table 2.3.

In consequence, this example points out the significance of synthesizing the different heights of the classical corrugated filter taking into account the differences between the theoretical and real magnitude of the local Γ_i. This is a key point to design more accurate filters using closed-form expressions without requiring optimizations or EM simulations.

In conclusion, the feasibility of designing classical corrugated LPFs by the novel quasi-analytical accurate synthesis method proposed in Section 2.3 has been demonstrated. The novel approach allows the designer to obtain a final prototype whose frequency response is very close to the ideal one. Even more interestingly, it must be stressed that, unlike previously proposed design methods, neither EM simulations nor optimizations are needed in the technique presented in this Chapter, which would allow accurate filter designs simply using Matlab or Python.

Table 2.2: Dimensions of the synthesized filter in Section 2.6.

UE	Z_i	b_i (mm)		l_i (mm)	
		[13]	This work	[13]	This work
0, 32	1.000	7.000	7.000	7.000	7.000
1, 31	0.859	6.0104	6.0132	6.3096	6.3185
2, 30	1.123	7.8617	7.8504	7.6675	7.6742
3, 29	0.738	5.1654	5.1799	5.7416	5.7670
4, 28	1.288	9.0156	8.9647	7.7482	7.7846
5, 27	0.664	4.6448	4.6675	5.3865	5.431
6, 26	1.387	9.7113	9.6264	7.7270	7.7811
7, 25	0.632	4.4221	4.4476	5.2319	5.2854
8, 24	1.432	10.0250	9.9230	7.7058	7.7699
9, 23	0.619	4.3314	4.3578	5.1693	5.2264
10, 22	1.452	10.1640	10.0535	7.6934	7.7638
11, 21	0.613	4.2914	4.3182	5.1428	5.2010
12, 20	1.461	10.2290	10.1144	7.6877	7.7608
13, 19	0.610	4.2728	4.2997	5.1294	5.1893
14, 18	1.466	10.2590	10.1425	7.6873	7.7594
15, 17	0.609	4.2651	4.2921	5.1194	5.1846
16	1.467	10.2670	10.1501	7.6919	7.7590

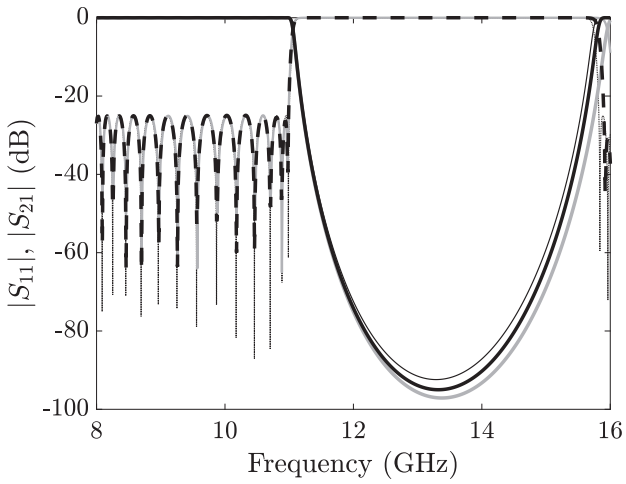

Figure 2.6: Entire frequency response comparison between the ideal (black thin line) and FEST3D frequency responses for the structure (Section 2.6) obtained with the novel method in Section 2.3 (black thick line) and with [13] (grey line). $|S_{11}|$ in dotted line and $|S_{21}|$ in solid line.

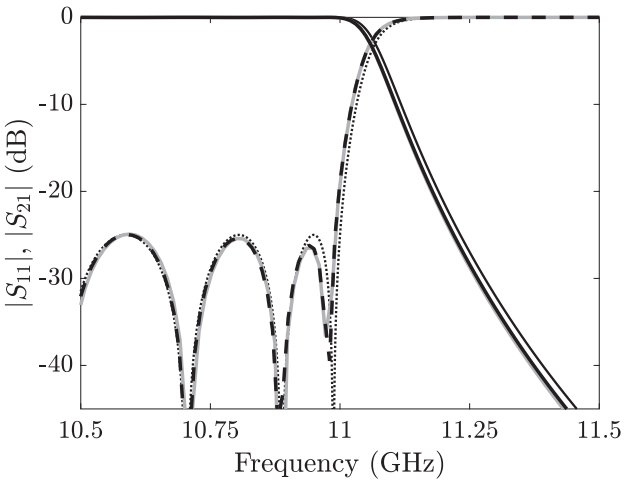

Figure 2.7: Detailed frequency response comparison between the ideal (black thin line) and FEST3D frequency responses for the structure (Section 2.6) obtained with the novel method in Section 2.3 (black thick line) and with [13] (grey line). $|S_{11}|$ in dotted line and $|S_{21}|$ in solid line.

Table 2.3: Differences between synthesized examples in Section 2.6.

	Ideal	[13]	This work
Max. attenuation	-92 dB	-97 dB	-95 dB
Difference	-	5 dB	3 dB
f_0	13.29 GHz	13.38 GHz	13.32 GHz
Difference	-	90 MHz	30 MHz
Max. freq. of the stopband	15.74 GHz	15.95 GHz	15.81 GHz
Difference	-	210 MHz	70 MHz
f_c	11 GHz	10.99 GHz	10.99 GHz
Difference	-	10 MHz	10 MHz

2.7 Design Example 2: Classical Corrugated LPF with Rounded Corners

In order to demonstrate the feasibility of the novel design technique proposed in Section 2.4, a corrugated waveguide LPF with rounded corners will be designed.

2.7.1 Specifications

This example must feature a pass band between 10.7 GHz and 12.3 GHz with return loss better than 20 dB. Moreover, around 60 dB rejection level for frequencies between 13.5 GHz to 38 GHz has to be also satisfied.

2.7.2 Design and Simulation

As the filter will be manufactured cutting by the H-plane, the DBB given in Figure 2.3(a) will be utilized to synthesize the desired filter. The design parameters of the proposed filter are given in Table 2.4. The physical dimensions of the synthesized filter (see Figure 2.8) are given in Table 2.5 and its simulated FEST3D frequency response along with the ideal one is compared in Figure 2.9. As it can be seen, the maximum attenuation of the filter synthesized in this Chapter is very close to the target. In consequence, an accurate result is obtained with the technique of this Chapter without neither EM simulations nor optimizations.

2.7.3 Fabrication and Measurement

A 3-step transformer has been added at the input and output ports to reach the standard WR75 port height. This filter has been fabricated in two halves, cutting by the

Table 2.4: Summary of design parameters of the synthesized filter in Section 2.7.

Filtering function type	Chebyshev
Order, N	27
In-band return loss	27.5 dB
Passband upper frequency, f_c	12.7 GHz
Maximum rejection frequency, f_0	24.5 GHz
Waveguide width, a	19.05 mm

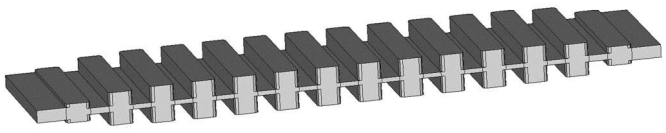

Figure 2.8: 3D view of the synthesized filter in Section 2.7.

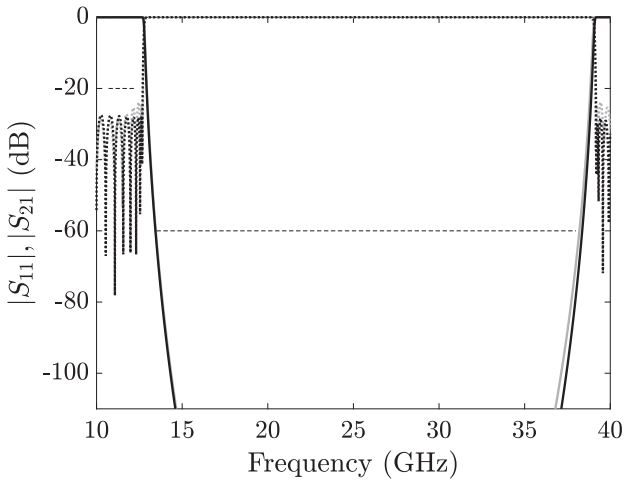

Figure 2.9: Ideal frequency response (grey line) and FEST3D frequency response for the structure (Section 2.7) obtained with the novel method in Section 2.4 (black line). $|S_{11}|$ in dotted line, $|S_{21}|$ in solid line. Frequency specifications in dashed line.

Table 2.5: Dimensions of the synthesized filter in Section 2.7.

UE	Z_i	b_i (mm)	l_i (mm)
0, 28	1.000	1.686	3.103
1, 27	1.506	2.539	3.293
2, 26	0.504	0.850	2.516
3, 25	2.614	4.408	3.220
4, 24	0.384	0.649	2.428
5, 23	2.927	4.935	3.192
6, 22	0.365	0.616	2.416
7, 21	3.008	5.072	3.186
8, 20	0.359	0.606	2.414
9, 19	3.039	5.124	3.184
10, 18	0.357	0.602	2.414
11, 17	3.053	5.147	3.184
12, 16	0.356	0.6	2.413
13, 15	3.058	5.156	3.183
14	0.356	0.6	2.413

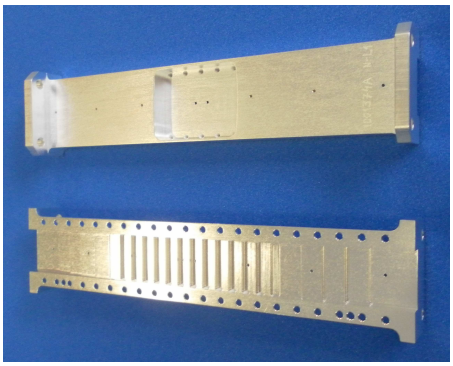

Figure 2.10: Photograph of the unassembled prototype of the filter designed in Section 2.7.

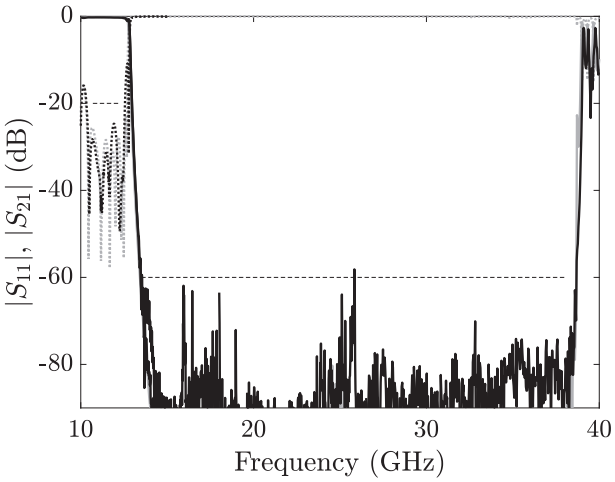

Figure 2.11: Frequency response of the filter designed in Section 2.7: measured (black line) and simulated with CST MWS (grey line). $|S_{11}|$ in dotted line and $|S_{21}|$ in solid line. Frequency specifications in dashed line.

H-plane, in bare aluminum by standard CCM (radius of the drill equal to 1 mm) and silver-plated. The fabricated prototype is shown in Figure 2.10. It has been measured obtaining excellent results, in agreement with the simulations, see Figure 2.11. It should be noted that the return-loss difference between the frequency response shown in Figure 2.9 and Figure 2.10 is due to the effect of the 3-step transformer.

To conclude, the possibility of designing classical corrugated LPF with rounded corners by using the new design technique presented in this Chapter has been proved. Indeed, it has been done through the design, simulation, and measurement of a filter with H-plane rounded corners. It should be emphasized that the measurement results are very close to the simulated ones.

Table 2.6: Summary of design parameters of the synthesized filter in Section 2.8.

Filtering function type	Zolotarev
Order, N	17
In-band return loss	23 dB
Passband upper frequency, f_c	11 GHz
Passband lower frequency, f_{Zolo}	8.1 GHz
Maximum rejection frequency, f_0	15 GHz
Waveguide width, a	19.05 mm

2.8 Design Example 3: Routing with Classical Corrugated LPF

In order to demonstrate the feasibility of the novel design technique proposed in Section 2.5, a corrugated waveguide LPF with routing capability will be designed.

2.8.1 Specifications

The novel filter will fulfil the following frequency specifications: passband from 10 GHz to 10.8 GHz with in-band return loss of 20 dB; and stopband between 13 GHz and 15 GHz with attenuation level of 60 dB. In this example, the standard input and output WR75 ports are required to be placed at the same plane.

2.8.2 Design and Simulation

With the design parameters detailed in Table 2.6 and the design technique in Section 2.3, the in-line solution is achieved very accurately (grey line in Figure 2.13). If the filter is directly bent to fit the pursued volume allocation, the frequency response is completely distorted (black line in Figure 2.13). Following instead the method described in Section 2.5, using equations (2.12) to (2.15), and FEST3D to simulate each DBB, all b_i and l_i are obtained in the filter. All physical dimensions are detailed in Table 2.7 and the frequency response is shown in grey line in Figure 2.14. As it can be seen, an excellent starting point for the final adjustment is directly accomplished. Slightly optimizing only the lengths, the final structure is achieved (Figure 2.12), see black line in Figure 2.14.

2.8.3 Fabrication and Measurement

The novel filter has been fabricated in aluminum in two halves in clam-shell configuration (Figure 2.15). The measurement results shown in Figure 2.16 are very close to the simulated ones and the filter fulfills not only the required frequency specifications but also the physical restrictions imposed.

In short, the feasibility of designing classical corrugated waveguide LPF with embedded bends with the new easy and quick design technique proposed in Section 2.5

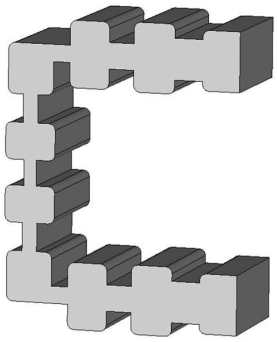

Figure 2.12: 3D view of the synthesized filter in Section 2.8.

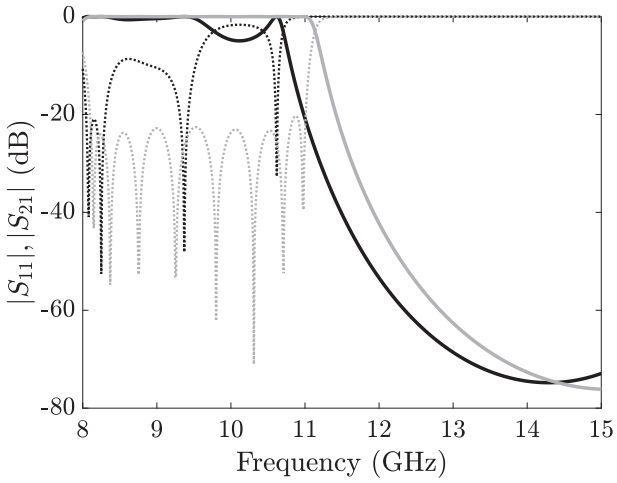

Figure 2.13: FEST3D simulated frequency response comparison between the in-line filter designed following the technique in Section 2.3 (grey line) and the directly bent counterpart in junctions 6 and 13 (black line). $|S_{11}|$ in dotted line and $|S_{21}|$ in solid line.

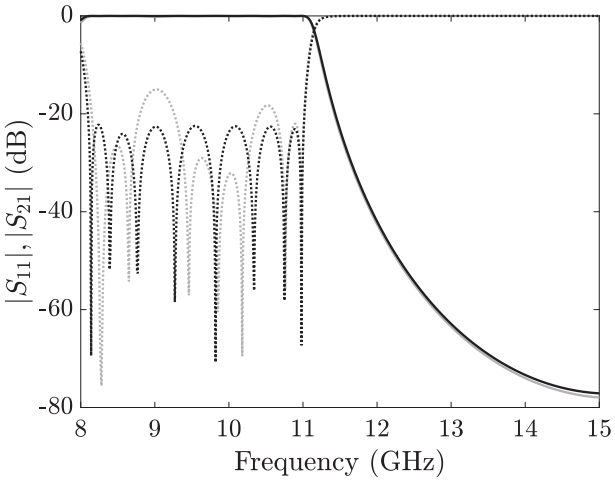

Figure 2.14: FEST3D simulated frequency response comparison between the novel filter designed in Section 2.8 with the technique in Section 2.5 without (grey line) and with the final adjustment (black line). $|S_{11}|$ in dotted line and $|S_{21}|$ in solid line.

Table 2.7: Final dimensions of the novel filter with embedded bends.

UE	Z_i	b_i (mm)	l_i (mm)	i-th DBB
0, 18	1.000	9.525	5.000	straight
1, 17	0.687	6.580	4.5	straight
2, 16	1.160	10.974	6.607	straight
3, 15	0.433	4.189	4.006	straight
4, 14	1.110	10.533	6.400	straight
5, 13	0.307	2.974	3.168	folded-down
6, 12	0.920	7.797	7.616	straight
7, 11	0.242	2.071	3.272	straight
8, 10	0.797	6.798	7.805	straight
9	0.221	1.895	3.365	

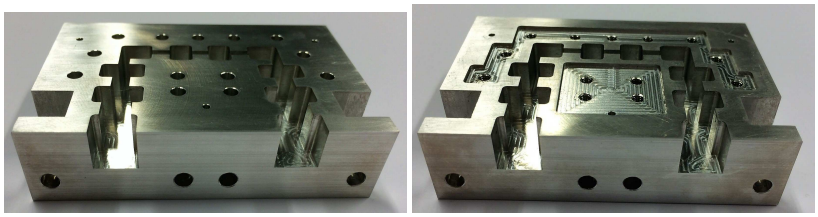

Figure 2.15: Photograph of the unassembled fabricated prototype of the novel filter designed in Section 2.8.

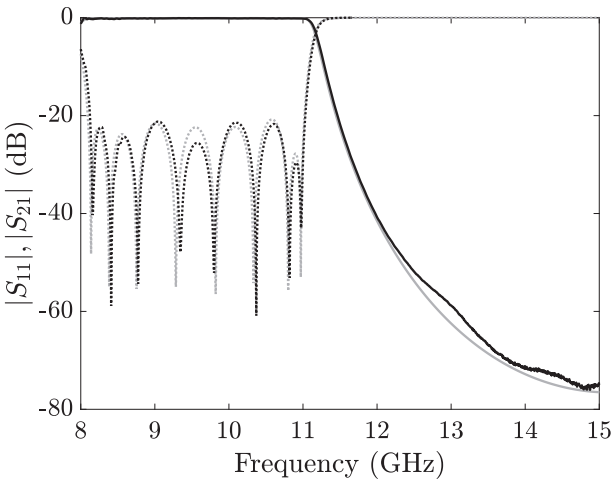

Figure 2.16: Frequency response measurements of the novel filter designed in Section 2.8 (black line) and CST MWS simulation of the novel filter with rounded corners (grey line). $|S_{11}|$ in dotted line and $|S_{21}|$ in solid line.

has been demonstrated in this example. This novel approach avoids cumbersome sub-assemblies reducing the insertion loss, weight, and PIM in ground terminals and multi-beam payloads. It has been proved with a 17th-order Zolotarev bent filter, whose frequency response measurements are very close to the simulated and targeted ones.

2.9 Conclusions

A novel quasi-analytical accurate synthesis method to design stepped-impedance LPFs in rectangular waveguide technology has been proposed in the first part of this Chapter. This technique is based on the calculation of the heights and lengths of the final structure taking into account the effect of the shunt capacitance which arises between two adjacent waveguide sections of different height in the magnitude and phase of the local reflection coefficients. This novel approach allows the designer to obtain a final prototype whose frequency response is very close to the ideal one. Actually, only closed-form equations are used during the synthesis procedure. After that, a very simple modular design method has been proposed to include the rounded of the corners if a CCM manufacturing is assumed. This technique can be easily integrated in a SW module obtaining excellent results in a negligible CPU time. Last but not least, the possibility of embed routing capability in this kind of filters has been also detailed, allowing designers to obtain routing LPFs with or without bends, avoiding subsequent bending structures and reducing insertion loss, volume/weight,

and PIM. All of these design procedures have been proved with design examples whose measurement results are very close to the simulated ones.

REFERENCES

[1] F. Teberio, I. Arnedo, J. M. Percaz, I. Arregui, T. Lopetegi, and M. A. G. Laso, "Accurate design of corrugated waveguide low-pass filters using exclusively closed form expressions," in *2017 47th European Microwave Conference (EuMC)*, Oct. 2017.

[2] F. Teberio, J. M. Percaz, I. Arregui, P. Martin-Iglesias, T. Lopetegi, M. A. G. Laso, and I. Arnedo, "Matlab accurate synthesis of classical stepped-impedance rectangular waveguide filters," in *2018 International Workshop on Microwave Filters (IWMF)*, Apr. 2018.

[3] ——, "Automated synthesis for stepped-impedance waveguide filters," *Submitted for consideration in Radio Science*, 2018.

[4] ——, "Routing with classical corrugated waveguide low-pass filters with embedded bends," *Progress In Electromagnetics Research Letters*, vol. 75, no. -, pp. 1–6, Apr. 2018.

[5] UPNA, "Design techniques for low-cost filters with reduced sensitivity to fabrication tolerances at high-frequencies," ESA and Thales Alenia Space, NPI 4000114859/15/NL/HK, 2018.

[6] V. Boria and B. Gimeno, "Waveguide filters for satellites," *Microwave Magazine, IEEE*, vol. 8, no. 5, pp. 60–70, Oct. 2007.

[7] G. Matthaei, L. Young, and E. M. T. Jones, *Microwave filters, impedance-matching networks and coupling structures*. Artech House, 1980.

[8] R. Cameron, C. Kudsia, and R. Mansour, *Microwave Filters for Communication Systems: Fundamentals, Design and Applications*. Wiley-Interscience, 2007.

[9] V. Boria, P. Soto, and S. Cogollos, "Distributed models for filter synthesis," *Microwave Magazine, IEEE*, vol. 12, no. 6, pp. 87–100, Oct. 2011.

[10] S. B. Cohn, "A theoretical and experimental study of a waveguide filter structure," *Office Naval Res.*, vol. 39, no. 11, Apr. 1948.

[11] R. Levy, "A generalized design technique for practical distributed reciprocal ladder networks," *IEEE Transactions on Microwave Theory and Techniques*, vol. 21, no. 8, pp. 518–526, Aug. 1973.

[12] M. Simeoni, F. Cacchione, S. Vanin, J. Molina-Perez, and D. Schmitt, "Automatic dimensional synthesis without optimization for stepped impedance low-pass filters," *Microwave Optical and Technology Letters*, vol. 44, no. 1, pp. 190–193, Jan. 2005.

[13] O. Monerris, P. Soto, S. Cogollos, V. Boria, J. Gil, C. Vicente, and B. Gimeno, "Accurate circuit synthesis of low-pass corrugated waveguide filters," in *2010 40th European Microwave Conference (EuMC)*, Sep. 2010, pp. 1237–1240.

[14] S. Cogollos, V. Boria, P. Soto, B. Gimeno, and M. Guglielmi, "Efficient CAD tool for inductively coupled rectangular waveguide filters with rounded corners," in *2001 31st European Microwave Conference (EuMC)*, Sep. 2001, pp. 1–4.

[15] H. Moheb, C. Robinson, and J. Kijesky, "Design amp; development of co-polarized ku-band ground terminal system for very small aperture terminal (vsat) application," in *IEEE Antennas and Propagation Society International Symposium. 1999 Digest. Held in conjunction with: USNC/URSI National Radio Science Meeting (Cat. No.99CH37010)*, vol. 3, Jul. 1999, 2158–2161 vol.3.

[16] H. Wolf, M. Schneider, S. Stirland, and D. Scouarnec, "Satellite multibeam antennas at airbus defence and space: State of the art and trends," in *2014 8th European Conference on Antennas and Propagation (EuCAP)*, Apr. 2014, pp. 182–185.

[17] A. Morini, M. Guglielmi, and M. Farina, "A technique for the measurement of the generalized scattering matrix of overmoded waveguide devices," *IEEE Transactions on Microwave Theory and Techniques*, vol. 61, no. 7, pp. 2705–2714, Jul. 2013.

[18] C. Carceller, P. Soto, V. E. Boria, and M. Guglielmi, "Design of hybrid folded rectangular waveguide filters with transmission zeros below the passband," *IEEE Transactions on Microwave Theory and Techniques*, vol. 64, no. 2, pp. 475–485, Feb. 2016.

[19] N. Marcuvitz, *Waveguide Handbook*. McGraw-Hill, 1951.

[20] R. Levy, “Tapered corrugated waveguide low-pass filters,” *IEEE Transactions on Microwave Theory and Techniques*, vol. 21, no. 8, pp. 526–532, Aug. 1973.

CHAPTER 3

MODULAR AND QUICK DESIGN PROCEDURE FOR WAFFLE-IRON LPFs WITH POSSIBLE TRANSMISSION ZEROS

In this Chapter, an accurate design procedure for waffle-iron waveguide LPFs is proposed [1], [2]. The novel design technique is based on the decomposition of the filter into a finite number of design entities (DEs), which are composed of a waffle-iron section inserted between two uniform rectangular waveguide sections. Then, the physical dimensions of each DE are calculated by means of their associated frequency responses along the device. The new technique can be utilized to design the classical structures without transmission zeros and with transmission zeros and, moreover, a new compact structure which provides wide-rejection and moderate power handling in a single device. The proposed method has been proved through the design of three examples, which shows a remarkable accordance between the ideal, simulated, and measured frequency response.
It is important to note that the techniques developed in this Chapter have been done within the framework of a NPI activity with the European Space Agency [3].

3.1 Background

Spurious modes may appear, for example, due to misalignments between waveguides [4], and the classical corrugated LPFs presented in Chapter 2 are not useful in applications where their suppression is mandatory. Indeed, a simple H-plane discontinuity between two waveguides leads to the excitation of the higher-order TE_{n0} modes [5]. The spurious passbands due to the higher-order TE_{n0} modes are well reported in [6], and can be perfectly suppressed with classical solutions such as waffle-iron filters [7] or evanescent-mode filters [8]. Classical waffle-iron filters provide very wide stopband (up to several harmonics) attenuating all the propagating modes in the required frequency band and have been extensively used in many widespread applications. Indeed, the waffle-iron filter is the classical low-pass solution utilized by the satellite industry since it allows the attenuation of all propagating waveguide modes whose frequency lies in the required stopband of the filter. Classical waffle-iron filters were originally developed for high-power systems where it was desirable to suppress the harmonic frequencies generated by the transmitter. Nowadays, they are typically utilized in multi-band feeders of reflector antennas of earth stations and in the output stage of the satellite communication payloads [9]–[12]. Moreover, they are also used in industrial microwave manufacturing processes to prevent the escape of radiation from the microwave chamber [13], [14].

Invented by S. B. Cohn [15], [16], its physical structure (see Figure 3.1) is based on the classical corrugated LPFs [7], [17], where longitudinal slots are added to conform the waffle-iron structure and to achieve the suppression of the higher-order TE_{n0} modes. The effect of the slots is very well explained in modern textbooks [18] and it can be summarized as follows: due to the fact that any TE_{n0} mode can be decomposed in two plane waves propagating at different angles, if the waffle-iron filter is designed roughly isotropic (having the same characteristics at a given frequency for any plane wave propagating in any direction), all these plane waves will be similarly attenuated. Thus, all the TE_{n0} modes will be properly suppressed. There are two classical synthesis procedures to design waffle-iron filters [7]. The first one starts designing a classical corrugated waveguide filter. Then, the longitudinal

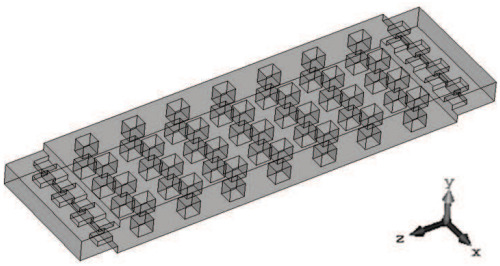

Figure 3.1: 3D view of a classical waffle-iron filter.

slots are incorporated in the low-height sections. This decreases their capacitance per unit length, which makes it necessary to reduce those heights using the tables in [15] to maintain the performance of the original structure. The second procedure proposes a new electrical model that includes the E-plane T-junction available in Marcuvitz's book [19] to predict the frequency behavior of the waffle-iron section. Both methods are rather complicated procedures that may be difficult to control, specifically to obtain the intended in-band return loss of the filter [20]. However, they are still used today to obtain an initial structure whose physical dimensions will be intensively optimized later (using different numerical analysis methods) to meet the desired frequency specifications [13], [21], [22].

The high-power performance of a waffle-iron filter can be improved by modifying the geometry of its teeth [23], by stacking several identical waffle-iron filters and dividing the power between them and combining their outputs [24] or by enlarging the minimum mechanical gap [25]. Applying the latter approach, if the maximum height is not altered, the attenuation and the rejection bandwidth are reduced or the electrical model is not satisfied. Thus, the maximum height needs to be increased. This leads to the appearance of a transmission zero within the rejection band. When the transmission zero is required close to the passband, the rejection bandwidth is severely decreased. Therefore, there is a trade-off between the mechanical gap of the structure (i.e., its power-handling capability) and the maximum frequency of the stopband (i.e., its rejection bandwidth). This limitation can be surpassed by connecting several waffle-iron filters with larger gaps whose narrow stopbands are concatenated to achieve the required wide stopband. Each waffle-iron filter is independently designed and then connected to each other by quarter-wave transformers, which is a time-consuming and bulky solution [12], [25].

In this Chapter, a novel accurate design procedure to design classical waffle-iron filters is proposed. The design method is based on a divide-and-rule strategy where the objective is to mimic the frequency response in reflection of two consecutive impedance steps (provided by the stepped-impedance low-pass filter prototype) with the physical dimensions of the so-called filter's design entity (DE). This allows for a simple modular design with negligible evanescently-excited high-order modes between the DEs which can be straightforwardly implemented in an EM SW design module, allowing designers to obtain from scratch a waffle-iron filter once a frequency specifications mask is provided [1]. After that, the new technique is extended to the design of high-power waffle-iron filters with transmission zeros at one frequency as those used in [25]. Finally, a new waffle-iron structure that provides very compact high-power wide-rejection filters with transmission zeros at multiple frequencies is presented along with its design procedure [2].

3.2 Objective

The main objective is to reduce design times by means of developing a new design technique which could be easily integrated in a SW to reduce the design times of classical waffle-iron filters as much as possible. It is important to note that, in the

space industry, each new design required by the customers is a simple re-scale and (hard) optimization of a pre-designed filter. Now, with the novel design technique presented in this Chapter, the designers will have the final dimensions of the structure (or a very good starting-point for a slight adjustment of the physical parameters) in a negligible CPU time.

3.3 Design Method

A new structure is proposed that alternates rectangular waveguide sections and waffle-iron sections (i.e., rectangular waveguide sections with longitudinal slots), see Figure 3.2 and Figure 3.3. This structure provides higher degrees of freedom than the classical ones, which implies a higher number of design variables, being necessary to present a complete design procedure.

Firstly, several physical parameters of all the waffle-iron sections are defined following the typical considerations for this kind of filters that appear in [7]. Particularly, the number of teeth, n_t, will be higher for wider stopbands. The length of the teeth, l_t, their width, w_t, and their separation, s_t, will be chosen equal (or very similar) and large enough to allow, simultaneously, an easy manufacturing and a good

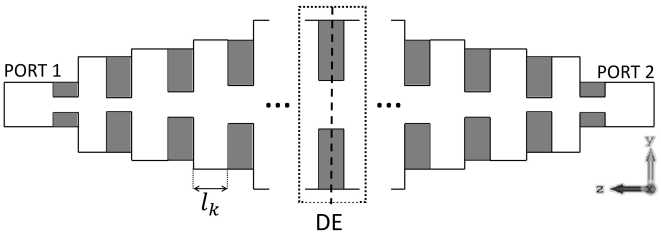

Figure 3.2: Longitudinal view of the entire waffle-iron structure.

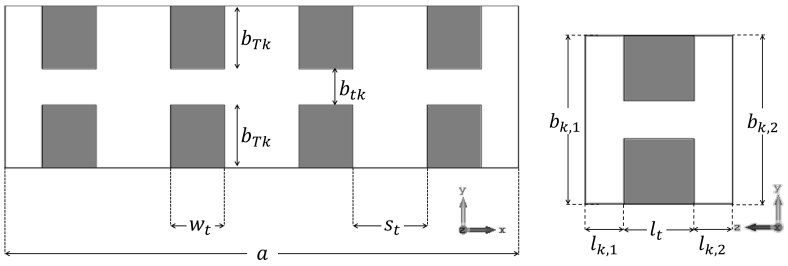

(a) **(b)**

Figure 3.3: (a) Transversal view of the waffle-iron section with labelled design parameters and (b) longitudinal view of the DE with its associated constituent parameters.

isotropy, providing the same characteristics, at a given frequency, for the TEM waves propagating in any direction.

The design method continues by defining the heights $b_{k,1}$ (see Figure 3.2), whose values depend on the type of waffle-iron selected by the designer:

- a waffle-iron without transmission zeros (Section 3.3.1);
- a waffle-iron with transmission zeros at a single frequency (Section 3.3.2);
- a novel waffle-iron filter with transmission zeros at multiple frequencies (Section 3.3.3).

Now, the low-pass stepped-impedance prototype, based on a set of $(2 \cdot N_{DE} + 1)$ transmission lines with characteristic impedances, Z_i, and electrical length, θ, is computed by means of the *Richards' transformation* and the Unit Element extraction procedure fully detailed in Annex A, [26], once the desired all-pole frequency response, the width of the structure, a, the required in-band return loss, the frequency of maximum rejection, f_0, and the maximum frequency of the passband, f_c, are fixed.

Instead of paying attention to the entire structure of Figure 3.2, notice how the filter is divided into N_{DE} Design Entities (DEs), see Figure 3.3(b), which are designed independently and then connected. Thus, each DE is defined as two half sections of uniform rectangular waveguide with a waffle-iron section between them, see Figure 3.3(b). The electrical model of each DE will be composed of half transmission line, one step, one transmission line, another step, and another half transmission line. Hence, the Z_i of the low-pass stepped-impedance prototype are combined in triplets in order to calculate the frequency response of the electrical model of the kth-DE in reflection and transmission by evaluating equations (3.1) and (3.2), respectively. The E_k is the transmission ABCD 2-by-2 matrix of the kth-DE calculated following equations (3.3) to (3.5). It is important to note that there is a frequency dependence of E_k through the propagation constant of the fundamental mode, $\beta_{10,f}$.

$$S_{11,k}(f) = \frac{E_{11,k} + \frac{E_{12,k}}{Z_{2k}} - E_{21,k} \cdot Z_{2k-2} - E_{22,k} \cdot \frac{Z_{2k-2}}{Z_{2k}}}{E_{11,k} + \frac{E_{12,k}}{Z_{2k}} + E_{21,k} \cdot Z_{2k-2} + E_{22,k} \cdot \frac{Z_{2k-2}}{Z_{2k}}} \qquad (3.1)$$

$$\text{for } k = 1 : N_{DE}$$

$$S_{21,k}(f) = \frac{2 \cdot \sqrt{\frac{Z_{2k-2}}{Z_{2k}}}}{E_{11,k} + \frac{E_{12,k}}{Z_{2k}} + E_{21,k} \cdot Z_{2k-2} + E_{22,k} \cdot \frac{Z_{2k-2}}{Z_{2k}}} \qquad (3.2)$$

$$\text{for} \quad k = 1 : N_{DE}$$

$$[E_k] = [R_{2k-2}] \cdot [W_{2k-1}] \cdot [R_{2k}] \qquad (3.3)$$

$$R_i = \begin{bmatrix} \cos\left(\frac{\theta}{2}\right) & \jmath \cdot Z_i \cdot \sin\left(\frac{\theta}{2}\right) \\ \frac{\jmath}{Z_i} \cdot \sin\left(\frac{\theta}{2}\right) & \cos\left(\frac{\theta}{2}\right) \end{bmatrix}$$

$$W_i = \begin{bmatrix} \cos\left(\theta\right) & \jmath \cdot Z_i \cdot \sin\left(\theta\right) \\ \frac{\jmath}{Z_i} \cdot \sin\left(\theta\right) & \cos\left(\theta\right) \end{bmatrix} \tag{3.4}$$

$$\text{for} \quad i = 0 : 2 \cdot N_{DE}$$

$$\theta = \frac{\beta_{10,f}}{\beta_{10,f_0}} \cdot \frac{\pi}{2} \tag{3.5}$$

With this, it is possible to calculate the rest of the physical dimensions of the kth-DE (clearly identified in Figure 3.3) that are:

- the height of the teeth, b_{Tk},
- the length of the input rectangular waveguide section, $l_{k,1}$,
- the length of the output rectangular waveguide section, $l_{k,2}$.

This is done by carrying out simple S-parameter EM simulations of each kth-DE on its own (where b_{Tk}, $l_{k,1}$, and $l_{k,2}$ are involved) to obtain the frequency response in reflection and transmission and compare them with frequency response of the electrical model of each kth-DE, i.e., expressions equations (3.1) and (3.2). Specifically, equations (3.6), (3.7), and (3.8) need to be satisfied in each kth-DE, where the $|S_{11,k}(f_c)|$ is the magnitude of equation (3.1) evaluated at the frequency f_c while the $|S'_{11,k}(f_c)|$ is the magnitude of the $S_{11}(f)$ of the kth-DE obtained with an EM simulator at f_c, the $\phi_{k,S_{11}}(f_c)$ is phase of equation (3.1) evaluated at f_c while $\phi'_{k,S_{11}}(f_c)$ is the phase of the $S_{11}(f)$ of the k-DE obtained with an EM simulator at f_c, and $\phi'_{k,S_{11}}(f_0)$ is the phase of the $S_{21}(f)$ of the kth-DE obtained with an EM simulator at f_0.

$$|S'_{11,k}(f_c)| = |S_{11,k}(f_c)| \tag{3.6}$$

$$\phi'_{k,S_{21}}(f_0) = 180^\circ \tag{3.7}$$

$$\phi'_{k,S_{11}}(f_c) = \phi_{k,S_{11}}(f_c) \tag{3.8}$$

Now, the lengths of the different sections, l_k, are simply computed by $l_k = l_{k-1,2} + l_{k,1}$ for $k = 2 : (N_{DE} - 1)$. Moreover, for simplicity, the first, l_1, and the last, $l_{N_{DE}}$, section lengths will be equal to $l_{1,1}$ (notice that this is just the length

of a uniform transmission line that affects to the phase only, as it is well known, of the frequency response of the whole structure).

It should be noted that although l_t has been fixed at the beginning and it kept constant through the kth-DE, it could be deduced from equations (3.3), (3.4), and (3.5), as in [25], that equation (3.9) should be also satisfied. If this condition is not met, the value of l_t should be accordingly modified and b_{Tk}, $l_{k,1}$, and $l_{k,2}$ recomputed, using again equations (3.6) to (3.8).

$$l_t + l_k \approx \frac{\lambda_{f_z}}{2} \tag{3.9}$$

Finally, a slight adjustment is needed to obtain the final frequency response of the required filter, mainly due to the effect of high-order modes that are evanescently present at the intersections of the DE.

3.3.1 Waffle-Iron Filter without Transmission Zeros

The overall filtering structure of a waffle-iron filter without transmission zeros [1] (see Figure 3.4(a)) is composed of the first DE with $b_{1,1} < b_{1,2}$ and the last $b_{N_{DE},1} > b_{N_{DE},2}$, while the rest of the structure is composed of DEs where $b_{k,1} = b_{k,2}$. For the sake of simplicity, a symmetrical end-to-end structure is assumed. Hence, the heights of the input and output ports, $b_{1,1}$ and $b_{N_{DE},2}$ respectively, are defined according to the minimum mechanical gap allowed in the filter and the desired stopband performance. After that, $b_{1,2}$ (and $b_{N_{DE},1}$ by symmetry as aforementioned) is set to a value lower than b_{max}, given by equation (3.10), to avoid the excitation of the higher-order non-TE_{n0} modes inside the structure (the TE_{01} mode in our case) at a selected maximum frequency, f_{max}. Thus, the DEs for $k = 2 : (N_{DE} - 1)$ will have $b_k = b_{k,1} = b_{k,2} = b_{1,2} < b_{max}$.

$$b_{max} = \frac{c}{2 \cdot f_{max}} \tag{3.10}$$

After that, starting with the first DE and following one by one independently, the physical dimensions of each kth-DE (b_{Tk}, $l_{k,1}$, and $l_{k,2}$) will be calculated satisfying equations (3.6), (3.7), and (3.8).

3.3.2 Waffle-Iron Filter with Transmission Zeros at One Frequency

In order to maximize the high-power behavior and the attenuation of the previous structure, several transmission zeros placed at the same frequency (denoted as f_z) in the stopband can be obtained by setting the height, b_k, around (but greater than) half-wavelength at f_z, following equation (3.11), [25].

$$b_{k,1} \gtrsim \frac{\lambda_{f_z}}{2} \tag{3.11}$$

The waffle-iron filter with several transmission zeros at one frequency has the same physical appearance as the filters in the last section. Indeed, the whole device,

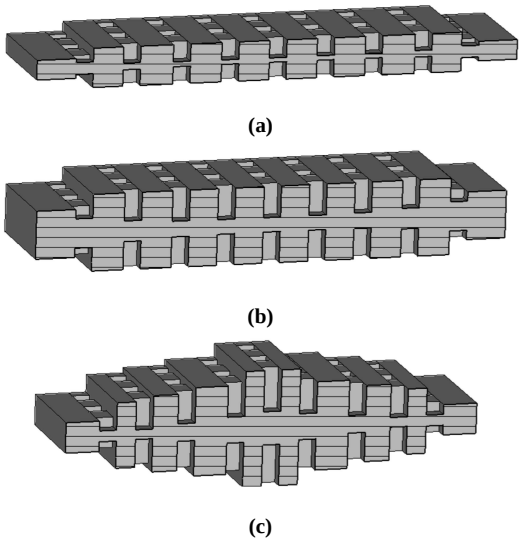

Figure 3.4: 3D cut-view of the (a) waffle-iron filter without transmission zeros, (b) waffle-iron filter with transmission zeros at one frequency, and (c) novel waffle-iron filter with transmission zeros at multiple frequencies.

see Figure 3.4(b), will be composed of the first DE with $b_{1,1} < b_{1,2}$ and the last DE with $b_{N_{DE},1} > b_{N_{DE},2}$. Therefore, $b_{1,1}$ and its counterpart $b_{N_{DE},2}$ at the output port are fixed to a value less than or equal to b_{max} (given by equation (3.10)) to suppress all the higher-order non-TE_{n0} modes up to f_{max}. The rest of the structure is composed of DEs where $b_{1,2} = b_{k,1} = b_{k,2} = b_{N_{DE},1}$ (Figure 3.2 and Figure 3.3) for $k = 2 : (N_{DE} - 1)$.

First, $b_{k,1}$ is estimated choosing the frequency at which the transmission zeros are desired. Thus, $b_{k,1}$ is usually calculated by equation (3.11) using $f_z = f_0$, since it maximizes the attenuation bandwidth and the power handling. However, if a frequency below f_0 is chosen, the stopband of the filter obtained will be narrower. On the other hand, if a frequency above f_0 is chosen, the transition slope between the passband and stopband is not improved and the rejection bandwidth hardly increases [25]. Therefore, a wide stopband and a transmission zero close to the passband cannot be obtained simultaneously. It is also important to notice that the actual location of f_z depends on the physical parameters b_{tk}, w_t, and b_{Tk}, [13], [19]. It is clear from inspection of Figure 3.2 and Figure 3.3 that the variables $b_{k,1}$, b_{Tk} and b_{tk} are related as follows:

$$b_{tk} = b_{k,1} - 2 \cdot b_{Tk} \tag{3.12}$$

Once $b_{k,1}$ is estimated by means of equation (3.11), the value of b_{Tk} (and hence b_{tk} by equation (3.12)) is computed by satisfying equation (3.6) to mimic the highest target magnitude value given by equation (3.1), since it will determine the minimum

b_{tk} of the filter. Then, if b_{tk} does not fulfill the minimum value required by the designer, it can be increased. However, it must be taken into account that it must be small enough to shift the cutoff frequency of the higher-order non-TE_{n0} modes beyond f_{max} besides minimizing the excitation of the higher-order modes in the inner part of each DE (since higher values of b_{tk} imply higher values of $b_{k,1}$ and lower values of $l_{k,1}$ and $l_{k,2}$ through a capacitive effect - phase shift contribution -). Then, $b_{k,1}$ and b_{Tk} are recalculated to fulfill equation (3.6) and the desired b_{tk} (with the previous constraints) simultaneously, considering that the critical DE is the one where the maximum value of equation (3.6) for each DE is attained. Next, once the final value of $b_{k,1}$ has been fixed, the b_{Tk} of each DE is calculated to satisfy equation (3.6). At the same time, $l_{k,1}$ and $l_{k,2}$ will be calculated by satisfying equations (3.7) and (3.8). In this case, as it will be exemplified in the examples, the synthesis procedure is more accurate if the transmission zeros are closer to f_{max}, since there will be less high-order modes contribution in the inner part of the device. In any case, only a slight adjustment of the lengths of the rectangular waveguide sections of the final filter will be needed to fulfill the required frequency specifications.

3.3.3 Novel Waffle-Iron Filter with Transmission Zeros at Multiple Frequencies

As it was mentioned in the Introduction, the classical approach to achieve a wide stopband and high-power handling at the same time is by cascading several waffle-iron filters (as those designed as in Section 3.3.2) separated by quarter-wavelength transformers of several sections for matching [12], [25]. These structures are long and not efficient in terms of mass and volume. In this case, a novel waffle-iron filter which can achieve, simultaneously, high-power handling, transmission zeros placed at multiple frequencies (very close to the passband if required), and a wide rejected band in a compact single structure is presented. The novel filter, see Figure 3.4(c), is obtained by cascading several DEs (Figure 3.2 and Figure 3.3) of different $b_{k,1}$, which implement different transmission zeros. Physically, the structure begins (and ends, by symmetry) with the DE which provides the transmission zero located farther from the passband. Then, the rest of DEs are cascaded in such a way that the DE that provides the transmission zero closest to the passband will be placed in the center of the device.

The design method starts by designing the DE that provides the transmission zero ($f_{z,k}$) closest to the passband ($k = N_{DE}/2$ if N_{DE} even or $k = (N_{DE}+1)/2$ if N_{DE} odd). Therefore, $b_{k,1}$ is computed following equation (3.11). After that, the value of b_{Tk} is calculated directly using equation (3.6), considering that the critical DE is the one where the maximum value of equation (3.6) for each DE is attained. Then b_{tk} is calculated by equation (3.12) to see if the balance between power handling and high-order mode excitation is adequate. If not, the desired b_{tk} is chosen high enough to provide high-power handling but small enough to achieve the suppression of the higher-order non-TE_{n0} modes beyond f_{max} as well as to minimize the excitation of higher-order modes due to the closeness between the waffle-iron sections. Then, $b_{k,1}$ and b_{Tk} are adjusted by satisfying equation (3.6). After that, $l_{k,1}$,

and $l_{k,2}$ are calculated by fulfilling equations (3.7) and (3.8). As it was aforementioned, if b_{Tk} is high, it maximizes the high-power behavior but produces narrow stopbands. Indeed, the maximum rejection frequency of each DE, $f_{max,k}$, can be easily computed by the out-of-band EM simulation of the kth-DE.

Subsequently, the design process continues by designing the contiguous DE on the left ($k = (N_{DE}/2 - 1)$ if N_{DE} is even or$k = [(N_{DE} + 1)/2 - 1)]$ if N_{DE} is odd). Note that the current $b_{k,2}$ will be equal to the $b_{k+1,1}$ previously computed. Therefore, $b_{k,1}$ for this DE is calculated by equation (3.11) to achieve a transmission zero which accomplishes the suppression of the frequencies around f_{max} of the previous DE but actually at a new position selected by the designer ($f_{z,k} \leq f_{z,k+1}$). Then, the value of b_{Tk} is computed satisfying equation (3.6) and the value of b_{tk} calculated by equation (3.12). Then, following the same criteria as in the previous DE, if b_{tk} is not the desired one, it can be modified (with the same limitations previously explained) and $b_{k,1}$ and b_{Tk} will be recalculated fulfilling equation (3.6). After that, $l_{k,1}$, and $l_{k,2}$ are computed by satisfying equations (3.7) and (3.8). In this way, proceeding iteratively, the physical parameters of each DE are defined as in the previous case to achieve the required transmission zero at $f_{z,k}$ fulfilling the target magnitude value given by equation (3.1) by using equation (3.6), and the corresponding phases by equation (3.7) and (3.8). It is important to note that the attenuation given by the transmission zeros can be reinforced if several identical DEs are chosen. The last DE to be designed is the one situated at the input port of the structure. In this case, $b_{1,1}$ will be set smaller than the value given by b_{max} through equation (3.10) to guarantee the suppression of the higher-order non-TE_{n0} modes up to f_{max}. Finally, the DEs on the right side of the devices will have the same physical parameters if, as we have said, we assume end-to-end symmetry for the shake of simplicity.

Design Examples

According to the design methodologies proposed, three different examples will be presented in this Chapter. Firstly, a classical waffle-iron without transmission zeros designed will be designed in Section 3.4 following the novel technique in Section 3.3.1, [1]. This filter has been also fabricated by CCM and measured, obtaining excellent results. The second example (Section 3.5) will demonstrate the feasibility of designing classical waffle-iron filters with transmission zeros at a single frequency following the novel design technique described in Section 3.3.2, [2]. Indeed, three different waffle-iron filters whose transmission zeros are located at three different single frequencies will be designed. The third example (Section 3.6) includes a novel compact high-power wide stopband waffle-iron filter with transmission zeros located at different frequencies following the novel design technique described in Section 3.3.3, [2]. Besides, a prototype of the novel filter will be also fabricated and measured.

3.4 Design Example 1: Waffle-Iron Filter without Transmission Zeros

3.4.1 Specifications

A Ku-band waffle-iron LPF has been designed to prove the novel synthesis procedure presented in Section 3.3.1. The filter will fulfill a passband from 10.7 GHz to 11.7 GHz with return loss better than 20 dB and a stopband defined between 17 GHz and 21 GHz (Ka-Tx-band) with attenuation levels higher than 60 dB and WR75 input and output ports.

3.4.2 Design and Simulation

The design procedure starts by selecting a Chebyshev function of order 17 (N_{DE}=9), and imposing the design parameters in Table 3.1. Then, the set of normalized Z_i are computed (also in Table 3.1). $b_{1,1}$ and $b_{1,2}$ are fixed to 3.5 mm and 6 mm, respectively, to obtain b_{tk} values higher than 1.2 mm and to shift the higher-order non-higher-order TE$_{n0}$ modes up to $fmax$, satisfying $b_{1,2} < b_{max}$, given by equation (3.10). For fabricability and to provide good isotropy for the TEM waves propagating in any direction, n_t=4, w_t=2 mm, s_t=2.072 mm, and l_t=2.5 mm are chosen. Following the design method described in Section 3.3.1, we calculate by means of equations (3.1) to (3.5) the targets of the stepped-impedance electrical model. After that, utilizing FEST3D for the calculations, the physical dimensions of each DE are computed by equations (3.6), (3.7), and (3.8)) to accomplish those targets, obtaining the waffle-iron filter whose frequency response is shown in Figure 3.5 along with the response of the initial electrical model. It is important to note that this filter already fulfills perfectly the frequency specifications. A slight adjustment has been performed in order to obtain an equiripple passband and its simulated frequency response using FEST3D is also shown in Figure 3.5. The final physical parameters are detailed in Table 3.2. The frequency response of the TE$_{20}$ mode is given in Figure 3.6.

3.4.3 Fabrication and Measurement

Finally, two transformers of three sections have been added to the previous structure to reach the WR75 ports. This filter has been fabricated in aluminum (see Figure 3.7).

The measured results fulfill perfectly the frequency specifications as can be seen in Figure 3.8. The insertion loss of the filter have kept below 0.15 dB (Figure 3.9).

Table 3.1: Summary of design parameters of the example in Section 3.4.

Filtering function type	Chebyshev
Number of DEs, N_{DE}	9
In-band return loss	25 dB
Maximum frequency of the passband, f_c	11.85 GHz
Maximum attenuation frequency, f_0	18.25 GHz
Maximum frequency of the stopband, f_{max}	25 GHz
Waveguide width, a	19.05 mm
Normalized characteristic impedances, Z_i	
$Z_0 = Z_{18}$= 1.000	$Z_1 = Z_{17}$= 0.750
$Z_2 = Z_{16}$= 1.484	$Z_3 = Z_{15}$= 0.517
$Z_4 = Z_{14}$= 1.874	$Z_5 = Z_{13}$= 0.459
$Z_6 = Z_{12}$= 1.986	$Z_7 = Z_{11}$= 0.445
$Z_8 = Z_{10}$= 2.016	Z_9= 0.443

Table 3.2: Final dimensions of the example in Section 3.4 synthesized with the technique in Section 3.3.1.

$b_{1,1}$=3.5 $b_{1,2}$=6		
DE	b_{Tk} (mm)	l_k (mm)
1, 9	0.523	-
2, 8	2.137	4.270
3, 7	2.332	5.148
4, 6	2.376	4.957
5	2.387	4.898

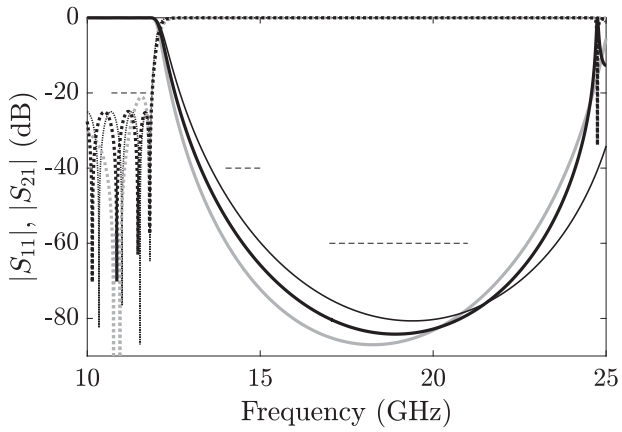

Figure 3.5: FEST3D simulated frequency response comparison between the waffle-iron filter designed with the technique in Section 3.3.1 without (grey line) and with (black thick line) the final adjustment. Theoretical response in black thin line. CST MWS simulated frequency response of the filter with the final adjustment in grey thick line. $|S_{11}|$ in dotted line and $|S_{21}|$ in solid line. Frequency specifications in dashed line.

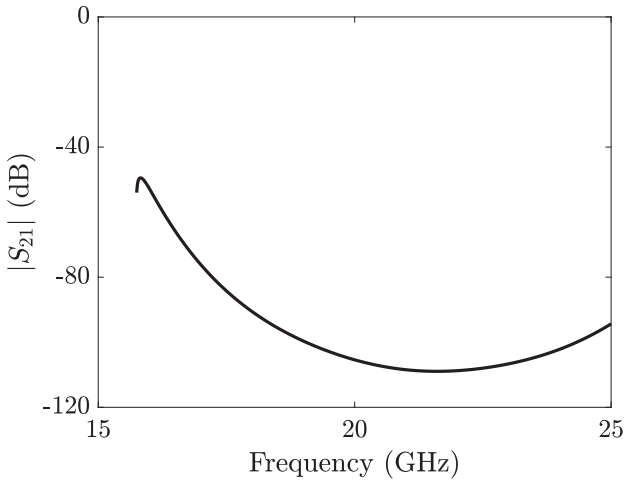

Figure 3.6: TE_{20}-mode FEST3D simulated frequency response of the waffle-iron filter with the final adjustment.

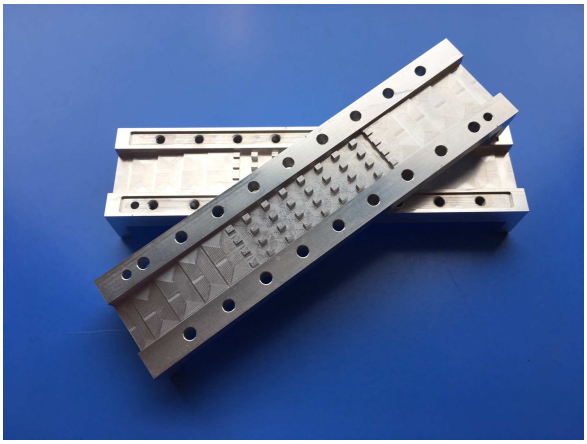

Figure 3.7: Photograph of the unassembled prototype.

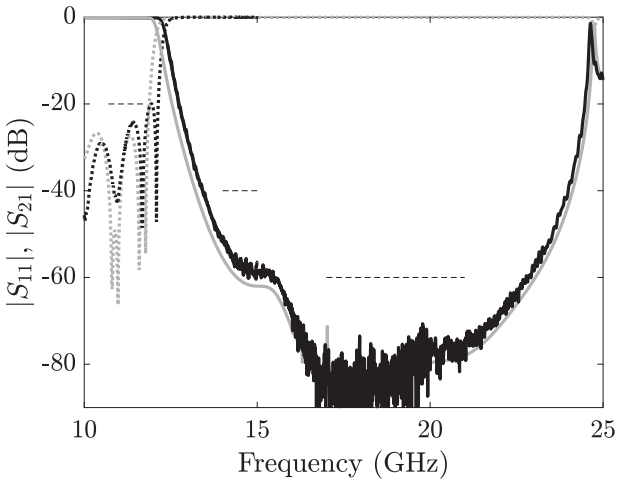

Figure 3.8: Frequency response comparison between the CST MWS simulated (grey line) of the proposed filter with rounded corners and measurements of the fabricated prototype (black line). $|S_{11}|$ in dotted line and $|S_{21}|$ in solid line. Frequency specifications in dashed line.

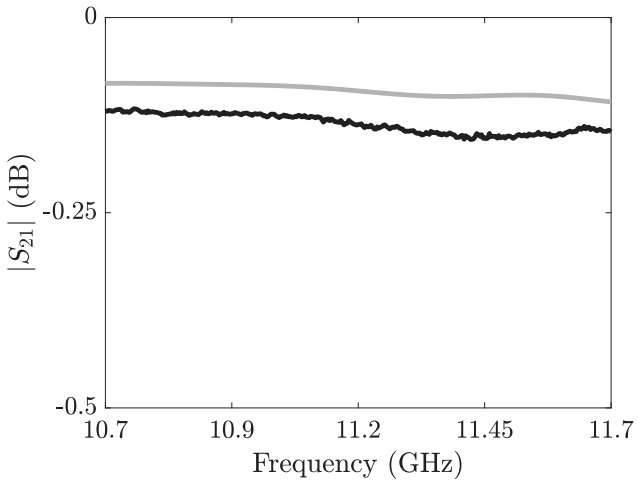

Figure 3.9: CST MWS simulation (black line) and measurement (grey line) of the in-band insertion loss of the proposed filter.

3.5 Design Example 2: Waffle-Iron Filter with Transmission Zeros at One Frequency

3.5.1 Specifications

Here, three different waffle-iron filters with transmission zeros at a single frequency will be designed with the parameters given in Table 3.3 and following the procedure described in Section 3.3.2. The fundamental difference between each filter is the location of the transmission zero. Indeed, the Waffle-Iron #1 will have a transmission zero further the passband but within the stopband (f_z = 25 GHz), the transmission zero of the Waffle-Iron #2 will be around the middle of the stopband (f_z = 20 GHz), and the Waffle-Iron #3 will have a transmission zero close to the passband (f_z = 15 GHz).

3.5.2 Design and Simulation

The process to obtain the final dimensions of the Waffle-Iron #1 is detailed hereinafter. The design process begins fixing n_t = 4, w_t =2 mm, s_t = 2.072 mm, and l_t =2 mm to achieve the suppression of the higher-order TE$_{n0}$ modes, besides minimizing the excitation of the higher-order modes in the inner part of the device and allowing an easy manufacturability.

Next, $b_{1,1}$ is set to 5 mm, using (3.10), to shift the higher-order non-TE$_{n0}$ modes up to f_{max}. (30 GHz). Then, $b_{k,1}$ is obtained by using (3.11). Consequently, to obtain a transmission zero around 25 GHz, $b_{k,1}$ is set following (3.11) equal to 6 mm. Now, it is calculated the targets of the stepped-impedance prototype given by

equations (3.1) and (3.2), using the design parameters given in Table 3.3. Next, b_{Tk} is computed by equation (3.6) and b_{tk}=0.826 mm is obtained following equation (3.12). As the obtained b_{tk} is smaller than the desired ones, the value of b_k is recalculated by satisfying equation (3.6) and $b_{tk} \geq$1.65 mm simultaneously, considering that the critical DE is the one where the maximum value of equation (3.6) for each DE is attained. After that, $b_{k,1}$, is fixed to 8.8 mm (3.10). Then, utilizing FEST3D for the EM simulations, the final dimensions of each DE are computed twofold: i) b_{Tk} is adjusted using equation (3.6), and ii) $l_{k,1}$, and $l_{k,2}$ are computed by satisfying equations (3.7) and (3.8). Finally, a slight adjustment of l_k is done. This process has been repeated in all the designed filters, obtaining the final dimensions detailed in Table 3.4.

The comparison between the ideal and the FEST3D simulated frequency response for the synthesized structures before and after the final adjustment is shown in Figure 3.10, Figure 3.11 and Figure 3.12 for the Waffle-Iron #1, #2, and #3 respectively. As can be observed, the design procedure is more accurate for synthesizing filters which have the transmission zero closer to f_{max}. The reason is that, if the transmission zero is close to the passband, its associated structure will have higher $b_{k,1}$ and shorter l_k, exciting more intensively the higher-order modes which propagate in the waffle-sections and are also present evanescently in the interface of the DE. As mentioned in Section 3.3, these effects are not directly considered in the design procedure. Even so, the adjustment needed to achieve the final response is enough to be performed in the l_k, making the optimization procedure quick and easy for an optimizer module such as the one included in FEST3D. Indeed, the final frequency response for the proposed filters is obtained in a few minutes by using the FEST3D Simplex optimization algorithm tool.

Table 3.3: Summary of design parameters of the waffle-iron filters designed in Section 3.5.

Filtering function type	Chebyshev
Number of DEs, N_{DE}	9
In-band return loss	25 dB
Maximum frequency of the passband, f_c	12.65 GHz
Maximum attenuation frequency, f_0	22 GHz
Maximum frequency of the stopband, f_{max}	30 GHz
Waveguide width, a	19.05 mm
Normalized characteristic impedances, Z_i	
$Z_0 = Z_{18}$= 1.000	$Z_1 = Z_{17}$= 0.702
$Z_2 = Z_{16}$= 1.681	$Z_3 = Z_{15}$= 0.450
$Z_4 = Z_{14}$= 2.146	$Z_5 = Z_{13}$= 0.402
$Z_6 = Z_{12}$= 2.259	$Z_7 = Z_{11}$= 0.392
$Z_8 = Z_{10}$= 2.288	Z_9= 0.390

Table 3.4: Final dimensions of the waffle-iron filters with transmission zeros at one frequency designed in Section 3.5.

	Waffle-Iron #1 $b_{1,1}$=5 b_k=8.8		Waffle-Iron #2 $b_{1,1}$=6 b_k=10.2		Waffle-Iron #3 $b_{1,1}$=8 b_k=13.35	
DE	b_{Tk} (mm)	l_k (mm)	b_{Tk} (mm)	l_k (mm)	b_{Tk} (mm)	l_k (mm)
1, 9	0.891	2.455	1.023	2.306	1.122	2.139
2, 8	3.216	3.500	3.559	3.518	4.167	2.983
3, 7	3.500	3.558	3.909	3.421	4.638	2.805
4, 6	3.558	3.308	3.980	3.121	4.715	2.268
5	3.575	3.297	4.000	3.092	4.717	2.332

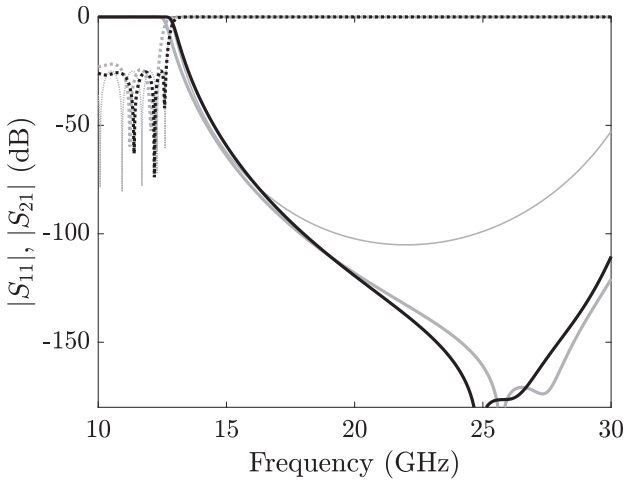

Figure 3.10: FEST3D simulated frequency response comparison between the ideal response (grey thin line) and the Waffle-Iron #1 synthesized with the technique in Section 3.3.2 without (grey thick line) and with the final adjustment (black line). $|S_{11}|$ in dotted line and $|S_{21}|$ in solid line.

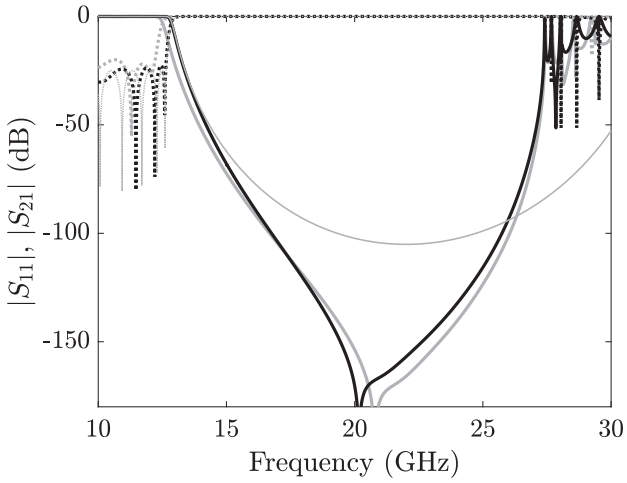

Figure 3.11: FEST3D simulated frequency response comparison between the ideal response (grey thin line) and the Waffle-Iron #2 synthesized with the technique in Section 3.3.2 without (grey thick line) and with the final adjustment (black line). $|S_{11}|$ in dotted line and $|S_{21}|$ in solid line.

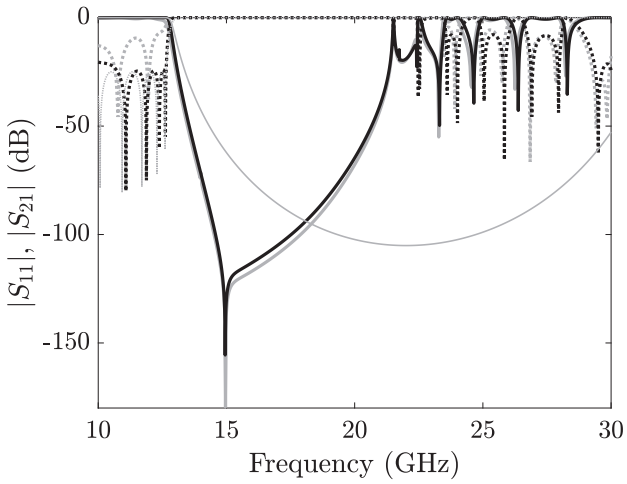

Figure 3.12: FEST3D simulated frequency response comparison between the ideal response (grey thin line) and the Waffle-Iron #3 synthesized with the technique in Section 3.3.2 without (grey thick line) and with the final adjustment (black line). $|S_{11}|$ in dotted line and $|S_{21}|$ in solid line.

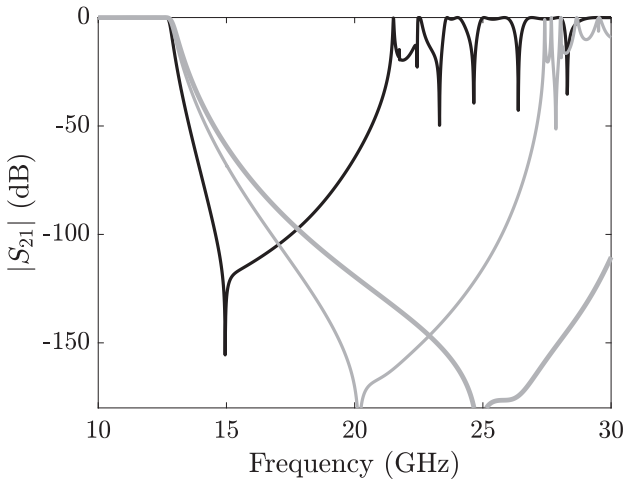

Figure 3.13: Staggered stopbands of Waffle-Iron #1 (grey thick line), Waffle-Iron #2 (grey thin line), and Waffle-Iron #3 (black line).

If the stopbands of the previous example are combined (see Figure 3.13), a very steep-slope and a wide rejected band might be simultaneously achieved if the different waffle-iron filters are cascaded by means of quarter-wave transformers of several sections as proposed in [25]. However, this is a bulky solution, not at all efficient in terms of mass and volume.

3.6 Design Example 3: Novel Compact High-Power Waffle-Iron Filter with Transmission Zeros at Multiple Frequencies

3.6.1 Specifications

Here, a novel compact high-power waffle-iron filter is presented utilizing the design technique proposed in Section 3.3.3 and fulfilling the frequency specifications given in Table 3.5. The novel filter is composed of different DEs which produce transmission zeros at different frequencies, achieving a high attenuation over a wide stopband and a steep slope between the passband and the stopband with a very compact geometry. Moreover, the designer has several degrees of freedom since, for the targeted specifications to be met, the number and positions of the transmission zeros can be selected, as well as the number of DE employed to create each zero (multiplicity). In this example, the transmission zeros will be accomplished by a single DE (for the transmission zero closer to the passband) or by two DEs for the rest of transmission zeros (actually, the multiplicity is four due to the end-to-end symmetry).

Table 3.5: Frequency specifications for the example in Section 3.6.

Passband	Return Loss	Stopband	Attenuation
10.7-12.5 GHz	20 dB	14.5-30 GHz	75 dB

Table 3.6: Final dimensions of the novel waffle-iron filter designed in Section 3.6.

DE	b_k (mm)	b_{Tk} (mm)	l_k (mm)
1, 9	3.500	1.122	3.240
2, 8	7.548	3.213	2.225
3, 7	8.800	3.388	2.883
4, 6	10.200	3.600	3.759
5	13.350	4.752	2.200

3.6.2 Design and Simulation

The design process begins by the calculation of the targets of the frequency response of the stepped-impedance prototype given by 3.1, using the design parameters given in Table 3.3. After that, the physical dimensions of the filter n_t=4, w_t=2 mm, s_t=2.072 mm, and l_t=2 mm are chosen to reveal a good isotropy, providing the same features (at a given frequency) for all TEM waves propagating in any direction to achieve the suppression of the higher-order TE$_{n0}$ modes, minimizing the excitation of the higher-order modes in the inner part of the device, and allowing an easy manufacturability.

Following the design technique described in Section 3.3.3, the design process continues by designing the 9th-DE, which will provide the transmission zero closer to the passband. In this case, $f_{z,5}$=15 GHz. Thus, the baseline value of b_{k5}=10 mm (given by equation (3.11)). Then, b_{t5}, is chosen higher than 3 mm and, utilizing FEST3D to fulfill equation (3.6), $b_5 = b_{5,1} = b_{5,2}$ is fixed to 13.35 mm and b_{T5} is adjusted to 4.76 mm. Moreover, the values of $l_{5,1}$ and $l_{5,2}$ are computed by satisfying equations (3.7) and (3.8). Then, the out-of-band performance is simulated to calculate $f_{max,5}$, which will be around 20 GHz. Hence, $f_{z,4}$=20 GHz, and the baseline value of b_4=7.5 mm. Then, to have b_t4 higher than 3 mm satisfying equation (3.6), $b_4 = b_{4,1} = b_{4,2}$ is fixed to 10.2 mm and b_{T4} is adjusted to 3.6 mm. $l_{4,1}$ and $l_{4,2}$ are calculated by equations (3.7) and (3.8). Then, proceeding iteratively, the physical dimensions of all DEs are computed. The last parameter to be fixed is $b_{1,1}$, which will be equal to 3.5 mm to ensure the suppression of the higher-order non-TE$_{n0}$ modes up to 30 GHz. Finally, a slight adjustment of the dimensions is performed, obtaining the final dimensions detailed in Table 3.6.

The frequency response of the synthesized prototype with and without the final adjustment is shown in Figure 3.14, along with the theoretical response of the electrical prototype. As can be seen in Figure 3.14, a very good starting point for the final

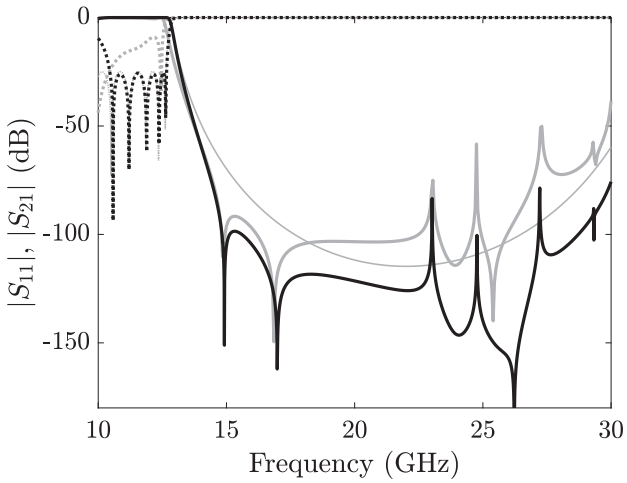

Figure 3.14: FEST3D simulated frequency response comparison between the ideal response (grey thin line) and the novel filter synthesized with the technique in Section 3.3.3 without (grey thick line) and with the final adjustment (black line). $|S_{11}|$ in dotted line and $|S_{21}|$ in solid line.

adjustment is obtained applying the proposed design procedure. In fact, the return loss is better than 10 dB for the entire passband. The final frequency response of the filter is obtained in a few minutes utilizing the Simplex algorithm of FEST3D. In Figure 3.14, the great improvement in the slope between the pass- and the rejected band can be also observed if we compare our novel solution with the classical stepped-impedance prototype. This result should be compared to a classical waffle-iron with and without transmission zeros. Unfortunately, none of the filter designed in the previous section fulfills the specifications in Table 3.5. Therefore, new designs should be accomplished.

Let's start designing a classical waffle-iron filter without transmission zeros. Following the technique in Section 3.3.1 and aiming 100 dB of attenuation at 15 GHz, the order of the filter must be increased to 27. The same applies to a waffle-iron filter with transmission zeros at one frequency placed at the middle of the passband. To demonstrate this issue, one waffle-iron filter without transmission zeros and one waffle-iron filter with transmission zeros at one frequency have been designed following the technique in Section 3.3.1 and Section 3.3.2 respectively. The design parameters are given in Table 3.7 and its final physical dimension are detailed in Table 3.8. The comparison between their frequency response and the response of the novel filter is shown in Figure 3.15. If we compare the three filters, the novel filter presents the most compact layout and low-loss solution (more than 40%-length reduction), and the multipactor threshold level is quite higher in comparison with the filter designed as in Section 3.3.1, [1], and similar to the waffle-iron filter with transmission zeros at one frequency. All the results are summarized in Table 3.9.

Table 3.7: Design parameters of the waffle-iron filters with and without transmission zeros designed in Section 3.6.

Filtering function type	Chebyshev
In-band return loss	25 dB
Maximum frequency of the passband, f_c	12.65 GHz
Maximum attenuation frequency, f_0	22 GHz
Maximum frequency of the stopband, f_{max}	30 GHz
Waveguide width, a	19.05 mm

Filter designed as in Section 3.4 Z_i - N_{DE}=14		Filter designed as in Section 3.5 Z_i - N_{DE}=13	
$Z_0 = Z_{28}$= 1.000	$Z_1 = Z_{27}$= 0.699	$Z_0 = Z_{26}$= 1.000	$Z_1 = Z_{17}$= 0.699
$Z_2 = Z_{26}$= 1.694	$Z_3 = Z_{25}$= 0.446	$Z_2 = Z_{24}$= 1.69	$Z_3 = Z_{17}$= 0.446
$Z_4 = Z_{24}$= 2.165	$Z_5 = Z_{23}$= 0.399	$Z_4 = Z_{22}$= 2.163	$Z_5 = Z_{17}$= 0.399
$Z_6 = Z_{22}$= 2.282	$Z_7 = Z_{21}$= 0.388	$Z_6 = Z_{20}$= 2.279	$Z_7 = Z_{17}$= 0.388
$Z_8 = Z_{20}$= 2.318	$Z_9 = Z_{19}$= 0.384	$Z_8 = Z_{18}$= 2.316	$Z_9 = Z_{17}$= 0.384
$Z_{10} = Z_{18}$= 2.333	$Z_{11} = Z_{17}$= 0.383	$Z_{10} = Z_{16}$= 2.330	$Z_{11} = Z_{17}$= 0.383
$Z_{12} = Z_{16}$= 2.340	$Z_{13} = Z_{15}$= 0.382	$Z_{12} = Z_{14}$= 2.336	Z_{13}= 0.382
	Z_{14}= 2.342		

Moreover, the novel filter suppresses all higher-order modes up to 30 GHz with a very high attenuation level, as can be observed in Figure 3.16.

3.6.3 Fabrication and Measurement

Finally, two quarter-wave transformers have been added to the input and output ports of the novel filter to reach the WR75 standard port dimensions. Then, a prototype of this filter has been fabricated by low-cost milling in bare aluminum in two halves cut by the H-plane. The unassembled prototype is shown in Figure 3.17. The frequency response measurement of the prototype has been carried out by an Agilent E8361C PNA Network Analyzer and by means of waveguide-to-coaxial transitions and linear tapers. The measured frequency response of the prototype is shown in Figure 3.18 along with the CST MWS simulation of the novel filter with rounded corners. As can be observed, a remarkable accordance between the measured and simulated results is obtained. The measured insertion loss is better than 0.15 dB with no glitch observed in the passband of the filter (see Figure 3.19).

Table 3.8: Final dimensions of the waffle-iron filters with and without transmission zeros designed in Section 3.6.

Filter designed as in Section 3.4 $b_{1,1}$=2.25 mm b_k=4.5 mm			Filter designed as in Section 3.5 $b_{1,1}$=2.25 mm b_k=8.8 mm		
DE	b_{Tk} (mm)	l_k (mm)	DE	b_{Tk} (mm)	l_k (mm)
1, 14	0.456	3.083	1, 13	0.905	2.439
2, 13	1.874	3.462	2, 12	3.234	3.440
3, 12	1.973	3.788	3, 11	3.518	3.531
4, 11	1.993	3.616	4, 10	3.578	3.261
5, 10	1.999	3.537	5, 9	3.599	3.278
6, 9	2.001	3.594	6, 8	3.604	3.240
7, 8	2.002	3.552	7	3.609	3.267

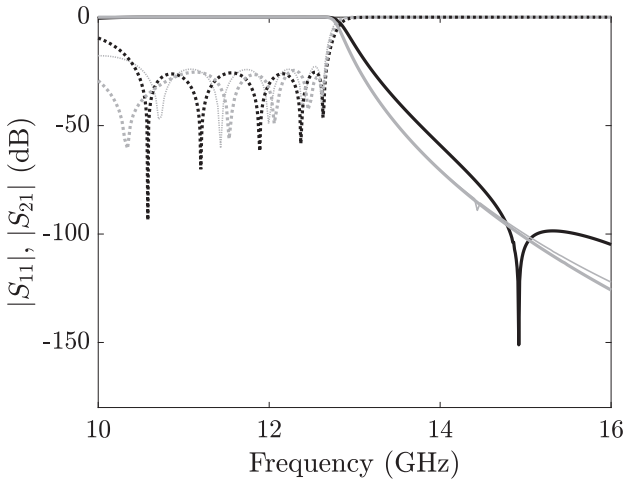

Figure 3.15: FEST3D simulated frequency response comparison between the novel filter (black line), the waffle-iron filter without transmission zeros (grey thin line), and the waffle-iron filter with transmission zeros at one frequency (grey thick line). $|S_{11}|$ in dotted line and $|S_{21}|$ in solid line.

Table 3.9: Performance comparison between the filters designed in Section 3.6.

	Filter designed as in Section 3.4	Filter designed as in Section 3.5	Novel filter
Size	74.12 mm	67.2 mm	40.1 mm
Power threshold (SPARK3D SEY-Ag)	280 W	1970 W	1855 W
Insertion loss (Al)	0.22 dB	0.19 dB	0.15 dB

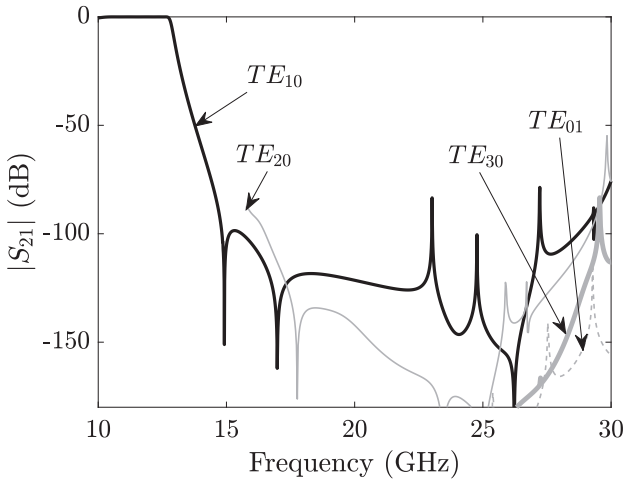

Figure 3.16: FEST3D simulated frequency response for the novel filter excited with the fundamental TE_{10} mode and the higher-order modes.

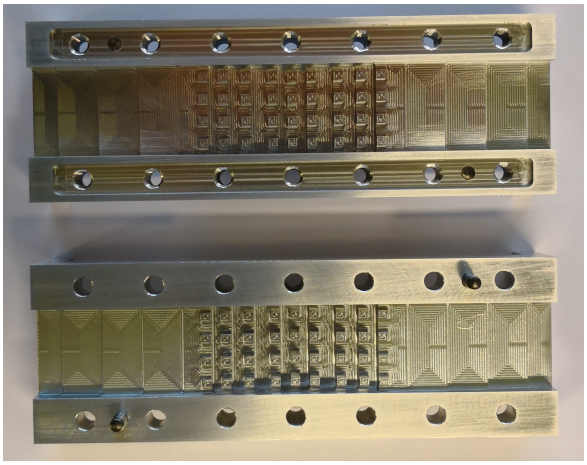

Figure 3.17: Photograph of the unassembled fabricated prototype designed in Section 3.6.

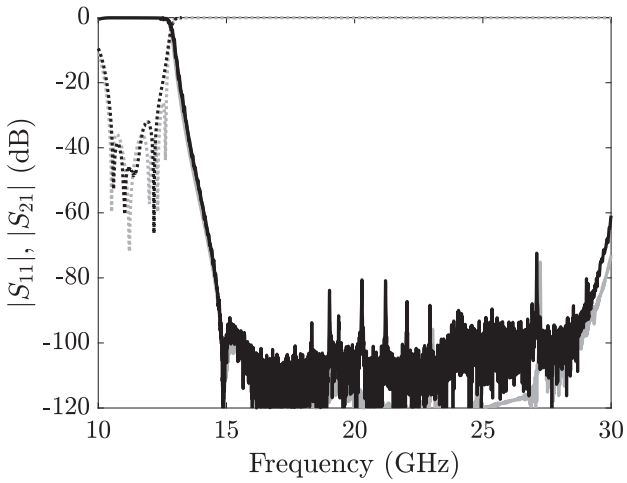

Figure 3.18: Frequency response comparison between the measurements of the fabricated prototype (black line) and the CST MWS simulation of the novel filter with transformers and rounded corners. $|S_{11}|$ in dotted line and $|S_{21}|$ in solid line.

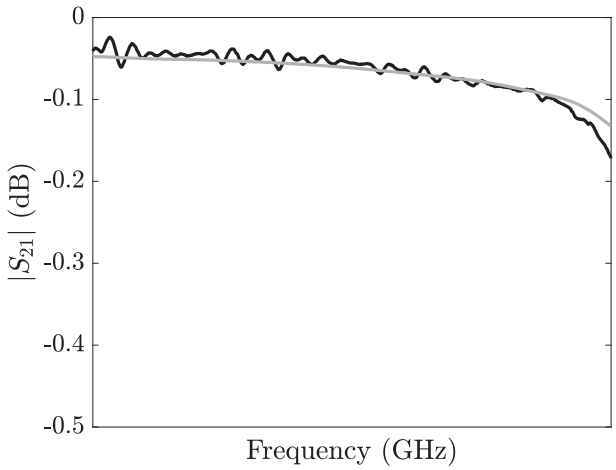

Figure 3.19: Insertion loss comparison between the measurements of the fabricated prototype (black line) and the CST MWS simulation (conductivity of aluminium) of the novel filter with transformers and rounded corners. $|S_{11}|$ in dotted line and $|S_{21}|$ in solid line.

3.7 Conclusions

In this Chapter, a novel high-power waffle-iron filter with a wide rejected band and transmission zeros at multiple frequencies in a single compact structure has been presented, including its design procedure. This procedure is based on mimicking the magnitude and phase responses of the classical stepped-impedance prototype with the set of DEs which compose the novel structure. The limitations for the proposed structure and the design technique are included in this Chapter with its physical insight. Moreover, the design method can be also utilized to produce classical waffle-iron filters without transmission zeros and with transmission zeros at one frequency. In order to demonstrate the feasibility of the technique, a novel filter has been designed, simulated, and compared with its classical counterparts. This novel filter dramatically reduces its size in comparison with the classical solution and has also lower insertion loss, maintaining the high-power performances and the wide rejection bandwidth. A prototype of the novel filter has been fabricated by milling, and the measurement results show an excellent agreement with the simulated one. As a final remark, it should be pointed out that the geometry of the teeth does not modify the design procedure. This can be used to enhance even more the performances of the waffle-iron filters proposed here.

REFERENCES

[1] F. Teberio, I. Arnedo, J. M. Percaz, I. Arregui, P. Martin-Iglesias, T. Lopetegi, and M. A. G. Laso, "Accurate synthesis procedure for waffle-iron low-pass filter," in *2018 IEEE MTT-S International Microwave Symposium Digest (IMS)*, Jun. 2018.

[2] F. Teberio, J. M. Percaz, I. Arregui, P. Martin-Iglesias, T. Lopetegi, M. A. G. Laso, and I. Arnedo, "Design procedure for new compact waffle-iron filters with transmission zeros," *Submitted for consideration in IEEE Transactions on Microwave Theory and Techniques*, 2018.

[3] UPNA, "Design techniques for low-cost filters with reduced sensitivity to fabrication tolerances at high-frequencies," ESA and Thales Alenia Space, NPI 4000114859/15/NL/HK, 2018.

[4] K.-L. Wu and G. McDonald, "Coping with hidden spurious harmonic modes in the design of low pass corrugated waveguide filters," *Microwave Journal*, vol. 44, no. 11, pp. 180–183, Nov. 2001.

[5] D. M. Pozar, *Microwave Engineering Fourth Edition*. Wiley, 2011.

[6] R. Levy, "Tapered corrugated waveguide low-pass filters," *IEEE Transactions on Microwave Theory and Techniques*, vol. 21, no. 8, pp. 526–532, Aug. 1973.

[7] G. Matthaei, L. Young, and E. M. T. Jones, *Microwave filters, impedance-matching networks and coupling structures*. Artech House, 1980.

[8] H. F. Chapelle, “Waveguide low-pass filters using evanescent mode inductors,” *Microwave Journal*, vol. 2A, no. 12, pp. 71–72, Dec. 1978.

[9] A. Saad, “Novel lowpass harmonic filters for satellite application,” in *1984 IEEE MTT-S International Microwave Symposium Digest (IMS)*, May 1984, pp. 292–294.

[10] M. Manuilov, K. Kobrin, G. P. Sinyavsky, and O. S. Labunko, “Full-wave hybrid technique for CAD of passive waveguide components with complex cross section,” *PIERS Online*, vol. 5, no. 6, pp. 526–530, 2009.

[11] H. Kirino and K. Ogawa, “A 76 ghz multi-layered phased array antenna using a non-metal contact metamaterial waveguide,” *IEEE Transactions on Antennas and Propagation*, vol. 60, no. 2, pp. 840–853, Feb. 2012.

[12] M. Baldelli and D. Maiarelli, “Design and qualification of an x-band output filter with extended harmonics rejection,” in *2018 International Workshop on Microwave Filters (IWMF)*, Apr. 2018.

[13] P. Soto, V. E. Boria, J. M. Catala-Civera, N. Chouaib, M. Guglielmi, and B. Gimeno, “Analysis, design, and experimental verification of microwave filters for safety issues in open-ended waveguide systems,” *IEEE Transactions on Microwave Theory and Techniques*, vol. 48, no. 11, pp. 2133–2140, Nov. 2000.

[14] F. J. Clemente-Fernandez, J. Monzo-Cabrera, J. M. Catala-Civera, J. l. Pedreno-Molina, A. J. Lozano-Guerrero, and A. Diaz-Morcillo, “Waveguide bandstop filter based on irises and double corrugations for use in industrial microwave ovens,” *Electronics Letters*, vol. 48, no. 13, pp. 772–774, Jun. 2012.

[15] S. B. Cohn, “Design relations for the wide-band waveguide filter,” *Proceedings of the IRE*, vol. 38, no. 7, pp. 799–803, Jul. 1950.

[16] S. B. Cohn, “Analysis of a wide-band waveguide filter,” *Proceedings of the IRE*, vol. 37, no. 6, pp. 651–656, Jun. 1949.

[17] F. Teberio, I. Arnedo, J. M. Percaz, I. Arregui, T. Lopetegi, and M. A. G. Laso, “Accurate design of corrugated waveguide low-pass filters using exclusively closed form expressions,” in *2017 47th European Microwave Conference (EuMC)*, Oct. 2017.

[18] R. E. Collin, *Foundations for Microwave Engineering*. McGraw Hill, 1992.

[19] N. Marcuvitz, *Waveguide Handbook*. McGraw-Hill, 1951.

[20] R. Levy, “Synthesis of high-power harmonic rejection waveguide filters,” in *1969 G-MTT International Microwave Symposium Digest (IMS)*, May 1969, pp. 286–290.

[21] F. Arndt and J. Brandt, “Direct em based optimization of advanced waffle-iron and rectangular combline filters,” in *2002 IEEE MTT-S International Microwave Symposium Digest (IMS)*, vol. 3, Jun. 2002, 2053–2056 vol.3.

[22] M. Manuilov and K. Kobrin, “Field theory CAD of waffle-iron filters,” in *2005 35th European Microwave Conference (EuMC)*, vol. 2, Oct. 2005, pp. 1–4.

[23] S. B. Cohn, “Rounded corners in microwave high-power filters and other components,” *IRE Transactions on Microwave Theory and Techniques*, vol. 9, no. 5, pp. 389–397, Sep. 1961.

[24] L. Young and B. M. Schiffman, “New and improved types of waffle-iron filters,” *Proceedings of the Institution of Electrical Engineers*, vol. 110, no. 7, pp. 1191–1198, Jul. 1963.

[25] E. Sharp, “A high-power wide-band waffle-iron filter,” *IEEE Transactions on Microwave Theory and Techniques*, vol. 11, no. 2, pp. 111–116, Mar. 1963.

[26] R. Cameron, C. Kudsia, and R. Mansour, *Microwave Filters for Communication Systems: Fundamentals, Design and Applications*. Wiley-Interscience, 2007.

CHAPTER 4

HIGH-POWER HARMONIC LPFs WITH SMOOTH PROFILE

This Chapter explains different design techniques for high-power LPFs with smooth profile [1]–[4]. Firstly, the background of these filters is insightfully reviewed and their application defined. Then, the design method is explained in detail. After that, the feasibility of designing high-power LPFs with smooth profile is demonstrated through simulations and measurements of three different examples. Indeed, the possibility of manufacturing the novel devices following the ideal profile by means of electroforming and using space-compatible procedures such as conventional milling is explored and demonstrated. Finally, the high-power behavior has been estimated and tested in some of these prototypes.

It is important to note that the novel high-power LPFs with smooth profile have been developed within the framework of different projects with the European Space Agency and TESAT Spacecom GmbH [5], [6]. The high-power tests were carried out at the ESA-VSC High-Power Laboratory.

4.1 Background

Modern satellite payloads are operated with an increasing number of communication channels and power level per channel [7], [8]. In the classical scheme of a broadcast communication payload (see Figure 4.1), before the signals are combined at the OMUX, a waveguide LPF is typically used for each channel in order to remove the spurious harmonics generated by the non-linear operation of the amplifiers [9]. This channelized approach is not efficient in terms of mass and volume and, hence, the use of a single high-power LPF at the output of the OMUX is seen as highly advantageous.

As it was mentioned in Chapter 2, the classical E-plane corrugated waveguide LPFs are the usual solution to implement harmonic LPFs for the fundamental TE_{10} mode in rectangular waveguide technology [11]–[13]. Similarly, the classical waffle-iron filters introduced in Chapter 3, have been extensively employed by the space industry when higher-order mode suppression is a requirement as well [11], [14]. Nevertheless, there are some intrinsic trade-offs in the design of these classical structures. For instance, it is not possible to achieve a high-power behavior and a wide stopband simultaneously. Besides, if a very steep slope between the pass- and the stopband is required, the order of the filter will be high and the device will not feature compact size and low insertion loss. This limitation is overcome in [15], [16], where a high-power non-wide rejection band E-plane corrugated filter is cascaded with several quasi-periodic E-plane sinusoidally-shaped waveguide sections, the former being responsible for the large minimum mechanical gap in the whole structure (which determines the maximum power handled by the total device) and the latter achieving the spurious rejection through an appropriate tuning of the sinusoidal per-

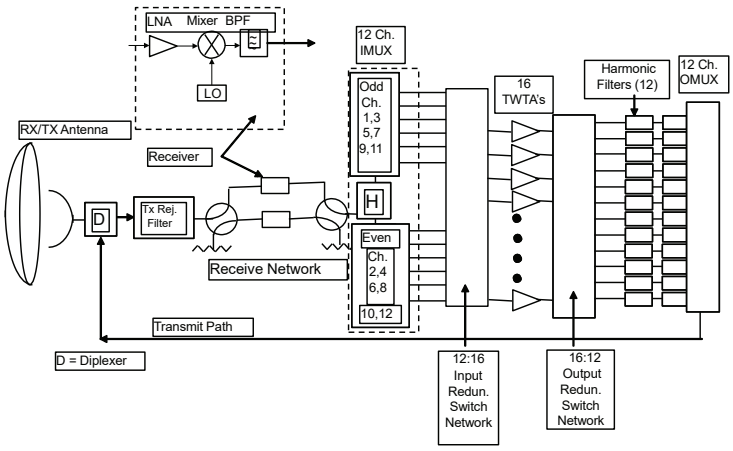

Figure 4.1: Typical payload architecture of a broadcast communications satellite with 12 transponders [10].

turbation periods (Bragg reflection). Furthermore, the benefits of smooth profiles to get high multipactor threshold levels were validated in [17], showing the interest of this kind of structures with smooth profile for high-power applications.

In this Chapter, an integrated design methodology of compact high-power LPFs is proposed [1]–[4], where the filters consist of multiple E-plane bandstop elements of sinusoidal profile and the tuning of the rejected frequencies is achieved through the height of the bandstop elements and not through the period of the structure. Unlike [15], [16], the proposals in this Chapter are not based on the Bragg phenomenon and no corrugated filter is required with this methodology. A windowing of the quasi-periodic structure height allows the implementation of LPFs with deep levels of out-of-band rejection in a broad band and with good in-band return loss.

4.2 Objective

In this Chapter, it will be shown that it is possible to design systematically a high-power LPF with smooth profile capable to provide the levels of rejection required by the space industry (attenuation up to the third harmonic) while maintaining large mechanical gaps, able to support high power levels without showing multipactor breakdown. The main advantage of this concept is that one single filter located after the OMUX can replace the channel LPFs which are commonly used to avoid harmonics. This is schematically shown in Figure 4.2. Therefore, the direct consequence of this development will be the possibility to save volume and mass in the satellite output section.

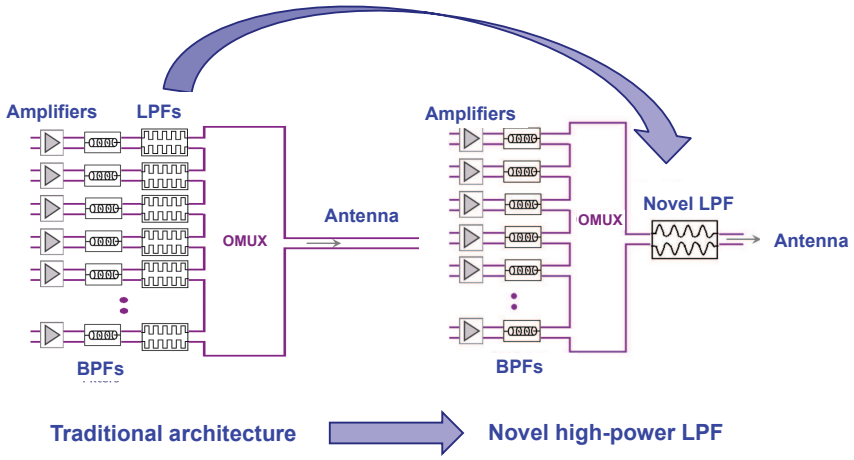

Figure 4.2: Schematics showing the architecture of the OMUX.

Last but not least, it will be demonstrated that the novel high-power LPFs with smooth profile can be manufactured using space-compatible fabrication procedures such as CCM in aluminum and then silver-plated.

4.3 Design Method

The design procedure of the high-power LPFs with smooth profile is divided into three Subsections. Following this stepwise approach, the design can be concluded at the end of any of the Subsections depending on the intended final higher-order mode behavior of the filter.

4.3.1 $\mathbf{TE_{10}}$-mode Suppression

The LPFs which will be designed following the method described in this Chapter consists of three different sections (L_1, L_2, and L_3) of sinusoidal-shape bandstop elements of length, l, distributed along the rectangular waveguide propagation z-axis (see Figure 4.3). L_2 mainly determines the attenuation of the stopband of the filter, while L_1 and L_3 mainly determine the in-band return loss of the filter.

The design method begins by fixing the heights of the highest (h_{max}) and shortest (h_{min}) bandstop elements in L_2 to reject the lowest (f_{min}) and the highest (f_{max}) frequency of the intended stopband respectively (Figure 4.3). The height of each bandstop element is around $\lambda_g/4$, being λ_g the guide wavelength of the fundamental TE_{10} mode at the frequency to be rejected. Between h_{max} and h_{min}, several bandstop elements with intermediate heights are used to reject the intermediate frequencies. A sinusoidal function is chosen as the bandstop element profile since a smooth shape has advantages in terms of power handling [17]. Moreover, a symmetric (as in this case) or asymmetric distribution of bandstop elements at both sides of the z-axis can be used.

Sections L_1 and L_3 achieve the height, b_0, of the standard ports used. Moreover, they are mainly responsible for the filter return loss. In the design process, first some bandstop elements equal to the highest one (section L_3) and some more equal to the shortest one (section L_1) are added. Then, sections L_1 and L_3 are windowed in the following way: (i) subtract $b_0/2$; (ii) multiply sections L_1 and L_3 by an appropriate windowing function; (iii) add $b_0/2$. Finally, the resulting profile is made symmetric in the E-plane, leading to the final device.

It is interesting to note that, as the number of bandstop elements in section L_2 between the highest and the shortest increases (and, hence, the total filter length, L, also increases), the attenuation in the stopband can be made higher. Moreover, if several additional bandstop elements with the largest height are included in section L_2, the slope between the pass- and the stopband will be steeper, since these additional elements reinforce the suppression of the lowest frequencies in the stopband. On the other hand, if the number of bandstop elements in section L_1 and L_3 is increased, the filter is better matched (higher in-band return loss).

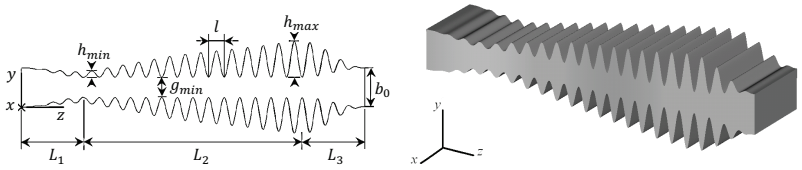

(a) **(b)**

Figure 4.3: Schematics (a) in the $(y-z)$ plane (side view) and (b) 3D view of the novel high-power filter with smooth profile.

Variations of the filter dimensions in a final application due to fabrication tolerances or thermal expansion, for example, barely modifies the return loss and it induces a slight frequency drift that can be easily taken into account in the design process through safety margins around the specifications.

4.3.2 Higher-order TE_{n0}-mode Suppression

Up to this point, the TE_{10} and the higher-order TE_{n0} modes are only rejected in some frequency ranges, as it happens with the classical E-plane corrugated filters [12]. Two different approaches have been developed to achieve the higher-order TE_{n0}-mode suppression. The first one is based on making the arrangement of E-plane bandstop elements two dimensional (waffle-iron inspired structure). The second is based on a reduction along the width of the device in the propagation direction. Although both structures accomplish the suppression of the higher-order TE_{n0} modes, the second one will be more useful in terms of fabrication.

4.3.2.1 2-D Arrangement of Bandstop Elements

In this case, the decomposition of a generic TE_{n0} mode into two plane waves will be utilized to get the higher-order TE_{n0}-mode suppression. As it is well known, the y-component of the TE_{n0}-mode electric field in a rectangular waveguide, $E_{y,n0}$ $(n \geq 0)$, can be given as the difference of two terms of the form $\exp(\pm jn\pi x/a_0 - j\beta_{n0}z)$, where a_0 is the waveguide width in the transversal x-direction (see Figure 4.4(a)), z is the propagation axis and β_{n0} is the phase constant of the higher-order TE_{n0} mode at the frequencies of the fundamental TE_{10}-mode stopband. Moreover, $E_{x,n0} = E_{z,n0} = 0$ [18]. If β_{n0} is expressed as $k_0 \cos\theta_{n0}$, being k_0 the wave-number in free space, and $n\pi/a_0$ as $k_0 \sin\theta_{n0}$, then the well-established relation $(n\pi/a_0)^2 + \beta_{n0}^2 = k_0^2$ for the TE_{n0} mode is still satisfied, and $E_{y,n0}$ can be conveniently rewritten as:

$$E_{y,n0} = \frac{k_0 \cdot a_0 \cdot \eta_0}{2 \cdot n \cdot \pi}\left(e^{-jk_0(x\sin\theta_{n0} + z\cos\theta_{n0})} - e^{-jk_0(-x\sin\theta_{n0} + z\cos\theta_{n0})}\right) \quad (4.1)$$

where η_0 is the free-space impedance. The electric field given in equation (4.1), can be interpreted as two plane TEM-waves propagating at different angles θ_{n0} be-

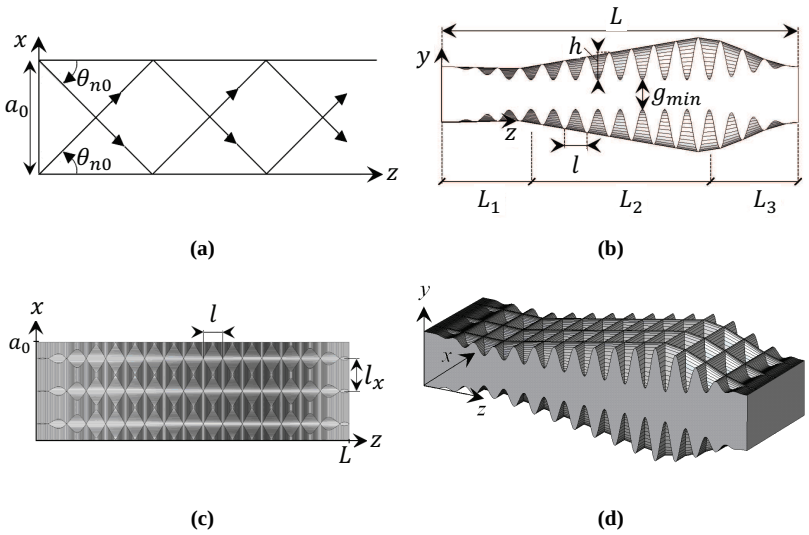

Figure 4.4: (a) Plane-wave decomposition of a TE_{n0} mode. Schematics in the (b) $(y-z)$ plane (side view), (c) $(x-z)$ plane (top view) of the novel high-power filter with smooth profile and 2-D arrangement of bandstop elements. (d) 3D view of the proposed structure.

tween the waveguide walls $x = 0$ and $x = a_0$ with respect to the z-axis, as it is depicted in Figure 4.4(a). Suggested by this decomposition of the TE_{n0} modes into plane waves, if the distribution of bandstop elements of the z-axis is extended along the x-axis too, the higher-order TE_{n0} modes will be suppressed by the two-dimensional arrangement at the same frequencies where the fundamental TE_{10} mode is rejected by the bandstop elements of the z-axis.

Hence, in order to implement this concept, the next steps must be followed. First of all, a filter has to be designed with the aid of the method proposed in Section 4.3.1, taking into account the frequency specifications for the fundamental TE_{10} mode only. As a result, the physical parameters L_1, L_2, L_3, l, h_{min}, h_{max}, will be determined (see Figure 4.4(b)). Afterwards, in order to reject the higher-order TE_{n0} modes with the proposed filters, the z-axis bandstop elements are replicated n_x times in the x-direction within the waveguide width, a_0. In Figure 4.4(c), l_x is $l_x = a_0/n_x$ (it is important to note that l_x and l may have different values). This will lead to a high-power LPF with a wide stopband where neither the fundamental TE_{10} nor the higher-order TE_{n0} modes can propagate, as it happens with classical waffle-iron filters (4.4(d)).

4.3.2.2 Width Variation

In [19], the following expression is used to predict the spurious responses:

$$f_{c,n0} = \sqrt{f_1^2 + (n^2 - 1) \cdot f_{co,10}^2} \tag{4.2}$$

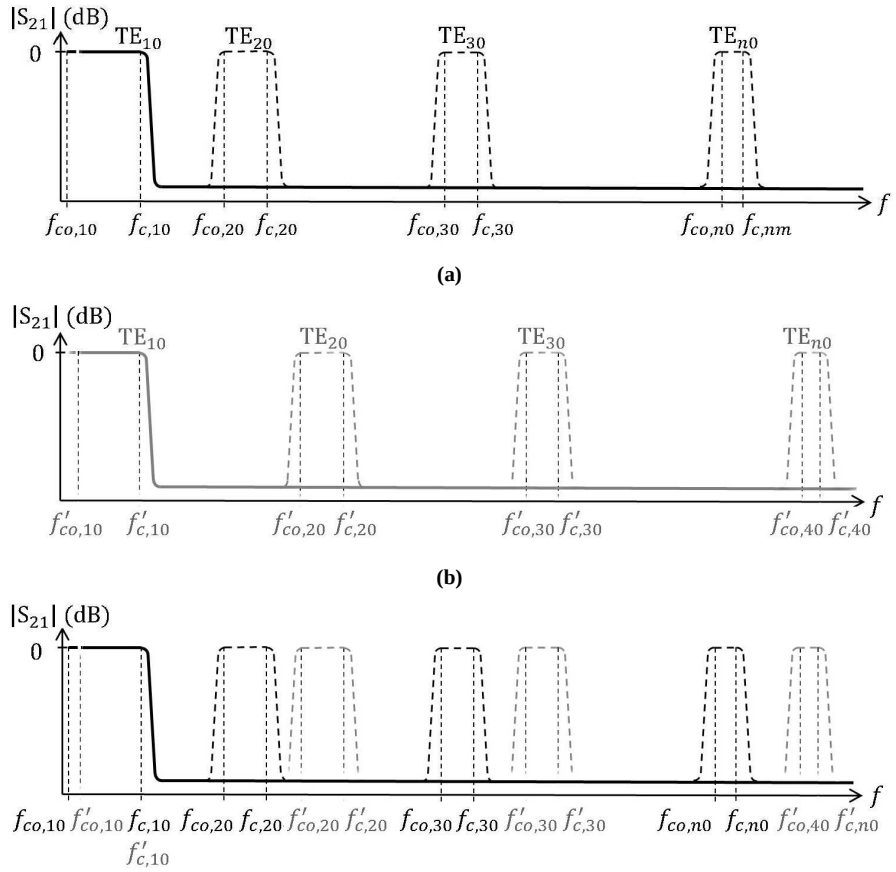

Figure 4.5: Higher-order TE_{n0}-mode behavior of the high-power filters presented in [1]: (a) filter width equal to a_0 (waveguide-port width), (b) filter width equal to a_0', lower than a_0, and (c) two filters with different width (a_0 and a_0', respectively) cascaded.

where $f_{c,n0}$ is the maximum frequency of the passband of each TE_{n0} mode, and $f_{co,10}$ is the cutoff frequency of the TE_{10} mode (see equation (1.1)). Considering an example of a filter like in Section 4.3.1 with a constant width equal to the rectangular waveguide port, a_0, its frequency behavior is depicted in Figure 4.5(a). Different passbands are observed, for each TE_{n0} mode, between its cutoff frequency, $f_{co,n0}$, and the maximum frequency of the passband, $f_{c,n0}$. A filter with the same frequency response for the fundamental TE_{10} mode but a constant width a_0', lower than a_0, can be also designed. In this case, shown in Figure 4.5(b), the passbands of the higher order TE_{n0} modes will be located at higher frequencies since the corresponding cut-off frequencies, $f'_{co,n0}$, and $f'_{c,n0}$ are higher.

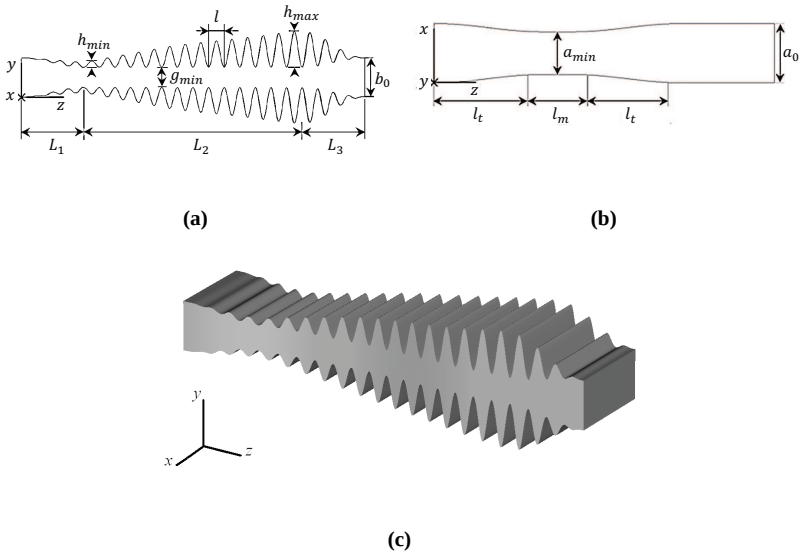

Figure 4.6: Schematics showing a high-power LPF with width reduction and suppression of the high-order modes: (a) side view, (b) top view, and (c) 3D view.

Therefore, a filter which rejects all the TE_{n0} higher-order modes can be achieved if two filters with different width, like the ones with the frequency responses shown in Figure 4.5(a) and Figure 4.5(b), are cascaded. The use of at least two filters with a different width guarantees that the passbands of the higher-order TE_{n0} modes of one filter are forced to coincide with the frequencies where these modes are rejected in the other filter (Figure 4.5(c)). Actually, the same idea can be implemented using only one filter if different widths (in a stepwise or continuous way) are used along the device. Now, the passbands of the higher-order TE_{n0} modes are forced to coincide with the frequencies where these modes are rejected by other sections with a different width of the same filter. This concept was already used in [19] to design inhomogeneous stepped-impedance corrugated LPFs, not intended for high-power. Reference [19] extends the design of those filters to reject higher-order modes and, although an improvement in the rejection of the higher-order TE_{n0} modes is achieved, the attenuation obtained for these modes is actually not very high. However, much higher rejection levels will be obtained when the variation in the width is applied (in a continuous way) to the high-power filters explained in Section 4.3.1.

In order to implement the width-variation concept to the high-power LPFs with smooth profile, the next steps must be followed. First of all, a filter has to be designed with the aid of the method proposed in Section 4.3.1, taking into account the frequency specifications for the fundamental TE_{10} mode only. As a result, the physical parameters L_1, L_2, L_3, l, h_{min}, h_{max}, will be determined (see Figure 4.6(a)). Afterwards, the minimum width of the filter, a_{min}, must be fixed to guarantee that

$f'_{co,n0} > f_{c,n0}$ is satisfied (except, of course, for the fundamental TE_{10} mode). A trade-off exists for the minimum value of a_{min}, since the cutoff frequency of the fundamental TE_{10} mode must be low enough to keep the intended TE_{10} passband. The length of the section with the minimum width, l_m, must be large enough to avoid a significant evanescent mode propagation. Once the minimum width is fixed, the transition between the standard waveguide ports, a_0, and the minimum width, a_{min}, must be defined (see Figure 4.6(b)). In order to preserve the good return loss of the filter, a smooth variation of the width must be performed, for instance, by means of a *Hanning* window with length l_t. The longer the window used the lower influence it has on the return loss of the designed filter. Finally, the height of the bandstop elements whose width values have been noticeably reduced may need to be finely tuned to larger values to fulfill the required stopband of the fundamental TE_{10} mode. However, this is a slight tuning process as the response of the bandstop element is mainly determined by its height and not by its width.

4.3.3 Higher-order non-TE_{n0} mode Suppression

The suppression of the higher-order non-TE_{n0} modes can be achieved by adjusting the minimum mechanical gap of the proposed filter, g_{min}, in order to shift the cutoff frequencies of the TE_{nm}/TM_{nm}, $m \neq 0$, to higher frequencies while keeping, independently, the TE_{n0} modes ($n \geq 1$) cutoff frequencies at the same values. As it is known, the cutoff frequency of a TE_{nm} mode, is given by equation (1.1), [20].

In order to get the suppression of all higher-order modes up to a certain frequency, the minimum mechanical gap can be reduced along the propagation direction in a sufficiently long section to make sure that the TE_{01} mode (the first non-TE_{n0} higher-order mode) is efficiently suppressed. In this way, all higher-order TE_{nm}/TM_{nm} modes ($m \neq 0$) will be rejected since these modes feature higher cutoff frequencies than the TE_{01} mode. Hence, if it is desired to design a novel filter with higher-order non-TE_{n0} mode suppression too, the design technique ends by setting adequately the minimum mechanical gap g_{min} (Figures 4.3, 4.4, and 4.6). As the mechanism to control the TE_{nm}/TM_{nm} modes ($m \neq 0$), is independent of the TE_{n0}-mode ($n \geq 1$) suppression, the minimum mechanical gap in the filters in this Chapter can be still made larger than in waffle-iron filters. This is due to the fact that although waffle-iron filters achieve higher-order mode suppression, very small gaps are actually needed to simply reject the fundamental TE_{10} mode while, in the proposed high-power LPFs with smooth profile, the higher-order TE_{01}-mode cutoff frequency can be easily shifted to higher frequencies still using large gaps.

On the other hand, it must be noted that since the profile of the bandstop elements in the proposed LPFs is sinusoidal, the minimum mechanical gap is strictly satisfied only in one point in each bandstop element. Higher-order mode suppression is merely efficient if the section with minimum gap is long enough (in this case by cascading several bandstop elements). It has been practised to define an effective minimum mechanical gap in the filter, g_{eff}, given by $g_{eff} = g_{min} + 2h_{min}$, which is slightly larger than the actual minimum mechanical gap, g_{min}. g_{eff} will be uti-

lized in the calculations to fix the required TE_{01}-mode cutoff frequency and obtain, afterwards, the physical parameter g_{min}.

Design Examples

According to the design methodologies proposed, three different examples of high-power LPF with smooth profile will be presented in this Chapter. Firstly, in Section 4.4, the feasibility of designing LPF with the suppression of only the fundamental mode following the technique detailed in Section 4.3.1, [1] will be demonstrated. Moreover, this example will be also utilized to characterize the high-power handling of this kind of devices with simulations and tests. The second example (Section 4.5) will include a novel LPF with smooth profile designed with the proposed method detailed in Section 4.3.2.1, [2], [3] where the higher-order modes are suppressed by means of a 2D-arrangement of bandstop elements. Finally, the third example (Section 4.6 will show a novel high-power LPF where the higher-order mode suppression is achieved by means of a width modification, following the procedure described in Section 4.3.2.2, [4]). It is important to stress that different prototypes will be fabricated in all the examples following space-compatible procedures, obtaining a remarkable accordance between the simulated and the measured results.

4.4 Design Example 1: High-Power LPF with only Fundamental $\mathbf{TE_{10}}$-mode Suppression

The main objectives of this example are the following:

- Demonstrate the feasibility of designing high-power LPFs with the technique in Section 4.3.1.
- Demonstrate that it is possible to manufacture the high-power LPFs with smooth profile presented in this Chapter using space-compatible procedures.
- Characterize the high-power behavior of the LPFs with smooth profile by means of simulations and multipactor tests.

In order to achieve these objectives, three novel high-power LPFs with smooth profile and the suppression of only the fundamental mode with different minimum mechanical gaps will be designed following the technique in Section 4.3.1. Moreover, a classical corrugated LPF fulfilling the previous specifications will be also designed for shake of comparison purposes during the multipactor test campaign (design method and example in Chapter 2.3).

4.4.1 Specifications

All filters will fulfill the specifications defined in Table 4.1. Moreover, the insertion loss will be better than 0.35 dB and WR75 standard ports will be used.

Table 4.1: Frequency specifications

Passband	Return loss	Stopband	Attenuation
10.7 - 12.3 GHz	20 dB (26 dB as goal)	13.5 - 38 GHz	60 dB

Table 4.2: Final Dimensions of the novel filter with 3-mm gap.

Section L_1	# elements = 15; window: Hanning
Section L_2	l = 3.82 mm; g_{min} = 3 mm; h_{max} = 8.59 mm; h_{min} = 2.6 mm; # elements = 29 (# elements with h_{max} = 4)
Section L_3	# elements = 15; window: Hanning

4.4.2 Design and Simulation

Three novel high-power LPFs with suppression of only the fundamental mode and with minimum mechanical gaps equal to 3, 4 and 6 mm respectively have been designed following the technique described in Section 4.3.1. In this example, WR75 input and output waveguide ports are used (a_0 = 19.05 mm, b_0 = 9.525 mm). As it has been explained above, the filter consists of three different sections. Section L_2 has the minimum E-plane gap of the filter, which in this case is fixed to 3, 4 and 6 mm respectively. The height of the largest and shortest E-plane bandstop elements in section L_2 are h_{max} = 8.6 mm and h_{min} = 2.6 mm, in order to reject the lowest and highest frequencies in the rejected band (f_{min} = 13.5 GHz and f_{max} = 38 GHz), respectively (the filter width is kept always constant and equal to the WR75 input/output port width, a_0, along the z-axis). Once the initial filter dimensions are obtained, an optimization process consisting of several full wave simulations is done. Before each iteration, changes in filter dimensions are guided by the discussion in Section 4.3.1. The shorter the device, the more difficult it is to achieve the required frequency specifications. The final design parameters of each novel filter are given in Table 4.2, 4.3, and 4.4 respectively. The total length of all structures, L, is 235.6 mm.

Moreover, a Chebyshev corrugated LPF of order 29 has been designed following the design method described in Chapter 2.3 for comparison purposes in terms of frequency response, size, and high-power behavior. The minimum mechanical gap of the structure is 0.6 mm and its total length is equal to 168 mm.

The frequency response of all devices has been simulated using CST MWS and is shown Figures 4.7, 4.8, and 4.9 along with the frequency response of its classical counterpart the corrugated LPF.

4.4.3 Fabrication by Electroforming and Measurement

The fabrication by electroforming of a device allows manufacturing the proposed filters following the ideal profile without modifications (the fabrication process is explained in detail in Section 1.6.3). This kind of fabrication technique allows di-

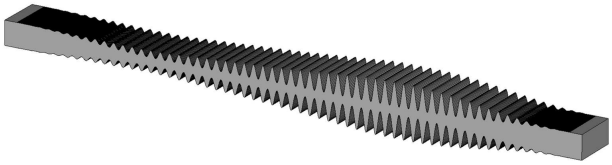

(a)

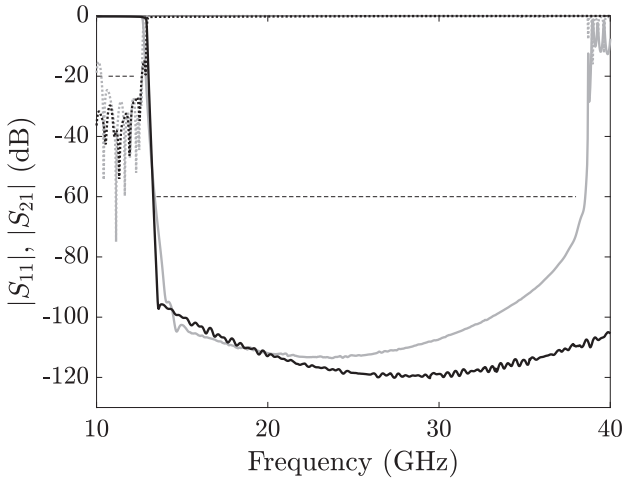

(b)

Figure 4.7: (a) 3D view of the novel filter with 3-mm gap. (b) Simulated frequency response with CST MWS of the novel filter with 3-mm gap (black line) and the classical corrugated LPF (grey line) designed fulfilling the same frequency specifications. $|S_{11}|$ in dotted line and $|S_{21}|$ in solid line. Frequency specifications in dashed line.

Table 4.3: Final Dimensions of the novel filter with 4-mm gap.

Section L_1	# elements = 17; window: Hanning
Section L_2	l = 3.82 mm; g_{min} = 4 mm; h_{max} = 8.52 mm; h_{min} = 2.6 mm; # elements = 25 (# elements with h_{max} = 4)
Section L_3	# elements = 17; window: Hanning

Table 4.4: Final Dimensions of the novel filter with 6-mm gap.

Section L_1	# elements = 12; window: Hanning
Section L_2	l = 3.82 mm; g_{min} = 6 mm; h_{max} = 8.60 mm; h_{min} = 1.5 mm; # elements = 45 (# elements with h_{max} = 4)
Section L_3	# elements = 8; window: Hanning

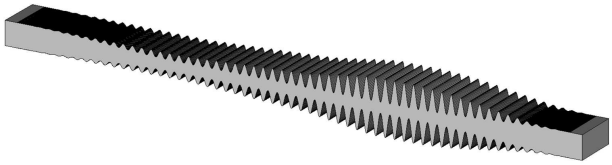

(a)

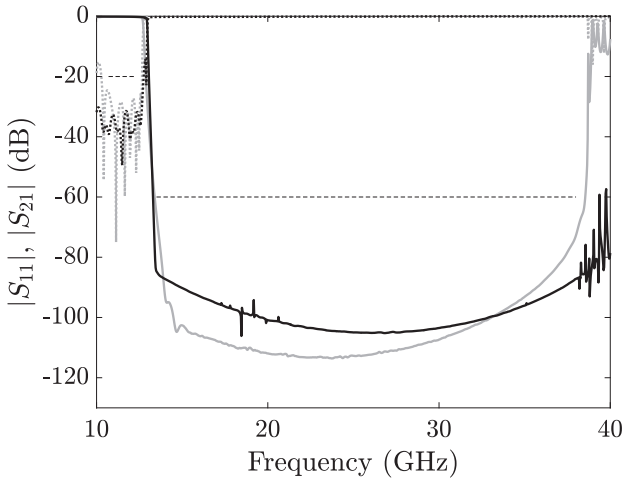

(b)

Figure 4.8: (a) 3D view of the novel filter with 4-mm gap. (b) Simulated frequency response with CST MWS of the novel filter with 4-mm gap (black line) and the classical corrugated LPF (grey line) designed fulfilling the same frequency specifications. $|S_{11}|$ in dotted line and $|S_{21}|$ in solid line. Frequency specifications in dashed line.

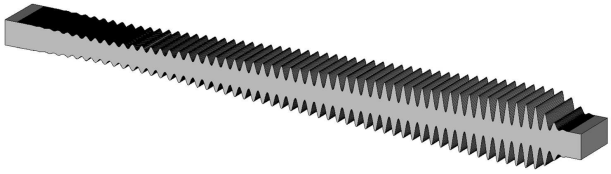

(a)

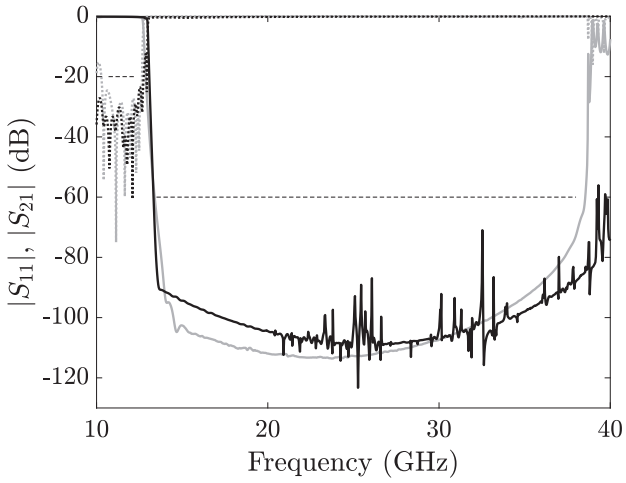

(b)

Figure 4.9: (a) 3D view of the novel filter with 6-mm gap. (b) Simulated frequency response with CST MWS of the novel filter with 6-mm gap (black line) and the classical corrugated LPF (grey line) designed fulfilling the same frequency specifications. $|S_{11}|$ in dotted line and $|S_{21}|$ in solid line. Frequency specifications in dashed line.

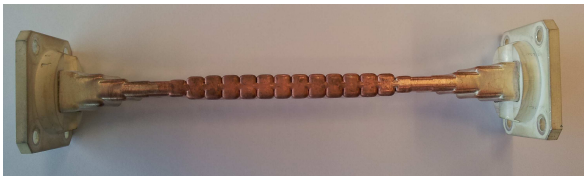

(a)

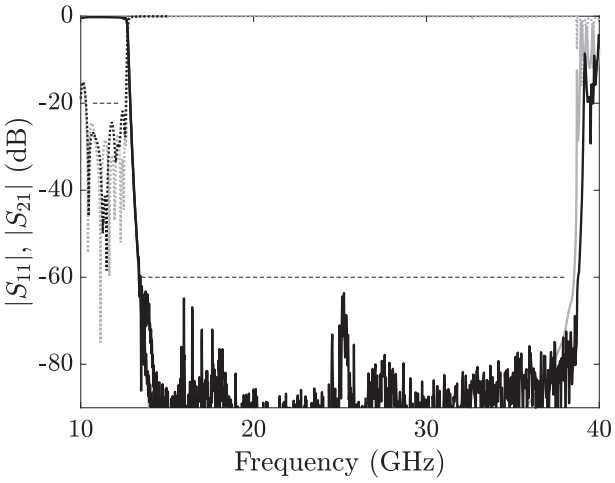

(b)

Figure 4.10: (a) Photograph of the corrugated E-plane LPF fabricated by electroforming in copper and silver plated and (b) its frequency response measured (black line) and simulated with CST MWS (grey line). $|S_{11}|$ in dotted line and $|S_{21}|$ in solid line. Frequency specifications in dashed line.

mensions tolerances within $\pm$ 5 μm. For all prototypes, 15 μm thickness of silver and then 1 mm of copper have been deposited onto the aluminum mandrel.

Measurements have been performed by means of an Agilent 8722 VNA, proper waveguide to coaxial transitions and calibration kits. Non-linear tapers have been used to avoid the mismatch between the higher frequency coaxial-to-waveguide transitions and the filter ports in order to minimize the excitation of higher-order modes at the filter input. The measurement results shown in Figures 4.10, 4.11, 4.12, and 4.13 confirm that an excellent level of spurious rejection around 60 dB up to the third harmonic is achieved, while the return loss is better than 20 dB in the pass band. The in-band insertion loss is kept below 0.3 dB in these fabrications. It is important to note that no further tuning of the filters is necessary after they are fabricated.

In the previous filters fabricated by electroforming, a visual inspection cannot be done to see the quality of the silver coating or imperfections in the manufacturing process. In this case, an X-ray inspection was performed at ESA-ESTEC to verify the quality of the finishing. In general, it was observed that there are some bubbles in the inner side solid (depicted in Figure 4.14). These bubbles could even (in some

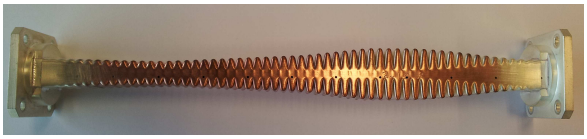

(a)

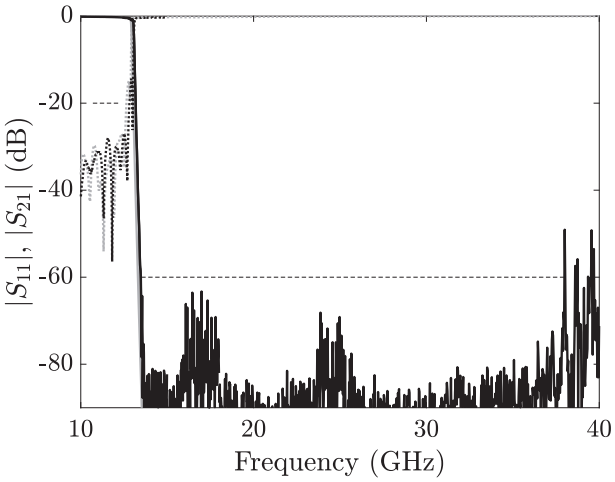

(b)

Figure 4.11: (a) Photograph of the novel filter with 3-mm gap fabricated by electroforming in copper and silver plated and (b) its frequency response measured (black line) and simulated with CST MWS (grey line). $|S_{11}|$ in dotted line and $|S_{21}|$ in solid line. Frequency specifications in dashed line.

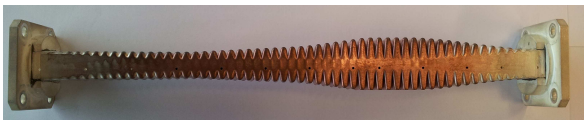

(a)

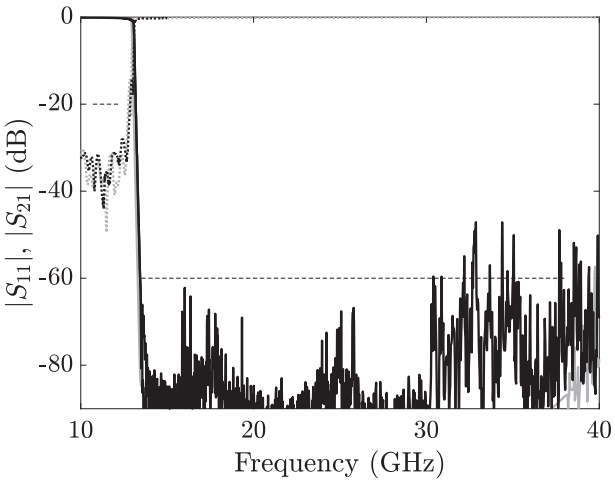

(b)

Figure 4.12: (a) Photograph of the novel filter with 4-mm gap fabricated by electroforming in copper and silver plated and (b) its frequency response measured (black line) and simulated with CST MWS (grey line). $|S_{11}|$ in dotted line and $|S_{21}|$ in solid line. Frequency specifications in dashed line.

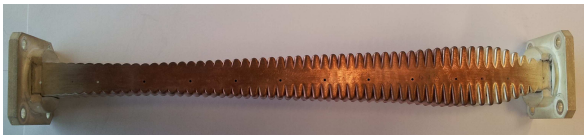

(a)

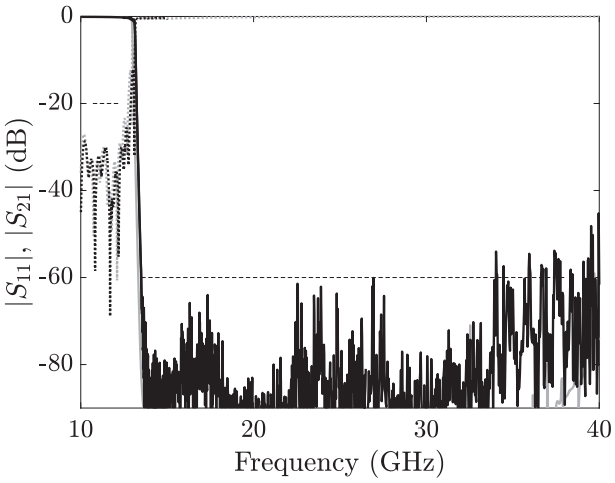

(b)

Figure 4.13: (a) Photograph of the novel filter with 4-mm gap fabricated by electroforming in copper and silver plated and (b) its frequency response measured (black line) and simulated with CST MWS (grey line). $|S_{11}|$ in dotted line and $|S_{21}|$ in solid line. Frequency specifications in dashed line.

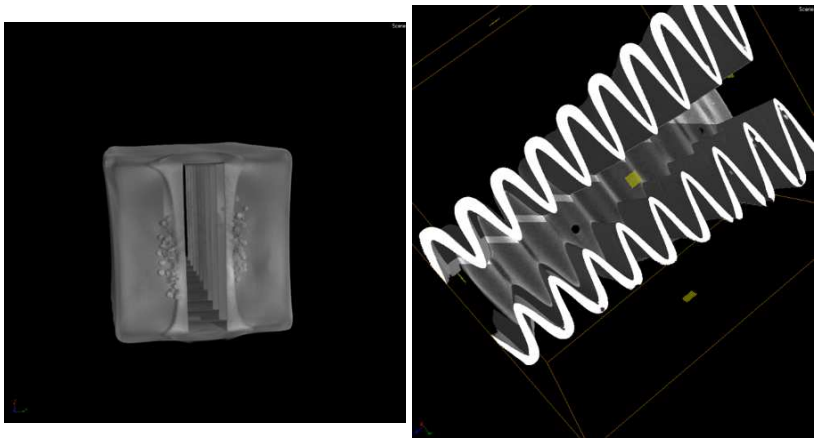

Figure 4.14: Photographs of the X-ray analysis.

cases) crack the surface up to certain point and have some influence on the frequency response of the filter. However, some corrective actions can be performed to avoid it, as it is explained in Section 1.6.3. It is important to note that do not hardly affect to the measured frequency response as it has been demonstrated.

4.4.4 Fabrication by CCM and Measurement

In order to demonstrate the feasibility of manufacturing the filters proposed in this Chapter following space-compatible procedures, all filters will be also fabricated by CCM (radius of the tool equal to 0.5 mm) in bare aluminum in two halves cut by the H-plane and then silver plated.

When CCM is assumed, it is not possible to mechanize perfect square corners or cavities with dimensions smaller than the tool (more details of the fabrication method can be found in Section 1.6.1). This limitation must be considered before the fabrication to avoid deviations between the predicted and the measured frequency response. In the novel filters presented in this Chapter, two modifications must be performed (Figure 4.15) when the filter is divided in two halves cutting by the H-plane. Although the lower parts of the highest bandstop elements are easily accessible by the tool, the upper parts are too narrow and must be rounded. This modification produces a shift towards lower frequencies in the frequency response and can be easily compensated reducing the height of the modified bandstop elements. Indeed, h_{max} has been reduced to 8.19 mm, 8.20 mm and 8.18 mm in the novel 3-, 4-, and 6-mm gap filters. Moreover, the four edges which define the rectangular waveguide must be also rounded according to the radius of the tool used. This modification has little influence in comparison with the previous one and hardly modifies the frequency response, requiring only an actual redesign of the filter if thick tools are employed.

Both simulated and measured results (carried out with an Agilent 8722 VNA following the same process as in the electroforming prototypes) are in very good agree-

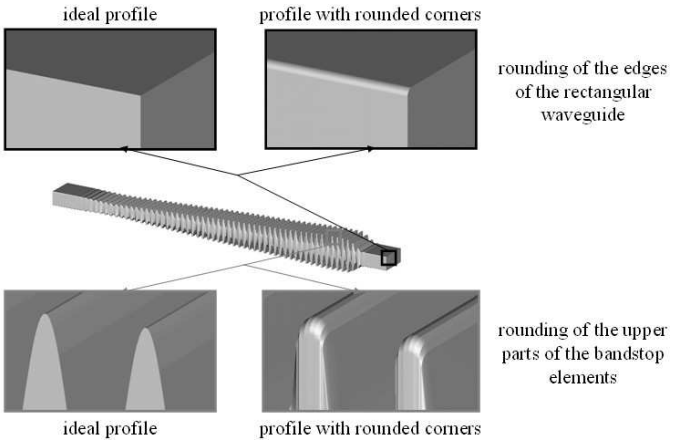

Figure 4.15: Schematics showing the fabrication differences in the novel filters.

ment for all prototypes (see Figures 4.16, 4.17, 4.18, and 4.19) and show that all filters presents excellent frequency behavior, fulfilling the specifications with attenuation levels around 60 dB in the required stopband and in-band return loss around 26 dB in the desired passband. Moreover, the measured and simulated insertion loss of all prototypes have been kept below 0.35 dB.

4.4.5 Fabrication Tolerance Considerations

Tolerance analyses are typically done in microwave devices to know the robustness of the designs with respect to variations in the dimensions (due to the manufacturing process). These analyses, based on statistical techniques [21], [22], require setting a tolerance for all the filter dimensions and randomly selecting a set of values for each dimension within the tolerance. Moreover, a large number of simulations with different values are required to have a valid analysis. Due to the fact that the filters with smooth profile proposed in this Chapter have a large number of different dimensions, this analysis would be cumbersome. Therefore, in order to show the frequency-response sensitivity of the filters, an increase or decrease of the filter profile has been used. Although, this is not an exhaustive analysis, it provides an estimation of the influence of the tolerance in the devices. Specifically, one of the examples of the previous Section has been utilized to analyze the sensitivity to manufacturing issues of the proposed structures. A tolerance value equal to 20 μm has been used (this is the typical tolerance value of conventional CCM). The resulting devices have been simulated with CST MWS and their frequency responses are shown in Figure 4.20. In both cases, the filters fulfill the frequency specifications, showing the robustness of the filters designed with the technique proposed in this Chapter.

(a)

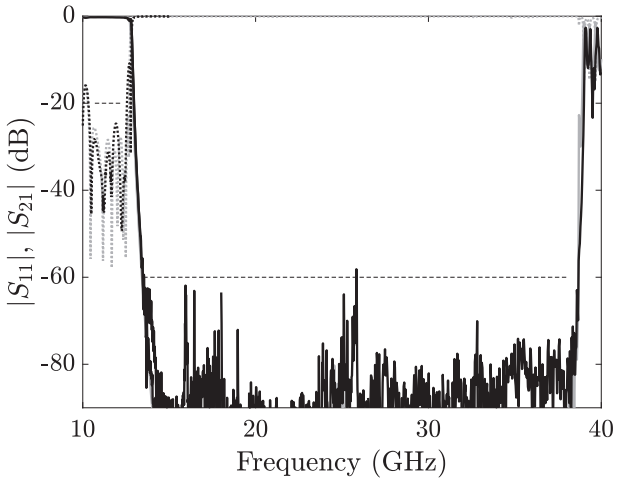

(b)

Figure 4.16: (a) Photograph of the corrugated E-plane LPF fabricated by CCM in aluminum and silver plated and (b) its frequency response measured (black line) and simulated with CST MWS (grey line). $|S_{11}|$ in dotted line and $|S_{21}|$ in solid line. Frequency specifications in dashed line.

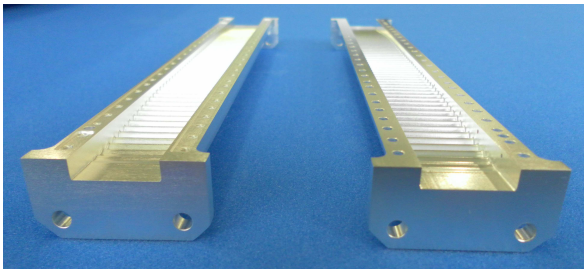

(a)

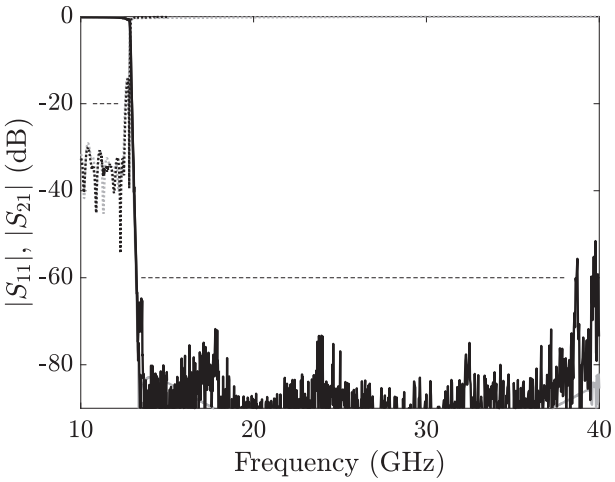

(b)

Figure 4.17: (a) Photograph of the novel filter with 3-mm gap fabricated by CCM in aluminum and silver plated and (b) its frequency response measured (black line) and simulated with CST MWS (grey line). $|S_{11}|$ in dotted line and $|S_{21}|$ in solid line. Frequency specifications in dashed line.

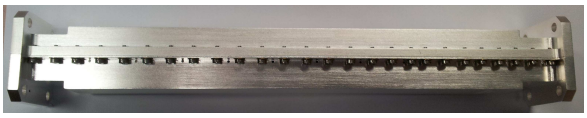

(a)

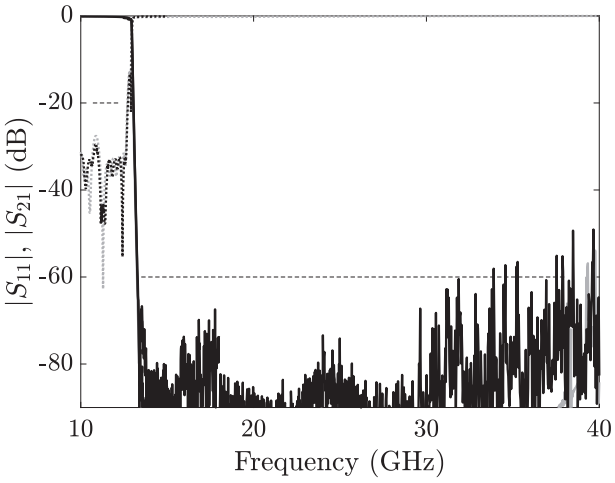

(b)

Figure 4.18: (a) Photograph of the novel filter with 4-mm gap fabricated by CCM in aluminum and silver plated and (b) its frequency response measured (black line) and simulated with CST MWS (grey line). $|S_{11}|$ in dotted line and $|S_{21}|$ in solid line. Frequency specifications in dashed line.

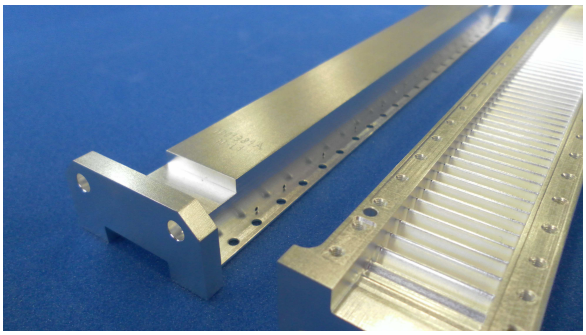

(a)

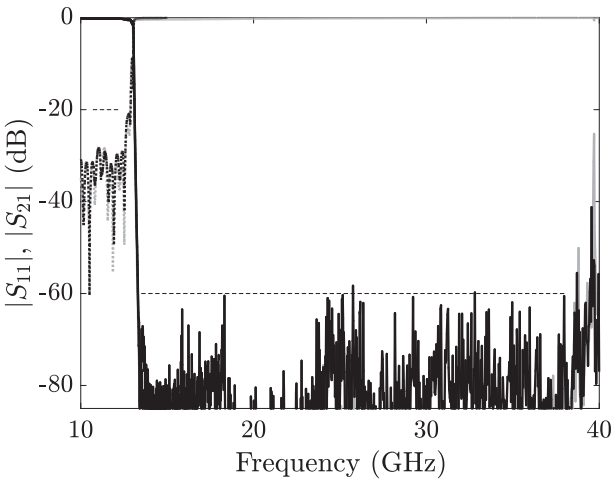

(b)

Figure 4.19: (a) Photograph of the novel filter with 6-mm gap fabricated by CCM in aluminum and silver plated and (b) its frequency response measured (black line) and simulated with CST MWS (grey line). $|S_{11}|$ in dotted line and $|S_{21}|$ in solid line. Frequency specifications in dashed line.

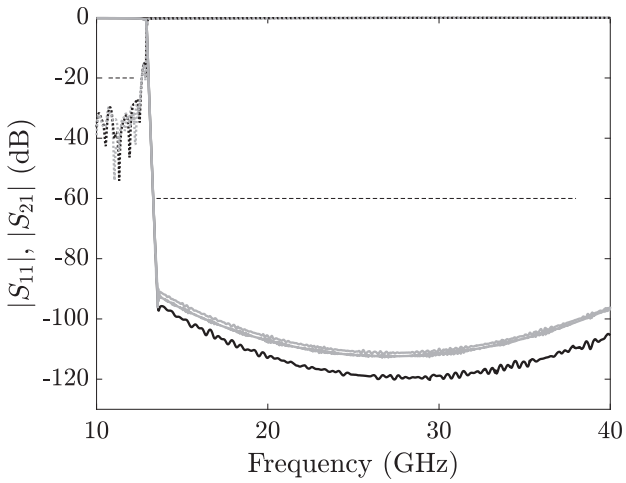

Figure 4.20: Simulated frequency response of the novel filter with 3-mm gap with CST MWS of the original filter (black line), original filter +20 μm and -20 μmmm (grey lines). $|S_{11}|$ in dotted line and $|S_{21}|$ in solid line. Frequency specifications in dashed line.

4.4.6 High-power Behavior

In order to estimate the power-handling capability of the previous devices, two different approaches have been utilized in this first analysis of the Thesis: the classical and conservative method based on the parallel-plate model (explained in detail in Section 1.4.1) and the PIC SW tool SPARK3D. The parallel-pate theory gives a very conservative estimation of the threshold input power level due to the fact that the infinite parallel-plate approach results in the worst scenario possible, and even more so when a smooth profile structure is considered. In order to have a more realistic and accurate multipactor analysis, the real EM fiel distribution inside the filter can be considered when a PIC SW tool as SPARK3D or CST Particle Studio is utilized.

4.4.6.1 High-power simulation

The high-power simulations have been performed with the aforementioned two different approaches:

- **Classical parallel-plate theory: ECSS multipactor tool**

Following the technique described in detail in Section 1.4 based on a parallel-plate theory, the multipactor threshold level has been predicted. Such an analysis is appropriate when considering cases close to parallel-plates with small gaps in which the field distribution is relatively homogeneous. However, the shapes of the filters proposed in this Chapter significantly differ from this situation and, as a consequence, it is expected that their breakdown power levels are higher than those obtained by the ESA charts.

- **PIC tool: SPARK3D**

In order to have a more realistic high power analysis, full numerical simulations based on the coupling between a full-wave EM solver and a particle tracking multipactor tool have been performed. In this case, two commercial solvers have been used: CST MWS frequency domain solver for the calculation of the EM fields coupled with the PIC tool SPARK3D. Indeed, this classical approach will not be utilized in the rest of the examples of this Thesis.

Two of the previous eight filters have been selected to explain the methodology followed (in this Chapter and also in all the examples in this Thesis whose multipactor behavior is estimated). Then, the breakdown power levels obtained are numerically compared to the classical approach (ECSS Multipactor Tool).

SPARK3D analysis of corrugated filter fabricated by milling

The corrugated filter fabricated by milling has been analyzed with CST MWS by using a large number of tetrahedra (around 230.000 in this case). The EM fields have been exported to a file compatible with SPARK3D.

The critical area is at the center of the component, where the gap is minimum and the EM fields are the highest. Figure 4.21 shows the mesh in this area. As it can be seen, it is a dense mesh which provides a high field resolution to be used in the SPARK3D. Since the breakdown shall occur at the center of the filter, this specific region can be chosen as analysis area surrounding such a volume. This allows being faster in the simulation and more accurate since the initial electrons are launched at the area of interest. Figure 4.22 shows the whole structure together with the region of analysis located at the center of the device.

SPARK3D analysis of novel 6mm-gap LPF fabricated by electroforming

The same philosophy as in the previous case has been followed in the novel 6mm-gap LPF fabricated by electroforming. The filter together with the EM fields is shown in Figure 4.23.

In order to check where the maximum field takes place, a 2D cut of the structure along the propagation direction has been performed. This is shown in Figure 4.24 where the region of maximum field is clearly identified in the highest bandstop elements area. Therefore, this analysis area is taken around such volume.

All the plot fields shown before have been done with a tetrahedral mesh of 430.000 tetrahedra which is extremely dense as seen in the next figure (Figure 4.25) where a zoom of the mesh in the region of interest has been performed.

As far as the material is concerned, all simulations have been firstly performed assuming the SEY of ECSS silver (see Figure 4.26, [23]). Moreover, the SEY has

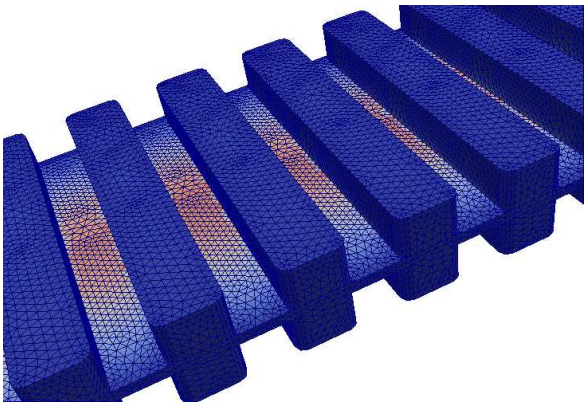

Figure 4.21: Mesh used to import the EM fields from CST MWS to SPARK3D. The rounded corners can be appreciated.

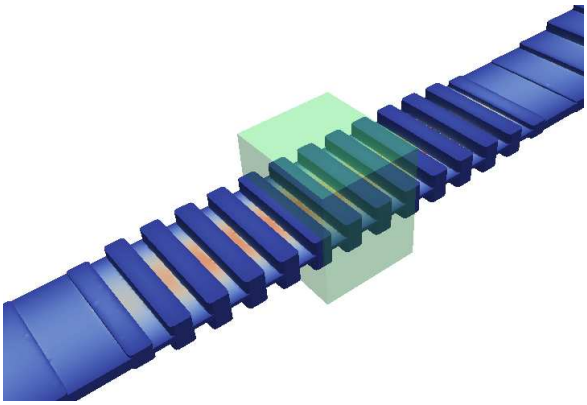

Figure 4.22: Detail of the volume under consideration.

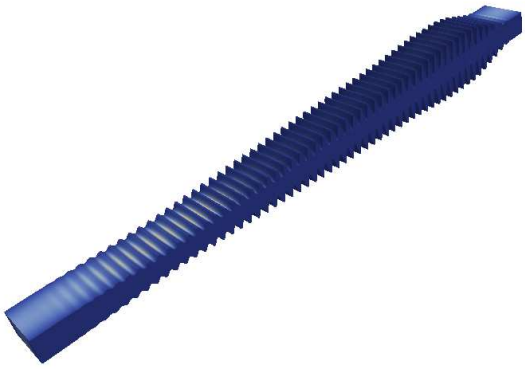

Figure 4.23: Fields calculated from CST MWS and imported to SPARK3D of the novel filter 4a.

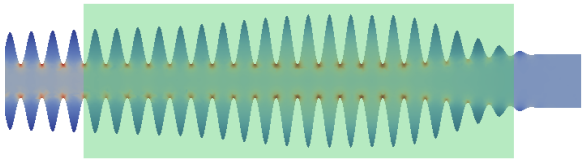

Figure 4.24: Detail of the analysis box in SPARK3D - novel filter 4a.

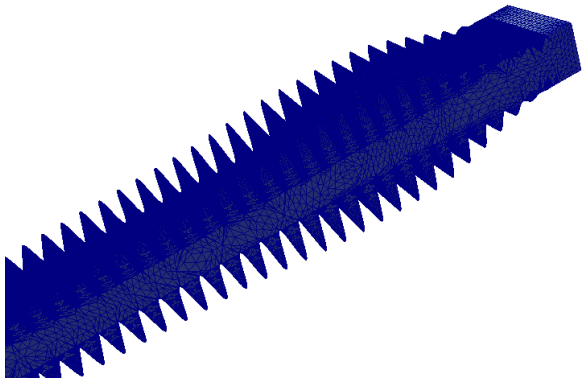

Figure 4.25: Mesh used to import the EM fields from CST MWS to SPARK3D for the novel filter 4a.

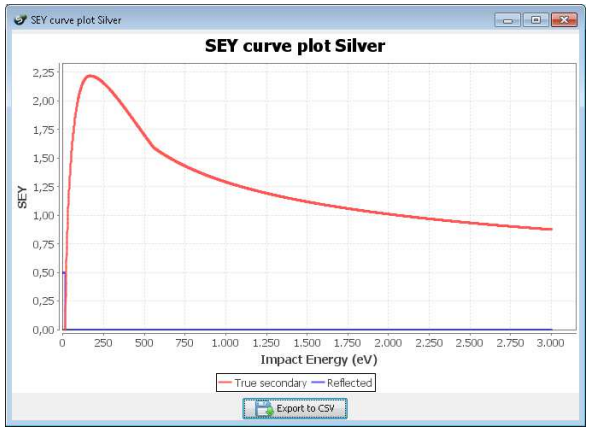

Figure 4.26: ECSS SEY curve.

been measured (in the CSIC laboratories in Madrid, Spain) for both electroforming and milling parts to be also utilized in the multipactor simulations in order to be close to the most realistic scenario. Figures 4.27 (a) and (b) show the different measured SEY. The most important parameters are summarized in Table 4.5.

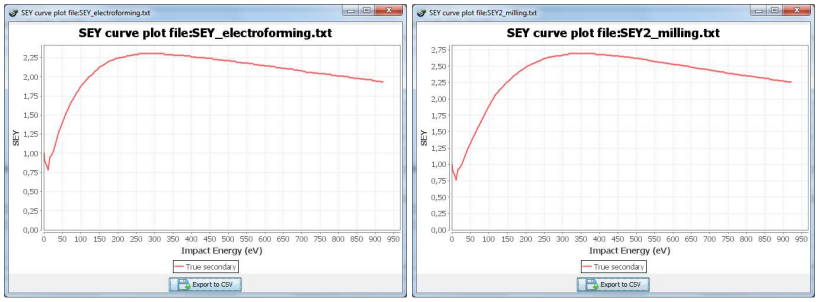

(a) **(b)**

Figure 4.27: SEY measured data on (a) electroforming and (b) milling sample.

Table 4.5: Relevant SEY parameters for multipactor prediction.

	Electroforming	Milling
E_1 (eV)	22	25.5
σ_{max}	2.3	2.69
E_{max} (eV)	290	350

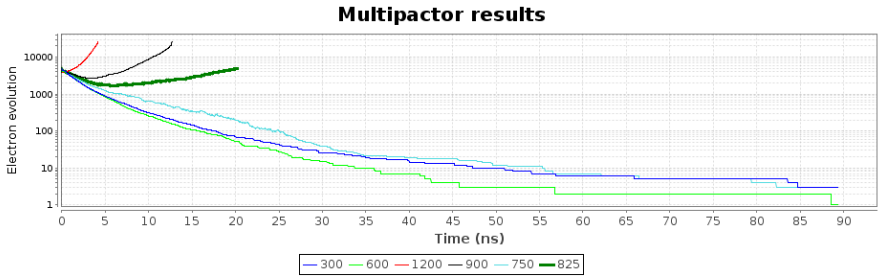

Figure 4.28: Electron population vs. time for different input power levels.

Finally, a large number of electrons (5000) have been used in order to ensure that enough initial electron seeding is available, which results in a stable breakdown power level. If a low power input signal is introduced into the device, multipactor process will not be established and the number of electrons will slowly decrease. On the contrary, the number of electrons will grow exponentially when the input power is high enough to produce the electron avalanche. The simulated time evolution of the particle number for different input power levels for the corrugated LPF fabricated by CCM are recorded and shown in Figure 4.28. Simulation results show that multipactor occurs when the input power is between 750 W and 825 W.

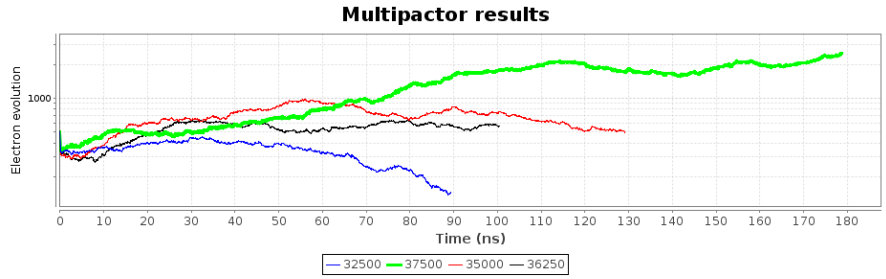

Figure 4.29: Electron population vs. time for different input power levels.

In Figure 4.29, the curves of electron population vs. time for the novel filter with 6-mm gap are presented at different power levels. It is seen that the breakdown is around 35 kW.

The simulated high-power threshold values of the rest of filters are detailed in Section 4.4.6.3.

4.4.6.2 High-power test

The multipactor test were conducted with the following parameters at ESA-VSC laboratory in Valencia, Spain:

- Frequency = 12.3 GHz.
- Pressure $< 1.5.10^{-5}$ mbar.
- Temperature = Ambient (reference Base Plate).
- Pulse width = 20 μs.
- PRF = 1 kHz
- RF power (Pulsed) = 1 kW for the E-plane corrugated filters (1a and 1b), and 14 kW for the novel filters.

All prototypes have been tested and two of the eight samples will be taken to explain the methodology followed and the breakdown power levels obtained.

- **Multipactor test of corrugated filter fabricated by milling**

  The classical E-plane corrugated filter fabricated by milling has been tested and the photograph of the device inside the thermal vacuum chamber (TVAC) is shown in Figure 4.30. The filter was kept under vacuum for around 18 hours before starting the test. No events were observed up to the first discharge, which occurred at 501 W. At this level of power, the electron monitoring shows a large increase in the number of electrons near the critical area of the device. Moreover, other detection methods confirm that a multipactor discharge has occurred.

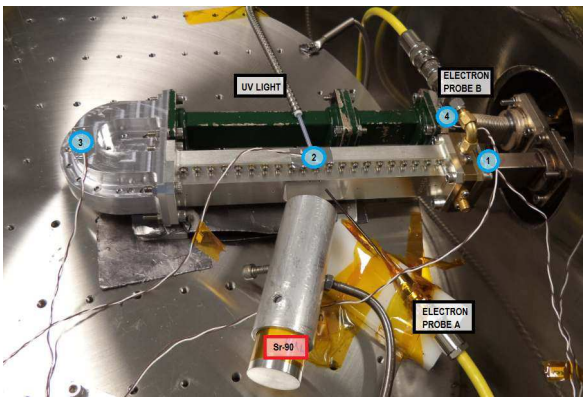

Figure 4.30: Classical E-plane corrugated filter fabricated by milling installed inside the TVAC for high power tests: radioactive source, UV lamp, thermocouples and local detection systems.

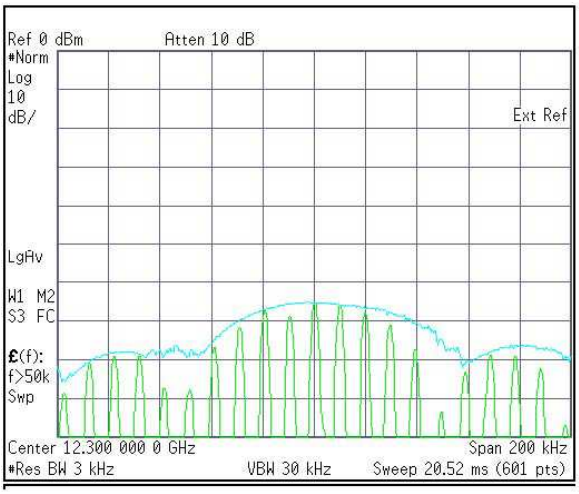

Figure 4.31: Multipactor test on the classical E-plane corrugated filter fabricated by milling: Nulling system. Event at 501 W.

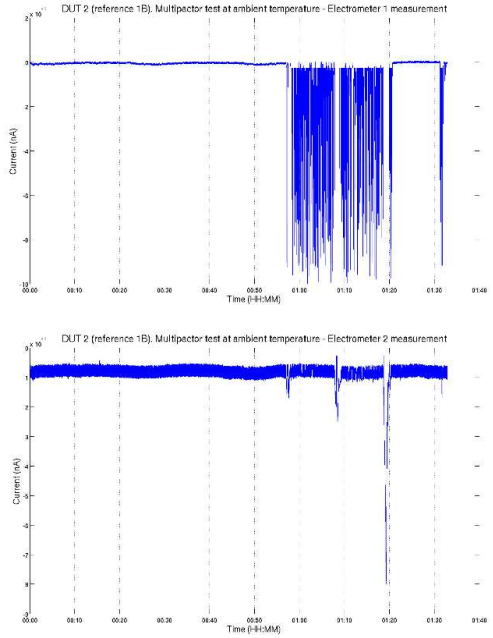

Figure 4.32: Multipactor test on filter *1b*: Electrometer A and B.

- **Multipactor test of novel 6mm-gap filter fabricated by electroforming**

  The novel filter with 6-mm gap fabricated by electroforming in copper and silver plated was installed inside the thermal vacuum chamber as shown in Figure 4.34. The filter was kept under vacuum for around 20 hours before starting the test. No events were observed up to the first discharge, which occurred at 9910 W. At this level of power, the electron monitoring shows an increase in the number of electrons near the critical area of the device. Moreover, other detection methods confirm that a multipactor discharge has occurred (Figures 4.35, 4.36, 4.37).

4.4.6.3 Summary of breakdown power levels

Different labels have been utilized to identify each filter, see Table 4.6. All simulated and tested results are summarized in Table 4.7.

First of all, it can be appreciated that the breakdown power levels of the same electroforming and milling samples are very similar. This makes sense since the rounded corners should not have a significant impact either in the EM response or in the resonance mechanism.

Moreover, in the light of the results obtained in the multipactor simulation and test, the general trend indicates that if the minimum mechanical gap increases the breakdown power level generally rises. However, a large discrepancy is obtained

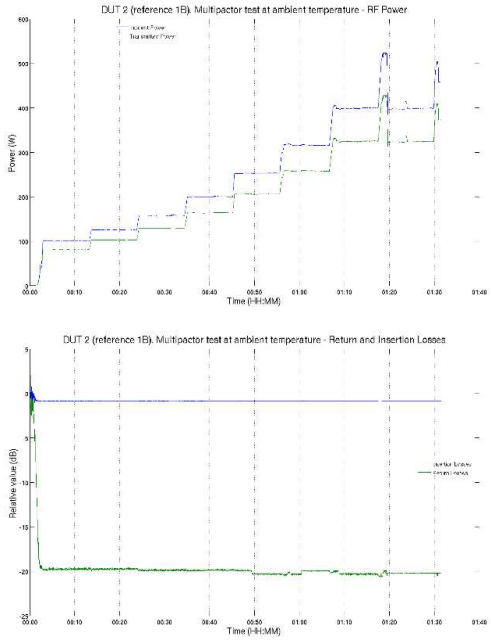

Figure 4.33: Multipactor test on filter *1b*: RF power and Return/Insertion Loss.

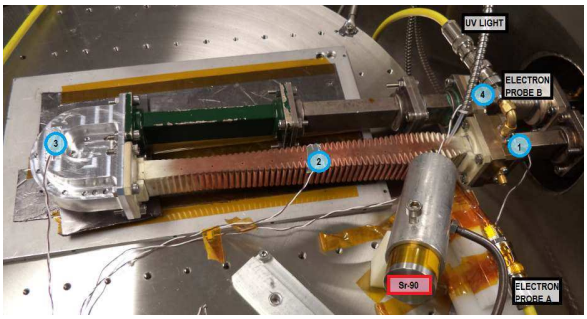

Figure 4.34: Novel filter with 6mm-gap fabricated by electroforming installed inside the TVAC for high power tests: radioactive source, UV lamp, thermocouples and local detection systems.

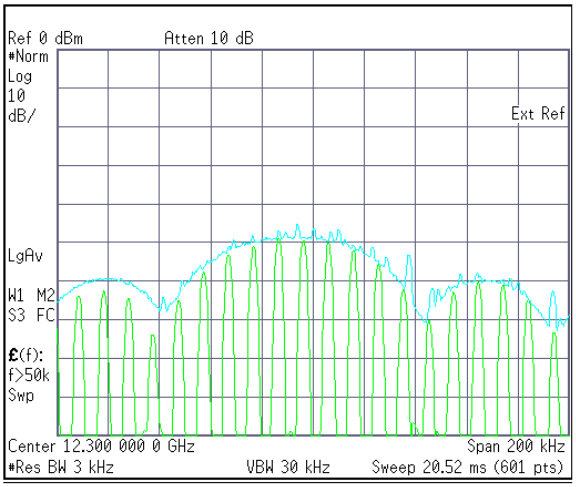

Figure 4.35: Multipactor test on the novel filter with 6mm-gap fabricated by electroforming: nulling system.

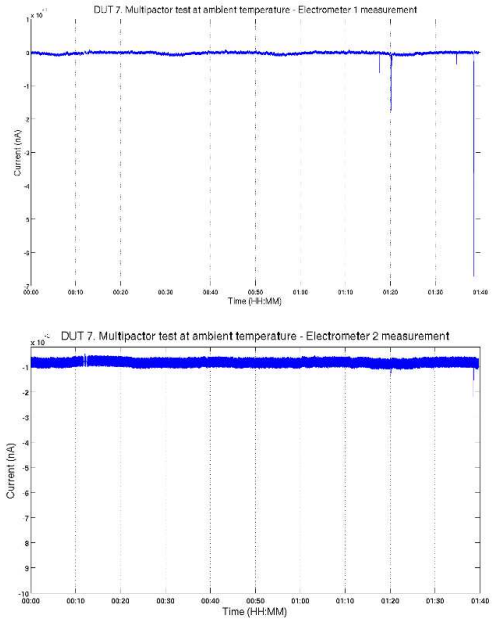

Figure 4.36: Multipactor test on on the novel filter with 6mm-gap fabricated by electroforming: Electrometer A and B.

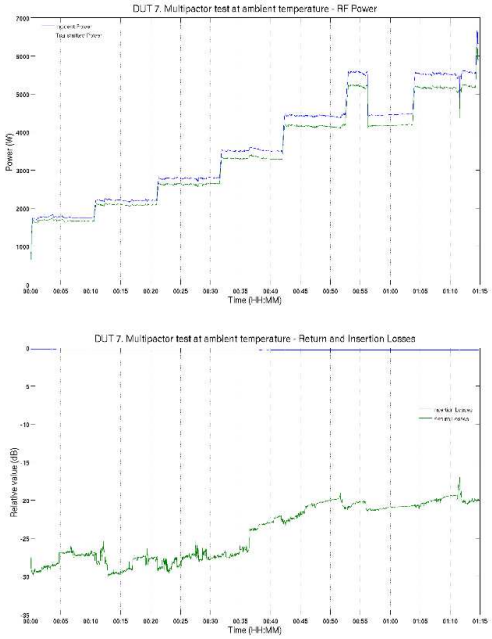

Figure 4.37: Multipactor test on on the novel filter with 6mm-gap fabricated by electroforming: RF power and return/insertion loss.

Table 4.6: Labels of the fabricated prototypes.

Filter	Label
1a	Classical E-plane corrugated LPF fabricated by electroforming.
1b	Classical E-plane corrugated LPF fabricated by CCM.
2a	Novel filter with 3 mm-gap fabricated by electroforming.
2b	Novel filter with 3 mm-gap fabricated by CCM.
3a	Novel filter with 4 mm-gap fabricated by electroforming.
3b	Novel filter with 4 mm-gap fabricated by CCM.
4a	Novel filter with 6 mm-gap fabricated by electroforming.
4b	Novel filter with 6 mm-gap fabricated by CCM.

Table 4.7: Summary of breakdown power levels for all samples together with the measurements.

Sample	Freq./ GHz	ECSS/W (Ag)	SPARK3D/W (Ag ECSS)	SPARK3D/W (Al ECSS)	SPARK3D/W (Measured SEY)	Test/W (First)	Test/W (Second)
1a	12.3	405	540	305	410	398	
1b	12.3	483	550	295	445	500	
2a	12.3	3900	8900	4400	6700	9900	
2b	12.3	3650	8100	4000	6700	1700/2200	1600
3a	12.3	5500	11000	5300	8000	7000/1100	14000
3b	12.3	6200	11000	5100	8500	3500/5500	3000
4a	12.3	10300	13500	6600	11800	9900/9000	14000
4b	12.3	11500	15000	7300	12400	7800	15000

between the breakdown test results of the *2b* and *3b* filters compared to the *2a* and *3a* filters. This is also evident when comparing these results with the simulation data. This large discrepancy can not be explained when using aluminum properties to perform simulations (almost 4 dB differences) or the ECSS prediction (which is still more than 3 dB above the test result).

A second campaign was performed to cross-check the most tricky results of the first test campaign (see Table 4.7). The result of this campaign has not shed light on the problem, since test results are very similar to those of the first campaign have been found. Moreover, in the case of the prototype *4b*, there is a 3 dB difference between both tests being this second test result in a better agreement with simulations.

As it can be seen in Table 4.7, the results obtained for the prototype *2b* using the measured SEY are not close to the test results. In order to be as conservative as possible in the simulation of the sample *2b*, the worst SEY combination of SEY parameters of different samples which were measured in different labs (EVEREST project [24]) have been taken into account. In other words, the maximum value of all SEY maxima have been taken, the lowest first crossover energy and the lowest energy at which the SEY is maximum. This would represent a very worst case out of all the SEY measured in the frame of such activity (see Table 4.8).

By using this parameters (shown in Table 4.8) in the SPARK3D simulation, the breakdown of the filter *2a* and *3b* are 2700 W and 3300 W respectively. It is seen that, although using these rather conservative SEY data, the simulation result of the filter *2b* is still 2-3 dB above the test. However, the result for the filter *3b* is in agreement with the test data.

Table 4.8: Worst SEY parameters selected to perform further multipactor analysis.

E_1 (eV)	σ_{max}	E_{max} (eV)
14	2.81	165

Trying to find the reason of the discrepancy, a microscopic visual inspection was performed on the *2b* and *4b* filters and nothing strange was found by visual inspection.

Another possible explanation of the abnormal low breakdown power level obtained in filters *2b* and *3b*, is that there could be some misalignments between the two halves manufactured by milling. Therefore, S-parameter simulations have been performed taking into account 20 μm of displacement (tolerances of the manufacturing method) in the waveguide width and in the propagation z-axis.The filter response is practically preserved. Considering the worst case SEY (since this is the closest result) and the two displacements, the simulated breakdown level decreased to 2500 W for both displacements.

4.4.7 Summary

In this example, it has been demonstrated the feasibility of designing novel high-power LPFs with smooth profile with the suppression of only the fundamental mode. Moreover, it has also been demonstrated that it is possible to manufacture this kind of filters using space-compatible procedures. Last but not least, the novel filters with smooth profile have been characterized in terms of high-power behavior with both simulations and multipactor tests. As expected, very high-power threshold levels have been obtained, proving the possibility of achieving simultaneously wide stopbands and high-power handling in a single device.

4.5 Design Example 2: High-power LPF with Higher-order Mode Suppression using a 2-D arrangement of Bandstop Elements

In this case, three high-power LPFs with higher-order mode suppression using a 2-D arrangement of bandstop elements will be designed following the design technique presented in Section 4.3.2.1. The novel filter will have the same fundamental TE_{10}-mode behavior but different higher-order mode suppression. By means of the analysis of simulation results, the control on the fundamental and the higher-order mode suppression following the method proposed in this Chapter in Section 4.3.2.1 will be demonstrated. As an example, one of the filters will be fabricated and its fundamental and higher-order mode behavior will be validated in measurement.

Summarizing, the main objectives of this example are the following:

- Demonstrate the feasibility of designing high-power LPFs with the technique in Section 4.3.2.1.
- Demonstrate that it is possible to control the higher-order mode suppression with different minimum mechanical gaps.

4.5.1 Specifications

All filters will fulfill the specifications defined in Table 4.9.

4.5.2 Design and Simulation

Firstly, the quasi-periodic structure in the z-direction to reject the fundamental TE_{10} mode is designed as the previous example. L_2, h_{max} and h_{min} are set to 8.6 mm and 1.6 mm in order to reject the lowest and highest frequency in the fundamental TE_{10}-mode stopband (f_{min} = 13.75 GHz and f_{max} = 38.1 GHz), respectively (the filter width, a_0, is kept constant, and equal to the WR75 input and output port width (a_0 = 19.05 mm, b_0 = 9.525 mm), along the z-axis). After matching L_2 to the WR75 ports through L_1 and L_3, all bandstop elements have been replicated in the x-direction (n_x = 5) [2], [3] in order to achieve the rejection of the higher-order TE_{n0} modes. The length of the bandstop elements l_x and l are set to the same value: $l_x = l = 3.81$ mm to have a roughly isotropic structure which achieves, simultaneously, the suppression of the higher-order TE_{n0} modes, minimizing the excitation of the higher-order modes in the inner part of the device, and allowing an easy manufacturability. Finally, the minimum mechanical gap, g_{min}, is adjusted to control the non-TE_{n0} mode behavior in the fundamental TE_{10}-mode stopband and the final filter dimensions are properly optimized. Three different values for g_{min} (5, 4 and 3 mm) are used to compare the results (see Figure 4.38).

The frequency response of the proposed structures is shown in Figure 4.39 along with the frequency response of a classical waffle-iron filter designed following the technique explained in Chapter 3 fulfilling the same frequency specifications. As it can be seen, the return loss is better than 20 dB in the passband while the attenuation in the stopband is higher than 60 dB for all the devices. Therefore, the requirements for the fundamental TE_{10} mode are fulfilled in all the devices.

As it has been explained in Subsection 4.3.2.1, the higher-order TE_{n0}-mode suppression is achieved by the two-dimensional arrangement of sinusoidal bandstop elements of the structure. As it is deduced from equation (1.1), the cutoff frequencies of the higher-order TE_{n0} modes only depend on the waveguide width, a_0, allowing a frequency behavior with higher-order TE_{n0}-mode suppression regardless of the minimum mechanical gap. By using CST MWS it is possible to excite a device with a

Table 4.9: Frequency specifications

Passband	Return loss	Stopband	Attenuation
10.7 - 12.7 GHz	20 dB	13.75 - 38.1 GHz	60 dB

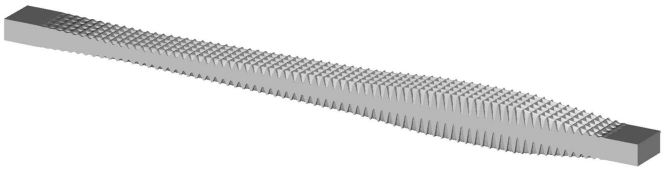

Figure 4.38: 3D view of the novel high-power LPF with higher-order mode suppression using a 2-D arrangement of bandstop elements and minimum mechanical gap equal to 5 mm.

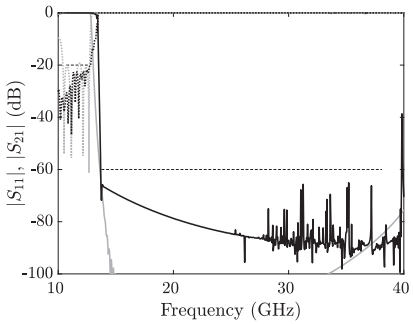

(a)

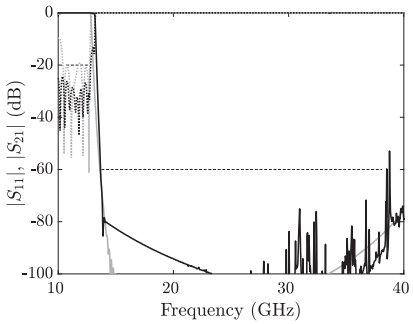

(b)

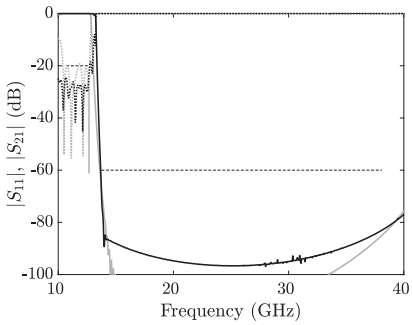

(c)

Figure 4.39: Simulated frequency response using CST MWS of the fundamental TE_{10} mode for the classical waffle-iron filter (grey line) and the new high-power LPFs (black line) with a minimum mechanical gap equal to (a) 5 mm, (b) 4 mm, and (c) 3 mm. $|S_{11}|$ in dotted line and $|S_{21}|$ in solid line. Frequency specifications in dashed line.

Table 4.10: Cutoff frequencies (GHz) of the higher-order non-TE_{n0} modes excited in the WR75 ports and in the devices (up to 38.1 GHz)

	$\mathbf{TE}_{01}$	$\mathbf{TE}_{11}$ $\mathbf{TM}_{11}$	$\mathbf{TE}_{21}$ $\mathbf{TM}_{21}$	$\mathbf{TE}_{31}$ $\mathbf{TM}_{31}$	$\mathbf{TE}_{02}$	$\mathbf{TE}_{12}$ $\mathbf{TM}_{12}$	$\mathbf{TE}_{41}$ $\mathbf{TM}_{41}$	$\mathbf{TE}_{22}$ $\mathbf{TM}_{22}$
WR75 ports	15.7	17.6	22.3	28.4	31.5	32.4	35.2	
5 mm-gap filter	18.7	20.3	24.4	30.1	37.5	36.6	>38.1	
4 mm-gap filter	28.5	29.6	32.6	37	>38.1			
3 mm-gap filter	>38.1							

single mode and obtain the simulated $|S_{21}|$ parameter of that mode. Hence, some simulations have been done exciting the filters with each higher-order TE_{n0} mode. In particular, the TE_{20}, TE_{30}, and TE_{40} modes can propagate in the stopband of the filters considered in this comparison from its corresponding cutoff frequencies ($f_{c,20}$ = 15.7 GHz, $f_{c,30}$ = 23.6 GHz, and $f_{c,40}$ = 31.5 GHz, respectively) up to the third harmonic (38.1 GHz). As it is depicted in Figure 4.40, all filters show an excellent rejection level for the TE_{n0} modes that is better than 60 dB in all cases.

If non-TE_{n0}-mode rejection is also required in all or part of the fundamental TE_{10}-mode stopband, attention must be paid to the minimum gap value as it is shown next.

Following the method described in Section 4.3.2.1, in order to reject the higher-order TE_{nm}/TM_{nm} modes ($m \neq 0$), it is necessary to guarantee that the mode with the lowest cutoff frequency (TE_{01} mode) is not able to propagate in the section of the device with the minimum mechanical gap. As it has been also explained, the effective minimum mechanical gap value, g_{eff}, is utilized in the calculations.

The filter with minimum mechanical gap equal to 5 mm has a g_{eff} equal to 8 mm and, following equation (1.1), the TE_{01}-mode cutoff frequency is 18.7 GHz (see 4.10) as it can be checked in Figure 4.41, where the filter is excited in simulation with the TE_{01} mode. The filter with minimum mechanical gap equal to 4 mm has a g_{eff} equal to 5.25 mm, achieving a TE_{01}-mode suppression up to the second harmonic (TE_{01}-mode cutoff frequency around 28.5 GHz). Finally, the filter with minimum mechanical gap equal to 3 mm has a g_{eff} equal to 3.5 mm achieving a TE_{01}-mode suppression up to the third harmonic (TE_{01}-mode cutoff frequency around 42.8 GHz). In Figure 4.42, it is represented how the 3 mm-gap filter rejects all higher order non-TE_{n0} modes propagating at the WR75 ports up to 38.1 GHz. Therefore, the technique presented in this Chapter can be also used for the control of the propagation of the non-TE_{n0} modes to conveniently suppress them in the bandwidth of interest.

4.5.3 Fabrication and Measurement

A prototype of the filter has been manufactured in aluminum by CCM (radius of the tool equal to 0.5 mm) and then silver plated, see Figure 4.43. As it has been mentioned in Section 4.4.4, when CCM is assumed, it is not possible to mechanize perfect square corners or cavities with dimensions smaller than the drill. Specifically, the prototype fabricated in this Section has been divided in four pieces (see

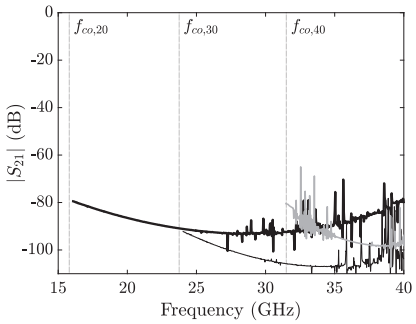

(a)

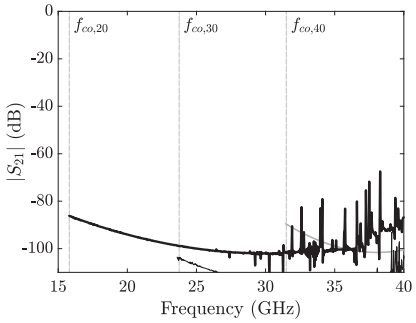

(b)

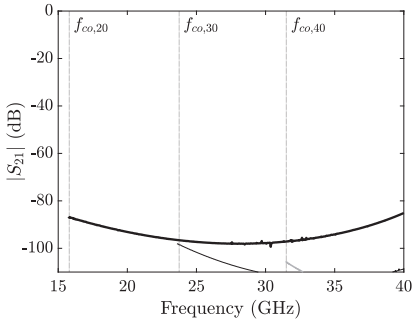

(c)

Figure 4.40: Simulated $|S_{21}|$ frequency responses using CST MWS of the higher-order TE_{n0} modes for the novel high-power harmonic filter with a minimum mechanical gap equal to (a) 5 mm, (b) 4 mm, and (c) 3 mm

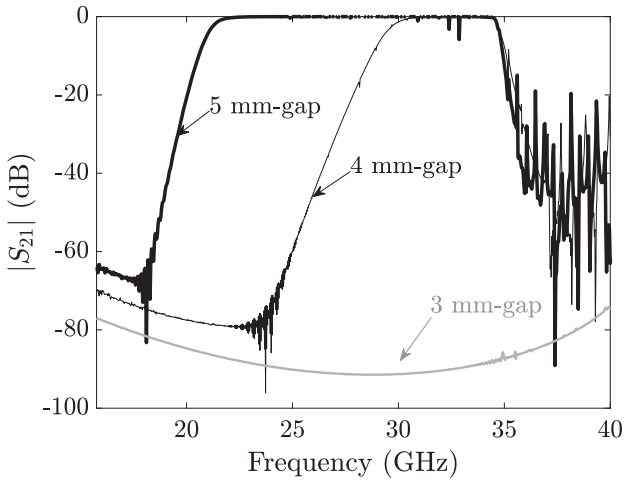

Figure 4.41: Simulated $|S_{21}|$ frequency response using CST MWS of the higher-order TE_{01} mode for the novel high-power LPF with a minimum mechanical gap equal to 5 mm (solid thick line), 4 mm (solid thin line), and 3 mm (solid grey line).

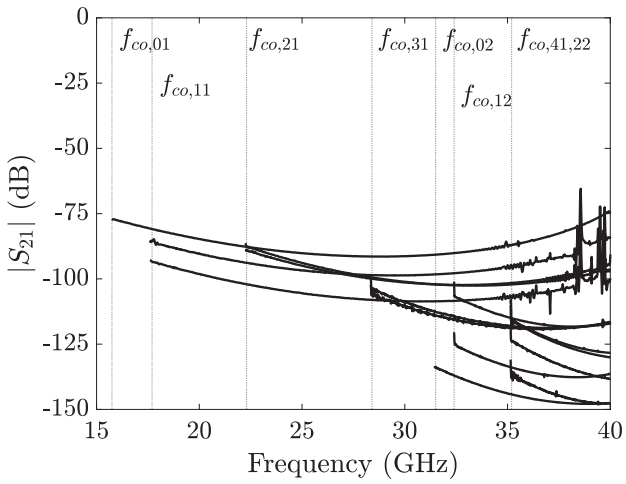

Figure 4.42: Simulated $|S_{21}|$ frequency responses using CST MWS of the non-TE_{n0} modes for the novel high-power harmonic filter with a minimum mechanical gap equal to 3 mm. Cutoff frequencies of the non-TE_{n0} higher-order modes at the WR75 waveguide ports are shown in thin grey line.

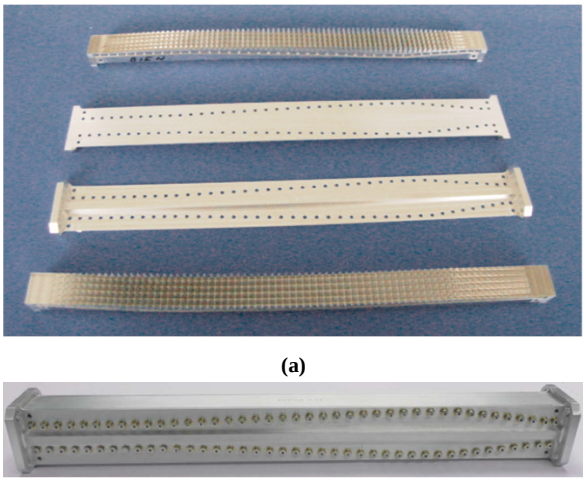

(a)

(b)

Figure 4.43: Photograph of the prototype fabricated by milling in aluminium and then silver-plated: (a) view of the four pieces and (b) assembled structure.

Figure 4.43(a)): two identical parts with the 2-D arrangement of bandstop elements (the upper part is easily accessible by the drill but the lower part is quite narrow and must be rounded) and two plain covers to close the filter (it avoids the rounded corners of the four edges which define the rectangular waveguide) (see Figure 4.43(b)). As the first example of this Chapter, this modification produces a shift towards lower frequencies in the frequency response that have been easily compensated by reducing the height of the modified bandstop elements. The radius of the tool utilized to manufacture the filter is equal to 0.5 mm.

The measurements have been carried out by means of an Agilent 8722 VNA, proper waveguide-to-coaxial transitions, waveguide tapers, and calibration kits. As it can be seen in Figure 4.44, the novel filter fulfills the fundamental TE_{10}-mode specifications. Moreover, following [25], 90° H-plane bends have been employed between the tapers and the filter ports to validate with a single measurement the rejection of the higher-order TE_{n0} modes (Figure 4.45 (a)). The 90°H-plane bend at the input of the filter couples the power of the fundamental TE_{n0} mode to the higher-order TE_{n0} modes. If they are not suppressed by the device, they are coupled back to the fundamental TE_{10} mode in the 90° H-plane bend at the output of the device, leading to peaks in the frequency response at the frequencies where the TE_{n0} modes are not rejected. However, when these modes are suppressed, as it is predicted in the simulation of Figure 4.40 for the novel filter, no peaks appear. In this case, as it can be seen in Figure 4.45 (b), the novel filter features excellent higher-order TE_{n0}-mode suppression, as expected.

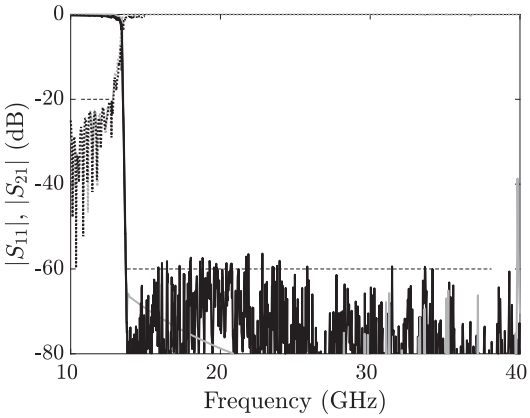

Figure 4.44: Measured (black line) and simulated (grey line) frequency response of the fundamental TE_{10} mode for the new high-power LPF (black line). $|S_{11}|$ in dotted line and $|S_{21}|$ in solid line. Frequency specifications in dashed line.

4.5.4 High-power Behavior

In the previous example (Section 4.4), it has been demonstrated that the method based on the parallel-plate waveguide model (ECSS multipactor tool) provides an estimation of the RF input power threshold that is, in many occasions, very conservative and restrictive. This is due to the fact that the infinite parallel-plate approach results in the worst scenario possible, just providing the lowest RF breakdown power threshold. Therefore, for the calculation of the RF input power threshold in this example (and in the rest of the Thesis) a PIC tool will be utilized.

In order to analyze the high-power handling capability of the novel high-power LPFs with higher-order mode suppression using a 2-D arrangement of bandstop elements and compare it with the classical waffle-iron filters, CST Particle Studio (CST PS) has been used to study the multipactor phenomenon in both structures. For this analysis, the filter fabricated in the previous subsection with the largest minimum gap (5 mm) has been chosen since it provides the largest power-handling capability. Its behavior has been compared with the equivalent waffle-iron (0.6 mm-gap) filter (designed following the technique in Chapter 3).

In CST PS, The first step to study the multipactor threshold is to fix the material employed and its associated SEY coefficient. Since the fabricated prototype was silver-plated, ECSS silver has been used in this high-power analysis. The simulations have been done at 12.7 GHz (upper bandpass edge), which is the frequency where the EM field is maximum and the power handling is minimum.

In the CST PS simulation, the initial seed macro-particles will follow a Gaussian function and will be emitted with a constant kinetic energy of 10 eV. If a low power input signal is introduced into the structure, multipactor could not be established and the number of electrons will slowly decrease. On the contrary, the number of

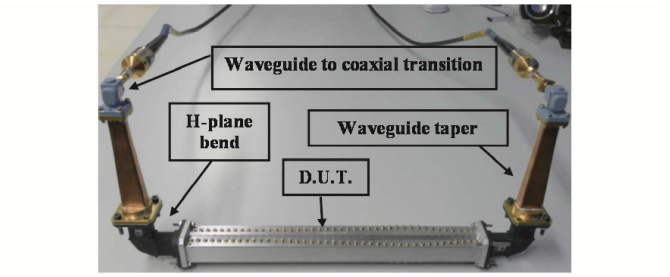

(a)

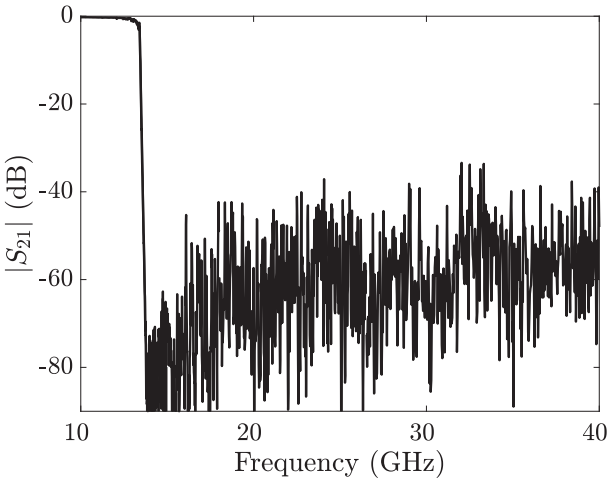

(b)

Figure 4.45: (a) Photograph of the prototype with the 90° H-plane bends in the measurement set-up for the characterization of the higher-order TE_{n0}-mode suppression, (b) measured $|S_{21}|$ frequency response of the fundamental TE_{10} mode for the new high-power LPF using the set-up depicted in (a)

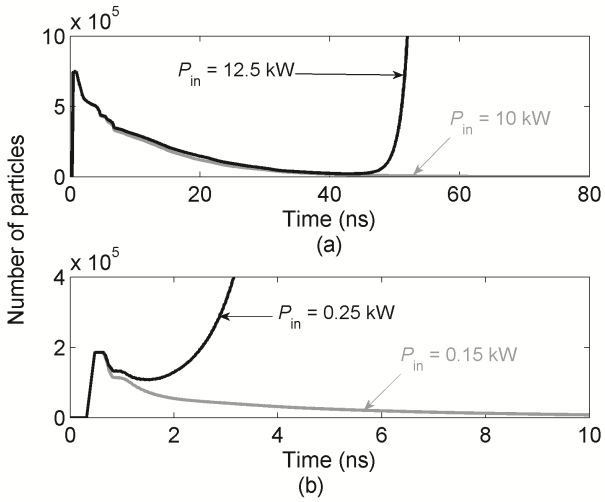

Figure 4.46: Number of particles as a function of time in the simulation of(a) the novel high-power filter and (b) the waffle-iron filter. Multipactor occurs (black line) or not (grey line) for the different input peak powers (P_{in}) indicated in the figure.

electrons will grow exponentially when the input power is high enough to produce the electron avalanche. The simulated time evolution of the number of particles for different input power levels are recorded and shown in Figure 4.46.

Simulation results clearly show that the new device has higher-power handling capability than the classical waffle-iron filter and is an excellent candidate for many high-power applications. In the novel high-power filter, multipactor never occurs when the input peak power is below 10 kW (Figure 4.46(a)), while in the classical waffle-iron filter multipactor occurs above only 150 W (Figure 4.46(b)).

Last but not least, apart from having a larger minimum mechanical gap, the smoother profile of the new device (and the novel filters of the first example) and the shorter minimum gap sections imply that the electrons can be easily deviated to deeper cavities making multipaction less probable and, therefore, highly increasing the overall power handling capability [17].

4.5.5 Summary

In this example, the possibility of designing high-power LPFs with a 2-D arrangement of smooth bandstop elements has been proved. Moreover, a high-level of control over the higher-order mode suppression has been also demonstrated with the free parameters of the proposed design technique. Furthermore, a prototype of a novel filter has been fabricated by CCM and the measurement results are very close to the simulated one. Finally, the high-power behavior has been also estimated and compared with its classical counterpart, the waffle-iron filter, showing that the proposed

Table 4.11: Frequency specifications

Passband	Return loss	Stopband	Attenuation
10.7 - 12.7 GHz	20 dB	13.75 - 38.1 GHz	60 dB

LPF can be utilized in high-power applications, where a very wide stopband and all higher-order mode suppression are also required.

4.6 Design Example 3: High-power LPF with Higher-order Mode Suppression using a Width Variation

In this last example, the possibility of designing high-power LPF with smooth profile and all higher-order mode suppression up to the third harmonic achieved by means of a width variation (following the technique given in Section 4.3.2.2) will be demonstrated.

4.6.1 Specifications

To do so, a WR75 device which fulfills a passband defined between 10.7 GHz and 12.7 GHz with an in-band return loss better than 20 dB and a stopband from 13.75 GHz up to the third harmonic (38.1 GHz) with attenuation higher than 60 dB will be designed (see Table 4.11).

4.6.2 Design and Simulation

A novel filter fulfilling the previous specifications has been designed using the novel technique described in Section 4.3.2.2. In this case, a novel filter with a minimum mechanical gap equal to 3 mm will be designed since, as it was demonstrated in the previous example, a very high attenuation will be achieved for the the higher-order non- TE_{n0} modes up to the third harmonic. The final dimensions of the filter are given in Table 4.12. The total size of the novel filter is 218 mm. Its simulated frequency response is shown in Figure 4.47 along with the frequency response of a classical waffle-iron filter designed fulfilling the same frequency specifications. As it can be seen in Figure 4.47, the filter fulfills perfectly the frequency specifications. Indeed, the attenuation levels attained with the filter are around 100 dB in the entire stopband. Moreover, the suppression of all higher-order modes is also accomplished as can be seen in Figure 4.48, and Figure 4.49.

4.6.3 Fabrication and Measurement

The filter has been fabricated by CCM (radius of the tool equal to 0.5 mm) in two halves cut by the H-plane in aluminum and then silver plated (see Figure 4.50).

Table 4.12: Final dimensions of the novel filter with width variation and 3-mm gap.

Section L_1	# elements = 12; window: Hanning
Section L_2	l = 3.82 mm; g_{min} = 3 mm; h_{max} = 8.50 mm; h_{min} = 0.4 mm; # elements = 32 (# elements with h_{max} = 5)
Section L_3	# elements = 13; window: Hanning
Width variation	# elements = 22; window: Hanning # elements a_{min} = 2 a_{min} = 15 mm

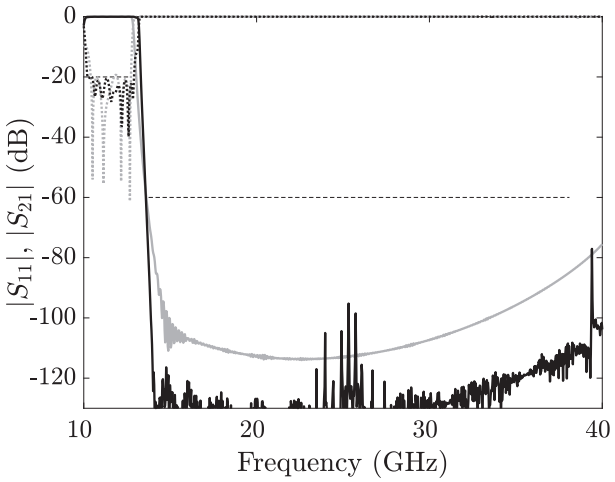

Figure 4.47: Simulated frequency response using CST MWS of the fundamental TE_{10} mode for the new filter (black line) and its classical counterpart the waffle-iron filter (grey line). $|S_{11}|$ in dotted line and $|S_{21}|$ in solid line. Frequency specifications in dashed line.

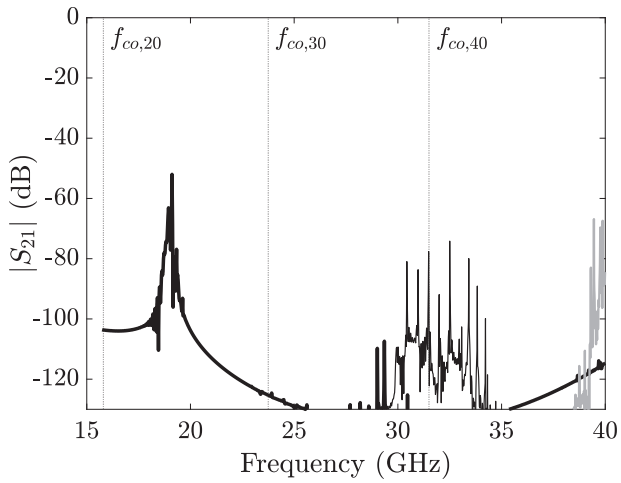

Figure 4.48: Simulated $|S_{21}|$ frequency responses using CST MWS of the higher-order TE_{n0} modes for the new filter.

Then, the same modifications mentioned in Section 4.4.4 to compensate the rounded-corners effect explained have been performed in this device.

The measurements have been carried out by means of an Agilent 8722 VNA, proper waveguide-to-coaxial transitions, waveguide tapers, and calibration kits. In Figure 4.51, the measured TE_{10}-mode frequency response of the novel filter is shown, fulfilling the specifications with an in-band insertion loss better than 0.38 dB (this value is higher than expected and is due to some issues in the surface treatment). Moreover, when 90° H-plane bends are included at the filter input and output ports to measure the high-order TE_{n0}-mode filter behavior, the novel filter features an excellent higher-order mode suppression (see Figure 4.52), as predicted.

4.6.4 High-Power Behavior

In this case, CST Particle Studio has been utilized for the calculation of the RF input power threshold in this example following the same procedure described in the previous example (Section 4.5). The SEY of silver has been used and the high-power threshold level has been calculated at 12.7 GHz where the EM-fields are maximum and the power threshold is minimum. The simulated threshold input peak power is between 10 kW and 12.5 kW while less than 250 W is obtained for its classical counterpart the waffle-iron filter designed fulfilling the same frequency specifications. As it has been observed in the previous Examples, in addition to the larger minimum gap, the smoother profile of the new device and the smaller area of the critical sections imply that the electrons can be easily deviated to higher cavities making multipactor phenomenon less probable and, therefore, highly increasing the power-handling capability.

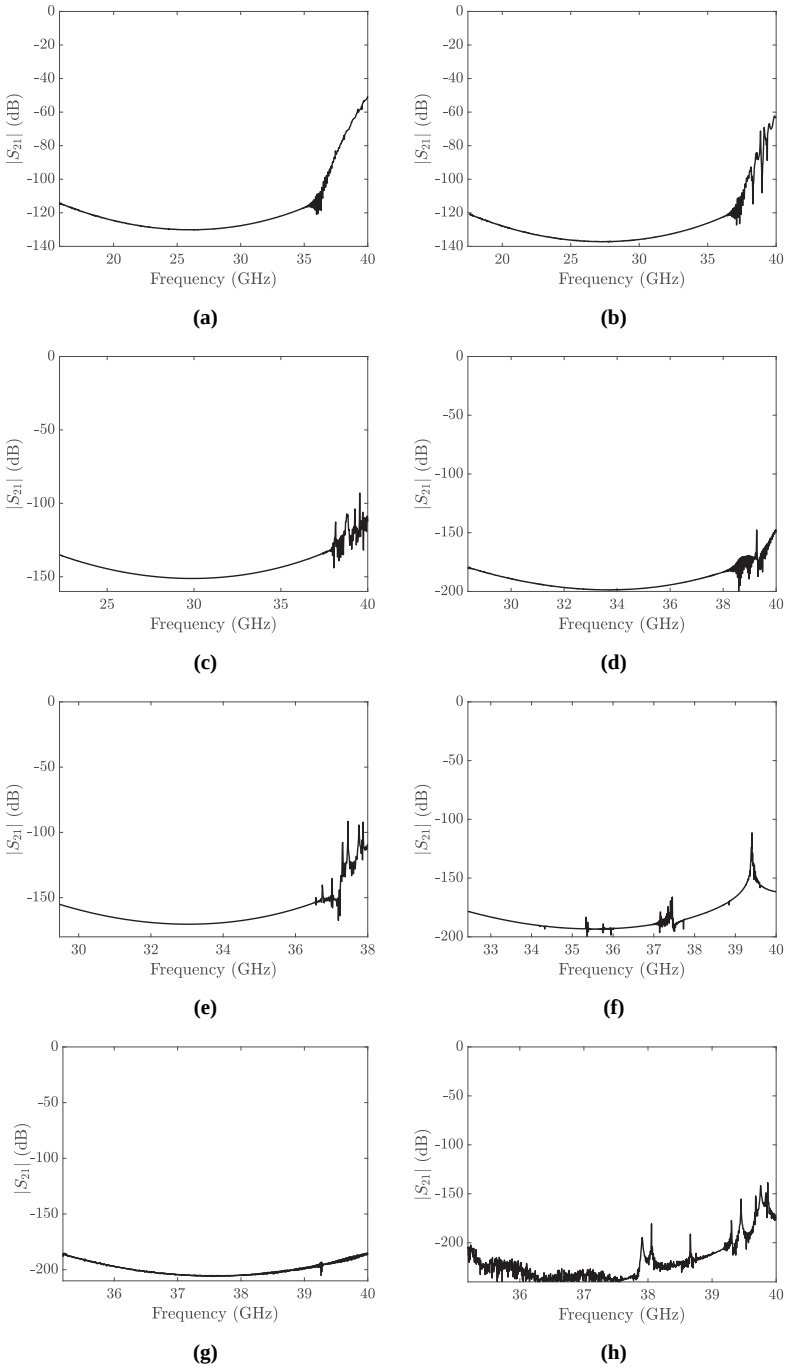

Figure 4.49: CST MWS simulated $|S_{21}|$ of the high-power filter with width reduction and suppression of all the higher-order modes when it is excited with the (a) TE_{01} mode, (b) TE_{11}/TM_{11} mode, (c) TE_{21}/TM_{21} mode, (d) TE_{31}/TM_{31} mode, (e) TE_{02} mode, (f) TE_{12}/TM_{12} mode, (g) TE_{41}/TM_{41} mode, and (h) TE_{22}/TM_{22} mode

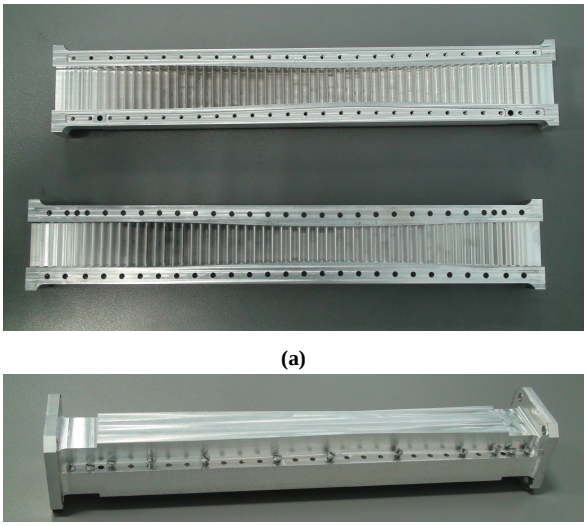

(a)

(b)

Figure 4.50: Photograph of the prototype fabricated by CCM in aluminium and then silver-plated: (a) unassembled and (b) assembled prototype.

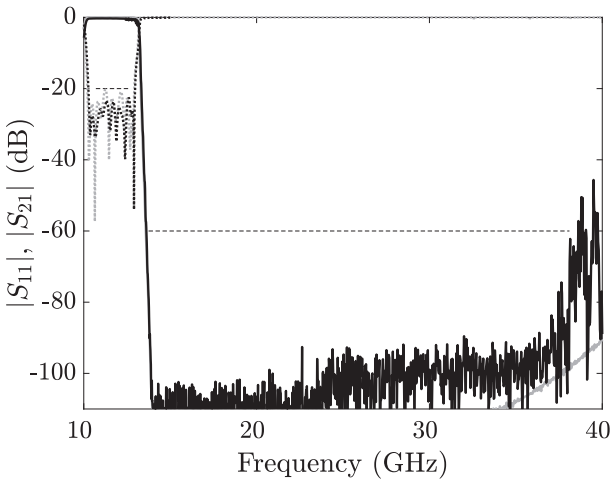

Figure 4.51: Measured (black line) and simulated with CST MWS (grey line) frequency responses of the fabricated prototype. $|S_{11}|$ in dotted line and $|S_{21}|$ in solid line. Frequency specifications in dashed line.

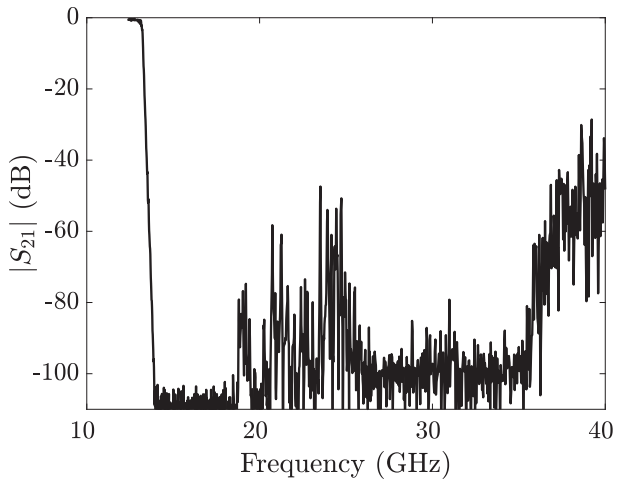

Figure 4.52: Measured $|S_{21}|$ frequency response of the fundamental TE_{10} mode for the new high-power harmonic filter using the H-plane bend set-up.

4.6.5 Summary

In this latter example, the feasibility of designing high-power LPF with smooth profile and width variation has been demonstrated. The novel filter achieves the suppression of the fundamental mode and all higher-order modes in a very wide stopband while a very high-power multipactor threshold level is attained simultaneously. This has been clearly demonstrated through the measurement results of a fabricated prototype which are very close to the simulated ones. Finally, the high-power behavior of the proposed LPF has been also estimated.

4.7 Software Application

The design methodology for the high-power LPFs with smooth profile developed in this Chapter has been implemented into a SW tool, where a 3D visualization tool (implemented in a free open source called Blender) linked to a SQL type database.

The design work-flow is divided into the following steps. Fist of all, a target frequency response is defined. This frequency response is determined by the lowest and highest frequency of the passband, the return loss of the passband, the lowest and highest frequency of the stopband, the attenuation of the stopband, the input/output WR standard ports and the type of structure required (1D (Section 4.3.1), 2D (Section 4.3.2.1) or 1D with width reduction (Section 4.3.2.2)).

Taking into account the target frequency specifications, an initial profile along with the physical parameters that define this profile is provided. This profile is displayed and it is possible to modify it by varying the corresponding design parameters.

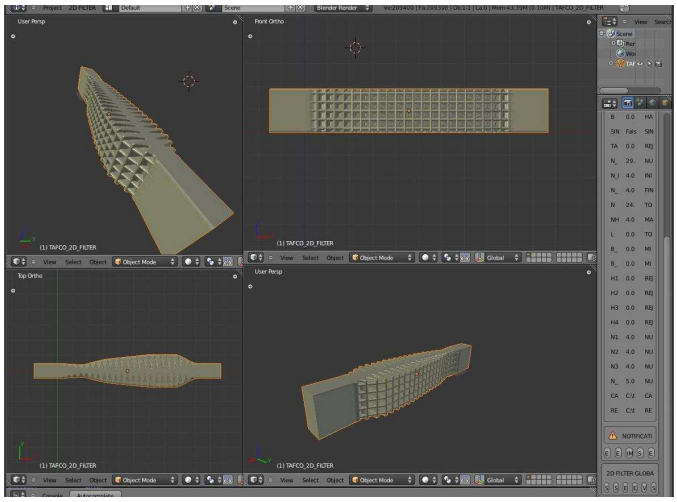

Figure 4.53: 3D view example of the SW tool with a novel high-power LPF with higher-order mode suppression using a 2-D arrangement of bandstop elements.

Then, an STL file is created in order to import and simulate it into a 3rd party SW, for instance, CST MWS or HFSS.

Once the device is imported into the 3rd party SW, it is simulated to obtain the S-parameters. After that, this results are imported into the design SW by means of an CSV file. Then, the application checks if the target frequency response is fulfilled or not.

If the frequency response obtained is satisfactory, the design process is finished. If not, a guided optimization process is performed until fulfilling the target frequency response. The guided optimization process includes the necessary modifications that can be performed in the physical parameters. Therefore, it starts with a pre-designed and simulated structure with similar specifications to the target frequency response which has been defined by the user.

4.8 Conclusions

In this Chapter, a novel stepwise design procedure for high-power LPFs with smooth profile has been proposed. Three different configurations of the novel filters can be achieved: the suppression of only the fundamental mode through a simple 1-D structure or both the fundamental and all higher-order mode suppression by means of a 2-D arrangement of bandstop elements or a width variation along the propagation direction. The three design technique have been proved with design examples which have been simulated, fabricated, and measured.Moreover, the high-power behavior of the filters has been estimated and tested in some of the devices, showing that large mechanical gaps able to support high-power levels of multipactor threshold and very wide stopbands can be accomplished simultaneously. Therefore, this kind of filters

are very convenient to be utilized in the last stage of the OMUX, replacing all the channel LPF which are commonly used to avoid harmonics. This have a enormous impact in the mass and volume of the payload, with a subsequent dramatic reduction of its associated launch costs.

REFERENCES

[1] I. Arregui, I. Arnedo, A. Lujambio, M. Chudzik, D. Benito, R. Jost, F. Gortz, T. Lopetegi, and M. Laso, "A compact design of high-power spurious-free low-pass waveguide filter," *IEEE Microwave and Wireless Components Letters*, vol. 20, no. 11, pp. 595–597, Nov. 2010.

[2] I. Arregui, F. Teberio, I. Arnedo, A. Lujambio, M. Chudzik, D. Benito, R. Jost, F.-J. Gortz, T. Lopetegi, and M. Laso, "High-power low-pass harmonic waveguide filter with TEn0-mode suppression," *IEEE Microwave and Wireless Components Letters*, vol. 22, no. 7, pp. 339–341, Jul. 2012.

[3] F. Teberio, I. Arregui, I. Arnedo, M. Chudzik, R. Jost, F.-J. Görtz, T. Lopetegi, and M. A. G. Laso, "Tailoring of higher-order mode suppression in a high-power alternative to classical waffle-iron filters," *Microwave Optical and Technology Letters*, vol. 56, no. 12, pp. 2967–2974, Dec. 2014.

[4] I. Arregui, F. Teberio, I. Arnedo, A. Lujambio, M. Chudzik, D. Benito, T. Lopetegi, R. Jost, F.-J. Gortz, J. Gil, C. Vicente, B. Gimeno, V. Boria, D. Raboso, and M. Laso, "High-power low-pass harmonic filters with higher-order TEn0 and non-TEn0 mode suppression: Design method and multipactor characterization," *IEEE Transactions on Microwave Theory and Techniques*, vol. 61, no. 12, pp. 4376–4386, Dec. 2013.

[5] Public University of Navarre (UPNA), Novalti S.A., Aurorasat S.L., Customer: TESAT, "Compact high-power spurious-free low-pass waveguide filters," ESA, ITI-B project EIN-RP-1401, Oct. 2014.

[6] UPNA, "Overall development of high-power filters for the output multiplexer of a communication satellite," TESAT Spacecom GmbH, 2013.

[7] V. Boria and B. Gimeno, "Waveguide filters for satellites," *Microwave Magazine, IEEE*, vol. 8, no. 5, pp. 60–70, Oct. 2007.

[8] M. Yu, "Power-handling capability for rf filters," *Microwave Magazine, IEEE*, vol. 8, no. 5, pp. 88–97, Oct. 2007.

[9] C. Kudsia, R. Cameron, and W.-C. Tang, "Innovations in microwave filters and multiplexing networks for communications satellite systems," *IEEE Transactions on Microwave Theory and Techniques*, vol. 40, no. 6, pp. 1133–1149, Jun. 1992.

[10] K. Zaki, "Microwave filters and multiplexers for space applications," in *2008 6th ESA International Workshop on Multipactor, Corona and Passive Intermodulation (MULCOPIM)*, Sep. 2008.

[11] G. Matthaei, L. Young, and E. M. T. Jones, *Microwave filters, impedance-matching networks and coupling structures*. Artech House, 1980.

[12] R. Cameron, C. Kudsia, and R. Mansour, *Microwave Filters for Communication Systems: Fundamentals, Design and Applications*. Wiley-Interscience, 2007.

[13] F. Teberio, I. Arnedo, J. M. Percaz, I. Arregui, T. Lopetegi, and M. A. G. Laso, "Accurate design of corrugated waveguide low-pass filters using exclusively closed form expressions," in *2017 47th European Microwave Conference (EuMC)*, Oct. 2017.

[14] F. Teberio, I. Arnedo, J. M. Percaz, I. Arregui, P. Martin-Iglesias, T. Lopetegi, and M. A. G. Laso, "Accurate synthesis procedure for waffle-iron low-pass filter," in *2018 IEEE MTT-S International Microwave Symposium Digest (IMS)*, Jun. 2018.

[15] I. Arnedo, J. Gil, N. Ortiz, T. Lopetegi, M. Laso, M. Sorolla, M. Thumm, D. Schmitt, and M. Guglielmi, "Ku-band high-power lowpass filter with spurious rejection," *IET Electronics Letters*, vol. 42, no. 25, pp. 1460–1461, Dec. 2006.

[16] I. Arregui, I. Arnedo, A. Lujambio, M. Chudzik, M. A. G. Laso, T. Lopetegi, and M. Sorolla, "Design method for satellite output multiplexer low-pass filters exhibiting spurious-free frequency behavior and high-power operation," *Microwave and Optical Technology Letters*, vol. 52, no. 8, pp. 1724–1728, Aug. 2010.

[17] V. Semenov, J. Rasch, E. Rakova, and J. Johansson, "General study of multipactor between curved metal surfaces," *IEEE Transactions on Plasma Science*, vol. 42, no. 3, pp. 721–728, Mar. 2014.

[18] R. E. Collin, *Foundations for Microwave Engineering*. McGraw Hill, 1992.

[19] R. Levy, "Inhomogeneous stepped-impedance corrugated waveguide low pass filters," in *2005 IEEE MTT-S International Microwave Symposium Digest (IMS)*, Jun. 2005, 4 pp.-.

[20] D. M. Pozar, *Microwave Engineering Fourth Edition*. Wiley, 2011.

[21] J. Bornemann, U. Rosenberg, S. Amari, and R. Vahldieck, "Tolerance analysis of bypass-, cross- and direct-coupled rectangular waveguide band-pass filters," *IEE Proceedings - Microwaves, Antennas and Propagation*, vol. 152, no. 3, pp. 167–170, Jun. 2005.

[22] F. Teberio, A. Gomez-Torrent, I. Arregui, J. M. Percaz, I. Arnedo, M. Chudzik, T. Lopetegi, and M. A. G. Laso, "Sensitivity analysis of a 3-d printed low-cost compact waveguide low-pass filter," in *2016 46th European Microwave Conference (EuMC)*, Oct. 2016, pp. 249–252.

[23] ESA, *ECSS Space engineering, multipactor design, and test*. Noordwijk, The Neederlands: ESA Publications Division, Apr. 2000, vol. ECSS-E-20-01.

[24] A. Al-Mudhafar, J. Puech, C. Miquel-Espanya, D. Raboso, H. Hartnagel, and E. Consortium, "EVEREST simulation campaign results on multipactor effect using CST particle studioTM," in *2014 8th European Conference on Antennas and Propagation (EuCAP)*, Apr. 2014, pp. 1464–1468.

[25] K.-L. Wu and G. McDonald, "Coping with hidden spurious harmonic modes in the design of low pass corrugated waveguide filters," *Microwave Journal*, vol. 44, no. 11, pp. 180–183, Nov. 2001.

CHAPTER 5

COMPACT EASY-TO-FABRICATE HIGH-POWER HARMONIC LPFs

In this Chapter, a novel fully-customized technique for the design of compact high-power waveguide LPFs with easy manufacturability, all-higher order mode suppression, and wide stopband is presented [1]–[7]. Firstly, the background of rectangular-shape filters is reviewed and their application defined. After that, the design procedure is exhaustively explained and its free parameters analyzed. Then, in order to assess the versatility of the proposed design procedure, four different examples are shown, discussed, and compared with their corresponding classical counterparts. The proposed devices and the classical structures have been compared in three different satellite applications: the output LPF for satellite payloads (as in Chapter 4, where power handling is crucial), a LPF for a Ka-band multi-beam payloads (where high-power but also compactness are key aspects), and high-performance diplexers for Ku-Ka-band satellite applications.
It is important to note that these devices were developed within the framework of different projects with the European Space Agency and TESAT Spacecom GmbH [8], [9]. The high-power tests were carried out at the ESA-VSC High-Power Laboratory.

5.1 Background

As it was introduced in Chapter 4, modern satellite payloads are becoming more demanding in terms of high-power handling capabilities in response to the growing need of higher traffic capabilities. This need is transformed into an increasing number of communication channels and still increasing power-level per channel [10], [11]. Indeed, it compromises the OMUX in a classical broadcast communication payload, and more precisely, the output LPF, which must withstand the combined power of all channels. Furthermore, other payload configurations, such as new multi-beam payloads, need high-power LPFs as well. In current Ka-band multi-beam satellite payloads, the four color scenario is the best compromise between system capacity and performance [12], [13] (see Figure 5.1). This means that two different frequency sub-bands and two orthogonal polarizations are used. Therefore, a single Traveling-Wave-Tube (TWT) amplifier is shared by two beams in order to reduce the number of high-power amplifiers embarked on the satellite (see Figure 5.2). This amplifier works in the non-linear regime, since it increases the available output power and the efficiency. In order to reject the intrinsic spurious harmonics of the non-linear operation, high-power LPFs which feature low-insertion loss must be employed in the transmission path of the payload [14]. Moreover, these LPFs must ensure a high attenuation over the reception band. As a major drawback, in large multi-beam satellites, up to hundreds of waveguide diplexers and LPFs must be used to accomplish different functions (e.g. frequency combination, splitting, and antenna sharing). A solution for the high-power LPF is based on classical corrugated LPFs or bulky waffle-iron approaches [15]. The current trend in the space sector is to develop very compact high-power LPFs in order to minimize the mass, volume, and cost of the payload [16]. Moreover, the filters must behave well in the real multi-carrier scenario and, due to the position of this kind of LPFs in the case of frequency separation (see Figure 5.2), where each sub-band is reflected by the diplexer-channels, the filters need to withstand the power of the direct and reflected signals.

Over the last years, some techniques based on quarter-wave rectangular stubs have appeared in the literature to achieve low-pass frequency responses. In [17], assembling plates with rectangular apertures of different dimensions in a sandwich configuration was proposed for a narrow rejected bandwidth. In this technique, both the length of the apertures and the length between the apertures are design parameters. This technique was surpassed by [18], where Levy introduced the design of low-pass devices by means of quarter-wave spaced stubs of specific impedances based on the method described in [19] for wider stopbands (but still limited) in comparison with the previous technique proposed by Rhodes [17]. As in the aforementioned case, the length of the stubs and the length between the stubs (in the propagation direction) are design parameters, and very small stub lengths can appear in the design which could cause machining problems if computer-controlled milling (CCM) is assumed as the fabrication technique.

For the classical waffle-iron LPF, the first improvements in terms of wider passbands, fractional bandwidths, and higher-power handling capability were reported in [20], [21]. Recently, a great improvement in EM simulators has taken place, allow-

ing an accuracy simulation of the frequency response within reasonable time [22], [23]. Lately, a waffle-iron filter with oblique boss pattern has been proposed [24]. In spite of higher-order mode suppression, waffle-iron filters are susceptible to the generation of spurious spikes in the passband, roll-off and stopband due to the excitation of waveguide modes not considered by established design methods. Moreover, the minimum mechanical gap in the waffle-iron filters is directly connected with the maximum frequency of the fundamental mode stopband. Thus, if the maximum frequency to be rejected is high, the E-plane mechanical gap will be small and, therefore, high-power operation will not be allowed.

In Chapter 4, some alternatives to the classical E-plane corrugated filter and the waffle-iron filter were proposed for very wide rejected bands and high-power applications [25]–[28]. These filters are based on E-plane stubs following a smooth (sinusoidal-like) profile which are used to maximize the high-power behavior of

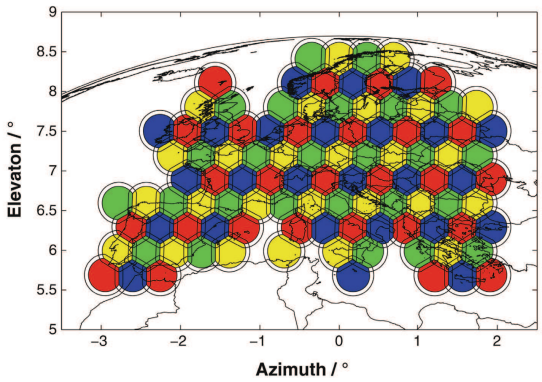

Figure 5.1: European multi-beam coverage [12].

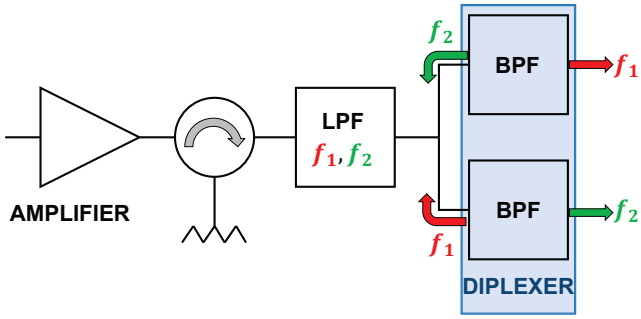

Figure 5.2: Position of the LPF in the multi-beam satellite application.

the filter [29], unfortunately making the manufacturing by CCM more complicated. Moreover, long windowed sections at the input and output ports are employed to achieve the matching of the filter, affecting the final size and consequently the insertion loss.

A waveguide diplexer is another application where waveguide LPFs can be easily found. It is a component for either splitting a broad frequency band into two narrower bands or combining two frequency bands into one broader frequency range. Waveguide diplexers have been used for many years in multi-service and multi-band communications systems. For instance, in satellite applications, the diplexer is an essential component to achieve the isolation between the transmission equipment and the sensitive receiver, which share a common antenna (for a notable reduction of the overall size and volume) [30].

High-performance diplexers are those whose inherent requirements demand overall bandwidths much larger than 20% and operation passbands larger than 5% [31]. A direct branching approach is usually employed to build the three-port junction [32]. Specifically, one port is dedicated to the common interface and the other two to the filters which will accomplish the required passbands. Most of published diplexers are based on bandpass filters using either inductive or capacitive irises [33], [34], or metal inserts [35], [36]. However, large overall bandwidths and, more precisely, broadband filters, discourage the use of this kind of filters due to the high orders required, that will not lead to a compact size and low insertion loss solution (in particular for the transmission band).

As an alternative to the BPF in the transmission band, the classical approach to design a low-pass broadband filter is the corrugated filter [37]. Nevertheless, if the overall bandwidth covers high above the cutoff frequency of the fundamental mode, the higher-order modes may be in propagation and the suppression of these spurious modes will be required. Current solutions for this problem include the evanescent-mode filters [38] and the classical waffle-iron filter [39]. Indeed, classical waffle-iron filters do not exhibit spurious mode responses but this kind of filters can be too long. An alternative to the waffle-iron filter is a classical corrugated filter with a width reduction which shifts up in frequency the higher-order modes [40]. However, it will also be too long to be used in a compact diplexer.

In this Chapter, the excellent higher-power threshold levels and wide stopbands achieved with the filters in Chapter 4 are now accomplished with novel LPF with easy manufacturability. In this case, the attenuation of the fundamental TE_{10} mode in the stopband is achieved by means of several easy-to-manufacture step-shaped bandstop elements separated by very short waveguide sections. Unlike [17] or [18], in this case the length in the propagation z-axis (i. e. the impedance) of the bandstop elements is a free parameter. In fact, it can be modified along the structure to achieve a very high multipactor threshold, as it will be demonstrated. Moreover, the length between them is not one quarter-wave but it can be made nominally zero or, in practice, as short as the fabrication technique permits. This fact yields very compact devices and it is beneficial for their power-handling capability too [41]. Additionally, the E-plane mechanical gap is also a free-parameter in the design technique, and it can be precisely defined to, simultaneously, ensure higher-order non-TE_{n0} mode suppres-

sion and high-power behavior of the filter. In order to validate the control of these free parameters, an in-depth examination and a comprehensive discussion will be presented through different examples in Section 5.4. The matching of the filter is accomplished by very short input/output networks based on a few stubs whose heights are optimized following classical mathematical methods implemented in commercial tools. These matching networks allow good levels of filter in-band return loss and contribute also to a remarkable filter compactness unlike previously proposed solutions, where the matching is accomplished by means of long windowed sections or classical tapers. Moreover, all higher-order mode suppression is obtained by a filter width modification along the propagation direction which rejects the higher-order TE_{n0} modes. Finally, four design examples are shown, discussed, and the measured frequency responses of the prototypes manufactured in two halves by CCM in aluminum and then silver-plated are presented. The high-power behavior of all examples are also discussed.

5.2 Objective

The main objectives of this Chapter are the following:

- To demonstrate that the novel technique can be utilized to design high-power output LPF for classical broadcast communication payloads, with the same or higher-power threshold levels in comparison with the technique in Chapter 4.
- To demonstrate the feasibility of the novel step-shaped LPFs in multi-beam payloads, where size and high-power are key design issues.
- To show the application of the proposed LPFs for the design of compact high-performance diplexers.
- To reduce costs in terms of manufacturing.

5.3 Design Method

The design procedure of the novel filter is divided into three subsections: the block filter and the input and output matching networks. The block filter is the main part of the filter and achieves the required rejected band and the suppression of the non-TE_{n0} modes. The matching networks accomplish the intended return loss of the filter. Finally, the suppression of the TE_{n0} modes is achieved by means of a filter width modification.

5.3.1 Block Filter

The design of the block filter (Figure 5.3(a)) begins by fixing the heights of the highest (h_{max}) and the shortest (h_{min}) bandstop elements in the filter to reject the

lowest (f_{min}) and the highest (f_{max}) frequency of the stopband, respectively. The height (in the y-axis) of the step-shaped bandstop elements is around $\lambda_g/4$, being λ_g the guide wavelength of the fundamental TE_{10} mode at the frequency to be rejected. Several bandstop elements with intermediate heights, h, are used between h_{max} and h_{min} to reject the intermediate frequencies between f_{min} and f_{max}. One of the most interesting advantages of this design technique is that if a reduced extra number of bandstop elements with the largest height, n_{hmax}, are included, it is very easy to achieve very steep slopes between the pass- and the rejected band with a substantial size reduction in comparison with the classical solutions, in which a large number of sections would be necessary.

The design process continues by setting the filter E-plane mechanical gap which partially controls the high-power behavior of the filter and ensures the suppression of the non-TE_{n0} modes. Unlike [18], the minimum mechanical gap is also a free variable in the technique presented in this Chapter, given a particular TE_{10}-mode response. In Figure 5.3(a), the gap is not constant but evolves linearly from b_{gmin} to b_{gmax}. As it is well known, the first non-TE_{n0} mode to appear is the TE_{01} mode, whose cutoff frequency, $f_{c,TE_{01}}$, is c / $2b_{gap}$, being b_{gap} the value of the minimal mechanical gap of the filter and c = $1/\sqrt{(\epsilon_0\mu_0)}$. Therefore, b_{gmin} must be small enough in order to ensure $f_{c,TE_{01}} > f_{max}$ and, hence, guarantee no higher-order non-TE_{n0}-mode propagation in the filter stopband. On the other hand, large values of the E-plane mechanical gap are desirable to increase the high-power handling capability of the filter [42] and get a low insertion loss too [43]. As it will be explained in Section 5.4.1, it has been observed that the maximum electric field levels inside the structures (where multipactor takes place) occur in the region where the highest bandstop elements are placed. Therefore, it is possible to achieve low insertion loss and high power-handling in the filter if a large value, b_{gmax}, is set between the highest stubs.

Finally, the waveguide length between the bandstop elements, l_{gap}, and the length of the bandstop elements, l_i, (which are free parameters) are fixed. Unlike other proposals, such as the classical corrugated filter, waffle-iron filters, or the device proposed in [18], where the length and separation between the corrugations are design parameters, in the filters presented in this Chapter, only the height of the stubs, h, is the critical variable since the passband will be determined by the matching networks (see Section 5.3.2). In particular, the length between bandstop elements, l_{gap}, has no influence on the filter frequency response and, in the proposed structures, is not one quarter-wave but it can be made nominally zero or, in practice, as short as the fabrication technique permits as it will be demonstrated in Section 5.4.2. This will be advantageous for the high-power handling (since the critical area with minimum mechanical gap is reduced) [44] and will also allow very compact structures. On the other hand, the length of the step-shaped bandstop elements, l_i, must be wide enough to (i) minimize the influence of the machining drill radius (i. e. rounded corners effect) on the frequency response and (ii) ensure high-power behavior; and, at the same time, short enough to allow compact structures. Therefore, different values of the length of the bandstop elements, l_i, could be defined to obtain the optimal structure for the required specifications. As it was previously mentioned, the maxi-

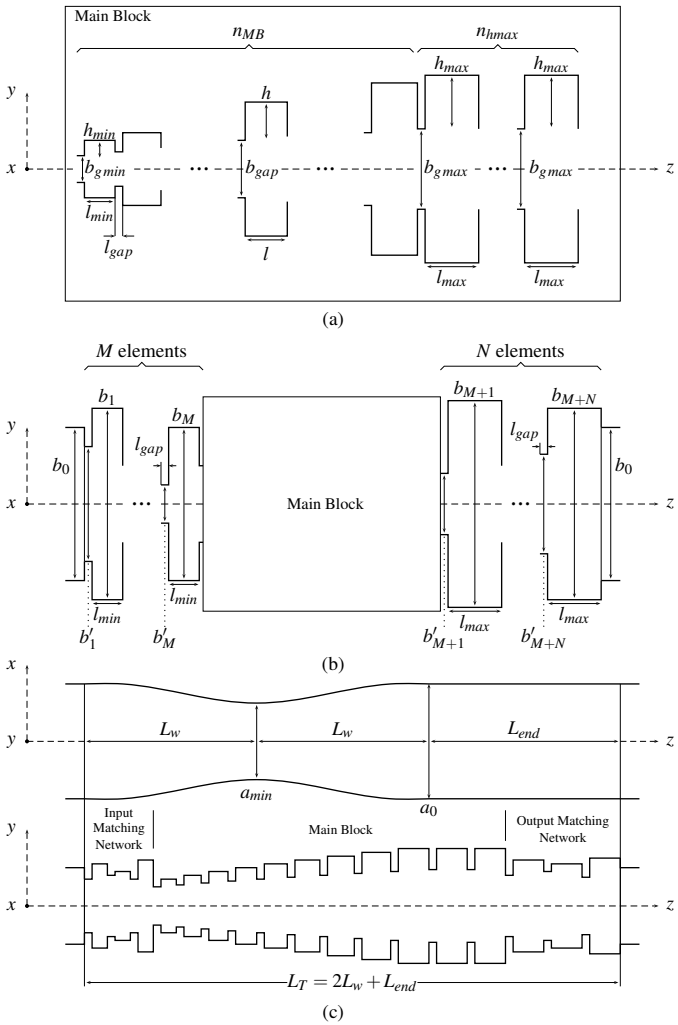

Figure 5.3: Schematics of the design procedure and main physical parameters: (a) block filter, (b) matching networks, and (c) final filter profile.

mum EM fields take place in the area of influence of the highest bandstop elements. As it will be demonstrated in Section 5.4.2 and Section 5.4.3, a significant EM field component may appear between the waveguide walls which compose each bandstop element (in the z-axis) and, therefore, it is possible to increase the power handling in the filter if a large value, l_{max}, is set in the highest bandstop elements. On the other hand, the EM fields are minimum in the region of the shortest bandstop elements and, hence, a short value, l_{min}, can be set for these elements in order to maintain a compact device. In summary, as it will be demonstrated below, a linear chirping applied to the length of the bandstop elements following equation (5.1), between l_{min} and l_{max}, will increase dramatically the multipactor threshold level. Although the idea is indeed very simple, the relevance of this strategy will be very important since it will allow power levels so high that the costly multipactor testing of filters in multi-carrier scenarios could be avoided.

$$l_i = \frac{l_{max} - l_{min}}{n_{MB}} \cdot (i-1) + l_{min} \qquad i = 1, 2, ..., n_{MB} \qquad (5.1)$$

5.3.2 Matching Networks

Using the technique described in the previous paragraph, it is feasible to easily design filters that have the intended stopband characteristics for the fundamental TE_{10} mode and the higher-order non-TE_{n0} modes. However, two matching networks must be still added at the input and output of the block filter (Figure 5.3(b)), the objective being twofold: i) to match the input/output dimensions of the block filter to the standard waveguide port height, b_0, and ii) to control the intended return loss in the passband. Therefore, the final filter realization consists of the block filter designed in Section 5.3.A adding M and N stubs at its input and output port, respectively. In Chapter 4, long windowed sections were employed to fulfill the objectives i) and ii) above. In [18], classical tapers were used to provide the device with the standard waveguide ports (objective i)) and specific values of the impedances of the quarter-wave spaced stubs had to be implemented to obtain the required return loss (objective ii)). In this case a different strategy is followed. Each one of the stubs in the matching networks is defined by its height, b_i, and its length. Moreover, all of them are separated by short waveguide sections (as it occurs in the block filter), each of which is defined again by its height, b'_i, and its length. For simplicity, the length of the stubs and their separation in the input/output matching networks will have the same values as in the block filter, l (l_{min} or l_{max}) and l_{gap} respectively, and will not be variables in the design. An optimization procedure on the matching network dimensions ensures the fulfillment of the demanded return loss. The only variables to be optimized will be the heights of the stubs, b_i, and the heights of the short waveguide sections between them, b'_i. The initial guess for b_i is a linear interpolation between the shortest (2 h_{min} + b_{gmin}) or the largest (2 h_{max} + b_{gmax}) step-shaped element of the block filter and the standard port height at each side of the waveguide, b_0, and for b'_i the initial guess is a linear interpolation between the minimum E-plane mechanical gap, b_{gap} (b_{gmin} or b_{gmax}), and the standard port height. Finally, an op-

Table 5.1: Frequency specifications.

Passband	Return loss	Stopband	Attenuation
10.7 - 12.7 GHz	20 dB	13.75 - 38.1 GHz	60 dB

timization process is run using a commercial optimizer (implemented in FEST3D in this case) and a device whose frequency response fulfils the return loss specifications with certain b_i and b_i' values is achieved as required.

5.3.3 Higher-order TE_{n0}-mode Suppression

In order to design a filter with all higher-order mode suppression, it only remains the suppression of the higher-order TE_{n0} modes. One way to achieve this goal consists of a smooth x-axis width tapering applied to the whole device [45] (see Figure 5.3(c)), so that the passbands of the higher-order TE_{n0} modes in one section are forced to coincide with the frequencies where these modes are rejected by other sections of the filter. The tapering starts from the port width, a_0, and down to the minimum width of the device, a_{min} (along L_w) and, again, returning to the port width, a_0. The value a_{min} has to be carefully chosen, avoiding the cutoff frequency of the fundamental TE_{10} mode to surpass the minimum frequency of the specifications. The length of the window, L_w, must be long enough to guarantee the TE_{n0}-mode suppression, and short enough to minimize the influence of the window on the slope between the pass- and the rejected band (defined by the h_{max} elements). Therefore, a section with constant width a_0 and length L_{end} is kept at the end of the filter.

5.4 Analysis of the Design Free Parameters

For a certain TE_{10} frequency response, there are three free parameters in the design method described above:

- the E-plane mechanical gap, b_{gap};
- the waveguide length between the bandstop elements, l_{gap};
- the length of the bandstop elements, l.

In this Section, the influence of these parameters over the insertion loss, size, and the high-power behavior will be shown and discussed through several examples.

Firstly, a WR75 device has been designed fulfilling the frequency specifications defined in Table 5.1 to provide a baseline for the comparisons.

The filter achieves the suppression of the fundamental TE_{10} and all the higher-order (TE_{n0} and non-TE_{n0}) modes in the stopband. For this assessment, in order to do a fair comparison, the total number of elements, both for the main block and for the matching networks, has been intentionally fixed identical in the step-shaped filter

Table 5.2: Final dimensions of the baseline filter.

Matching Networks	M = 12 and N = 13		
Main Block	h_{min} = 0.4 mm	h_{max} = 6.15 mm	n_{hmax} = 5
	b_{gmin} = 3 mm	b_{gmax} = 3 mm	n_{MB} = 32
	l_{min} = 1.91 mm	l_{max} = 1.91 mm	l_{gap} = 1.91 mm
Width reduction	a_{min} = 15 mm	L_w = 91 mm	L_{end} = 36 mm

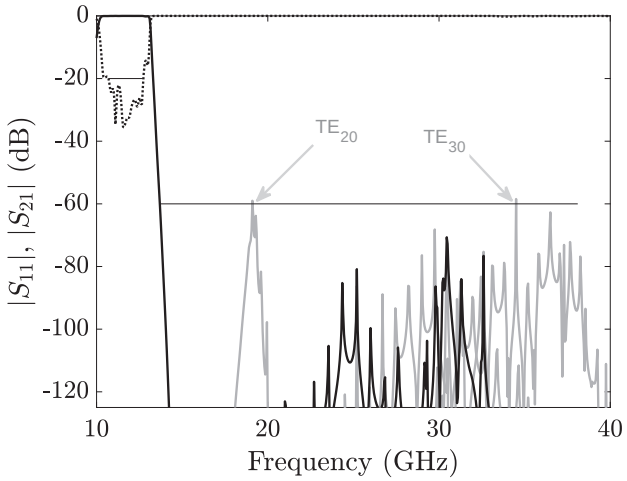

Figure 5.4: FEST3D simulated frequency response for the TE_{10} mode in the baseline filter with constant 3 mm-gap (black line) and for the higher-order modes (grey lines) (rest of higher-order modes not shown are kept below -130 dB). $|S_{11}|$ in dotted line and $|S_{21}|$ in solid line. Frequency specifications in dashed line.

as in [28]. Besides, l, and l_{gap}, have been set both equal to 1.91 mm, and the E-plane mechanical gap has been fixed constant and equal to 3 mm as in [28]. This choice of values does not take full advantage of the benefits of the presence of free parameters in the technique. However, the frequency response of this device and [28] coincide. The final dimensions of the filter are shown in Table 5.2 and its simulated frequency response in Figure 5.4, showing that the required specifications are fulfilled.

In order to analyze the high-power behavior of the filter, the multipactor phenomenon has been studied, which can cause the breakdown due to high EM fields in vacuum conditions in space applications [46]. Aiming at enhancing the high-power behavior of the filter, it is indispensable to know accurately the EM field distribution inside the device. The maximum EM fields of the step-shaped filter are obtained at 12.7 GHz, which is the upper passband edge frequency. As it can be seen in Figure 5.5, this kind of filters show a quite interesting field distribution inside the structure. As it can be observed, the maximum fields are placed in the highest step-shaped

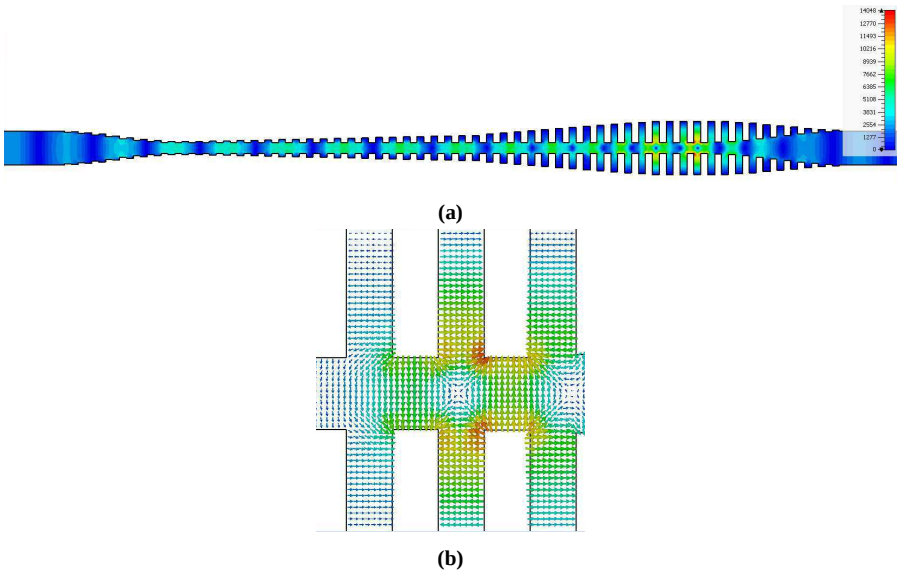

Figure 5.5: E-field distribution (V/m) simulated using CST MWS at 12.7 GHz for the baseline filter in (a) the whole structure and (b) in the highest bandstop elements area.

bandstop elements region. Specifically, as it is illustrated in Figure 5.5, two different field directions can be observed, which will affect to the free-electron trajectories and, therefore, to the high-power multipactor threshold. The first one is the field component placed in the waveguide section between two bandstop elements, and the second one is the field component placed inside the bandstop elements. Therefore, enhancing both critical sections should provide better high-power behavior. Specifically, if the designer desires to prevent the multipactor phenomenon in the E-plane mechanical gap, the simplest way to do this is to enlarge it [42] (by means of larger values of b_{gap}, see 5.4.1) and/or decrease the length of the waveguide section between the bandstop elements [41] (through shorter values of l_{gap}, see 5.4.2). In the same way, if wider bandstop elements (l_i is increased) are fixed, and assuming that b_{gap} is large enough, the high-power behavior of the filter will be enhanced (see 5.4.3). All of these solutions are possible since all these parameters, b_{gap}, l_{gap} and l_i, are free variables in the design method presented in this Chapter, unlike classical filters or other methods proposed in the literature.

5.4.1 Influence of the E-plane Mechanical Gap, b_{gap}, over the High-Power Behavior and the Insertion Loss

When the higher-order non-TE_{n0} mode suppression is a requirement, it is necessary to guarantee that the mode with the lowest cutoff frequency (TE_{01} mode in the examples of this Chapter) is not able to propagate in the section with minimum E-plane mechanical gap, b_{gmin}. In fact, as it has been demonstrated in Figure 5.4, with an E-

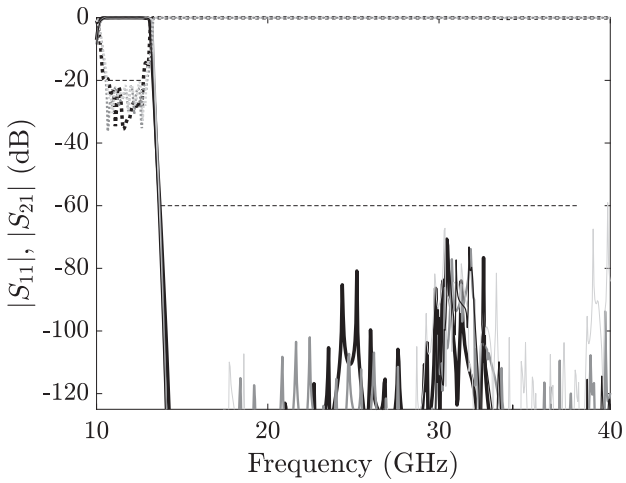

Figure 5.6: FEST3D simulated frequency response for the TE_{10} mode in the step-shaped filter with: constant 3 mm-gap (thick black line), gap variation between 3 – 4 mm (thin black line), gap variation between 3 – 5 mm (thick grey line) and gap variation between 3 – 6 mm (thin grey line). $|S_{11}|$ in dotted line and $|S_{21}|$ in solid line. Frequency specifications in dashed line.

plane mechanical gap equal to 3 mm the TE_{01}-mode cutoff frequency will be shifted up to the third harmonic for a filter fulfilling the specifications defined in Table 5.1 for the fundamental mode.

As pointed out earlier, the maximum EM fields at the critical frequency are placed between the highest step-shaped bandstop elements. If the high-power behavior of the filter is required to be increased, b_{gmax} can be adjusted between the highest bandstop elements. Therefore, higher-order non TE_{n0}-mode suppression and high-power behavior can be achieved simultaneously if a linear variation of the E-plane mechanical gap is performed. Additionally, it will be also advantageous for having lower insertion loss [43].

For the specifications defined in Table 5.1, three step-shaped filters following the technique described in Section 5.3 have been also designed using a WR75 port standard. The only difference between them and the baseline filter (constant 3 mm-gap) is the applied linear variation of the E-plane mechanical gap (see Figure 5.3(a)) between b_{gmin} = 3 and b_{gmax} = 4, 5, and 6 mm. As it is depicted in Figure 5.6, all filters show an excellent attenuation level and in-band return loss, demonstrating that the E-plane mechanical gap can be changed without altering the TE_{10} frequency response. Nevertheless, as expected, the high-power simulation of the filters shows that the input power threshold level increases with the size of the E-plane mechanical gap (see Table III). In fact, in opposition to the baseline filter, the EM field distribution mainly oscillates between the bandstop element walls in the propagation direction (z-axis) and becomes quite weaker in the waveguide between the bandstop elements (see Figure 5.5 and Figure 5.7).

Table 5.3: Comparison of the high-power behavior of the filters with different gap variation.

E-plane mechanical gap	Power threshold (kW) (SPARK3D)
Smooth profile filter (Chapter 4, [28])	7.5
Constant 3 mm-gap (baseline filter)	5.5
Gap variation between 3 – 4 mm	6.6
Gap variation between 3 – 5 mm	7.0
Gap variation between 3 – 6 mm	8.0

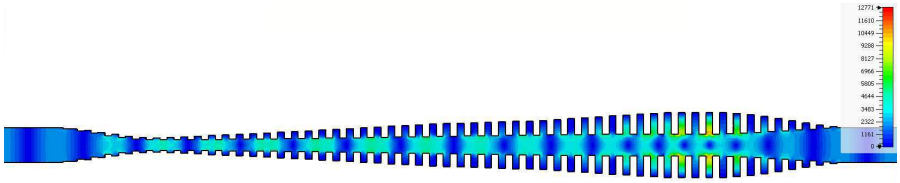

(a)

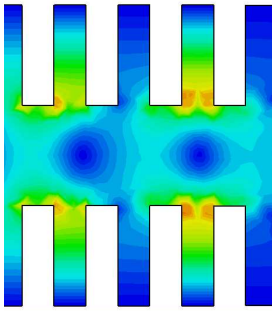

(b)

Figure 5.7: E-field distribution (V/m) simulated with CST MWS at 12.7 GHz for the step-shaped filter with: (a) gap variation between 3 – 6 mm and l_{gap} = 1.91 mm and l = 1.91 mm. (a) Complete structure. (b) Highest bandstop elements area.

Additionally, this minimum mechanical gap increases along the propagation direction (z-axis) produces a slight improvement in the insertion loss of the filter [43]. For instance, the baseline constant 3-mm gap filter shows an in-band insertion loss better than 0.25 dB (vs. 0.3 dB [28]), while the in-band insertion loss of the filter with a gap variation between 3 to 6 mm is kept below 0.22 dB.

5.4.2 Influence of the Waveguide Length between the Bandstop Elements, l_{gap}, over the High-Power Behavior and the Size

As it is well known and it has been extensively studied in the literature [41], [44], the multipactor discharge threshold increases when the length of the iris is decreased. This is translated, in the novel filters proposed in this Chapter, into a reduction of the

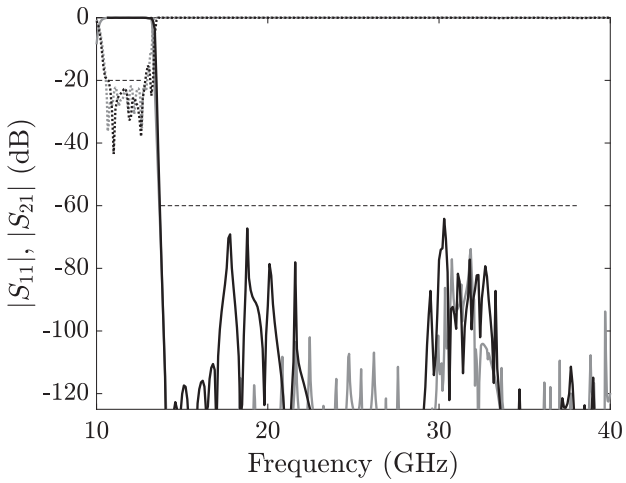

Figure 5.8: FEST3D simulated frequency response for the TE_{10} mode in the step-shaped filter with gap variation between 3 – 6 mm and: l_{gap} = 1.91 mm (grey line) or l_{gap} = 0.825 mm (black line). S_{11} in dotted line and S_{21} in solid line. Frequency specifications in dashed line.

waveguide length between the bandstop elements. Moreover, this reduction yields to more compact structures. In fact, the waveguide length between the bandstop elements has no influence in the TE_{10}-mode frequency response of the step-shaped filter and it can be ideally reduced to zero although, in practice, it must has a real value which will be determined by the fabrication technique. In this case, l_{gap} can be fixed to 0.825 mm since this is the minimum value permitted in the fabrication facilities utilized to fabricate the devices developed in this Chapter (to obtain a stiff device using CCM).

If a novel filter identical to the previous one with gap variation between 3 to 6 mm but now with l_{gap} equal to 0.825 mm is redesigned, the specifications in Table 5.1 are perfectly fulfilled as can be seen in Figure 5.8. The total length of the filter L is equal to 156 mm, which implies a reduction of 25% in size. Moreover, this filter shows a slight improvement in the insertion loss (0.21 dB). The power handling capability is not improved as much as it initially could have guessed though (P_{thr} = 8.2 kW). This is due to the fact that the maximum EM field component oscillates mainly between the waveguide walls of the bandstop elements in the propagation direction (z-axis) (as can be observed in Figure 5.9). This leads to the conclusion that, if a higher handling capability is desired, the bandstop elements length, l, must be properly adjusted.

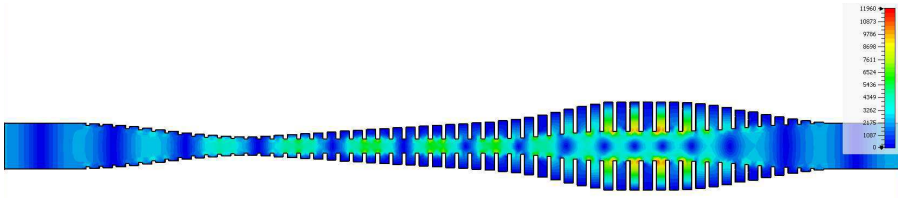

(a)

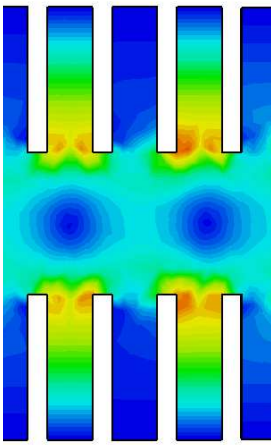

(b)

Figure 5.9: E-field distribution (V/m) simulated with CST MWS at 12.7 GHz for the step-shaped filter with: (a) gap variation between 3 – 6 mm and l_{gap} = 0.825 mm and l = 1.91 mm. (a) Complete structure. (b) Highest bandstop elements area.

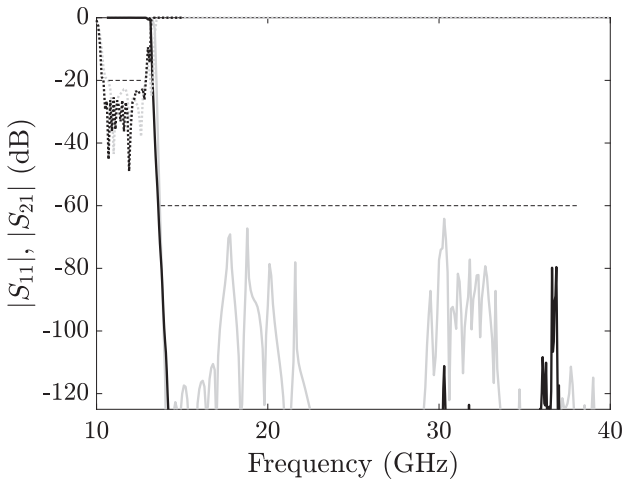

Figure 5.10: FEST3D simulated frequency response for the TE_{10} mode in the step-shaped filter with: gap variation between 3 – 6 mm, l_{gap} = 0.825 mm and: l = 1.91 mm (grey line) or l = 3.82 mm (black line). S_{11} in dotted line and S_{21} in solid line. Frequency specifications in dashed line.

5.4.3 Influence of the Bandstop Elements Length, l, over the High-Power Behavior

As it was previously shown, if the E-plane mechanical gap is large enough, the EM field distribution between the walls of the bandstop elements in the propagation direction (z-axis) is the most significant component for the estimation of the multipactor threshold. Hence, the bandstop element length should be fixed appropriately if a higher-power behavior is necessary. Indeed, l is a free parameter, and could be increased without negatively affecting to the frequency response.

In order to dissect the most appropriate l values, four step-shaped filters have been designed with the same parameters as the example proposed in Subsection 5.4.2 (E-plane mechanical gap variation between 3 and 6 mm and l_{gap} equal to 0.825 mm) with different values of l (l = 2.39, 2.87, 3.35, and 3.82 mm). As it is demonstrated in Figure 5.10 as an example, the filter with largest l fulfills perfectly the frequency specifications defined in Table 5.1. Moreover, as it can be observed in Table IV, the multipactor threshold is highly increased in the critical area (see also 5.11), making it high enough to reach power levels which will avoid future multipactor tests in multicarrier systems. In a practical case, in order to design a filter with minimum total length and highest power-handling capability, the length of the bandstop elements is not constant but linearly chirped between l_{min} and l_{max}, so that l_{min} is the length of the h_{min}-height stubs and l_{max} is the length of the h_{max}-height stubs in the critical region (this will be used in a design example in 5.4).

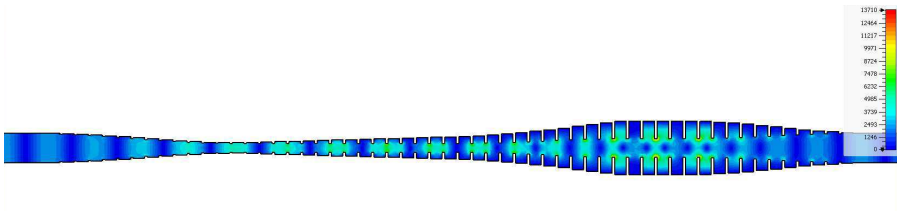

(a)

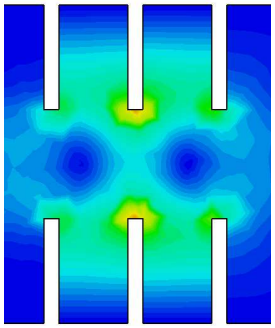

(b)

Figure 5.11: E-field distribution (V/m) simulated with CST MWS at 12.7 GHz for the step-shaped filter with: (a) gap variation between 3 – 6 mm and l_{gap} = 0.825 mm and l = 3.82 mm. (a) Complete structure. (b) Highest bandstop elements area.

Table 5.4: Comparison of the high-power behavior of the filters with different bandstop element length.

l (mm)	Power threshold (kW) (SPARK3D)
1.91 (previous Subsection)	8.2 kW
2.39	11.8
2.87	16
3.35	$>$ 100
3.82	$>$ 100

5.5 CCM Fabrication Issues

For a low-cost manufacturing, it is usually necessary during the design phase to take into account the rounding of the corners typically present in classical milling procedures. Indeed, the novel high-power LPFs with smooth profile presented in Chapter 4 need a slight adjustment in the height of the bandstop elements which reject the minimum frequency of the stopband to compensate the frequency shift of the frequency response. However, in the novel high-power LPFs with easy manufacturability presented in this Chapter, any correction must be done in the physical parameters of the filters when the rounded of the corners is performed (for typical tool radius between 0.5 mm and 1 mm). This is because the filters proposed in this Chapter are robust enough not to be affected by the rounded corners. This speeds up the design procedure and optimization, thus implying lower costs and higher production yields.

5.6 Fabrication Tolerance Considerations

The practical realization of the LPFs presented in this Chapter is not obvious due to the inherent manufacturing tolerances of the CCM fabrication procedure [4]. Therefore, the sensitivity analysis due to manufacturing errors is much needed to foresee the effect of the fabrication method on the final design frequency performance. The purpose of this Section is to analyse, compare, and discuss the proposed LPF solution with respect to the fabrication tolerances with its classical counterparts in order to demonstrate that the technique in this Chapter can be used to manufacture very low-cost prototypes. There are multiple studies in the literature on how to perform a sensitivity analysis in waveguide filters [47] and components [48]. Indeed, Monte Carlo analysis [49] or analogous statistical techniques [50] are used to demonstrate the robustness of the devices. The sensitivity analysis utilized in this Section is based on an automatic study of the effects that deviations in the physical dimensions of the filter have on the frequency response. These include variations in the height, length, and width (variables in the analysis) of the waveguide sections which compose each one of the structures. By doing so, it is considered all different alternatives present in a real fabrication procedure (cutting plane, growth direction, etc.). The different physical dimensions are randomly generated by a Gaussian probability density function with a standard deviation equal to 0,05 ($\pm$ 120 μm). This poor value of tolerances has been used just to check in a very worst-case the robustness of the novel LPFs for manufacturing tolerances and compare it with the behavior of its classical counterpart. Finally, one hundred iterations have been performed to obtain the predicted manufacturing yield of each filter.

Two waveguide LPFs designed following two different methods will be considered in this Section. The first design will be a classical waffle-iron filter (Chapter 3, [39]), and the second device will be a novel compact LPF following the design technique described in this Chapter. Both filters will fulfill the following frequency specifications: a passband between 10.8 and 12.8 GHz, with an in-band return loss better than 20 dB, and a stopband between 15.5 and 20 GHz with an attenuation level

Table 5.5: Final dimensions of the novel filter designed in Section 5.6.

Matching Networks	M = 2 and N = 2		
Main Block	h_{min} = 5.6 mm	h_{max} = 5.6 mm	n_{hmax} = 4
	b_{gmin} = 3 mm	b_{gmax} = 3 mm	n_{MB} = 4
	l_{min} = 1.91 mm	l_{max} = 1.91 mm	l_{gap} = 1.91 mm
Width reduction	a_{min} = 14.5 mm	L_w = 9.975 mm	L_{end} = 6.65 mm

better than 60 dB. WR-75 standard ports will be used at the input and output of the filters.

Following the technique described in Chapter 3, [39], a classical waffle-iron filter has been designed fulfilling the aforementioned frequency specifications (see Figure 5.12(a)). The filter has order 7 and the matching of the filter to the standard WR-75 ports has been achieved with two transformers of two waveguide sections respectively, at the input and output ports of the filter. The final device shows a total length equal to 77.3 mm. The sensitivity analysis of the filter has been performed considering the aforementioned variables. As it can be observed in Figure 5.12, curves show a large dispersion, in particular for the in-band return loss (Figure 5.12(b)), and frequency specifications are not easily fulfilled. In fact, the predicted manufacturing yield is equal to 12% (simulations were run using FEST3D).

A novel filter has been designed according to the technique reported in this Chapter, fulfilling the same specifications as in the previous case. The physical parameters of the filter are given in Table 5.5. As it can be seen in Figure 5.13, the in-band return loss of the filter is better than 20 dB and the stopband shows an attenuation level larger than 60 dB. The total length of the filter is only 33.25 mm. A full sensitivity analysis has been performed to foresee future issues. Now, most of the trials satisfy the frequency specifications, showing a predicted manufacturing yield of 94% (see Figure 5.13).

Although the tolerance analysis performed in this Section covers the entire frequency response of the filter, it is important to note that the stopband of the filter is less sensitive than the in-band return loss performance. Therefore, the significant differences between the predicted manufacturing yields are mainly due to the return loss. The novel compact LPF has the best predicted manufacturing yield and less deviation in the frequency response is observed. The main reason for this is the different geometry of both devices. In the case of the novel filter, the structure is defined by a very simple geometry, based on rectangular bandstop elements separated by very short waveguide sections. However, the multi-ridge structure which defines the waffle-iron filter is more complex, since it includes more critical dimensions, such as the separation between the teeth.

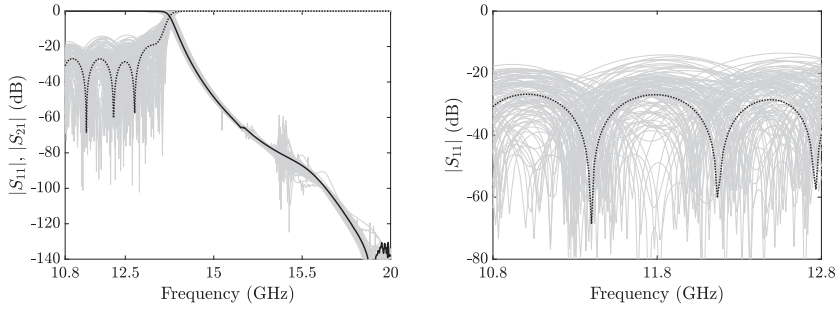

(a) **(b)**

Figure 5.12: Sensitive analysis in the (a) entire frequency response and (b) in-band return loss behavior of the classical waffle-iron filter designed in Section 5.6 varying the physical parameters of the filter. Black line: baseline filter, grey lines: simulation trials. $|S_{11}|$ in dotted line and $|S_{21}|$ in solid line.

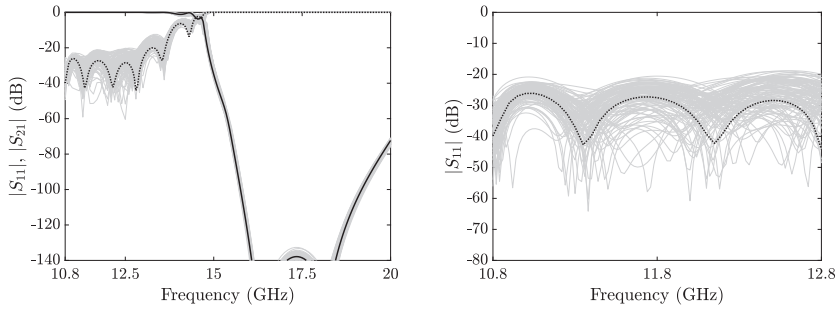

(a) **(b)**

Figure 5.13: Sensitive analysis in the (a) entire frequency response and (b) in-band return loss behavior of the novel filter designed in Section 5.6 varying the physical parameters of the filter. Black line: baseline filter, grey lines: simulation trials. $|S_{11}|$ in dotted line and $|S_{21}|$ in solid line.

Design Examples

According to the design methodologies proposed, four different examples of high-power easy-to-fabricate LPFs will be presented in this Chapter. Firstly, in Section 5.7, the feasibility of designing LPF with the suppression of only the fundamental mode following the technique detailed in Section 5.3, [1] will be demonstrated. The second example (Section 5.8) will fully exploit the free parameters of the proposed technique to obtain a multipactor-free LPF, where all higher-order modes are also suppressed up to the third harmonic [3], [6]. After that, to demonstrate the tailored method presented in this Chapter, a compact high-power LPF for Ka-band multi-beam payloads will be designed in Section 5.9, [2], [7]. The objective in this example will be to obtain a very compact high-power device able to be manufactured in mass-production. Finally, the possibility of including this kind of LPF in high-performance diplexers will be proved in the last example (Section 5.10), [5]. It is important to stress that different prototypes will be fabricated in the examples, obtaining a remarkable accordance between the simulated and the measured results.

5.7 Design Example 1: High-Power Compact Alternative to the Corrugated LPF

As a first example, a novel high-power low-loss compact LPF with the suppression of only the fundamental mode in the stopband following the design procedure described in Section 5.3 has been designed, manufactured, and characterized.

5.7.1 Specifications

The filter features a TE_{10}-mode passband between 10.3 and 12.7 GHz with in-band return loss better than 20 dB and a rejection level better than 60 dB from 13.5 GHz up to 40 GHz. WR75 input/output ports have been used (a_0 = 19.05 mm, b_0 = 9.525 mm).

5.7.2 Design and Simulation

As it is explained in Section 5.3, the method starts by designing the block filter to define the rejected band. l_{gap} is chosen to be 0.825 mm, since this is the minimum separation between bandstop elements that the available fabrication facilities permit. The length of the step-shaped bandstop elements is fixed to $l_{min} = l_{max} = l$ = 3 mm. The heights of the largest and shortest bandstop elements in the filter are h_{max} = 6.6 mm and h_{min} = 2 mm, in order to reject the lowest and highest frequencies in the LPF stopband (the stubs are $\lambda_g/4$ at f_{min} = 13.5 GHz and f_{max} = 40 GHz), respectively. The filter width is kept always constant and equal to the WR75 input/output port width, a_0, along the z-axis. The heights of the largest and shortest bandstop elements have been further refined after a few simulations with FEST3D and the final values are h_{max} = 5.9 mm and h_{min} = 2.25 mm. The intermediate

bandstop element heights are linearly interpolated in the block filter. The stringent slope between the pass- and the stop-band has been accomplished by adding extra bandstop elements with the largest height (n_{hmax} = 5 in this case). Finally, the minimum E-plane mechanical gap, has been fixed to b_{gmin} = b_{gmax} = b_{gap} = 3 mm. An attenuation better than 60 dB is achieved with a total of n_{MB} = 15 bandstop elements, fulfilling the rejection levels required in the stopband.

In order to obtain the demanded passband return loss and the matching between the block filter and the height of the WR75 standard ports, b_0, the design method continues with the synthesis of the matching networks. Three (M = 3) and two (N = 2) stubs have been added as the input and output matching networks, respectively. Both matching networks have l_{gap} = 0.825 mm and l = 3 mm as in the block filter. As it was mentioned, the initial heights, b_i and b'_i, of the stubs in both the input and output matching networks are obtained by using a linear interpolation between b_0 and the block filter. Then, the heights have been optimized with the FEST3D optimizer tool.

The frequency response of the final device (consisting of the block filter and its matching networks) is shown in Figure 5.14 along with the response of the equivalent corrugated waveguide filter designed with the technique in Section 2.3, [37], for the same specifications. Both the novel filter and the classical corrugated filter fulfill the initial specifications. As it can be seen, the in-band return loss is better than 20 dB while the attenuation in the rejected band is higher than 60 dB. However, regarding the size of both solutions, the novel filter is only 85 mm-long while the classical corrugated filter has a total length of 163 mm. Hence, the new device is notably more compact (around 48% of size reduction is achieved in this example). A great advantage of having a more compact structure with a large gap value is that the insertion loss is drastically lower than in the classical corrugated filter when a steep slope and a wide stopband are required. The simulated insertion loss in the proposed filter is better than 0.12 dB (silver conductivity was used) while in the classical E-plane corrugated filter it is below 0.38 dB. Therefore, the novel filter allows steeper slopes with very compact size and lower insertion loss in comparison with the classical corrugated filter. Finally, the E-plane mechanical gap is 3 mm (vs. 0.6 mm in the corrugated filter).

5.7.3 Fabrication and Measurement

A prototype of the filter has been machined in two halves (cut by the H-plane) by CCM (drill radius r = 0.5 mm) in aluminium and then silver-plated (Figure 5.15).

The measurements have been carried out using an Agilent 8722 VNA, proper waveguide-to-coaxial transitions, waveguide tapers, and calibration kits. The measurement results shown in Figure 5.16 confirm an excellent stopband behavior while the return loss is better than 20 dB in the passband, as required. The in-band insertion loss is kept below 0.17 dB in the fabrication of the novel filter (see Figure 5.17). Moreover, a remarkable accordance between the measurement results and the CST MWS simulated frequency response of the filter taking into account rounded corners is also obtained.

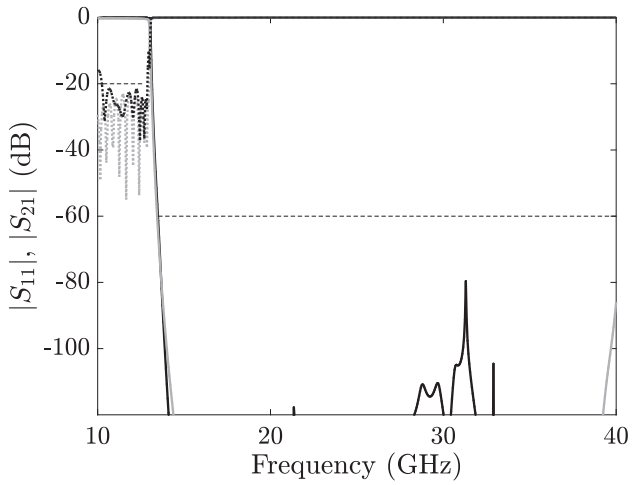

Figure 5.14: FEST3D simulated frequency response of the Chebyshev classical corrugated LPF (grey line) and of the new filter (black line) designed in Section 5.7 for the same frequency specifications. S_{11} in dotted line and S_{21} in solid line. Frequency specifications in dashed line.

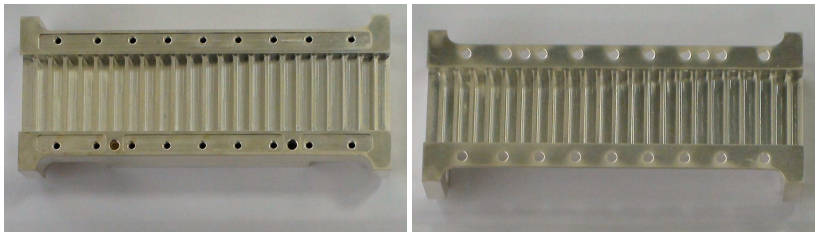

Figure 5.15: Photograph of the unassembled prototype of the novel filter designed in Section 5.7.

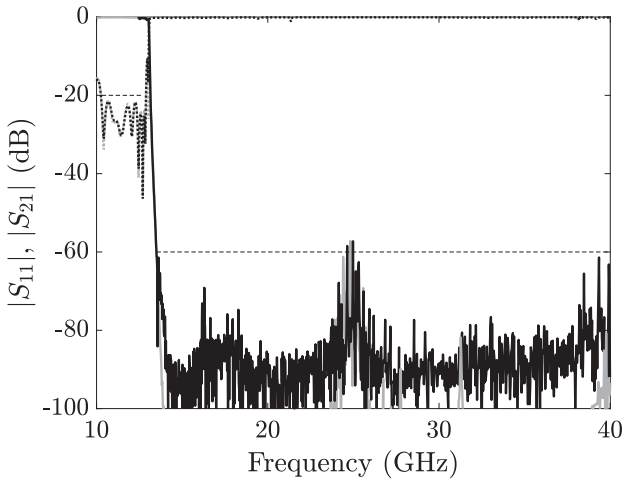

Figure 5.16: Measured (black line) and simulated with CST MWS (grey line) frequency response of the novel filter designed in Section 5.7. S_{11} in dotted line and S_{21} in solid line. Frequency specifications in dashed line.

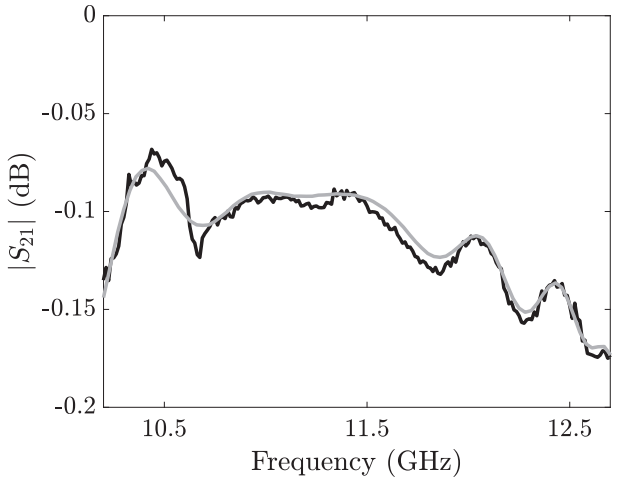

Figure 5.17: Detail of the insertion loss of the novel filter designed in Section 5.7: measured (black line) and simulated with CST MWS using conductivity of silver (grey line).

5.7.4 High-Power Behavior

The high-power behavior of the novel filter and the classical E-plane corrugated filter has been estimated by means of SPARK3D, considering the E-fields previously calculated with CST MWS. The simulations have been done at 12.7 GHz (upper passband edge) which is the frequency where the E-field is maximum and the multipactor threshold is minimum, using silver as background material. For the novel filter, the maximum E-fields are placed in the region where the highest bandstop elements are located, and the lowest breakdown power threshold is 8 kW. This value is much larger than for the classical corrugated filter, which is only 500 W.

5.7.5 Summary

The LPF designed in this example shows very compact size and lower insertion loss compared to the classical E-plane corrugated filter. Specifically, the total length and insertion loss are halved for the same frequency specifications. A prototype has been fabricated by conventional CCM in aluminum and then silver-plated and its frequency behavior has been measured and compared with simulations showing an excellent agreement.

5.8 Design Example 2: Multipactor-Free Ku-band LPF

The requirements imposed in terms of power handling, might sometimes make very difficult and costly to fully assess multipactor experimentally in these filters due to the high power levels involved at high frequencies. Therefore, it would be very useful for the space industry to have LPFs which could handle at least 6 dB above the equivalent peak power to avoid testing the devices following the recommendation in [51]. For instance, if a multi-carrier system with 12 carriers of 120 W each is assumed, the peak power that the filter has to withstand is, in the most pessimistic scenario [52], 17.3 kW (120 x 122) and, thus, the filter should handle in analysis at least 70 kW (6 dB above 17.3 kW). Getting this extreme values is not possible with the proposals found in the literature up to now, and it would make an important impact on industry.

5.8.1 Specifications

As a design example for the previous application, a novel multipactor-free low-loss harmonic waveguide LPF with the fundamental TE_{10} mode as well as all higher-order modes suppressed in the stopband following the procedure in Section 5.3 has been designed, manufactured, and characterized, fulfilling the frequency specifications given in Table 5.6. In the case in point, a linear chirping technique has been applied to the length of the step-shaped bandstop elements so that cumbersome and costly multipactor tests in multi-carrier systems could be avoided.

Table 5.6: Frequency specifications for the novel filter designed in Section 5.8.

Passband	Return loss	Stopband	Attenuation
10.7 - 12.7 GHz	20 dB	13.75 - 38.1 GHz	60 dB

5.8.2 Design and Simulation

The heights of the largest and shortest bandstop elements have been set to $\lambda_g/4$ at the minimum and maximum stopband frequency, respectively, and further refined with a few simulations using FEST3D. Their final values are h_{max} = 5.88 mm and h_{min} = 0.5 mm. Moreover, the steep slope between the pass- and the rejected-band is easily achieved with n_{hmax} = 5. The E-plane mechanical gap is linearly defined between b_{gmin} = 3 mm and b_{gmax} = 6 mm, since this allows high power operation, low insertion loss, and higher-order non-TE_{n0} modes suppression simultaneously. l_{gap} is chosen to be 0.825 mm, and a linear chirp has been defined between l_{min} and l_{max} which are fixed to 1.91 mm and 3.26 mm, respectively. Once the main block filter is designed and the required stopband of the filter is achieved, the next step is the design of the matching networks to get the required pass-band return loss and the matching of the main block to the standard port dimensions. M = 7 and N = 2 stubs have been added at the input and output, respectively. Then, an optimization process is run using the FEST3D optimizer module. Finally, a width reduction with a Hanning window between a_0 and a_{min} = 14.85 mm along L_w = 65.5 mm, is introduced to guarantee the TE_{n0}-mode suppression (L_{end} = 79.15 mm).

The simulated frequency response of the final whole filter is depicted in Figure 5.18 along with the frequency response of a classical waffle-iron filter designed to fulfill the same frequency specifications following [53]. For both filters, the in-band return loss is better than 20 dB and the attenuation level in the stopband is kept below 60 dB. All higher-order modes are perfectly suppressed as it is shown in Figure 5.19 for the novel filter. Compared to the classical waffle-iron filter and [28], the novel filter shows improved insertion loss (0.22 dB vs 0.26 dB and 0.3 dB, respectively, using the conductivity of silver) and much higher power handling capability as it will be demonstrated in Section 5.8.4.

5.8.3 Fabrication and Measurement

A prototype of the novel filter has been manufactured in two halves by CCM (machining radius equal to 0.75 mm – see Figure 5.20) in bare aluminum and then silver-plated (Figure 5.21).

The measurements of the device were carried out using an Agilent 8722 VNA, proper waveguide-to-coaxial transitions, waveguide tapers, and calibration kits. The measurements show an attenuation larger than 60 dB up to 40 GHz and the in-band return loss is kept better than 20 dB in the passband (see Figure 5.22). The worst value of the insertion loss of the filter is 0.21 dB (Figure 5.23). Higher-order mode suppression was checked by introducing bends and misalignments at the filter input

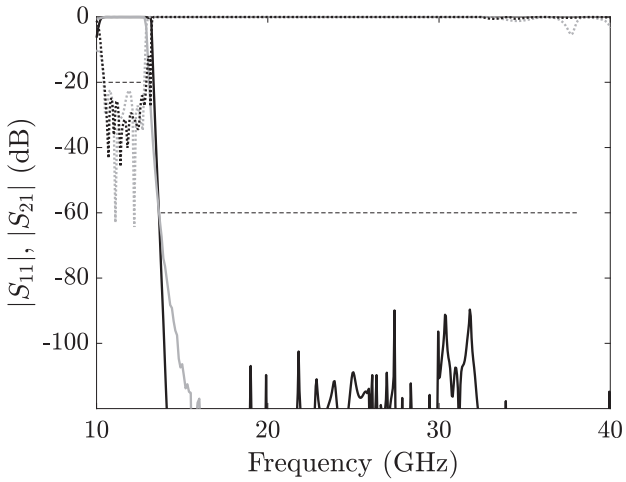

Figure 5.18: FEST3D simulated frequency response for the TE_{10} mode in the novel filter designed in Section 5.8 (black line), the filter with smooth profile designed following the technique described in Chapter 4.3.2.2, [28] (grey thick line), and the classical waffle-iron filter (grey thin line): $|S_{11}|$ in dotted line and $|S_{21}|$ in solid line. Specifications in dashed line.

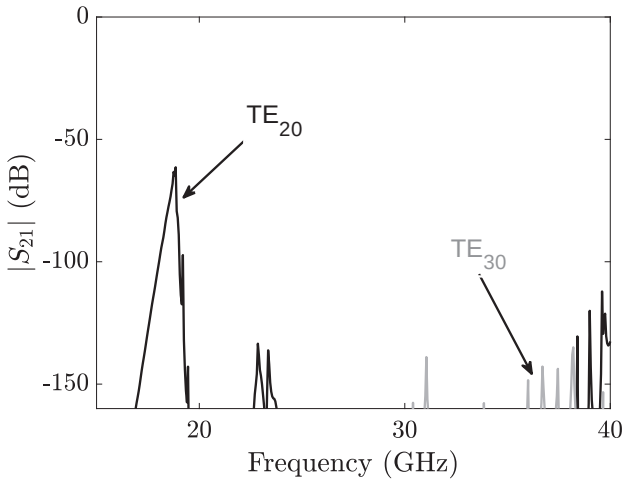

Figure 5.19: FEST3D simulated frequency response for the higher-order modes in the novel filter.

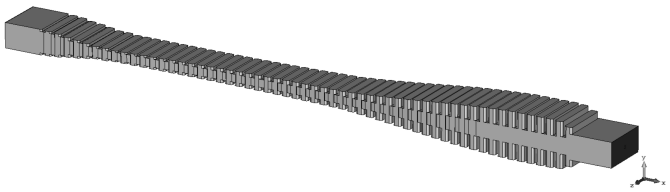

Figure 5.20: 3D view of the novel filter designed in Section 5.8 with rounded corners.

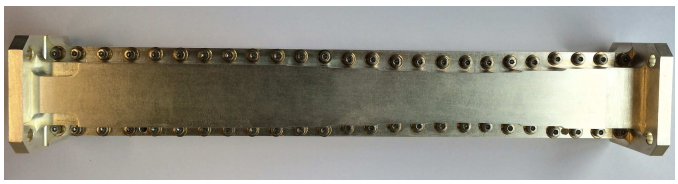

Figure 5.21: Photograph of the assembled prototype designed in Section 5.8.

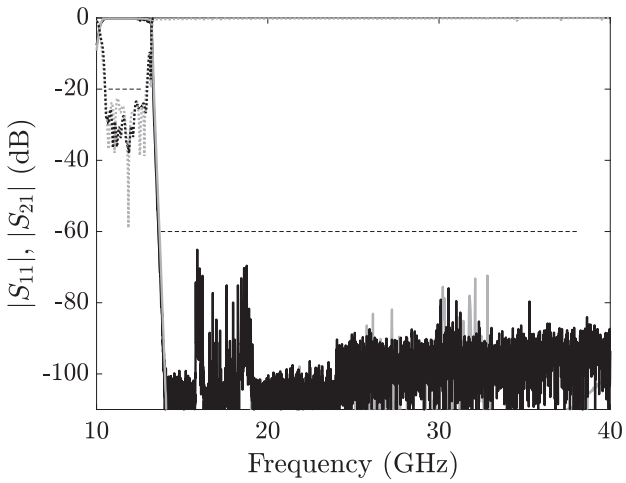

Figure 5.22: Measured (black line) and simulated with CST MWS (grey line) frequency response of the novel filter designed in Section 5.8. S_{11} in dotted line and S_{21} in solid line. Frequency specifications in dashed line.

and output ports [54]. For instance, 90° H-plane bends were used to observe the higher-order TE_{n0}-mode filter behavior (Figure 5.22, grey line). As predicted, the novel filter features an excellent higher-order mode suppression. Last but not least, the novel design technique allows an easy manufacturing by CCM in comparison with [28] and it does not suffer from passband glitches in measurement, as it usually happens with classical waffle-iron filters.

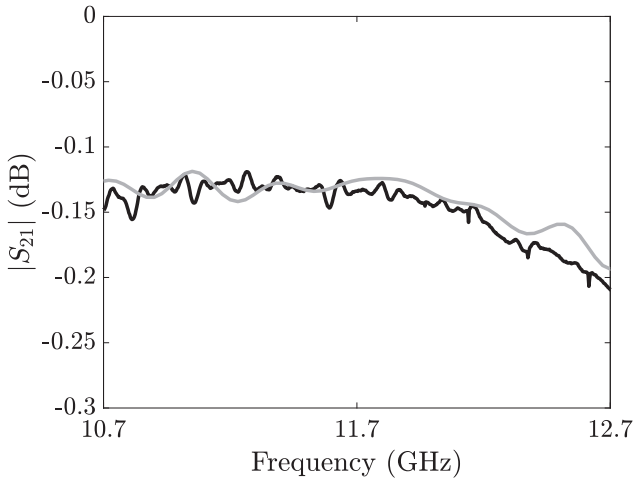

Figure 5.23: Detail of the insertion loss of the novel filter designed in Section 5.8: measured (black line) and simulated with CST MWS using the conductivity of silver (grey line).

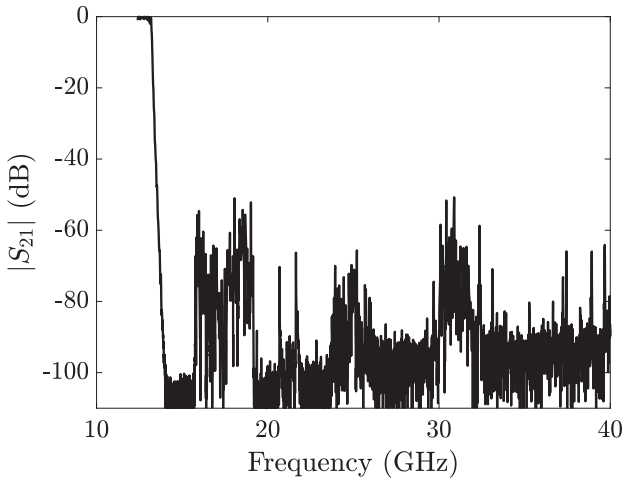

Figure 5.24: Measured $|S_{21}|$ frequency response of the fundamental TE_{10} mode for the novel filter designed in Section 5.8 using the H-plane bend set-up.

5.8.4 High-Power Behavior

The high-power behavior of the novel chirped filter and the classical waffle-iron filter for the same frequency specifications has been estimated by means of SPARK3D, considering the EM fields previously calculated with CST MWS. The simulations have been done at 12.7 GHz (upper passband edge) which is the frequency where the EM fields are maximum and the multipactor threshold will be minimum, using silver as background material.

As it has been aforementioned and well discussed in Section 5.4, the maximum EM fields are placed in the region where the highest bandstop elements are located. The filter gap in this area has been made so large (6 mm) and the length of the highest bandstop elements is also so large (3.26 mm) that the EM field is very weak in this region and, therefore, a very high power handling capability is possible. In fact, the multipactor threshold power levels obtained in this example are better than 100 kW (vs. only 0.15 kW in the classical waffle-iron filter and 7.5 kW in the filter designed following the technique in Chapter 4.3.2.2, [28]). Therefore, this filter could be used to avoid a multipactor test in a multi-carrier system with, for example, 12 carriers of 120 W each (equivalent multi-carrier peak power equal to 17.3 kW), since it handles power levels larger than 70 kW in analysis (6 dB above the peak power), meeting the safety margins prescribed by the ECSS-ESA document on high-power testing [51].

5.8.5 Summary

In this example, a very simple-to-use chirping technique has been applied to the design of high-power compact low-loss waveguide harmonic LPFs with all higher-order modes suppressed in the stopband. This proposal has been shown to avoid, for instance, cumbersome multipactor testing campaigns in multi-carrier systems. The main characteristic of this method is that the multipactor threshold of the filter can be freely adjusted as high as the application requires. In particular, the multipactor threshold has been shown to increase from around 8 kW (non-chirped case) to more than 100 kW (chirped case) in the proposed filter, simply by using this chirping strategy. Moreover, the filter can be easily manufactured by conventional machining methods such as CCM. Compared to a classical waffle-iron filter for the same frequency specifications, the novel device benefits from a better insertion loss and a multipactor-free operation: more than 100 kW for the novel filter vs. only 0.15 kW for the waffle-iron case. Such high multipactor thresholds have never been reported for such kind of filters. A prototype has been manufactured in silver-plated aluminum and its frequency behavior has been measured and compared with the simulations showing a remarkable accordance.

Table 5.7: Frequency specifications for the novel filter designed in Section 5.9.

Passband	Return loss	Stopband	Attenuation	Insertion Loss	Power
		23.5-25.8 GHz	$>$ 30 dB		
17 - 21 GHz	$>$ 25 dB	25.8-31 GHz	$>$ 80 dB	$<$ 0.2 dB	125 W x 2 carriers
		31-50 GHz	$>$ 50 dB		

5.9 Design Example 3: High-Power Compact LPF for Ka-band Multi-beam Payloads

5.9.1 Specifications

Based on the method described above, a compact high-power LPF for Ka-band multi-beam satellite payloads has been designed and simulated fulfilling stringent and relevant specifications (given in Table 5.7).

5.9.2 Design and Simulation

To achieve the required out-of-band attenuation in the stopband of the filter, the highest bandstop element, h_{max}, has been set to 3 mm and the shortest bandstop element, h_{min}, has been set to 1 mm to reject f_{min} and f_{max} respectively. The steep slope between the pass- and the stopband is achieved using n_{hmax} = 5 bandstop elements. To fulfill the attenuation of the entire stopband, a total of only n_{MB} = 15 bandstop elements have been used. l_{gap} is 0.825 mm, and l is 1.5 mm in all bandstop elements (l_{min}=l_{max}=l) since this value will allow both high-power handling capability and a very compact size. The use of chirping techniques to further increase the power-handling by avoiding lateral (z-axis) multipactor discharges is not needed in this case for the levels in the scenario considered in Table 5.7. The minimum mechanical gap of the structure has been defined constant and equal to 2 mm (b_{gmin}=b_{gmax}=b_{gap}), since it allows the suppression of the non-TE_{n0} modes up to 50 GHz (f_{max}) and a high-power behavior simultaneously. Moreover, a width tapering (x-axis) of a_{min} =9.5 mm has been performed to suppress the higher-order TE_{n0} modes. Finally, two matching networks of M=2 and N = 2 elements have been optimized to accomplish the required pass-band return loss and the matching of the filter to the standard WR51 ports.

The simulated frequency response of the final filter is depicted in Figure 5.25 along with the frequency response of a classical waffle-iron filter designed fulfilling the same frequency specifications, Chapter 3.3, [39]. Both filters show an in-band return loss better than 25 dB in the passband and an out-of-band attenuation higher than 80 dB in the stopband of the filter. Furthermore, all higher-order modes are perfectly suppressed with the novel filter as it can be seen in Figure 5.26. Unlike the classical approach, the proposal in this Example has a lower insertion loss value (0.11 dB vs. 0.21 dB) and it is also more compact (55.8 mm vs. 79.6 mm), and

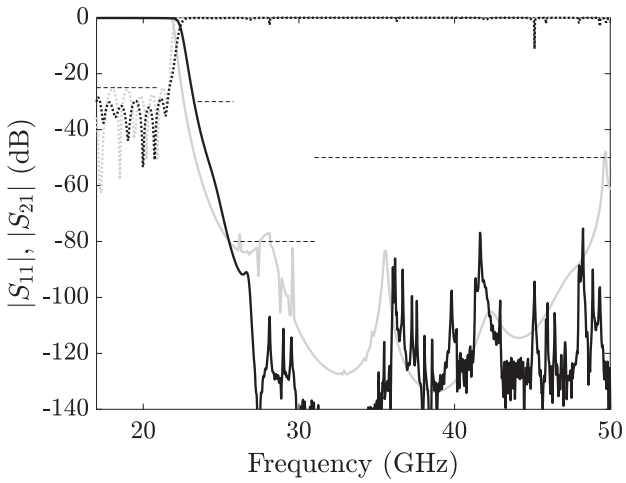

Figure 5.25: FEST3D simulated frequency response for the TE_{10} mode in the novel filter designed in Section 5.9 (black line) and the classical waffle-iron filter (grey line). $|S_{11}|$ in dotted line and $|S_{21}|$ in solid line. Specifications in dashed line.

Table 5.8: Comparison of the filters designed in Section 5.9.

	Length	Simulated IL (silver)	Gap
Waffle-iron filter	79.6 mm	0.21 dB	0.65 mm
Novel filter	55.8 mm	0.11 dB	2 mm

has higher multipactor threshold level (as shown in Table 5.8 and Table 5.9 in the next Subsection). Therefore, the novel LPF developed turns out to be especially attractive in the design of very compact high-power architectures in Ka-band multi-beam satellite payloads, due to its more compact size (saving mass and volume), lower insertion loss, excellent power-handling behavior, and it benefits also from a simple (standard) manufacturing.

5.9.3 Fabrication and Measurement

Two prototypes of the filter have been manufactured by milling in two halves cut by the H-plane (machining tool equal to 0.75 mm). The filters were fabricated in aluminum and then silver-plated. Photographs of the manufactured components are shown in Figure 5.27.

The two manufactured filters were measured in terms of their electrical response (see Figure 5.28 and Figure 5.29). Specifically, in band and out of band measurements were performed to cross-check the result with the design. As it can be seen, both filters meet the specifications and agree well with the simulation.

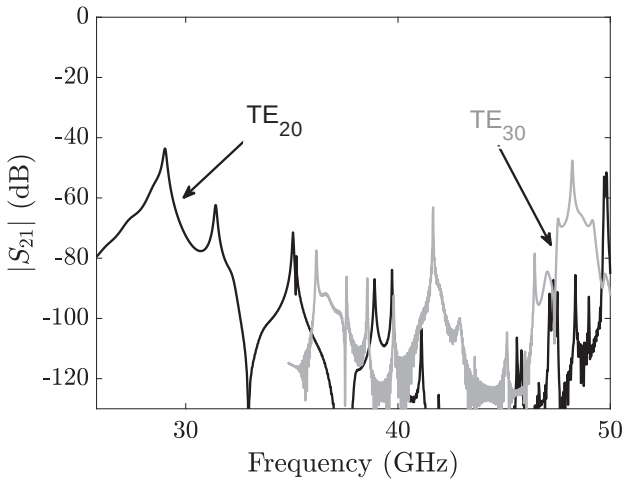

Figure 5.26: FEST3D simulated frequency response for the higher-order modes in the novel filter.

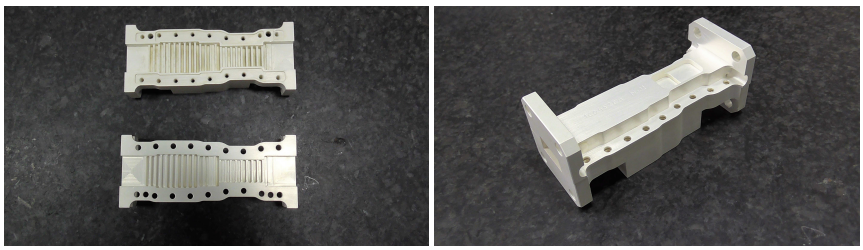

(a) **(b)**

Figure 5.27: Photograph of the (a) unassembled and (b) assembled fabricated prototype of the novel filter designed in Section 5.9.

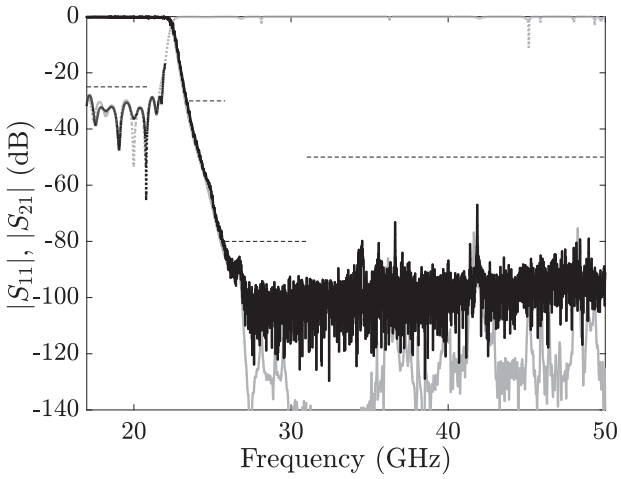

Figure 5.28: Measured (black line) and simulated with CST MWS (grey line) frequency response of the prototype no. 1 of the novel filter designed in Section 5.9. S_{11} in dotted line and S_{21} in solid line. Frequency specifications in dashed line.

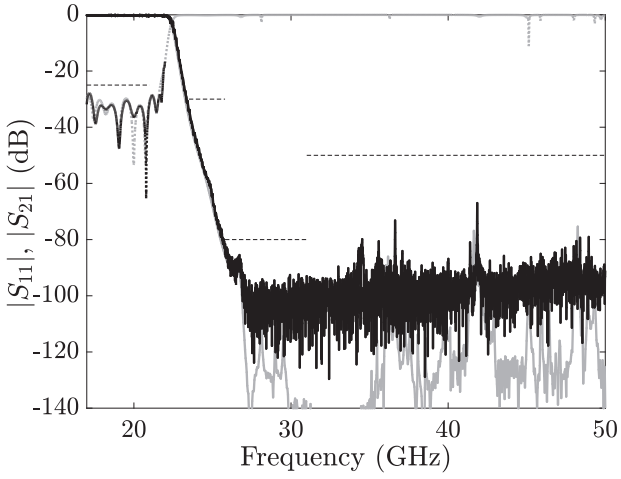

Figure 5.29: Measured (black line) and simulated with CST MWS (grey line) frequency response of the prototype no. 2 of the novel filter designed in Section 5.9. S_{11} in dotted line and S_{21} in solid line. Frequency specifications in dashed line.

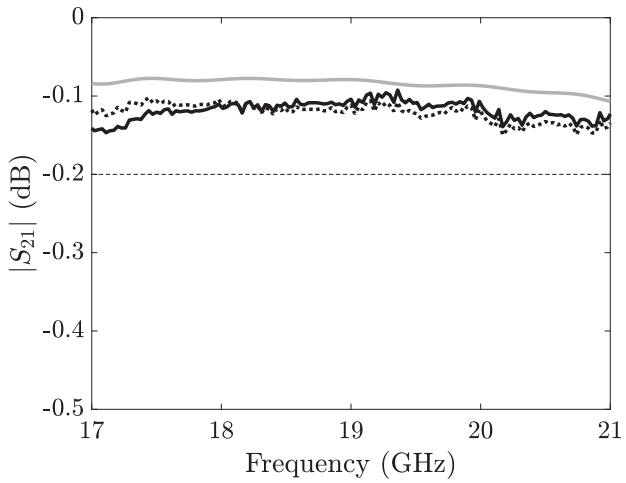

Figure 5.30: Detail of the insertion loss of the novel filter designed in Section 5.8: measured prototype no. 1 (black solid line), measured prototype no. 2 (black dotted line), and simulated with CST MWS using the conductivity of silver (grey line). Frequency specifications in dashed line.

The insertion loss is shown in detail in Figure 5.30. It is proved that, also in terms of insertion loss, specifications are fulfilled.

5.9.4 High-Power Behavior

Based on the high-power specifications (Table 5.7), if a multi-carrier system of 2 carriers of 125 W each is assumed, the peak power that the filter needs to withstand will be 0.5 kW (125 W x 2^2) [52]. Additionally, the power of the direct and reflected signals of the diplexer must be considered. This issue corresponds to a margin of 6 dB above the previous value in the very worst case (full reflection). Therefore, the required multipactor threshold will be 2 kW. However, the ECSS document on multipactor analysis [51] indicates that the filter should handle at least 8 kW in (single-carrier) analysis (6 dB above the peak power) to avoid multipactor test in multi-carrier systems.

5.9.4.1 High-Power Simulation

The high-power behavior of the novel filter and the classical waffle-iron filter for the same frequency specifications as in Table 5.7 has been estimated using SPARK3D. For the simulations, the EM fields calculated with CST MWS have been employed. Simulations have been done at three different frequency points covering the whole band (17 - 21 GHz). Finally, for the breakdown analysis, the SEY of silver has been selected.

The results (see Table 5.9) show that the worst case, as expected, occurs at 21 GHz (upper passband edge) since the Electric field amplitude is maximum at such a fre-

Table 5.9: Filter high-power comparison of the filters designed in Section 5.9.

	Frequency (GHz)	Breakdown Power Threshold (kW)
Waffle-iron filter	21	2.1
Novel filter	21	19
Waffle-iron filter	19	2.8
Novel filter	19	27
Waffle-iron filter	17	2.8
Novel filter	17	30

quency. The multipactor threshold level obtained for the novel filter is 19 KW, whereas the classical waffle-iron filter presents a breakdown of 2100 W. Therefore, the new developed filter shows a margin of almost 10 dB over the peak power of the multi-carrier scenario considering complete short circuit. Consequently, in an industrial environment, this filter could avoid any test and it could be used safely for the intended application. It is important to remark that this is not the case for the waffle iron filter since it does not provide almost any margin, and therefore, it would require testing.

5.9.4.2 High-Power Tests

High-power tests were performed in the two filters at the ESA-VSC laboratory in Valencia, Spain, by means of the test set-up described in Figure 5.31. In order to achieve during the test a maximum power level as large as possible, a ring resonator in Ka-Band was employed. The ring resonator permits to reinforce the field levels of the traveling wave created in the ring structure, which includes the critical gap area of the DUT. This allows to increase the field levels inside the device and perform the multipactor tests at larger values than the one provided by the TWTA, making it possible to fully characterize filters with high-power handling capability. As it can be seen in Figure 5.31, several multipactor detection methods have been used: 2 harmonic detection systems, 2 electron avalanche monitoring systems, and 2 fast diode (broad video bandwidth" monitoring systems). In order to have enough electrons in the critical gap area, 2 beta emitting radioactive sources $90Sr$ were placed near the DUT aiming at the most critical area, and a UV light source was placed also near this area (see Figure 5.32). Moreover, the following parameters have been employed during the multipactor test: pressure lower than 1.5 mbar, ambient temperature, pulse width of 20 μs, and pulse duty cycle equal to 2%. The maximum available power was 9.500 W.

After the test campaign, no discharges were observed in any filter up to the maximum available power, as expected.

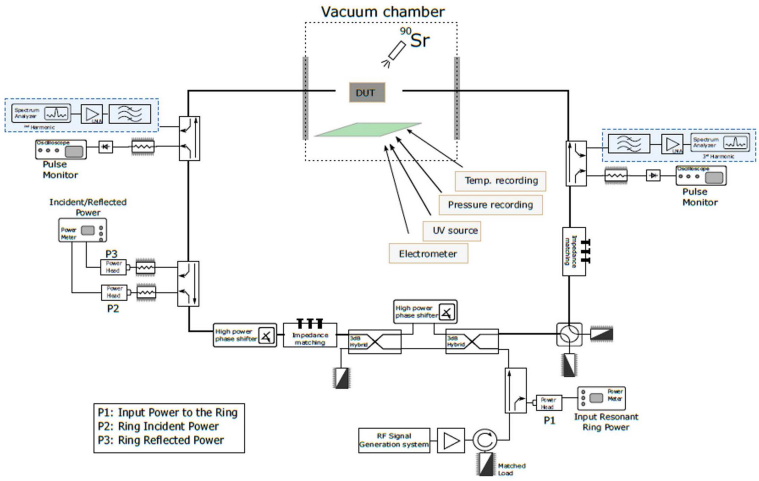

Figure 5.31: Configuration of the multipactor test set-up.

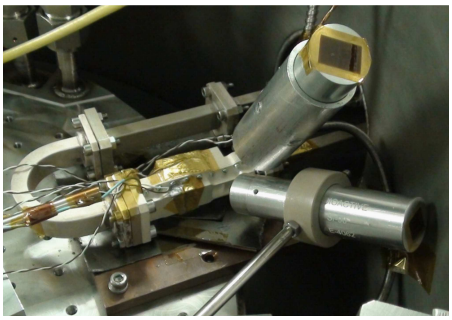

Figure 5.32: Photograph of the novel filter inside the TVAC for the multipactor test.

5.9.5 Summary

In this example, an alternative to the waffle-iron filter for the design of LPFs for very compact high-power architectures in Ka-band multi-beam satellite payloads is presented. The novel LPF is more compact (around 1.4 times smaller), has almost half losses, and it also benefits from higher power-handling capability (can handle at least 10 dB more power) in comparison with its classical counterpart. Moreover, the proposed filter can be easily fabricated by conventional milling, making it particularly attractive to mass-production in multi-beam satellite applications, where a lot of filters must be manufactured.

5.10 Design Example 4: High-Performance Diplexer for Ku-K band Satellite Payloads

5.10.1 Design Considerations and Constituent Filters

The specifications used in this Section for the final diplexer are shown in Table 5.10. The fractional bandwidths for the Ku-Tx and Ku-Rx bands are 19.4% and 7.3%, respectively, and the overall bandwidth of the whole diplexer is 53.4%.

5.10.1.1 Requirements and Proposed Solution

According to the specifications, and due to the large bandwidth of the Ku-Tx-band filter, the LPF solution presented in this Chapter is a very good approach, since it is compact, low-loss, and high-power. The Ku-Rx-band filter will be a classical H-plane filter of inductive irises, because the fractional bandwidth is not very large (7.3%). However, the couplings between the cavities will be performed in an optimum way to minimize the final footprint of the whole diplexer. Lastly, the diplexer is

Table 5.10: Summary of specifications for the diplexer designed in Section 5.10.

Ku-Tx-band filter ($f_{1,TX} - f_{2,TX}$)	10.7 – 13 GHz
Ku-Rx-band filter ($f_{1,RX} - f_{2,RX}$)	17.2 – 18.5 GHz
Return loss at interface ports	$>$20 dB
Insertion loss at interface ports	$<$0.2 dB
Attenuation at Tx band ($Att_{1,TX}$)	$>$50 dB
Attenuation at Rx band ($Att_{2,RX}$)	$>$80 dB
Ku Tx-band interface port	WR75
K Rx-band interface port	WR51
Common interface port	WR75
Multipactor threshold level	$>$2.5 kW

Table 5.11: Final dimensions of the K-Tx band LPF designed in Section 5.10.

Matching Networks	M = 2 and N = 2		
Main Block	h_{min} = 5.6 mm	h_{max} = 5.6 mm	n_{hmax} = 6
	b_{gmin} = 3 mm	b_{gmax} = 3 mm	n_{MB} = -
	l_{min} = 2.5 mm	l_{max} = 2.5 mm	l_{gap} = 0.825 mm
Width reduction	a_min = 14.5 mm	L_w = 9.975 mm	L_T = 33.25 mm

constituted by an E-plane T-junction. The common interface port will be connected to the T-junction by a matching network, similar to the matching networks used for the LPFs in this Chapter, and the filters will be finally connected with a direct coupling to either side of the T-junction. The main advantages of using this topology are the high isolation between channels and an easy-to-manufacture geometry of the diplexer.

5.10.1.2 LPF Design (Ku-Tx-Band Filter)

The Ku-Tx-band low-pass filter in this example has been designed according to the technique presented in this Chapter. In this case, the required stopband is much narrower than in previous examples and, consequently, an extremely compact structure can be designed. Specifically, the LPF has been designed fulfilling the frequency specifications given in Table 5.10. The final dimensions of the filter are shown in Table 5.11. Its simulated frequency response (FEST3D) is shown in Figure 5.33, along with the response of an equivalent classical waffle-iron filter and a corrugated filter with width reduction designed following [39] and [40], respectively, for the same frequency specifications. Both classical solutions fulfil the frequency specifications but, as it was expected, the novel filter is only 33.25 mm-long while the classical waffle-iron filter has a total length of 75 mm, and the corrugated filter with width reduction is 58.90 mm-long. All filters suppress all higher-order modes up to 18.5 GHz (see Figure 5.34) and show similar insertion loss (better than 0.1 dB, taking into account the conductivity of aluminum). Additionally, the high-power behavior has been estimated using SPARK3D and the simulated multipactor threshold level is better than 2.5 kW in the three devices.

5.10.1.3 BPF Design (Ku-Rx-Band Filter)

As it was aforementioned, an H-plane cavity structure based on inductive irises has been chosen for the realization of the Ku-Rx band filter. The filter has been designed following the technique well described in [30] and using FEST3D. The filter has 5 cavities, 2 of which are bended to obtain the minimum footprint. The simulated frequency response is shown in Figure 5.35. As it can be seen, the filter fulfills the frequency specifications.

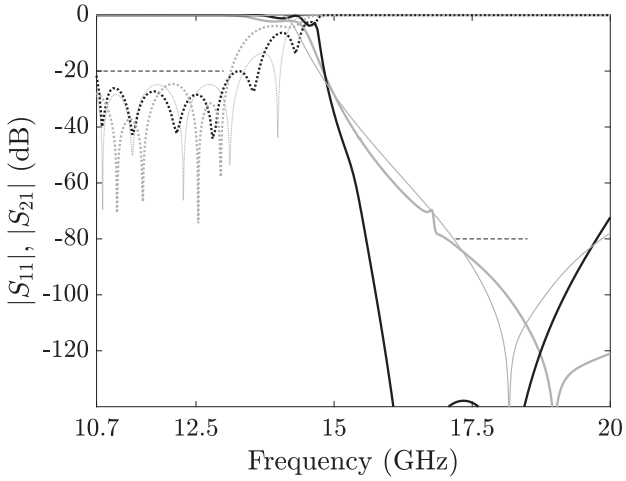

Figure 5.33: FEST3D simulated frequency response for the fundamental TE_{10} mode of the classical waffle-iron filter (grey thin line), the corrugated filter with width reduction (grey thick line), and the Tx-band filter designed in Section 5.10 (black thin line). S_{11} in dotted line and S_{21} in solid line. Frequency specifications in dashed line.

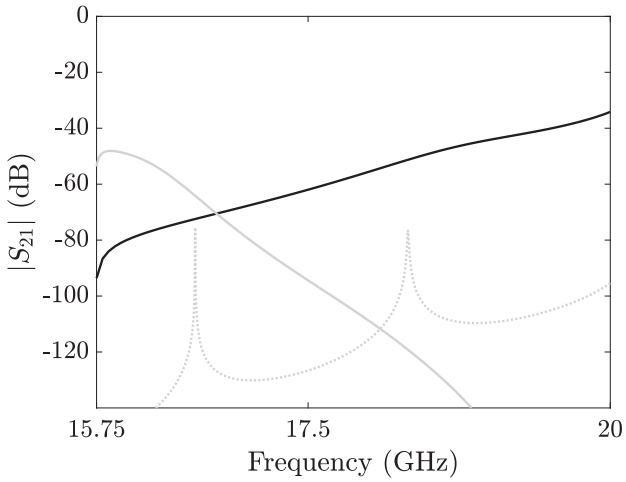

Figure 5.34: FEST3D simulated frequency response for the TE_{20} mode of the classical waffle-iron filter (grey thin line), the corrugated filter with width reduction (grey thick line), and the Tx-band filter designed in Section 5.10 (black thin line). S_{11} in dotted line and S_{21} in solid line. Frequency specifications in dashed line.

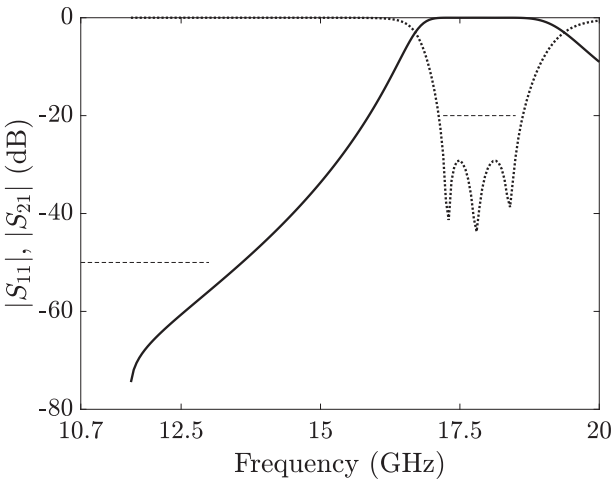

Figure 5.35: FEST3D simulated frequency response of the Rx-band H-plane BPF. S_{11} in dotted line and S_{21} in solid line. Frequency specifications in dashed line.

5.10.1.4 Junction and Common Port Interface

There are some different direct branching solutions, i.e., bifurcations, Y or T-junctions (E- and H-plane), manifolds. In this case, an E-plane T-junction has been chosen due to the wide overall bandwidth of the diplexer (53.4%) in order to obtain the minimum footprint of the structure. The E-plane T-junction has been defined with a 19.05-mm width and a 6.477- mm height. Finally, the common port interface is reached by means of a matching network designed following the technique also described in this Chapter.

5.10.2 Diplexer Design: Simulation and Measurement

Once both filters are designed fulfilling the frequency specifications of each particular frequency band and the junction is chosen, all parts are connected together. Filters are joined directly to the E-plane T-junction, and the standard height of the common port is achieved with a very short matching network of 3 elements. Figure 5.36 depicts the outline of the final diplexer configuration. After that, final optimizations are run in FEST3D to achieve the required performance of the diplexer. Firstly, the dimensions of the T-junction and the matching network of the common port are optimized. In a subsequent step, the dimensions of the BPF are added to the optimization procedure. Then, the dimensions of the BPF are deselected, and the low-pass filter is optimized along with the dimensions of the junction and the matching network of the common port. In the last step, all parameters are finely optimized. The computations throughout this whole optimization process have considered, of course, the rounding of the corners which will be necessary for a final realization with classical milling

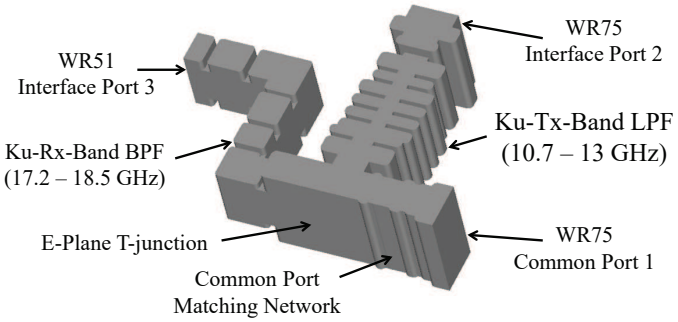

Figure 5.36: Sketch of the proposed diplexer solution in Section 5.10.

techniques. Simulation results can be seen in Figure 5.38. The footprint of the novel diplexer is 45 x 65 mm.

The diplexer has been manufactured by milling (radius of the tool equal to 1 mm) in aluminum in two identical halves cut by the E-plane (see Figure 5.37). It is important to note that the prototype does not need any tuning. The measured results shown in Figure 5.38 fulfill the stringent frequency specifications and show an excellent agreement with simulations. The insertion loss is kept below 0.2 dB for both the Ku Tx- and the Ku Rx-bands.

5.10.3 Summary

A novel high-performance diplexer for satellite applications has been proposed in this Section. The diplexer shows an overall bandwidth up to 50%, high-power handling capability, low-loss, and an extremely compact footprint. Indeed, the low-pass filter designed for the Ku-Tx band has around 50%-length reduction in comparison with a classical waffle-iron filter or a corrugated filter with width reduction designed for the same frequency specifications. Moreover, a BPF based on inductive irises with optimum coupling positions has been used to implement the Ku-Rx band, providing the minimum mass and volume to the final diplexer. A prototype has been manufactured by milling in two E-plane halves in aluminum demonstrating the validity of this novel approach, which has been confirmed with simulations and measurements.

5.11 Conclusions

In this Chapter, a novel fully-customized technique for the design of high-power compact low-loss waveguide harmonic LPFs with all higher-order mode suppression

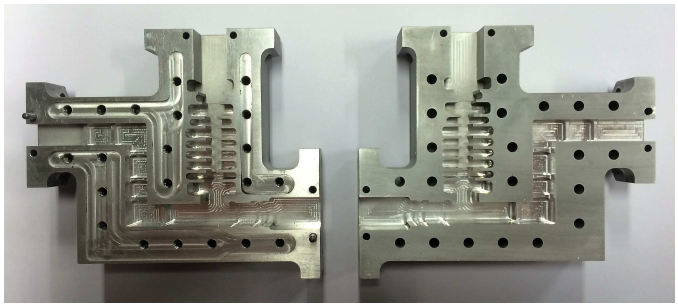

(a)

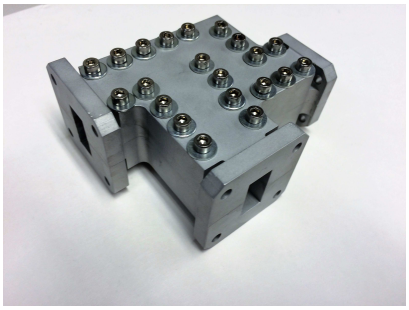

(b)

Figure 5.37: Photograph of the (a) unassembled and (b) assembled prototype of the diplexer designed in Section 5.10.

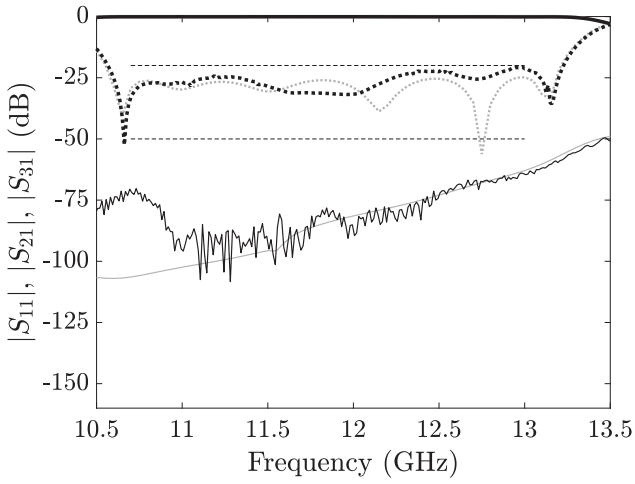

(a)

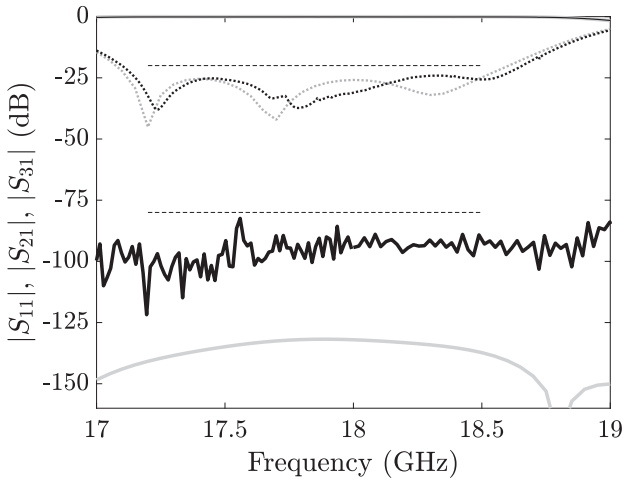

(b)

Figure 5.38: FEST3D simulated frequency response (grey line) of the final diplexer with rounded corners and measurements of the prototype (black line), (a) Ku-Tx band and (b) Ku-Rx band. S_{11} in dotted line, S_{21} in solid thick line, and S_{31} in solid thin line. Frequency mask for return loss and out-of-band rejection with dashed line.

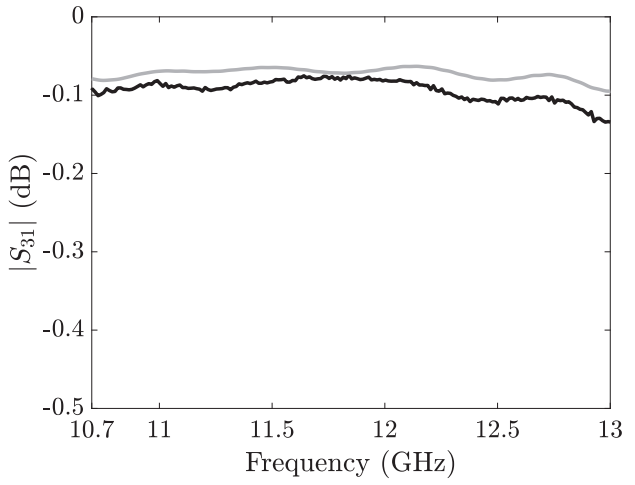

(a)

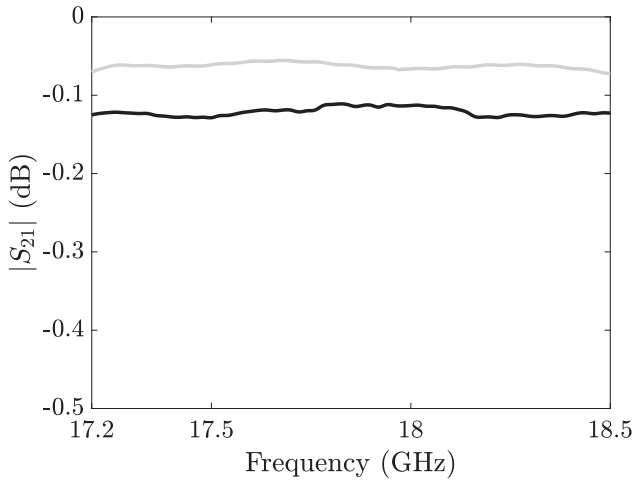

(b)

Figure 5.39: Measured insertion loss detail of the fabricated prototype in Section 5.10 (black line). CST MWS simulation in grey line.

has been presented. The main characteristic of this method is that unprecedented values of multipactor threshold can be obtained by means of chirping the bandstop elements length. Moreover, these filters can be easily manufactured by conventional milling. Specifically, the method has been demonstrated with three different satellite examples. The first one is the output LPF for a Ku- and Ka-band satellite payloads (where power handling is key point), the second is a LPF for a Ka-band multi-beam payload (where a very compact size and high-power handling are equally important), and a high-performance diplexer (where minimizing the size is the fundamental objective). These applications have been covered through four examples which have been designed, simulated, manufactured, and the measurement results show a remarkable accordance with simulations. Finally, SPARK3D has been utilized to estimate the multipactor threshold level, showing that the proposed filters handle much more power than their classical counterparts, making them especially attractive to be utilized in different satellite applications.

REFERENCES

[1] F. Teberio, I. Arregui, A. Gomez-Torrent, E. Menargues, I. Arnedo, M. Chudzik, M. Zedler, F. J. Görtz, R. Jost, T. Lopetegi, and M. A. G. Laso, "Low-loss compact ku-band waveguide low-pass filter," in *2015 IEEE MTT-S International Microwave Symposium Digest (IMS)*, May 2015, pp. 1–4.

[2] ——, "High-power waveguide low-pass filter with all-higher-order mode suppression over a wide-band for ka-band satellite applications," *IEEE Microwave and Wireless Components Letters*, vol. 25, no. 8, pp. 511–513, Aug. 2015.

[3] F. Teberio, I. Arregui, A. Gomez-Torrent, I. Arnedo, M. Chudzik, M. Zedler, F. J. Görtz, R. Jost, T. Lopetegi, and M. A. G. Laso, "Chirping techniques to maximize the power-handling capability of harmonic waveguide low-pass filters," *IEEE Transactions on Microwave Theory and Techniques*, vol. 64, no. 9, pp. 2814–2823, Sep. 2016.

[4] F. Teberio, A. Gomez-Torrent, I. Arregui, J. M. Percaz, I. Arnedo, M. Chudzik, T. Lopetegi, and M. A. G. Laso, "Sensitivity analysis of a 3-d printed low-cost compact waveguide low-pass filter," in *2016 46th European Microwave Conference (EuMC)*, Oct. 2016, pp. 249–252.

[5] F. Teberio, I. Arregui, M. Guglielmi, A. Gomez-Torrent, P. Soto, M. A. G. Laso, and V. E. Boria, "Compact broadband waveguide diplexer for satellite

applications," in *2016 IEEE MTT-S International Microwave Symposium Digest (IMS)*, May 2016, pp. 1–4.

[6] F. Teberio, I. Arregui, C. Vicente, J. Gil, P. Martin-Iglesias, M. Zedler, J. A. Lorente, and M. A. G. Laso, "Fully-customized waveguide harmonic low-pass filters for high-power satellite applications," in *2017 9th International Workshop on Multipactor, Corona and Passive Intermodulation in Space RF Hardware (MULCOPIM)*, Apr. 2017.

[7] F. Teberio, I. Arregui, C. Vicente, J. Gil, M. Zedler, J. A. Lorente, D. Raboso, and M. A. G. Laso, "High-power low-pass filter for ka-band multibeam payload," in *2018 International Workshop on Microwave Filters (IWMF)*, Apr. 2018.

[8] UPNA, NOVALTI, AURORASAT, TESAT, "Compact high-power ka-band low-pass filters for multibeam satellite payloads," ESA, ITI-B project ES-RP-1702-ILM, Oct. 2017.

[9] UPNA, "New high-power low-pass harmonic filters with easy manufacturability," TESAT Spacecom GmbH, 2016.

[10] V. Boria and B. Gimeno, "Waveguide filters for satellites," *Microwave Magazine, IEEE*, vol. 8, no. 5, pp. 60–70, Oct. 2007.

[11] M. Yu, "Power-handling capability for rf filters," *Microwave Magazine, IEEE*, vol. 8, no. 5, pp. 88–97, Oct. 2007.

[12] M. Schneider, C. Hartwanger, and H. Wolf, "Antennas for multiple spot beam satellites," *CEAS Space Journal*, vol. 2, no. 1, pp. 59–66, Dec. 2011.

[13] H. Wolf, M. Schneider, S. Stirland, and D. Scouarnec, "Satellite multibeam antennas at airbus defence and space: State of the art and trends," in *2014 8th European Conference on Antennas and Propagation (EuCAP)*, Apr. 2014, pp. 182–185.

[14] E. Reiche, S. Stirland, C. Hartwanger, U. P. Hong, R. Gehring, and H. Wolf, "A dual circular combined k/ka-band rf sensing feed chain for multi beam satellite antennas," in *2011 5th European Conference on Antennas and Propagation (EuCAP)*, Apr. 2011, pp. 3198–3202.

[15] H. Yukawa, K. Yoshida, T. Mizuno, T. Owada, and M. Miyazaki, "Ku/ka-band compact orthomode junction with low pass filters for high power applications," in *2013 43rd European Microwave Conference (EuMC)*, Oct. 2013, pp. 1175–1178.

[16] D. Scouarnec, S. Stirland, and H. Wolf, "Current antenna products and future evolution trends for telecommunicatio satellites application," in *2013 IEEE-APS Topical Conference on Antennas and Propagation in Wireless Communications (APWC)*, Sep. 2013, pp. 1412–1415.

[17] J. Rhodes, "Waveguide sandwich filters," *IEEE Transactions on Microwave Theory and Techniques*, vol. 22, no. 4, pp. 394–399, Apr. 1974.

[18] R. Levy, "Compact waveguide bandstop filters for wide stopbands," in *2009 IEEE MTT-S International Microwave Symposium Digest (IMS)*, Jun. 2009, pp. 1245–1248.

[19] O. Gupta and R. Wenzel, "Design tables for a class of optimum microwave bandstop filters (correspondence)," *IEEE Transactions on Microwave Theory and Techniques*, vol. 18, no. 7, pp. 402–404, Jul. 1970.

[20] L. Young and B. M. Schiffman, "New and improved types of waffle-iron filters," *Proceedings of the Institution of Electrical Engineers*, vol. 110, no. 7, pp. 1191–1198, Jul. 1963.

[21] E. Sharp, "A high-power wide-band waffle-iron filter," *IEEE Transactions on Microwave Theory and Techniques*, vol. 11, no. 2, pp. 111–116, Mar. 1963.

[22] R. Bunger and F. Arndt, "GSM/moment-method CAD of waffle-iron-filters with round teeth," in *1999 IEEE MTT-S International Microwave Symposium Digest (IMS)*, vol. 4, Jun. 1999, 1691–1694 vol.4.

[23] M. Manuilov and K. Kobrin, "Field theory CAD of waffle-iron filters," in *2005 35th European Microwave Conference (EuMC)*, vol. 2, Oct. 2005, pp. 1–4.

[24] T. Stander, P. Meyer, P. van der Walt, and W. Steyn, "Waffle-iron filters with oblique boss patterns," in *Electromagnetics in Advanced Applications (ICEAA), 2012 International Conference on*, Sep. 2012, pp. 1256–1257.

[25] I. Arregui, I. Arnedo, A. Lujambio, M. Chudzik, D. Benito, R. Jost, F. Gortz, T. Lopetegi, and M. Laso, "A compact design of high-power spurious-free low-pass waveguide filter," *IEEE Microwave and Wireless Components Letters*, vol. 20, no. 11, pp. 595–597, Nov. 2010.

[26] I. Arregui, F. Teberio, I. Arnedo, A. Lujambio, M. Chudzik, D. Benito, R. Jost, F.-J. Gortz, T. Lopetegi, and M. Laso, "High-power low-pass harmonic waveguide filter with TEn0-mode suppression," *IEEE Microwave and Wireless Components Letters*, vol. 22, no. 7, pp. 339–341, Jul. 2012.

[27] F. Teberio, I. Arregui, I. Arnedo, M. Chudzik, R. Jost, F.-J. Görtz, T. Lopetegi, and M. A. G. Laso, "Tailoring of higher-order mode suppression in a high-power alternative to classical waffle-iron filters," *Microwave Optical and Technology Letters*, vol. 56, no. 12, pp. 2967–2974, Dec. 2014.

[28] I. Arregui, F. Teberio, I. Arnedo, A. Lujambio, M. Chudzik, D. Benito, T. Lopetegi, R. Jost, F.-J. Gortz, J. Gil, C. Vicente, B. Gimeno, V. Boria, D. Raboso, and M. Laso, "High-power low-pass harmonic filters with higher-order TEn0 and non-TEn0 mode suppression: Design method and multipactor characterization," *IEEE Transactions on Microwave Theory and Techniques*, vol. 61, no. 12, pp. 4376–4386, Dec. 2013.

[29] V. Semenov, J. Rasch, E. Rakova, and J. Johansson, "General study of multipactor between curved metal surfaces," *IEEE Transactions on Plasma Science*, vol. 42, no. 3, pp. 721–728, Mar. 2014.

[30] R. Cameron, C. Kudsia, and R. Mansour, *Microwave Filters for Communication Systems: Fundamentals, Design and Applications*. Wiley-Interscience, 2007.

[31] U. Rosenberg, A. Bradt, M. Perelshtein, and P. Bourbonnais, "Extreme broadband waveguide diplexer design for high performance antenna feed systems," in *2010 40th European Microwave Conference (EuMC)*, Sep. 2010, pp. 1249–1252.

[32] J. Uher, J. Bornemann, and U. Rosenberg, *Waveguide Components for Antenna Feed Systems: Theory and CAD*. Artech House, 1993.

[33] J. M. Rebollar, J. R. Montejo-Garai, and A. Ohoro, "Asymmetric H-plane T-junction for broadband diplexer applications," in *IEEE Antennas and Propagation Society International Symposium. Transmitting Waves of Progress to the Next Millennium. 2000 Digest. Held in conjunction with: USNC/URSI National Radio Science Meeting (C*, vol. 4, Jul. 2000, 2032–2035 vol.4.

[34] J. Bornemann and M. Mokhtaari, "The bifurcated E-plane T-junction and its application to waveguide diplexer design," in *in Proc. German Microwave Conference*, vol. 1a-5, Mar. 2006, 4 p.

[35] J. Dittloff and F. Arndt, "Computer-aided design of slit-coupled H-plane T-junction diplexers with E-plane metal-insert filters," *IEEE Transactions on Microwave Theory and Techniques*, vol. 36, no. 12, pp. 1833–1840, Dec. 1988.

[36] E. Ofli, R. Vahldieck, and S. Amari, "Novel E-plane filters and diplexers with elliptic response for millimeter-wave applications," *IEEE Transactions on Microwave Theory and Techniques*, vol. 53, no. 3, pp. 843–851, Mar. 2005.

[37] F. Teberio, I. Arnedo, J. M. Percaz, I. Arregui, T. Lopetegi, and M. A. G. Laso, "Accurate design of corrugated waveguide low-pass filters using exclusively closed form expressions," in *2017 47th European Microwave Conference (EuMC)*, Oct. 2017.

[38] R. V. Snyder, "New application of evanescent mode waveguide to filter design," in *1977 IEEE MTT-S International Microwave Symposium Digest (IMS)*, Jun. 1977, pp. 294–297.

[39] F. Teberio, I. Arnedo, J. M. Percaz, I. Arregui, P. Martin-Iglesias, T. Lopetegi, and M. A. G. Laso, "Accurate synthesis procedure for waffle-iron low-pass filter," in *2018 IEEE MTT-S International Microwave Symposium Digest (IMS)*, Jun. 2018.

[40] W. Hauth, R. Keller, and U. Rosenberg, "Cad of waveguide low-pass filters for satellite applications," in *1987 17th European Microwave Conference (EuMC)*, Sep. 1987.

[41] R. Udiljak, D. Anderson, M. Lisak, J. Puech, and V. Semenov, "Multipactor in a waveguide iris," *IEEE Transactions on Plasma Science*, vol. 35, no. 2, pp. 388–395, Apr. 2007.

[42] C. Kudsia, R. Cameron, and W.-C. Tang, "Innovations in microwave filters and multiplexing networks for communications satellite systems," *IEEE Transactions on Microwave Theory and Techniques*, vol. 40, no. 6, pp. 1133–1149, Jun. 1992.

[43] D. M. Pozar, *Microwave Engineering Fourth Edition*. Wiley, 2011.

[44] D. Wolk, C. Vicente, H. L. Hartnagel, M. Mattes, J. R. Mosig, and D. Raboso, "An investigation of the effect of fringing fields on multipactor breakdown," in *2005 5th International Workshop on Multipactor, Corona and Passive Intermodulation in Space RF Hardware (MULCOPIM)*, Sep. 2005.

[45] R. Levy, "Inhomogeneous stepped-impedance corrugated waveguide low pass filters," in *2005 IEEE MTT-S International Microwave Symposium Digest (IMS)*, Jun. 2005, 4 pp.-.

[46] J. Vaughan, "Multipactor," *IEEE Transactions on Electron Devices*, vol. 35, no. 7, pp. 1172–1180, Jul. 1988.

[47] J. Bornemann, U. Rosenberg, S. Amari, and R. Vahldieck, "Tolerance analysis of bypass-, cross- and direct-coupled rectangular waveguide band-pass filters," *IEE Proceedings - Microwaves, Antennas and Propagation*, vol. 152, no. 3, pp. 167–170, Jun. 2005.

[48] J. R. Aitken and J. Hong, "Tolerance considerations for wireless backhaul diplexer circuits," in *2014 44th European Microwave Conference (EuMC)*, Oct. 2014, pp. 620–623.

[49] K. C. Gupta, R. Garg, and R. Chadha, *Computer aided design of microwave circuits*. Artech House, 1981.

[50] X. P. Liang, K. A. Zaki, and A. E. Atia, "Channel expansion and tolerance analysis of waveguide manifold multiplexers," *IEEE Transactions on Microwave Theory and Techniques*, vol. 40, no. 7, pp. 1591–1594, Jul. 1992.

[51] ESA, *ECSS Space engineering, multipactor design, and test*. Noordwijk, The Neederlands: ESA Publications Division, Apr. 2000, vol. ECSS-E-20-01.

[52] S. Anza, C. Vicente, J. Gil, M. Mattes, D. Wolk, U. Wochner, V. Boria, B. Gimeno, and D. Raboso, "Prediction of multipactor breakdown for multicarrier applications: The quasi-stationary method," *IEEE Transactions on Microwave Theory and Techniques*, vol. 60, no. 7, pp. 2093–2105, Jul. 2012.

[53] G. Matthaei, L. Young, and E. M. T. Jones, *Microwave filters, impedance-matching networks and coupling structures*. Artech House, 1980.

[54] K.-L. Wu and G. McDonald, "Coping with hidden spurious harmonic modes in the design of low pass corrugated waveguide filters," *Microwave Journal*, vol. 44, no. 11, pp. 180–183, Nov. 2001.

CHAPTER 6

COMPACT BPFs FOR HIGH-PERFORMANCE DIPLEXERS

In this Chapter, two novel compact diplexers for satellite applications are presented [1]. The first covers the Ku band with two closely spaced channels (Ku-Tx band: 10.7-13 GHz and Ku-Rx band: 13.75-14.8 GHz). The second is wider than the first (overall bandwidth up to 50%), achieves the suppression of the higher-order modes, and covers the Ku/K band with a Rx channel between 17.2 and 18.5 GHz. Both diplexers are composed of two novel BPFs, joined together with an E-plane T-junction. The BPFs are designed by combining a low-pass filtering function and a high-pass filtering structure [1], [2]. The novel diplexers show a very compact footprint, are easy to fabricate, and are especially attractive for wide-band applications. A prototype Ku/K band diplexer has also been fabricated by milling. Measurements show an excellent agreement with simulations, thereby demonstrating the validity and manufacturing robustness of the proposed topology.
It is important to note that the devices presented in this Chapter were developed in collaboration with the Universitat Politècnica de València.

6.1 Background

Communication satellite hardware requirements have become extremely stringent and demand high-power, compact, low-weight, and low-cost products as it was aforementioned in previous Chapters, [3]–[5]. Furthermore, an efficient design and manufacturing process is essential to obtain competitive products. The state-of-the-art of 3D EM simulation tools and the accuracy of CCM machines offer great advantages in terms of production time and high-quality components. In order to obtain more economic devices, design time must be decreased, and manufacturing tolerances must be relaxed while maintaining a high production yield. Therefore, the development of filters and diplexers less sensitive to fabrication techniques and their associated tolerances is very important.

The RF feed chain of communication satellites uses architectures with high performance diplexers (overall bandwidths much larger than 20%, and passbands larger than 5%) to combine reception (Rx) and transmission (Tx) in a common antenna [6]–[8] (see Figure 6.1). There are many diplexers in the technical literature which are based on classical BPFs with either inductive or capacitive couplings [9], [10], or metal inserts [11], [12]. If the relative bandwidth of the Tx or Rx band is large, the use of this kind of filtering structures is not recommended. These scenarios normally require high order filters and, hence, compact size and low insertion loss cannot be achieved (in particular for the Tx band). Moreover, if the overall bandwidth of the diplexer covers a very wide frequency range, higher-order modes might appear in the Rx band. In such cases, the suppression of these higher-order modes is an important requirement that cannot be accomplished with standard filters. In particular, this issue can indeed be solved in the Tx band with evanescent-mode filters [13], classical waffle-iron filters [14], or corrugated filters with a width reduction which shifts up in frequency the higher-order modes [15]. Lately, however, a high-power compact LPF based on quarter-wave step-shaped bandstop elements separated by very short (ideally zero-length) waveguide sections has been proposed [16]. The performance of this novel structure has been compared with its classical counterparts in a high-performance diplexer showing that the size of the LPF is dramatically reduced [8].

The high-performance diplexer designed in the previous Chapter in Section 5.10 [8] uses, in the Rx band, a classical inductive-iris filter designed with an optimum position of the couplings between the cavities to reduce the layout of the final diplexer. However, filters based on resonant cavities are quite sensitive to manufacturing tolerances [17], [18]. Some ideas to reduce the influence of the fabrication tolerances in classical coupled resonant structures (with inductive and capacitive irises) such as the most obvious one, i.e. designing the filters to have sufficient margin to fulfill the frequency specifications at the cost of increasing the filter order (and length), have been proposed in the literature [19]. In [20], higher-order resonances of some waveguide cavities were exploited to improve tolerance issues. However, the latter implies that the overall size of the filter (and consequently the diplexer) increases. Furthermore, using this approach, spurious resonances may appear below the passbands [21]. These problems do not occur in the novel BPFs proposed in this Chapter. Relaxed fabrication tolerances and a compact size are indeed simultaneously achieved.

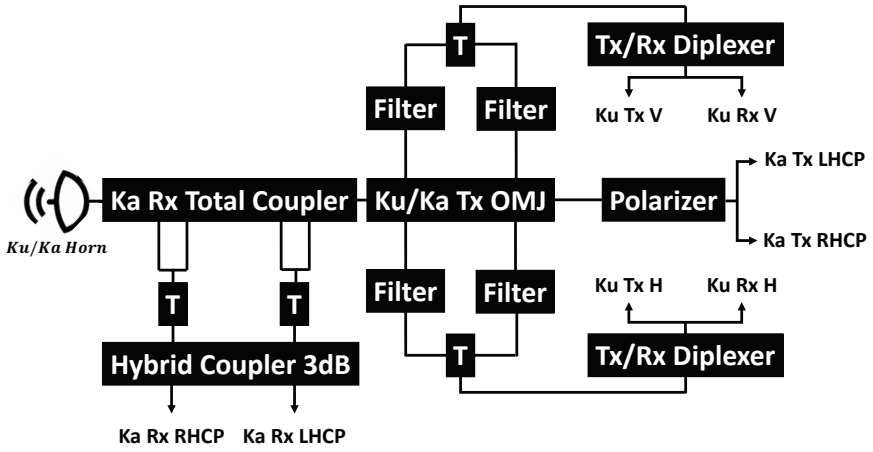

Figure 6.1: Example of Ku/Ka Tx/Rx multi-frequency feed architecture.

Moreover, waveguide BPFs based on either E-plane inserts [12], and classic inductive or capacitive irises [22] can show spurious responses in the upper stopband, specifically due to undesired resonances or the propagation of higher-order modes. Solutions based on evanescent mode filters [13] can extend the spurious-free region, but require narrow and reduced-height below cut-off housings with deep ridges, thus implying higher insertion losses and poor power handling performance [23]. Conversely, the topology proposed in this Chapter is able to avoid unwanted resonances in the stopband without any limitations in power handling or losses, due to the inherent harmonic suppression behavior of the band-pass structures included in the diplexer.

6.2 Objective

In this Chapter, the main objective is to develop a BPF design method to be utilized in high-performance satellite diplexers. These BPFs have to show relaxed manufacturing tolerances and a compact size to reduce as much as possible the mass and volume of the final diplexer and to allow a mass production with a very high fabrication yield.

6.3 Design Method

The in-band frequency response of the novel BPFs proposed in this Chapter is not based on coupled resonant structures as it happens in [20], [21], or in transmission lines of different characteristic impedances as it occurs in [15]. Instead, the passband

characteristic has been realized by combining a reduced-loss low-pass waveguide filter designed following the technique described in the previous Chapter in Section 5.3 and a high-pass configuration based on the cut-off effect [15]. The design procedure can be summarized in two steps: i) estimation of the required width and total length of the high-pass section, and ii) design of the BPF utilizing the LPF function and the previously calculated parameters. Since the method proposed in this Chapter is based on the combination of a high-pass and a low-pass response, a large variety of bandwidths can be easily addressed, even very large ones. In fact, the advantages of the method in terms of size and manufacturing robustness are more significant if wide passbands are required.

6.3.1 HPF Function

As it is well known, a rectangular waveguide can be seen as a high-pass filter where energy propagates only above the fundamental TE_{10}-mode cutoff frequency [15].

The fundamental TE_{10}-mode cutoff frequency of the high-pass filter function, f', only depends on the dimensions of the waveguide and, specifically, on the width of the waveguide. Therefore, it should be chosen between the lower passband edge, f_1, and the higher frequency of the lower stopband (LSB), f_{LSB}, of the BPF. Hence, the width of the high-pass filter section, a', will be fixed according to equation (6.1).

$$a' = \frac{c}{2 \cdot f'} \tag{6.1}$$

The fields of the traveling waves below cutoff attenuate exponentially along the filter length in the propagation direction (z-axis), following , where L_z is the length of the waveguide section, and α is the attenuation constant, which depends on the cutoff frequency as well as the width of the filter following equation (6.2).

$$\alpha = \frac{\pi}{a'}\sqrt{1 - \left(\frac{f_{LSB}}{f'}\right)^2} \tag{6.2}$$

Therefore, the value of f' is chosen low enough to fulfill the required in-band return loss specifications of the lower passband edge f_1, and to obtain a compact structure fulfilling the required attenuation (Att_1) at f_{LSB} following equation (6.3).

$$Att_1 = 20 \cdot \log\left(e^{\alpha \cdot L_z}\right)(dB) \tag{6.3}$$

Finally, a constant (simple to fabricate) width reduction (Figure 6.2(a)) can be utilized in the design of the BPF to accomplish very steep characteristics near the cutoff frequency. It is important to note, however, that the previous equations provide, along with the value of the waveguide length of width a', that is necessary to obtain the required attenuation in the LSB, Att_1. Since this estimation is obtained assuming a straight waveguide section, and the device will present height variations, shorter lengths will be actually required. In fact, as it will be shown in this work, a much shorter length will actually be required if large variations of the height are introduced along the propagation direction. So, L_z will determine an upper limit

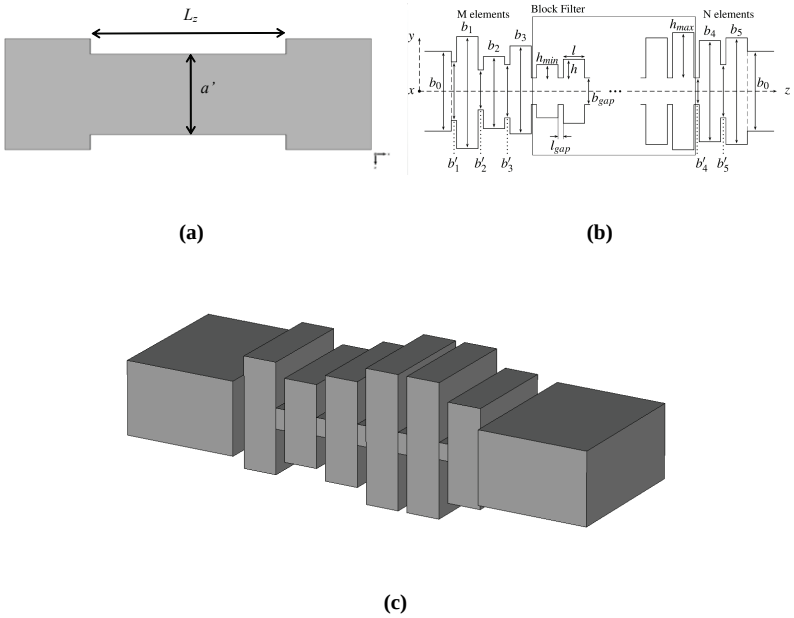

Figure 6.2: Schematics showing novel BPF composed of superposed low-pass and high-pass structures: (a) top view, (b) side view, and (c) 3D view.

for the length of the reduced width section which is required in the LPF function designed in the following Subsection.

6.3.2 LPF Function

In Chapter 5, the possibility of achieving LPF structures for the suppression of the fundamental mode over a very wide stopband was demonstrated. This technique will be used, in combination with the theory described in the previous Subsection, to design the BPF proposed in this Chapter. The attenuation of the upper stopband (USB) of the filter is achieved by means of n_{MB} λ_g/4-step-shaped bandstop elements of different heights, h (see Figure 6.2(b)). The attenuation at the minimum frequency (f_{min}) of the USB is achieved by means of the highest bandstop element (h_{max}), and the maximum frequency of the upper stopband (f_{max}) will be achieved with the shortest bandstop elements (h_{min}). The length of the bandstop elements, l, and the length of the waveguide sections between them, l_{gap}, as well as the minimum mechanical gap of the structure, b_{gap}, are free parameters and can be fixed to obtain the desired high-power performance of the filter (see Section 5.3). One of the most interesting advantages of the new LPF structure is that very steep slopes can be achieved with a very compact size by means of adding a few bandstop elements of the highest height, h_{max}, which introduces Tx zeros close to the minimum frequency of the upper stopband. The width of the bandstop elements and the width of the waveguide

sections between them will be determined by the high-pass filtering function calculated in the previous Subsection. Finally, two matching networks are added to the input and output ports of the filtering structure to obtain the required in-band return loss of the filter. In the case of all the filters in this Chapter, very short matching networks, actually consisting of only a single matching element will be needed.

Design Examples

According to the design methodology proposed, two different examples will be presented in this Chapter whose difference is the separation between the bands [1].

6.4 Design Example 1: Ku-Band Diplexer with Closely Spaced Bands

6.4.1 Requirements and Proposed Solution

The novel Ku-band diplexer requires a Tx-band filter with a passband defined between 10.7 GHz and 13 GHz, and a Rx-band filter with a passband between 13.75 GHz and 14.8 GHz. The overall bandwidth is 32%. The in-band return loss of both passbands is required to be better than 20 dB. The attenuation of the Rx channel over the Tx band must be better than 50 dB, whereas the Tx channel must provide at least 80 dB of rejection over the Rx band. In this case, the bands are separated 750 MHz and cover the classic Ku Tx and Rx bands.

The proposed solution consists of two novel BPFs (see Figure 6.2(c)) with WR75 waveguide ports, designed as described in Section 6.3, and connected together with a classical E-plane T-junction. As it will be shown, this solution is more compact and less sensitive to manufacturing tolerances in comparison with a classical diplexer based on two inductive-iris filters [24] designed to fulfill the same frequency specifications.

6.4.2 BPF for the Tx Band with Attenuation over the Rx band

A BPF following the technique presented in Section 6.3 has been designed. f'_{TX} is set to 10 GHz, low enough to fulfill the intended in-band return loss specifications of the lower passband edge, $f_{1,TX}$ (which is equal to 10.7 GHz). The reduced width of the structure has been fixed to 15 mm to achieve the high-pass filtering function. Since there are not specific requirements for the LSB in this filter, the length of the width reduction along the propagation direction, which achieves the high-pass filtering function, does not have to be fixed to a specific value. In order to fulfill the required USB in this filter, the heights of the four bandstop elements have been set to $\lambda_g/4$ (h_{max}=h_{min}=7.5 mm since the USB is narrow in this case). The length of the bandstop elements and the length of the waveguide sections between them have been fixed to 2.5 mm and 0.825 mm, respectively, to obtain a very compact structure (since they are free parameters in the design technique presented Section 6.3). The

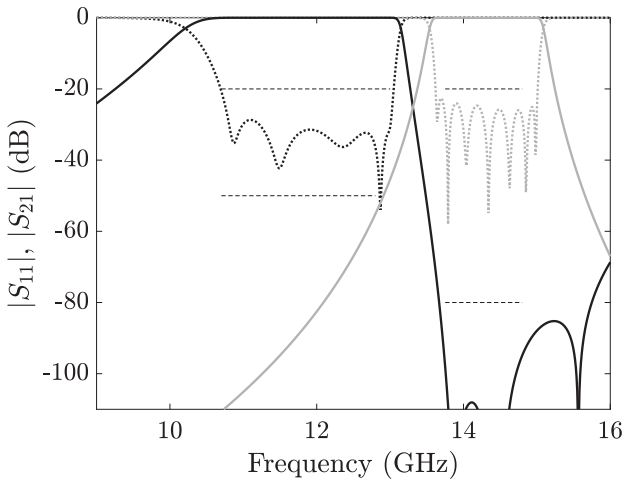

Figure 6.3: FEST3D simulated S-parameters ($|S_{11}|$ in dotted line and $|S_{21}|$ in solid line) for the proposed Ku-Tx-band BPF with attenuation over the Ku-Rx band (black line) and for the proposed Ku-Rx-band BPF with attenuation over the Ku-Tx band (grey line). Frequency specifications in thin lines.

Table 6.1: Final dimensions of the baseline filter.

Matching Networks	M = 1 and N = 1		
Main Block	h_{min} = 7.5 mm	h_{max} = 7.5 mm	n_{hmax} = 4
	b_{gmin} = 3 mm	b_{gmax} = 3 mm	n_{MB} = 4
	l_{min} = 2.5 mm	l_{max} = 2.5 mm	l_{gap} = 0.825 mm
High-pass	a' = 15 mm	L_s = 19.95 mm	

parameter b_{gap} has been fixed to 3 mm to accomplish a low-loss and high-power behavior. Finally, as stated above, a single matching element has been added to the input and output ports of the filtering structure to obtain the required passband specifications. The physical dimensions of the final BPF are detailed in Table 6.1. The simulated frequency response with FEST3D is shown in Figure 6.3.

6.4.3 BPF for the Rx Band with Attenuation over the Tx band

A very compact BPF has been designed following again the technique proposed in Section 6.3. $f_{1,RX}$, is equal to 13.75 GHz, and the required attenuation ($Att_{1,TX}$) over the Tx band (f_{LSB} = 13 GHz) is equal to 50 dB. Therefore, if f'_{RX} equal to 13.45 GHz is chosen , the reduced width, a', will be 11.15 mm, the attenuation constant α = 71.8 Np/m and the required length L_z for the high-pass filtering function will be around 80.2 mm (using equations (6.1), (6.2), and (6.3)). As it has been previ-

Table 6.2: Final dimensions of the baseline filter.

Matching Networks	M = 1 and N = 1		
Main Block	h_{min} = 6 mm	h_{max} = 6 mm	n_{hmax} = 4
	b_{gmin} = 3 mm	b_{gmax} = 3 mm	n_{MB} = 4
	l_{min} = 4 mm	l_{max} = 4 mm	l_{gap} = 4 mm
High-pass	a' = 11.15 mm	L_s = 48 mm	

ously explained, the L_z-length value is a first-order approximation of the final length in the reduced width section of the Rx filter. The required length of the proposed filter will be actually shorter due to the height variations of the structure.

Although there are not specific frequency requirements in the USB, the $\lambda_g/4$-step-shaped bandstop elements easily provide a high attenuation (more than 50 dB) at 16 GHz. The final physical dimensions of the filter are detailed in Table 6.2. The frequency performance of the final filter is shown in Figure 6.3.

6.4.4 Diplexing Junction

An E-plane T-junction has been chosen, although other different solutions could have also been used, e.g. bifurcations, manifolds, Y-junctions or H-plane T-junctions. An E-plane T-junction is a simple and wideband solution which allows fabricating the final device in clam-shell configuration, thus reducing the measured insertion loss of the prototype and the PIM products. The size of each port of the T-junction is 9.525 x 19.05 mm.

6.4.5 Design and Simulation

Once both filters are designed fulfilling the frequency specifications, they are connected together with the E-plane T-junction. Filters are joined directly to the junction by a waveguide section of minimum mechanical length, since it minimizes the effect of spurious resonances between filters.

Recently, a systematic method to design manifold-coupled multiplexers for wideband applications has been proposed in [25]. In the design of the diplexer of this Chapter, a similar stepwise optimization procedure has also been used to obtain the final frequency response of the diplexer. The length of each port of the E-plane T-junction are first optimized. Then, the dimensions of the transformers and the short waveguide sections which connect each filter to the junction are added to the optimization procedure. After that, the dimensions of the first elements of each filter are optimized and, once the frequency response is very close to the required performance, all dimensions of the diplexer are finely adjusted. The optimization has been performed using the FEST3D optimizer module.

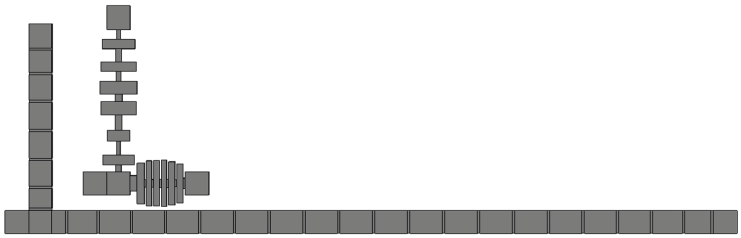

(a)

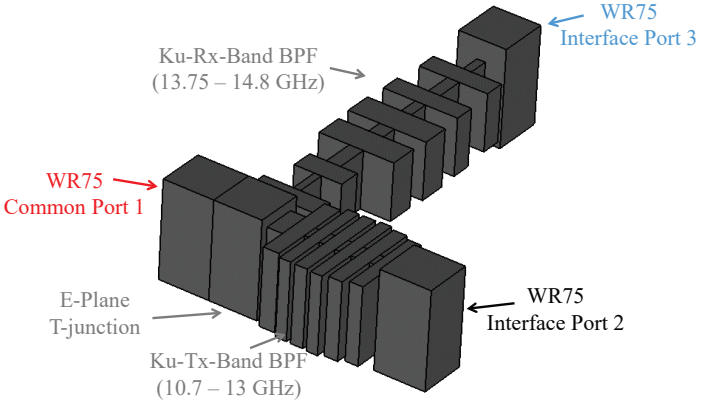

(b)

Figure 6.4: (a) Top view of the novel compact diplexer with closely spaced bands and its classical counterpart and (b) detail of the novel compact diplexer with closely spaced bands.

The final configuration of the Ku-band diplexer (Figure 6.4) has a total footprint of 55 x 70 mm. For comparison purposes, a classical diplexer, with two inductive iris filters connected with an E-plane T junction, has been designed fulfilling the same frequency specifications. The required order for the filters were 6 and 19, due to the relatively small separation between channels, resulting in a total footprint of 285 x 72 mm. The five-fold reduction in volume (and the corresponding mass reduction) is indeed a great advantage for satellite applications.

The simulated frequency response of the Ku-band diplexer with contiguous bands is presented in Figure 6.5 along with the classical diplexer with inductive filters.

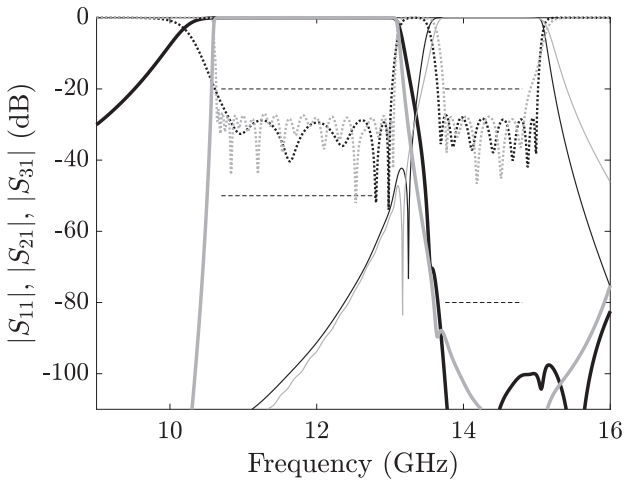

Figure 6.5: FEST3D simulated S-parameters ($|S_{11}|$ in dotted thick line, $|S_{21}|$ in solid thick line, and $|S_{31}|$ in solid thin line) for the proposed Ku-band diplexer with closely spaced bands (black line) and for a classical diplexer with inductive iris filters (grey line). Frequency specifications in thin lines.

6.4.6 Sensitivity Analysis

A sensitivity analysis to manufacturing tolerances has been performed to prove the advantage in terms of manufacturing robustness of the novel diplexer configuration. One hundred simulations varying all dimensions of the waveguide sections which compose the whole diplexer (heights, lengths, and widths) have been performed using FEST3D. The different physical dimensions are randomly generated by a Gaussian probability density function with a standard deviation equal to 15 μm with respect to the ideal (baseline) filter dimensions. This function corresponds, approximately, to a worst-case error value of $\pm$ 37.5 μm (i.e., low-cost milling tolerances). As it can be seen in Figure 5 and Figure 6, curves show a better fitting to the ideal frequency response for the novel diplexer (see Figure 6.6), resulting in an 87% manufacturing yield even in this low-cost milling case. However, using the same error distribution, the diplexer based on classical inductive iris filters shows a much worse performance with virtually 0% manufacturing yield (see Figure 6.7).

6.5 Design Example 2: Wideband Ku-K-Band Diplexer

6.5.1 Requirements and Proposed Solution

The specifications used in this Chapter to design a high-performance wideband non-contiguous Ku/K diplexer will be the same as those in the last Example of the previous Chapter in Section 5.10, [8] (detailed in Table 6.3) with an additional attenuation in the Rx channel to Ka-band signals between 27.5 and 31.5 GHz. The overall band-

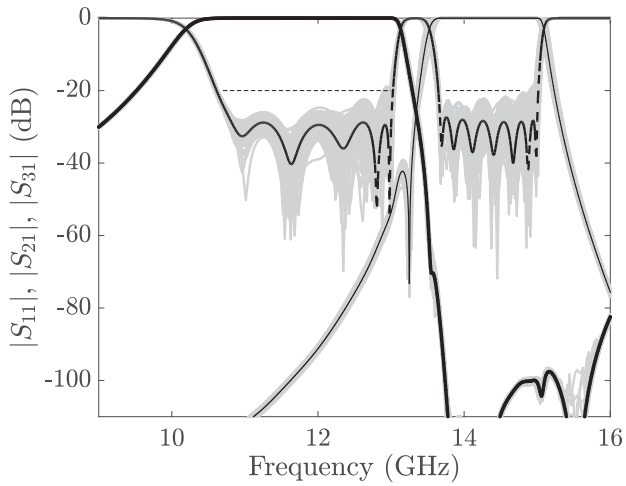

Figure 6.6: Sensitivity analysis to fabrication tolerances ($\pm$ 37.5 μm) of the novel Ku-band diplexer with closely spaced bands varying the physical dimensions of the filter. $|S_{11}|$ in dotted line, $|S_{11}|$ in solid thick line, and $|S_{11}|$ in solid thin black line for the baseline filter. Grey lines: simulation trials. Frequency specifications in thin lines.

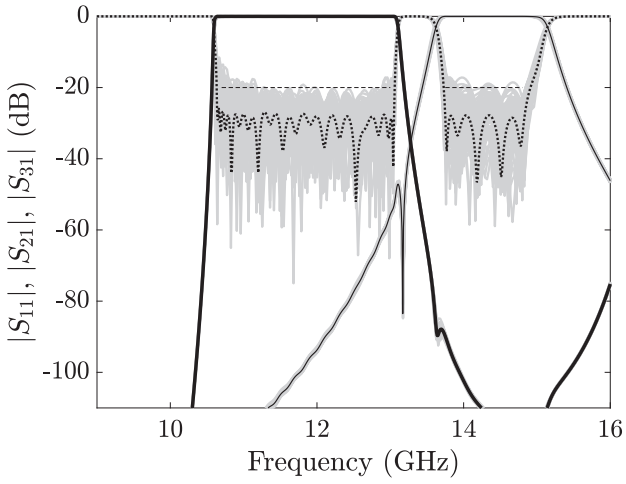

Figure 6.7: Sensitivity analysis to fabrication tolerances ($\pm$ 37.5 μm) of the classical Ku-band diplexer with closely spaced bands varying the physical dimensions of the filter. $|S_{11}|$ in dotted line, $|S_{11}|$ in solid thick line, and $|S_{11}|$ in solid thin black line for the baseline filter. Grey lines: simulation trials. Frequency specifications in thin lines.

Table 6.3: Summary of the wideband diplexer specifications.

Ku-Tx-band filter ($f_{1,TX} - f_{2,TX}$)	10.7 – 13 GHz
Ku-Rx-band filter ($f_{1,RX} - f_{2,RX}$)	17.2 – 18.5 GHz
Return loss at interface ports	$>$20 dB
Insertion loss at interface ports	$<$0.2 dB
Attenuation at Tx band ($Att_{1,TX}$)	$>$50 dB
Attenuation at Rx band ($Att_{2,RX}$)	$>$80 dB
Ku Tx-band interface port	WR75
K Rx-band interface port	WR51
Common interface port	WR75
Multipactor threshold level	$>$2.5 kW

width of the diplexer is 53.4%, and the fractional bandwidths are 19.4% and 7.3% for the Tx and Rx band, respectively. During the diplexer design, the filters and the junction are designed independently, and then put together to obtain the final diplexer configuration.

The novel Ku/K-band diplexer is based on two BPFs following the design technique in this Chapter, connected together with an E-plane T junction. Unlike the novel filter of the previous Example, the proposed filter for the Ku-Tx band must avoid the propagation of the higher-order modes which could appear in the intended Rx band.

The proposed diplexer will be compared to a conventional diplexer composed of an E-plane T-junction which uses a classical corrugated LPF with reduced width to deal with the higher-order TE_{n0} modes and a classical inductive iris filter, fulfilling the same frequency specifications. The main advantage of the final diplexer configuration in comparison with the classical diplexer, and also with the diplexer in Section 5.10, [8], will be a dramatic footprint reduction.

6.5.2 BPF for the Tx Band with Attenuation over the Rx band

In Section 5.10, [8], a more compact low-pass alternative to the classical waffle-iron filter or the corrugated filter with width modification was used. In this Chapter instead, a BPF following the technique of Section 6.3 has been designed. To do so, f'_{TX} is set to 10 GHz, low enough to fulfill the intended in-band return loss specifications of the lower passband edge, $f_{1,TX}$ (which is equal to 10.7 GHz), and to avoid the higher-order TE_{20} mode propagation over the Rx band. The reduced width of the structure has been therefore fixed to 15 mm, which achieves both features. The minimum mechanical gap of the structure, b_{gap}, has been fixed to 3 mm to achieve a high power handling capability, and the suppression of the higher-order non-TE_{n0}

Table 6.4: Final dimensions of the K-Tx-band filter.

Matching Networks	M = 1 and N = 1		
Main Block	h_{min} = 5.6 mm	h_{max} = 5.6 mm	n_{hmax} = 3
	b_{gmin} = 3 mm	b_{gmax} = 3 mm	n_{MB} = 3
	l_{min} = 3 mm	l_{max} = 3 mm	l_{gap} = 0.825 mm
High-pass	a' = 15 mm	L_s = 19.125 mm	

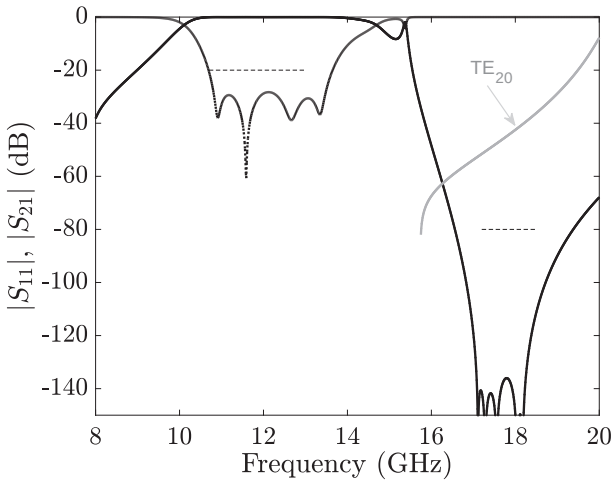

Figure 6.8: FEST3D simulated S-parameters ($|S_{11}|$ in dotted line and $|S_{11}|$ in solid line) for the TE_{10} mode in the proposed Ku-Tx-band BPF (black line) and for the higher-order modes (grey line) (rest of higher-order modes not shown are kept below -150 dB). Frequency specifications in dashed line.

modes (TE_{01}, TE_{11}, and TM_{11}). The physical dimensions of the final BPF are given in Table 6.4.

The FEST3D simulated frequency response is shown in Figure 6.8. Since in this example there is a wide transition between the Tx and the Rx band, some spikes may appear in this frequency range during the optimization process (at 16 GHz in this case) which are not relevant as long as the filter/diplexer fulfills the frequency specifications. Specifically, in this case the filter shows an attenuation level better than 80 dB over the Rx band and return loss better than 20 dB in the Tx band. Finally, the insertion loss of the filter is kept below 0.2 dB and the power threshold is better than 10 kW, as it will be shown in Section 6.5.8. Note also that the filter achieves successfully the suppression of all higher-order modes up to 18.5 GHz.

Table 6.5: Final dimensions of the K-Rx-band filter.

Matching Networks	M = 1 and N = 1		
Main Block	h_{min} = 4.24 mm	h_{max} = 4.26 mm	n_{hmax} = 2
	b_{gmin} = 2 mm	b_{gmax} = 2 mm	n_{MB} = 2
	l_{min} = 4 mm	l_{max} = 4 mm	l_{gap} = 0.825 mm
High-pass	a' = 9.375 mm	L_s = 19.3 mm	

6.5.3 BPF for the Rx Band with Attenuation over the Tx Band

A compact BPF has been designed following Section 6.3. $f_{1,RX}$, is equal to 17.2 GHz, f_{LSB} = 13 GHz, and the required attenuation ($Att_{1,TX}$) over the Tx band is equal to 50 dB (see Table 6.3). Hence, if f'_{RX} equal to 16 GHz is chosen, the reduced width, a', will be 9.375 mm, the attenuation constant α = 195.1 Np/m and the required length L_z for the high-pass filtering function will be around 29.5 mm (using equations (6.1), (6.2), and (6.3)). As it has been previously explained, the L_z-length value is an approximation of the current final length, as the required length of the final filter will be shorter due to the height variations of the structure.

The quarter-wave step-shaped bandstop elements are fixed to accomplish the required additional attenuation in the Rx channel to signals between 27.5 and 31.5 GHz. The final physical dimensions of the filter are detailed in Table 6.5. It is important to note that a filter with a length of only 19.3 mm is now needed to reach the required attenuation in the LSB, in comparison with the 26.85 mm needed in Section 5.10, [8] (around 30%-length reduction).

The frequency performance of the final filter is shown in Figure 6.9. The insertion loss of the filter is kept below 0.2 dB and the multipactor threshold level is higher than 10 kW, as it will be shown in Section 6.5.8. Furthermore, the Rx-band BPF achieves the suppression of the higher-order modes up to 31.5 GHz (while the classical inductive-iris filter proposed in Section 5.10, [8] does not achieve it).

6.5.4 Duplexing Junction

As in the previous Example, an E-plane T-junction has been chosen because it minimizes the measured insertion loss of the prototype and the PIM products. The size of each port of the T-junction is 5 x 15 mm. These dimensions ensure single-mode operation in the junction. In this case, a height and width transformer has been utilized for the connection to the standard common port, since it leads to less spurious resonances in the final diplexer frequency response in comparison with the matching network that was used in Section 5.10, [8].

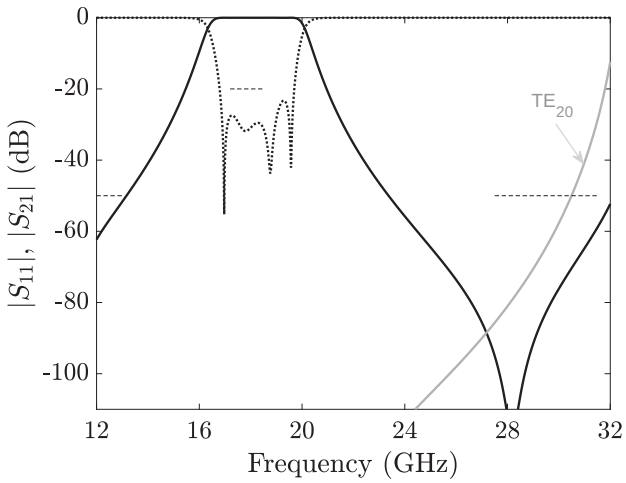

Figure 6.9: FEST3D simulated S-parameters ($|S_{11}|$ in dotted line and $|S_{11}|$ in solid line) for the TE_{10} mode in the proposed K-Rx-band BPF (black line) and for the higher-order modes (grey line) (rest of higher-order modes not shown are kept below -150 dB). Frequency specifications in dashed line.

6.5.5 Design and Simulation

The final configuration of the Ku/K-band diplexer can be seen in Figure 6.10, showing a footprint of 34 x 42 mm, about half of the size than the diplexer in Section 5.10, [8] (45 x 65 mm). This volume reduction is mainly due to the Rx-band filter length reduction, and from the new topology of BPFs that allows a more suitable physical arrangement within the diplexer.

The frequency response of the diplexer (FEST3D) is presented in Figure 6.11. The in-band return loss over both passbands is better than 20 dB. The attenuation level over the Rx band is kept below 80 dB. Furthermore, the rejection over the Tx band is better than 50 dB. Also, a 50 dB attenuation in the Rx channel to signals between 27.5 and 31.5 GHz is accomplished (see Figure 6.12).

Similarly, the simulated frequency response of a classical diplexer is also shown in Figure 6.11 (FEST3D). This diplexer is composed of a classical corrugated filter (order 11) with width modification (to suppress all the higher-order modes) and a classical H-plane BPF with inductive irises (order 5) connected together with the same E-plane T-junction used in this example. As in the comparison with Section 5.10, [8], the configuration in this Section is more compact than the classical diplexer (34 x 42 mm vs. 136 x 50 mm).

6.5.6 Sensitivity Analysis

The sensitivity analysis performed to demonstrate the robustness of the prototype is the same as in the previous Example. One hundred simulations varying all di-

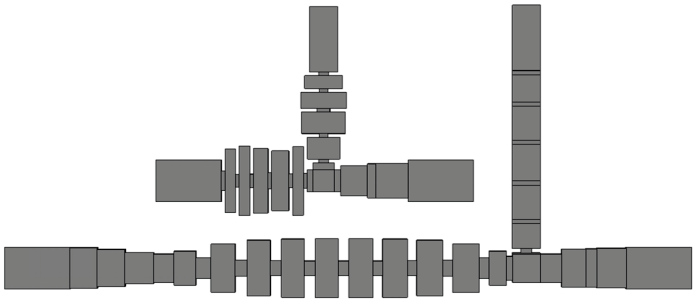

(a)

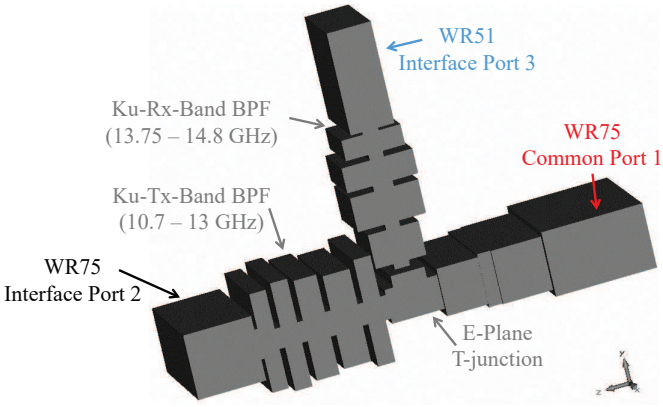

(b)

Figure 6.10: (a) Top view of the novel compact wideband diplexer and its classical counterpart and (b) detail of the novel compact wideband diplexer.

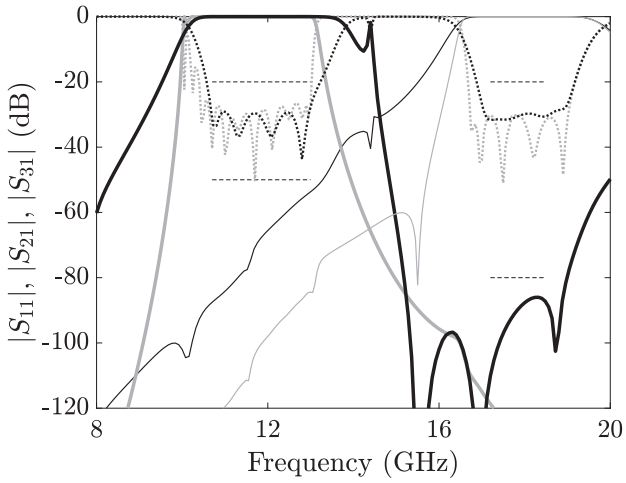

Figure 6.11: FEST3D simulated frequency response for the novel compact wideband diplexer (black line), and for the conventional diplexer (grey line). $|S_{11}|$ in dotted line, $|S_{21}|$ in solid thick line, and $|S_{31}|$ in solid thin line. Frequency specifications in thin line.

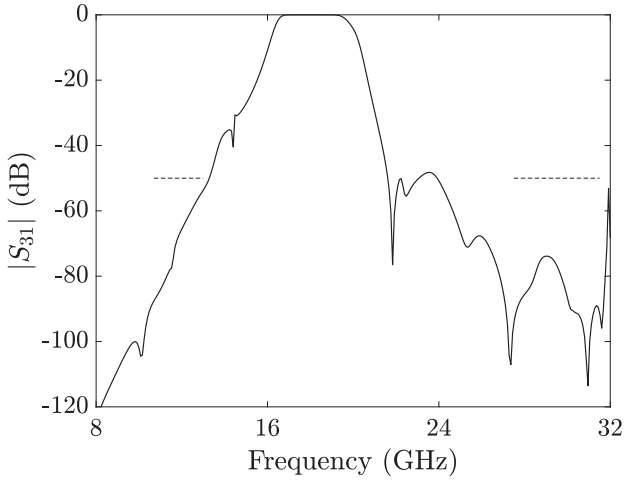

Figure 6.12: FEST3D simulated $|S_{31}|$ parameter of the novel compact wideband diplexer showing the additional 50 dB attenuation in the Rx channel to signals between 27.5 and 31.5 GHz. Frequency specifications in thin line.

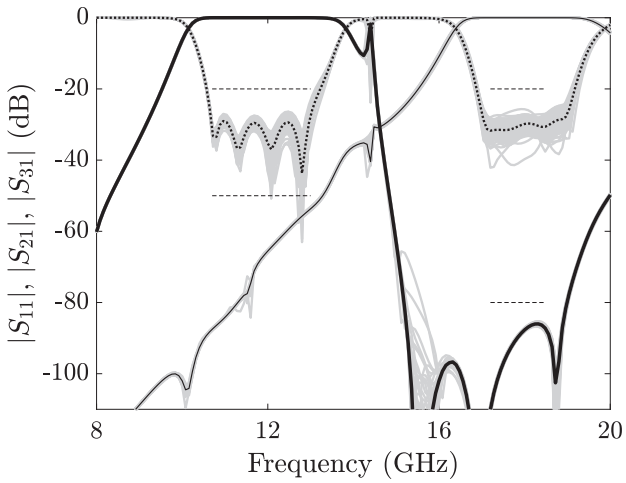

Figure 6.13: Sensitivity analysis to fabrication tolerances ($\pm$ 25 μm) in the entire frequency response of the novel compact wideband diplexer varying the physical dimensions of the filter. $|S_{11}|$ in dotted line, $|S_{21}|$ in solid thick line, and $|S_{31}|$ in solid thin black line for the baseline filter. Grey lines: simulation trials. Frequency specifications in thin lines.

mensions following a Gaussian probability density function (standard deviation of 10 μm) have been performed using FEST3D. This function corresponds, approximately, to a worst-case manufacturing error of $\pm$ 25 μm (consistent with a low-cost manufacture) with respect to the ideal filter dimensions. As it can be seen in Figure 6.13, the curves show again a very good fitting to the ideal frequency response. On the contrary, the filter based on resonant cavities (K-Rx-band filter in Figure 6.14) shows much stronger variations in the in-band return loss in comparison with the novel filter in this Chapter. The high-order corrugated filter of the classical diplexer implementation also provides worse deviations than the novel filter proposed for the Tx channel.

In conclusion, the previous analyses (Figures 6.6, 6.7, 6.13, and 6.14) clearly demonstrate that the novel diplexers proposed in this Chapter are more robust to manufacturing deviations than traditional diplexer implementations. As a consequence, the novel compact diplexer configuration proposed here can be more easily produced by low-cost high-yield CCM manufacturing techniques.

6.5.7 Fabrication and Measurement

An aluminum prototype has been fabricated using CCM according to a clam-shell configuration (two identical halves). For a low-cost manufacturing, it is usually necessary during the design phase, to take into account the rounding of the corners typically present in classical milling procedures. Unlike Section 5.10, [8], the rounding of the corners (radius of the tool equal to 1 mm) was not considered in the optimiza-

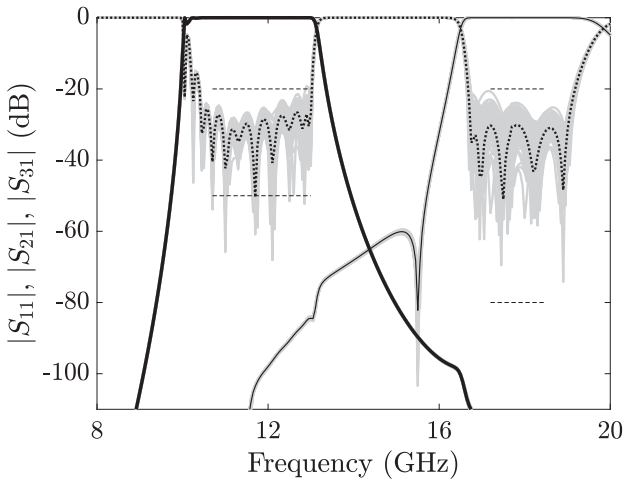

Figure 6.14: Sensitivity analysis to fabrication tolerances ($\pm$ 25 μm) in the entire frequency response of a classical wideband diplexer varying the physical dimensions of the filter. $|S_{11}|$ in dotted line, $|S_{21}|$ in solid thick line, and $|S_{31}|$ in solid thin black line for the baseline filter. Grey lines: simulation trials. Frequency specifications in dashed lines.

tion procedure of the diplexer in this Chapter. This is because the filters proposed in this work (in contrast to the more sensitive classical inductive-coupled filters [26]) are robust enough not to be affected by the rounded corners. This speeds up the design procedure and optimization, thus implying lower costs and higher production yields. The final configuration of the diplexer, taking also into account rounded corners, is shown in Figure 6.15. As it can be seen in Figure 6.16, there are no (relevant) differences between the frequency response of the diplexer with sharp corners and the one with rounded corners.

The fabricated prototype is shown in Figure 6.17. The diplexer has been measured using an Agilent E8364B PNA, proper waveguide-to-coaxial transitions, waveguide tapers, loads, and calibration kits. The measurements have been carried out in the WR90 (8-10 GHz), WR75 (10-15 GHz), and WR51 (15-20 GHz) bands. The results show, as required, a rejection better than 80 dB in the Tx-band, and better than 50 dB in the Rx band (see Figure 6.18). Moreover, the measured in-band return loss of the filter is kept better than 20 dB in both the Tx and the Rx band. The insertion loss of the diplexer is kept below 0.2 dB for each band even without silver-plating.

Finally, the additional rejection in the Rx channel has been measured in WR28 (26.5-32 GHz). As it can be seen in Figure 6.19, the attenuation achieved for these frequencies is better than 50 dB, fulfilling also this goal.

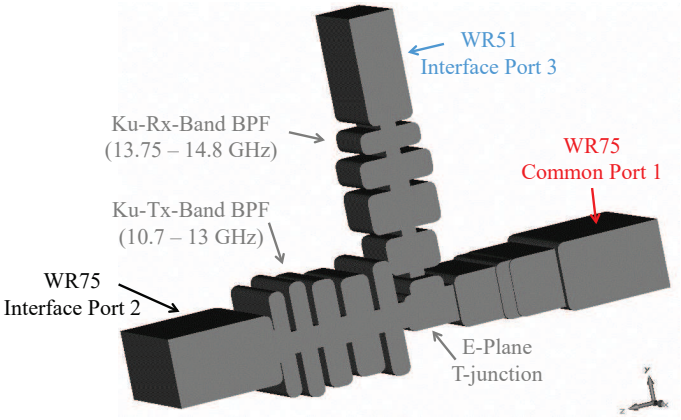

Figure 6.15: 3D view of the diplexer designed in Section 6.5.

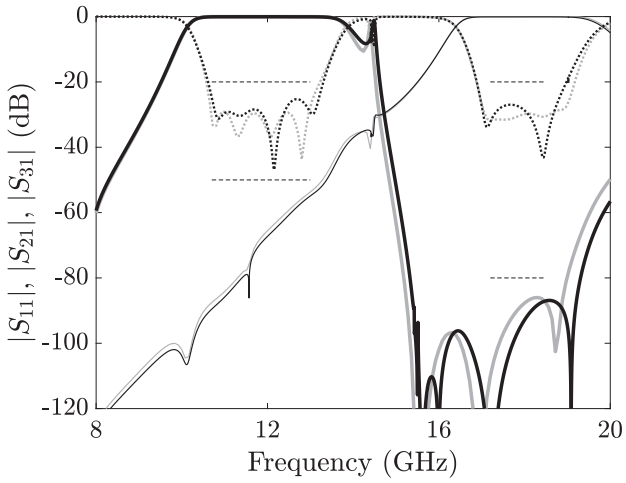

Figure 6.16: Comparison between the simulated frequency response taking into account the rounding of the corners (CST MWS) on the proposed diplexer designed in Section 6.5 with (black line), and without the rounded corners (FEST3D) (grey line). $|S_{11}|$ in dotted line, $|S_{21}|$ in solid thick line, and $|S_{31}|$ in solid thin line. Frequency specifications in thin lines.

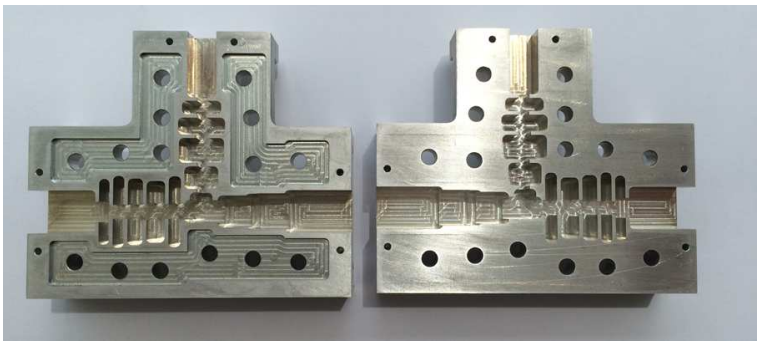

Figure 6.17: Photograph of the unassembled prototype of the diplexer designed in Section 6.5 and fabricated by computer-controlled milling in aluminum in clam-shell configuration.

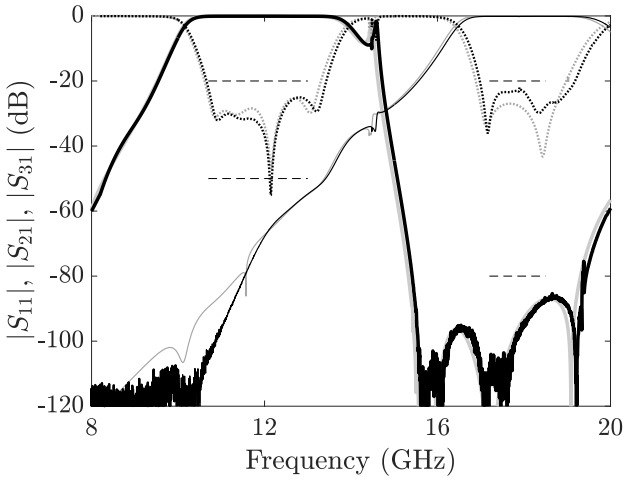

Figure 6.18: Comparison between the CST MWS simulated frequency response (grey line) of the final diplexer designed in Section 6.5 with rounded corners and measurements of the fabricated prototype (black line). $|S_{11}|$ in dotted line, $|S_{21}|$ in solid thick line, and $|S_{31}|$ in solid thin line. Frequency specifications in thin lines.

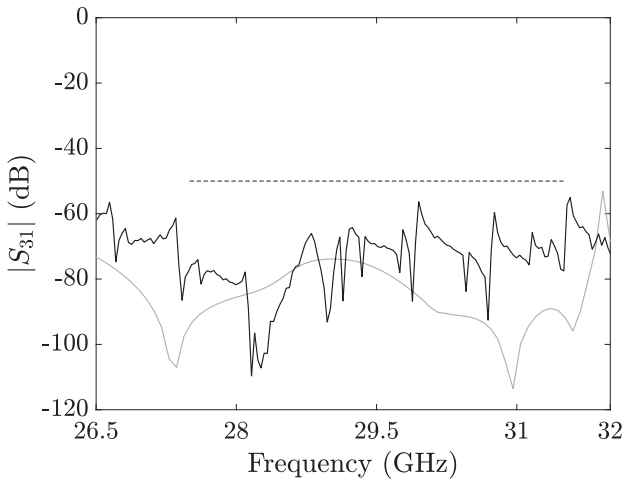

Figure 6.19: Detail of the additional rejection in the 27.5 – 31.5 GHz in the Rx band. Comparison between the CST MWS simulated $|S_{31}|$ parameter (grey line) of the final diplexer designed in Section 6.5 with rounded corners and measurements of the fabricated prototype (black line). Frequency specifications in dashed line.

6.5.8 High-Power Behavior

In a typical communication payload, the Tx-band filter of a diplexer needs to handle all the power combined in the manifold and generated in the satellite. This power is much higher than the one received from the Earth (through the Rx-band filter) and, therefore, the Tx-band filter typically limits the overall power-handling capability of the diplexer. However, in the following, a high-power analysis will be conducted in the whole device to make sure that no power limitations are observed anywhere in the diplexer. The multipactor threshold level has been estimated by means of SPARK3D, considering the EM fields previously calculated with CST MWS (see Figure 6.20). The four passband frequencies edges have been utilized in the analysis (10.7 GHz, 13 GHz, 17.2 GHz, and 18.5 GHz), since these are the critical frequencies at which EM fields are maximum. The SEY of ECSS aluminum has been used [27].

The worst case of multipactor threshold level has been obtained at 13 GHz (all results are summarized in Table 6.6). The novel compact high-performance diplexer can handle up to 10 kW. It is important to note that if the diplexer was silver-plated, the multipactor threshold level would have been higher (since the SEY of silver is lower than the SEY of aluminum).

6.6 Conclusions

In this Chapter, two very compact diplexers for Ku- and K- band satellite applications have been presented, based on novel BPF structures. The proposed BPFs are

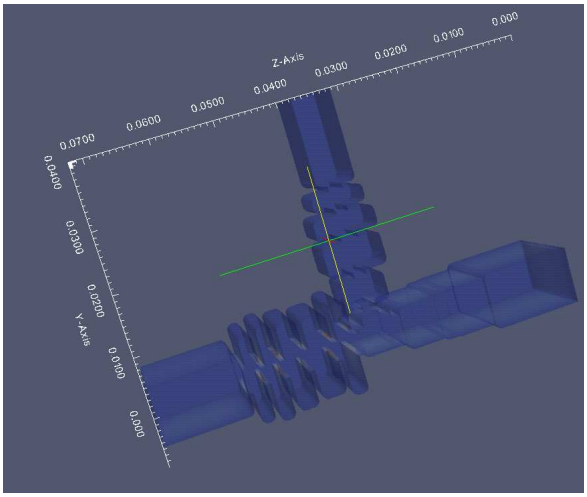

Figure 6.20: EM fields simulated with CST MWS and imported to SPARK3D for the novel diplexer designed in Section 6.5.

Table 6.6: Summary of multipactor threshold levels obtained with SPARK3D for the novel diplexer designed in Section 6.5.

10.7 GHz	13 GHz	17.2 GHz	18.5 GHz
$>$40 kW	$>$10 kW	$>$80 kW	$>$100 kW

designed by combining low-pass and high-pass responses. The high-pass response is achieved by means of a width reduction along the propagation direction of the filter, making use of the waveguide cutoff effect. The low-pass response is based on quarter-wave step-shaped bandstop elements separated by very short waveguide sections. Two extremely short matching networks are added on both sides of the filter to accomplish the required return loss. This technique allows to design and manufacture very practical, compact BPFs with very wide rejection bands, low losses and high power-handling. Moreover, very steep slopes between the passband and the rejection bands can be accomplished in a very compact size (this does not occur in classical implementations, where high orders are needed). The novel diplexers benefit from this very compact size, which makes them especially attractive for satellite applications, where compact hardware is needed to reduce mass and volume. Besides, the rounding of the corners, typically present in milling fabrication procedures, does not affect the filter behavior, thereby further simplifying the design process. A high-performance wideband Ku/K-band prototype has been manufactured in clam-shell configuration demonstrating the validity of the novel diplexer configuration. Finally, the very close agreement achieved between simulations and measurements fully validates the novel diplexer configuration proposed in this Chapter.

REFERENCES

[1] F. Teberio, I. Arregui, P. Soto, M. A. G. Laso, V. E. Boria, and M. Guglielmi, "High-performance compact diplexers for ku/k-band satellite applications," *IEEE Transactions on Microwave Theory and Techniques*, vol. 65, no. 10, pp. 3866–3876, Oct. 2017.

[2] I. Arregui, F. Teberio, I. Arnedo, A. Gomez-Torrent, J. M. Percaz, M. Chudzik, M. A. G. Laso, and T. Lopetegi, "Resonant quasi-periodic structure for rectangular waveguide technology with wide stopband and ban-pass behaviour," *Progress In Electromagnetics Research C*, vol. 69, pp. 97–104, Nov. 2016.

[3] D. Scouarnec, S. Stirland, and H. Wolf, "Current antenna products and future evolution trends for telecommunicatio satellites application," in *2013 IEEE-APS Topical Conference on Antennas and Propagation in Wireless Communications (APWC)*, Sep. 2013, pp. 1412–1415.

[4] A. Abramowicz, A. Sibiga, and M. Znojkiewicz, "Design and realization of low cost waveguide filters and diplexers," in *2002 14th International Conference on Microwaves, Radar and Wireless Communications (MIKON)*, vol. 2, 2002, 603–606 vol.2.

[5] J. R. Aitken and J. Hong, "Tolerance considerations for wireless backhaul diplexer circuits," in *2014 44th European Microwave Conference (EuMC)*, Oct. 2014, pp. 620–623.

[6] J. Uher, J. Bornemann, and U. Rosenberg, *Waveguide Components for Antenna Feed Systems: Theory and CAD*. Artech House, 1993.

[7] U. Rosenberg, A. Bradt, M. Perelshtein, and P. Bourbonnais, "Extreme broadband waveguide diplexer design for high performance antenna feed systems," in *2010 40th European Microwave Conference (EuMC)*, Sep. 2010, pp. 1249–1252.

[8] F. Teberio, I. Arregui, M. Guglielmi, A. Gomez-Torrent, P. Soto, M. A. G. Laso, and V. E. Boria, "Compact broadband waveguide diplexer for satellite applications," in *2016 IEEE MTT-S International Microwave Symposium Digest (IMS)*, May 2016, pp. 1–4.

[9] J. M. Rebollar, J. R. Montejo-Garai, and A. Ohoro, "Asymmetric H-plane T-junction for broadband diplexer applications," in *IEEE Antennas and Propagation Society International Symposium. Transmitting Waves of Progress to the Next Millennium. 2000 Digest. Held in conjunction with: USNC/URSI National Radio Science Meeting (C*, vol. 4, Jul. 2000, 2032–2035 vol.4.

[10] J. Bornemann and M. Mokhtaari, "The bifurcated E-plane T-junction and its application to waveguide diplexer design," in *in Proc. German Microwave Conference*, vol. 1a-5, Mar. 2006, 4 p.

[11] J. Dittloff and F. Arndt, "Computer-aided design of slit-coupled H-plane T-junction diplexers with E-plane metal-insert filters," *IEEE Transactions on Microwave Theory and Techniques*, vol. 36, no. 12, pp. 1833–1840, Dec. 1988.

[12] E. Ofli, R. Vahldieck, and S. Amari, "Novel E-plane filters and diplexers with elliptic response for millimeter-wave applications," *IEEE Transactions on Microwave Theory and Techniques*, vol. 53, no. 3, pp. 843–851, Mar. 2005.

[13] R. V. Snyder, "New application of evanescent mode waveguide to filter design," in *1977 IEEE MTT-S International Microwave Symposium Digest (IMS)*, Jun. 1977, pp. 294–297.

[14] F. Teberio, I. Arnedo, J. M. Percaz, I. Arregui, P. Martin-Iglesias, T. Lopetegi, and M. A. G. Laso, "Accurate synthesis procedure for waffle-iron low-pass filter," in *2018 IEEE MTT-S International Microwave Symposium Digest (IMS)*, Jun. 2018.

[15] W. Hauth, R. Keller, and U. Rosenberg, "Cad of waveguide low-pass filters for satellite applications," in *1987 17th European Microwave Conference (EuMC)*, Sep. 1987.

[16] F. Teberio, I. Arregui, A. Gomez-Torrent, I. Arnedo, M. Chudzik, M. Zedler, F. J. Görtz, R. Jost, T. Lopetegi, and M. A. G. Laso, "Chirping techniques to maximize the power-handling capability of harmonic waveguide low-pass filters," *IEEE Transactions on Microwave Theory and Techniques*, vol. 64, no. 9, pp. 2814–2823, Sep. 2016.

[17] J. Bornemann, U. Rosenberg, S. Amari, and R. Vahldieck, "Tolerance analysis of bypass-, cross- and direct-coupled rectangular waveguide band-pass filters," *IEE Proceedings - Microwaves, Antennas and Propagation*, vol. 152, no. 3, pp. 167–170, Jun. 2005.

[18] P. S. Pacheco, V. E. B. Esbert, C. C. Candau, C. P. V. Quiles, J. G. Raga, and B. G. Martínez, "Em-based synthesis and design of bandpass waveguide filters including manufacturing effects with fest 3d," *International Journal of RF and Microwave Computer-Aided Engineering*, vol. 22, no. 1, pp. 93–103, 2012.

[19] A. Morini, G. Venanzoni, M. Farina, and T. Rozzi, "Practical design of a high-power tuning-less w-band triplexer for ground radar surveillance systems," *IET Microwaves, Antennas Propagation*, vol. 1, no. 4, pp. 822–826, Aug. 2007.

[20] J. R. Aitken and J. Hong, "Design of millimetre wave diplexers with relaxed fabrication tolerances," *IET Microwaves, Antennas Propagation*, vol. 9, no. 8, pp. 802–807, 2015.

[21] G. Cannone and M. Oldoni, "High-yield E-band diplexer for fixed radio point-to-point equipment," *International Journal of RF and Microwave Computer-Aided Engineering*, vol. 24, no. 9, pp. 508–512, Dec. 2013.

[22] G. Matthaei, L. Young, and E. M. T. Jones, *Microwave filters, impedance-matching networks and coupling structures*. Artech House, 1980.

[23] P. Soto, D. d. Llanos, V. E. Boria, E. Tarín, B. Gimeno, A. Oñoro, I. Hidalgo, and M. J. Padilla, "Performance analysis and comparison of symmetrical and asymmetrical configurations of evanescent mode ridge waveguide filters," *Radio Science*, vol. 44, no. 06, pp. 1–16, Dec. 2009.

[24] R. Cameron, C. Kudsia, and R. Mansour, *Microwave Filters for Communication Systems: Fundamentals, Design and Applications*. Wiley-Interscience, 2007.

[25] C. Carceller, P. Soto, V. Boria, M. Guglielmi, and J. Gil, "Design of compact wideband manifold-coupled multiplexers," *IEEE Transactions on Microwave Theory and Techniques*, vol. 63, no. 10, pp. 3398–3407, Oct. 2015.

[26] S. Cogollos, V. Boria, P. Soto, B. Gimeno, and M. Guglielmi, "Efficient CAD tool for inductively coupled rectangular waveguide filters with rounded corners," in *2001 31st European Microwave Conference (EuMC)*, Sep. 2001, pp. 1–4.

[27] ESA, *ECSS Space engineering, multipactor design, and test*. Noordwijk, The Neederlands: ESA Publications Division, Apr. 2000, vol. ECSS-E-20-01.

CHAPTER 7

STEPPED-IMPEDANCE BPFs WITH REDUCED SENSITIVITY TO FABRICATION TOLERANCES FOR Q/V BANDS

In this Chapter, a novel BPFs with very low sensitivity to fabrication tolerances is proposed [1]–[4]. It exploits the inherent first passband replica of the commensurate-line stepped-impedance LPF and utilizes a constant width reduction to obtain a significant enhancement in the fabrication yield. This improvement in the tolerances is especially attractive for space applications in the millimeter-wave range. The validity of the novel design techniques have been demonstrated with two examples: a BPF with constant width reduction and a BPF with narrower bandwidth in comparison with the previous one, both aimed at utilizing in Q-band payloads. In fact, the manufacturing yield has been dramatically improved when compared to its classical counterparts. A prototype has been fabricated using CCM showing an excellent agreement between simulated and measured results.
It is important to note that the BPFs developed in this Chapter were done within the framework of a NPI activity (UPNA – ESA – Thales Alenia Space - Spain) [5].

7.1 Background

Broadband satellite communications currently demand higher traffic capabilities between gateways and satellites. Recently, there have been multiples studies in both the academia and the industry focused on the exploration of higher frequencies for future payload applications. In fact, it supports the trend to use the Q/V bands (around 40 GHz for the downlink and around 50 GHz for the uplink) in the near and far future for commercial telecommunication programs [6]–[10]. The payload of these satellites uses architectures with waveguide BPFs aiming to remove unwanted spurious harmonics coming from other instruments embarked in the same platform [11]–[13].

Typical solutions for BPFs for Q-, V-, W-bands use the traditional concept of coupled resonant cavities. Indeed, inductive iris and capacitive iris filters are the most commonly employed solutions [14]–[17]. However, filters based on resonant cavities are sensitive to manufacturing tolerances [18]–[20]. At these frequencies, the key-design dimensions are of the same order as the radius of the machining-tool if a conventional CCM fabrication method is used. This issue requires both imposing more stringent tolerances to the manufactured devices and sometimes, the use of tuning elements to fulfill the frequency specifications. Nevertheless, this is not always possible due to the size of the tuning screws and the cavities. Moreover, classical design methods in combination with tuning elements and traditional manufacturing techniques are quite limited in terms of achievable quality factor, which determines the spectral efficiency.

Some ideas to relax the fabrication tolerances and avoid tuning screws in classical coupled resonant structures (inductive and capacitive iris devices) such as the most obvious, designing the filters to have sufficient margin to fulfill the frequency specifications have been proposed in the literature [14]. The number of resonating structures can be minimized as well as make the resonator lengths larger to improve the tolerance issues [15]. However, the latter will imply that the overall size of the filter may increase and spurious resonances may appear below the passbands, which usually does not occur when half-wavelength resonators are used [16]. E-plane filters are a very good alternative to classical filters in millimeter-wave applications since the pattern can be fabricated with high precision using photolithography or electro-deposition techniques [21], making it particularly attractive to low-cost mass

Figure 7.1: Q-band inductive-iris BPFs courtesy of Thales Alenia Space - Spain.

production. Despite their favorable characteristics, E-plane filters suffer from their relative narrow bandwidth due to the minimum realizable width of the metallic strip and the narrow second stopband. Lately, many novel E-plane filters have been developed to improve the filter performance [22].

Stepped-impedance structures have been classically employed in rectangular waveguide to implement LPFs or transformers [23], [24]. In this Chapter, a novel BPFs is designed using the first inherent passband replica of the classical commensurate-line stepped-impedance low-pass structure. Actually, Matthaei *et al.* [25] pointed out the possibility of using this technique to design BPFs, but without direct practical application and only as a conceptual prototype for the ulterior implementation of wide-band reactance-coupled half-wave filters. The BPFs proposed in this Chapter are made of transmission line sections of alternate high and low characteristic impedance (stepped-impedance) that are implemented by means of a cascade of rectangular waveguide sections of different heights and where the waveguide width is reduced in a constant manner to improve dramatically the manufacturing yield of the final prototype [1].

7.2 Objective

The aim of this Chapter is to find a novel design technique that leads to low sensitivity Q-V band BPFs. The technique should provide geometries that can be readily fabricated by means of low-cost CCM without additional requirements in terms of fabrication tolerances, i.e. avoiding the use of tuning screws.

7.3 Design Method

The proposed N-th order BPFs are built by cascading a set of $N+2$ rectangular waveguide sections (including the input/output ports). They are designed utilizing the first inherent passband replica of the classical distributed low-pass prototype (presented in Chapter 2), which is based on the connection of high and low impedance transmission lines (see Figure 7.2(a)), all with the same electrical length θ (commensurate lines - Unit Elements). The different Unit Elements which compose this structure have the same frequency behavior, since they are commensurate and homogeneous. Indeed, all sections ideally have the same physical length l, and show the same wavelength λ_g, at any frequency. These properties allow to define the frequency behavior of the prototype as a function of the electrical length of a section.

$$\theta = \beta \cdot l = \frac{2 \cdot \pi}{\lambda_g} \cdot l \tag{7.1}$$

As it was mentioned in Chapter 2, each commensurate line has a different Z_i which value can be extracted by applying the well-known *Richards' transformation* and the iterative procedure detailed in Annex A ([26]) to satisfy any all-pole filtering function (e.g. Chebyshev, Butterworth, Zolotarev, Chained function). Then, a local

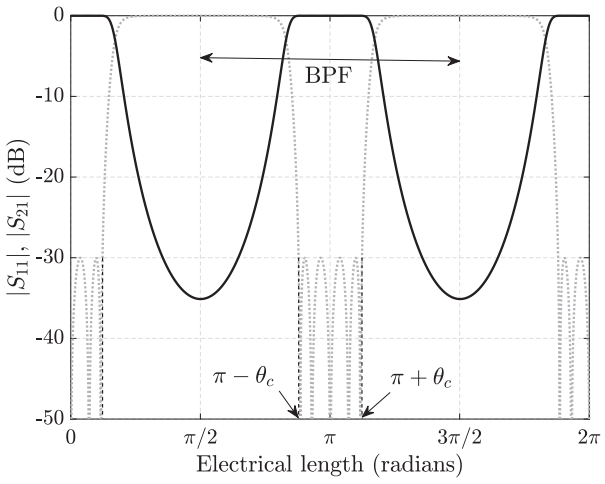

(a)

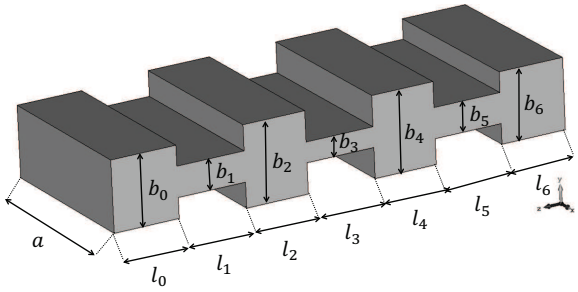

(b)

Figure 7.2: Example of a 5th order commensurate-line stepped-impedance filter prototype (a) $|S_{11}|$ (grey line) and $|S_{21}|$ (black line) parameters, and (b) filter 3D view.

reflection coefficient, Γ_i, is produced in each connection between two commensurate lines by the Z_i mismatch, whose value is given by equation (7.2).

$$\Gamma_i = \frac{Z_i - Z_{i-1}}{Z_i + Z_{i-1}} \tag{7.2}$$

The combination of all these local reflections placed θ rad apart produces the aimed frequency response of the filter (see Figure 7.2).

The synthesis procedure begins by fixing the width of the structure, a, the order of the filter, N, the required in-band return loss, and its lower and upper frequencies, f_1 and f_2, corresponding to $\theta_1 = \pi - \theta_c$ and $\theta_2 = \pi + \theta_c$, respectively (see Figure 7.2(b)), where θ_c is computed following equation (7.3). It should be stressed that the maximum rejection of the lower and upper stopbands takes place at $\theta = \pi/2$ and

$\theta = 3\pi/2$, respectively. Notice also that the central frequency of the passband, f_π, corresponds to $\theta = \pi$.

$$\theta_c = \pi \cdot \frac{\lambda_{g,f_1} - \lambda_{g,f_2}}{\lambda_{g,f_1} + \lambda_{g,f_2}} \tag{7.3}$$

$$f_\pi = \sqrt{\left(\frac{c}{2 \cdot a}\right)^2 + \left(\frac{c \cdot (\lambda_{g,f_1} + \lambda_{g,f_2})}{2 \cdot \lambda_{g,f_1} \cdot \lambda_{g,f_2}}\right)^2} \tag{7.4}$$

Typically, the width dimension, a, is fixed as the standard port width. However, unlike in classical inductive iris filters, this value can be reduced to improve the manufacturing yield of the filter. This is due to the fact that, if the width of the commensurate-line BPF is conveniently reduced, the bandwidth of the filter (in the electrical-length axis) will be wider and, hence, a higher value of θ_c will be needed, reducing the impedance ratios required and, consequently, obtaining more relaxed fabrication tolerances. Note that the constant width reduction produces a shifting towards the passband of the maximum rejection frequencies of the lower and upper stopbands, as well as an increase of the section length l, which are taken into account in the design process.

Then, the novel method continues by computing the b_i values of the final structure. First, b_0 is set. This value is usually fixed in accordance with the requirements of power handling and stopband performance. As it is explained in [1], [27], a simple relationship between Z_i and b_i can be utilized (b_i is directly proportional to Z_i) and, consequently, equation (7.2) can be rewritten by simply interchanging Z_i and b_i obtaining:

$$\Gamma_i^{aprox} = \frac{b_i - b_{i-1}}{b_i + b_{i-1}} \tag{7.5}$$

However, this simple relationship between Z_i and b_i neglects the effect of the higher-order mode excitation at the discontinuity. This effect can be modeled by a shunt capacitance related to the reactive energy stored around the discontinuity between the adjacent waveguides of different heights. The presence of the shunt capacitance modifies the local Γ_i magnitude ([2], [4]), as follows :

$$|\Gamma_i'| = \sqrt{\frac{(b_i - b_{i-1})^2 + (b_i \cdot B)^2}{(b_i + b_{i-1})^2 + (b_i \cdot B)^2}} \tag{7.6}$$

where B is the parasitic shunt capacitance that can be directly computed by the approximate expressions available in [28] and included here for the sake of completeness – equation (7.7).

$$B = \frac{2b_{i-1}}{\lambda_{g,f_\pi}}\left\{ ln\left[\left(\frac{1-\alpha^2}{4\alpha}\right)\left(\frac{1+\alpha}{1-\alpha}\right)^{0.5(\alpha+\frac{1}{\alpha})}\right] + 2\cdot\frac{A+D+2C}{A\cdot D-C^2} + \left(\frac{b_{i-1}}{4\lambda_{g,f_\pi}}\right)^2\left(\frac{1-\alpha}{1+\alpha}\right)^{4\alpha}\left(\frac{5\alpha^2-1}{1-\alpha^2}+\frac{4}{3}\frac{\alpha^2\cdot C}{A}\right)^2\right\} \tag{7.7}$$

where

$$A = \left(\frac{1+\alpha}{1-\alpha}\right)^{2\alpha}\cdot\frac{1+\sqrt{1-\left(\frac{b_{i-1}}{\lambda_{g,f_\pi}}\right)^2}}{1-\sqrt{1-\left(\frac{b_{i-1}}{\lambda_{g,f_\pi}}\right)^2}} - \frac{1+3\alpha^2}{1-\alpha^2}$$

$$D = \left(\frac{1+\alpha}{1-\alpha}\right)^{\frac{2}{\alpha}}\cdot\frac{1+\sqrt{1-\left(\frac{b_i}{\lambda_{g,f_\pi}}\right)^2}}{1-\sqrt{1-\left(\frac{b_i}{\lambda_{g,f_\pi}}\right)^2}} + \frac{3+\alpha^2}{1-\alpha^2}$$

$$C = \left(\frac{4\alpha}{1-\alpha^2}\right)^2$$

$$\alpha = \frac{b_i}{b_{i-1}}$$

Therefore, once b_0 is fixed, the next height, b_1, is calculated to satisfy that $|\Gamma'_1| = |\Gamma_1|$ since $|\Gamma_1|$ is known at the beginning. Then, proceeding iteratively, once a certain b_{i-1} is known, b_i is calculated to assure that equation (7.5) provides the reflection value prescribed by equation (7.2), i.e., $|\Gamma'_i| = |\Gamma_i|$. When $i = N+1$, all b_i in the final structure will have been calculated without involving any EM simulations.

The synthesis method continues with the calculation of the lengths of each waveguide section, l_i of the final structure. In this case, the phase of the local Γ_i is also affected by the aforementioned high-order mode excitation which is produced in the vicinity of a junction between two waveguide sections of different height, and needs to be compensated. This idea was firstly published in [27]. However, unlike in [27], any EM simulations will be utilized in this Section to calculate the correcting factors. Therefore, l_i will be calculated following equation (7.8) where two correcting factors obtained from equation (7.9) and equation (7.10) are added to the commensurate length, l, given by equation (7.11).

$$l_i = l + \delta_i^{(2)} + \delta_{i+1}^{(1)} \tag{7.8}$$

$$\delta_{i+1}^{(1)} = \frac{\lambda_{g,f_\pi}}{2\pi} \cdot \frac{\phi_i^{(1)}}{2} \tag{7.9}$$

$$\delta_{i+1}^{(2)} = \frac{\lambda_{g,f_\pi}}{2\pi} \cdot \frac{\phi_i^{(2)}}{2} \tag{7.10}$$

$$l = \frac{\lambda_{g,f_1} \cdot \lambda_{g,f_2}}{\lambda_{g,f_1} + \lambda_{g,f_2}} = \frac{\lambda_{g,f_\pi}}{2} \tag{7.11}$$

In equations (7.9) and (7.10), $\phi_i^{(1)}$ and $\phi_i^{(2)}$ are the phases of the local reflection coefficient from the right super index (1) and from the left super index (2), respectively, in the ith waveguide junction. These phases take into account the previously calculated reactive load B (equation (7.7)) and are calculated using the following expressions:

$$\phi_i^{(1)} = \tan^{-1}\left(\frac{-2 \cdot b_i^2 \cdot B}{b_i^2 - b_{i-1}^2 - b_i^2 \cdot B^2}\right) \tag{7.12}$$

$$\phi_i^{(2)} = \tan^{-1}\left(\frac{-2 \cdot b_{i-1} \cdot b_i \cdot B}{b_{i-1}^2 - b_i^2 - b_i^2 \cdot B^2}\right) \tag{7.13}$$

To summarize, the novel quasi-analytical synthesis method allows the designer to obtain a very accurate physical structure whose simulated frequency response will be very close to the ideal one. Moreover, neither EM simulations nor optimizations are needed since the final physical dimensions of the filter are directly obtained from closed-form expressions in a negligible CPU time. It is important to note that this method only takes into account two higher-order modes to model the inherent shunt capacitive effect related to the reactive energy stored around the discontinuity between two adjacent waveguides of different height [28]. Depending on the height of the sections, the synthesis procedure could not be accurate enough to mimic the ideal frequency response. As an alternative to the quasi-analytical models, the EM solvers (such as FEST3D or CST MWS) can be also utilized for the previous calculus to obtain more accurate results.

7.4 Design Example: BPF with Constant Width Reduction

7.4.1 Specifications

The filter will fulfil the following frequency specifications: in-band return loss better than 20 dB in a passband defined between 37.5 GHz and 42.5 GHz (Tx Q-band) and an attenuation level better than 60 dB in both, the lower stopband, defined between 33 and 35.5 GHz, and the higher stopband, defined between 45 and 50 GHz (Rx Q-band).

Table 7.1: Summary of design parameters of the example in Section 7.4 (designed utilizing only closed-form expressions).

Filtering function type	Chebyshev
Order, N	13
In-band return loss	25 dB
Passband lower frequency, f_1	37 GHz
Passband upper frequency, f_2	43 GHz
Waveguide width, a	4.65 mm
Input height, b_0	1.4 mm

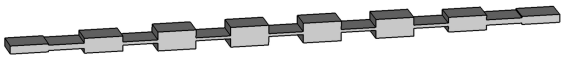

Figure 7.3: 3D view of the example in Section 7.4 (designed utilizing only closed-form expressions).

Table 7.2: Final dimensions of the example synthesized with the quasi-analytical technique in Section 7.4.

UE	Z_i	b_i (mm)	l_i (mm)
0, 14	1.000	1.400	6.431
1, 13	0.666	0.932	6.103
2, 12	1.843	2.580	6.563
3, 11	0.408	0.571	5.948
4, 10	2.353	3.295	6.515
5, 9	0.368	0.516	5.918
6, 8	2.456	3.439	6.507
7	0.362	0.507	5.914

7.4.2 Design and Simulation

Utilizing only the closed-form expressions given in Section 7.3, a novel filter with constant width reduction has been designed. The main design parameters of the example are given in Table 7.1. The physical dimensions of the synthesized filter (see Figure 7.3) are given in Table 7.2 and its simulated FEST3D frequency response along with the ideal one are compared in Figure 7.4. As it can be seen, the simulated frequency response of the filter is very close to the ideal one. Moreover, it is important to highlight that the final dimensions of the filter have been directly obtained without any EM simulation nor optimizations.

The quasi-analytical method takes into account only two higher-order modes to model the inherent shunt capacitive effect related to the reactive energy stored around

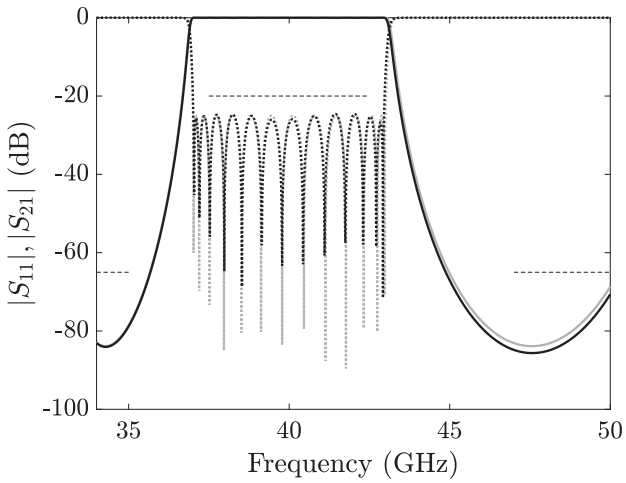

Figure 7.4: Ideal frequency response (grey line) and FEST3D frequency response for the structure obtained with the novel method in Section 7.4 (designed utilizing only closed-form expressions) (black line). $|S_{11}|$ in dotted line and $|S_{21}|$ in solid line.

the discontinuity between two adjacent waveguides of different height [28]. Depending on the maximum height of the waveguides, the synthesis procedure might not be accurate enough to mimic the ideal frequency response. As an alternative to the quasi-analytical models, the EM solvers (FEST3D or CST MWS) can be utilized for the previous calculus to attain more accurate results. This assertion has been demonstrated through the design and fabrication of the latter Q-band example.

In order to fabricate a prototype with conventional CCM technique in favour of seeking the lowest cost, the minimum mechanical gap has been increased to 1 mm (to utilize a 0.5 mm-radius milling tool). If a novel BPF with constant width reduction and minimum mechanical gap higher than 1 mm is synthesized with the proposed quasi-analytical method and then simulated with FEST3D (see Figure 7.5 black thin line), it can be observed that the frequency response of the synthesized filter is not as accurate as the previous one. On the other hand, if the prototype is synthesized by using an EM SW instead of the equations in Section 7.3, a more accurate result is obtained since, in this case, higher number of higher-order modes can be considered to compensate the errors produced by the parasitic shunt capacitance of each discontinuity. The dimensions of the prototype designed with the EM SW are given in Table 7.4 and its frequency response in Figure 7.5 (black thick line).

7.4.3 Sensitivity Analysis

A sensitivity analysis has been performed to prove the dramatic advantage of the proposed BPF when compared to its classical counterparts in terms of manufacturing robustness. Two hundred iterations varying all dimensions have been performed

Table 7.3: Final dimensions of the example synthesized with the EM simulator (FEST3D) in Section 7.4.

UE	Z_i	b_i (mm)	l_i (mm)
0, 14	1.000	2.845	6.686
1, 13	0.666	1.904	5.769
2, 12	1.843	5.029	6.704
3, 11	0.408	1.166	5.441
4, 10	2.353	6.268	6.611
5, 9	0.368	1.048	5.373
6, 8	2.456	6.528	6.594
7	0.362	1.031	5.362

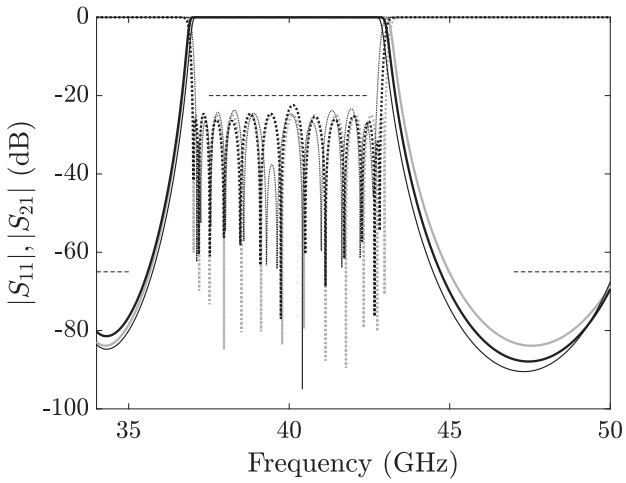

Figure 7.5: Ideal frequency response (grey line) and FEST3D frequency responses for the proposed final structure in Section 7.4 whose physical parameters have been obtained with quasi-analytical method in Section 7.3 (black thin line) and with the EM solver (black thick line). $|S_{11}|$ in dotted line and $|S_{21}|$ in solid line.

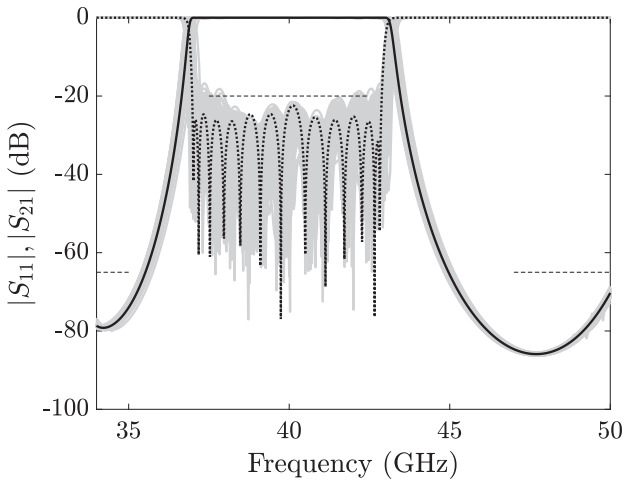

Figure 7.6: Sensitivity analysis to fabrication tolerances ($\pm 25\mu$m) in the entire frequency response of the proposed filter in Section 7.4. $|S_{11}|$ in dotted black line and $|S_{21}|$ in solid black line for the baseline filter. Grey lines for the simulation trials. Frequency specifications in dashed line.

using FEST3D. A Gaussian probability function with standard deviation of $\pm 10\mu$m (which corresponds to a worst-case error value of $\pm 25\mu$m) has been used. As it can be seen in Figure 7.6, the novel filter shows an excellent manufacturing yield, 92%, while the classical one shows very poor results with only an 8% manufacturing yield for the classical inductive-iris BPF (see Figure 7.7), 8% for the inductive-iris BPF with a width reduction (a = 4.65 mm) (see Figure 7.8), and 44% for the inductive-iris BPF using TE102 resonant cavities (see Figure 7.9). It must be also stressed that this filter does not fulfil the frequency specifications in the upper stopband.

7.4.4 Fabrication and Measurement

A 3-step transformer has been added at the input and output ports to reach the standard WR22 port width (a=5.69 mm, b=2.845 mm). This filter has been fabricated in two halves, cutting by the E-plane (to reduce the measured insertion loss), in bare aluminum by standard CCM (radius of the drill equal to 0.5 mm). The fabricated prototype is shown in Figure 7.10. The measurements have been carried out by means of an Agilent E8364B PNA, proper waveguide-to-coaxial transitions and the calibration kit for the WR22 standard (33-50 GHz) obtaining excellent results, in agreement with the simulations, as it can be observed in Figure 7.11. The measured insertion loss of the prototype (see Figure 7.12) are below 0.5 dB in the worst case (0.38 dB at f_π).

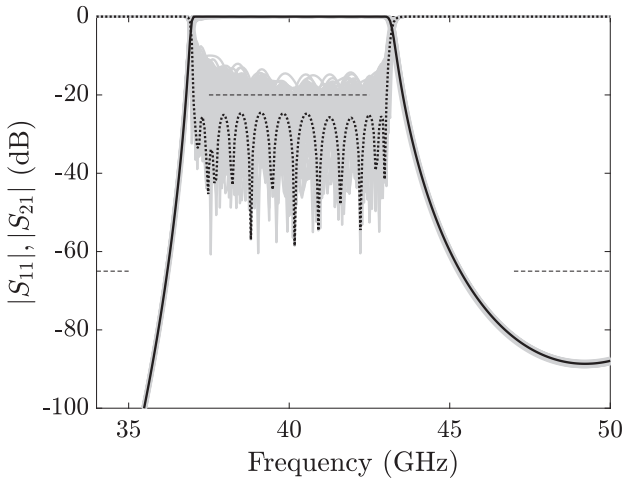

Figure 7.7: Sensitivity analysis to fabrication tolerances ($\pm 25\mu$m) in the entire frequency response of the inductive filter. $|S_{11}|$ in dotted black line and $|S_{21}|$ in solid black line for the baseline filter. Grey lines for the simulation trials. Frequency specifications in dashed line.

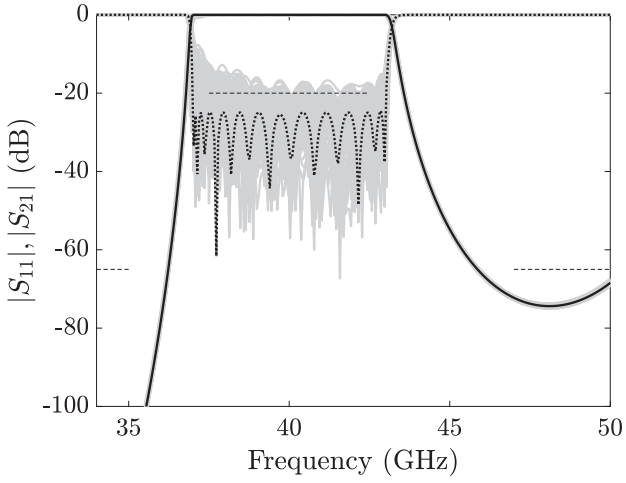

Figure 7.8: Sensitivity analysis to fabrication tolerances ($\pm 25\mu$m) in the entire frequency response of the inductive filter with a width reduction. $|S_{11}|$ in dotted black line and $|S_{21}|$ in solid black line for the baseline filter. Grey lines for the simulation trials. Frequency specifications in dashed line.

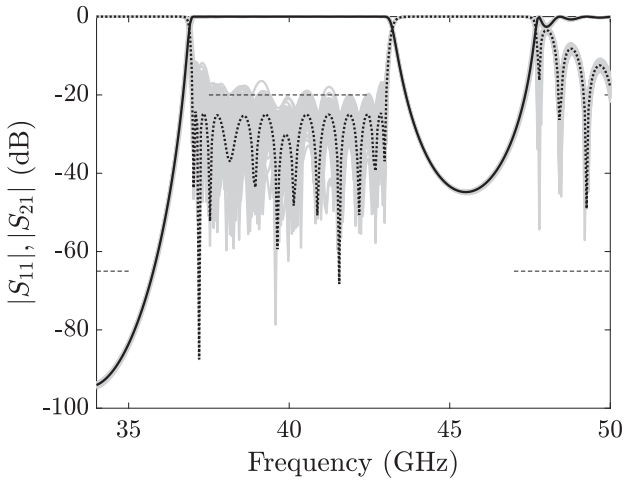

Figure 7.9: Sensitivity analysis to fabrication tolerances ($\pm 25\mu$m) in the entire frequency response of the inductive filter with TE102 resonant cavities. $|S_{11}|$ in dotted black line and $|S_{21}|$ in solid black line for the baseline filter. Grey lines for the simulation trials. Frequency specifications in dashed line.

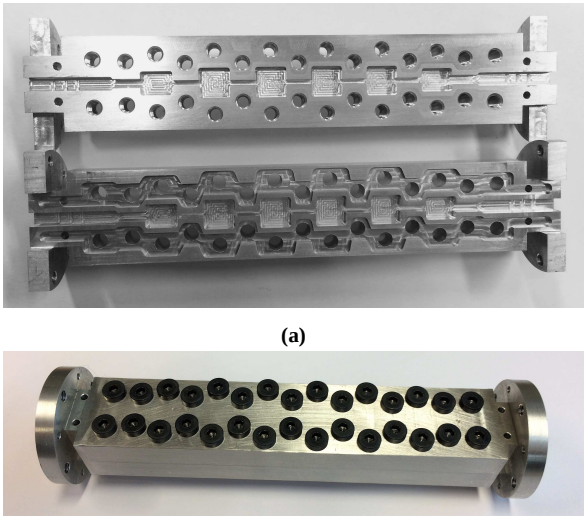

(a)

(b)

Figure 7.10: Photograph of the (a) unassembled and (b) assembled prototype.

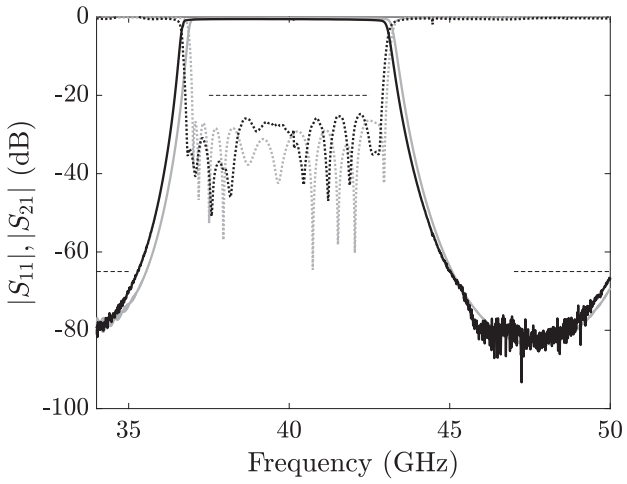

Figure 7.11: Comparison between the CST MWS simulated frequency response (grey line) of the proposed filter with rounded corners and measurements of the fabricated prototype (black line). $|S_{11}|$ in dotted line and $|S_{21}|$ in solid line. Frequency specifications in dashed line.

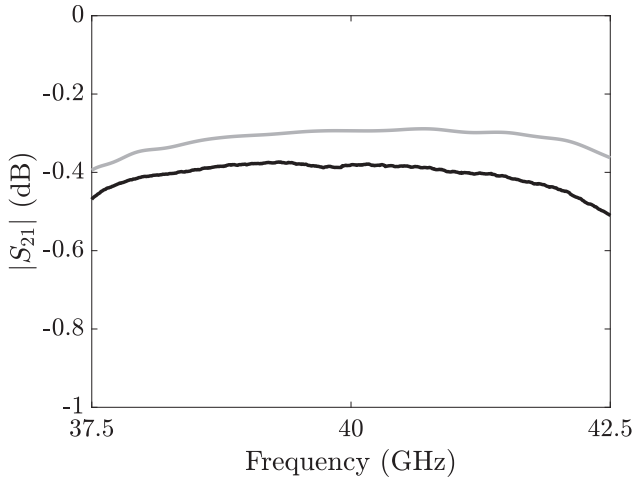

Figure 7.12: Detail of the insertion loss. CST MWS simulation (conductivity of Al) of the proposed filter with rounded corners (grey line) and measurements of the fabricated prototype (black line).

7.4.5 High-Power Behavior

The high-power behavior of the filter has been also estimated with SPARK3D. The EM fields have been previously simulated with CST MWS at 37.5 and 42.5 GHz which are the frequencies of the utilization band of the filter (satellite Tx band) and the SEY of aluminum. The simulated multipactor threshold level is higher than 5 kW at 37.5 GHz.

7.5 Conclusions

In this Chapter, a novel BPFs with reduced sensitivity to manufacturing tolerances has been proposed. The presented filters base their design on the use of the first inherent passband replica of the stepped-impedance low-pass prototype and exploit this issue along with a constant width reduction to enhance the manufacturing tolerances of a Q-band BPF. To do so, a new technique which only utilizes closed-form expressions and allows designers to calculate in a negligible CPU time the final dimensions of the filters is proposed. Additionally, the limitations of this technique has been assessed and a solution for a real case has been proposed based on EM simulators. The method has been proved with a novel BPF with reduced sensitivity to fabrication tolerances. The manufacturing yield of this filter has been dramatically improved when compared with its classical counterpart, i.e. the inductive-iris BPF (92% vs. 8%).

REFERENCES

[1] F. Teberio, P. Soto, I. Arregui, T. Lopetegi, S. Cogollos, I. Arnedo, P. Martin-Iglesias, V. E. Boria, and M. A. G. Laso, "Waveguide band-pass filter with reduced sensitivity to fabrication tolerances for q-band payloads," in *2017 IEEE MTT-S International Microwave Symposium Digest (IMS)*, Jun. 2017, pp. 1464–1467.

[2] F. Teberio, J. M. Percaz, I. Arregui, P. Martin-Iglesias, T. Lopetegi, M. A. G. Laso, and I. Arnedo, "Matlab accurate synthesis of classical stepped-impedance rectangular waveguide filters," in *2018 International Workshop on Microwave Filters (IWMF)*, Apr. 2018.

[3] ——, "Automated synthesis for stepped-impedance waveguide filters," *Submitted for consideration in Radio Science*, 2018.

[4] F. Teberio, P. Martin-Iglesias, I. Arregui, J. M. Percaz, T. Lopetegi, M. A. G. Laso, and I. Arnedo, "Quasi-analytical design of commensurate-line waveguide band-pass filters," in *IEEE MTT-S International Conference on Numerical Electromagnetic and Multiphysics Modeling and Optimization (NEMO)*, Aug. 2018.

[5] UPNA, "Design techniques for low-cost filters with reduced sensitivity to fabrication tolerances at high-frequencies," ESA and Thales Alenia Space, NPI 4000114859/15/NL/HK, 2018.

[6] J. V. Evans and A. Dissanayake, "Prospects for commercial satellite services at q- and v-bands," in *1998 IEEE Military Communications Conference (MILCOM)*, vol. 1, Oct. 1998, 1–7 vol.1.

[7] T. Rossi, E. Cianca, M. Lucente, M. D. Sanctis, C. Stallo, M. Ruggieri, A. Paraboni, A. Vernucci, L. Zuliani, L. Bruca, and G. Codispoti, "Experimental italian q/v band satellite network," in *2009 IEEE Aerospace conference*, Mar. 2009, pp. 1–9.

[8] M. Aloisio, P. Angeletti, F. Coromina, and R. D. Gaudenzi, "Technological challenges of future broadband telecommunication satellites in q/v-band," in *2012 IEEE International Conference on Wireless Information Technology and Systems (ICWITS)*, Nov. 2012, pp. 1–4.

[9] A. Martellucci, J. R. Castro, P. Sivac, and E. Benzi, "The alphasat aldo paraboni scientific experiment: An overview of the activities of the european space agency," in *2016 10th European Conference on Antennas and Propagation (EuCAP)*, Apr. 2016, pp. 1–4.

[10] B. Palacin, N. J. G. Fonseca, M. Romier, R. Contreres, J. C. Angevain, G. Toso, and C. Mangenot, "Multibeam antennas for very high throughput satellites in europe: Technologies and trends," in *2017 11th European Conference on Antennas and Propagation (EuCAP)*, Mar. 2017, pp. 2413–2417.

[11] U. Rosenberg, J. Ebinger, and S. Amari, "Advanced receive/transmit diplexer design for emerging mm-wave access radio applications," in *2006 IEEE MTT-S International Microwave Symposium Digest (IMS)*, Jun. 2006, pp. 1217–1220.

[12] R. Ravanelli, P. Cecchini, R. Mizzoni, G. Addamo, O. A. Peverini, R. Tascone, and G. Virone, "A k/ka/ehf feed chain for dual-use telecom," in *2015 9th European Conference on Antennas and Propagation (EuCAP)*, May 2015, pp. 1–5.

[13] R. Roberts, P. Booth, G. Fox, S. Stirland, and M. Simeoni, "Q/v-band feed system development," in *2016 10th European Conference on Antennas and Propagation (EuCAP)*, Apr. 2016, pp. 1–5.

[14] A. Morini, G. Venanzoni, M. Farina, and T. Rozzi, "Practical design of a high-power tuning-less w-band triplexer for ground radar surveillance systems," *IET Microwaves, Antennas Propagation*, vol. 1, no. 4, pp. 822–826, Aug. 2007.

[15] J. R. Aitken and J. Hong, "Design of millimetre wave diplexers with relaxed fabrication tolerances," *IET Microwaves, Antennas Propagation*, vol. 9, no. 8, pp. 802–807, 2015.

[16] G. Cannone and M. Oldoni, "High-yield E-band diplexer for fixed radio point-to-point equipment," *International Journal of RF and Microwave Computer-Aided Engineering*, vol. 24, no. 9, pp. 508–512, Dec. 2013.

[17] B. Yang, Z. Li, J. Zhang, X. Yao, C. Zheng, X. Shang, and J. Miao, "Design of H-plane inductance diaphragm waveguide band-pass filter for millimeter imaging frontend," *Progress in Electromagnetics Research*, vol. 48, pp. 141–150, Mar. 2014.

[18] J. Bornemann, U. Rosenberg, S. Amari, and R. Vahldieck, "Tolerance analysis of bypass-, cross- and direct-coupled rectangular waveguide band-pass filters," *IEE Proceedings - Microwaves, Antennas and Propagation*, vol. 152, no. 3, pp. 167–170, Jun. 2005.

[19] P. S. Pacheco, V. E. B. Esbert, C. C. Candau, C. P. V. Quiles, J. G. Raga, and B. G. Martínez, "Em-based synthesis and design of bandpass waveguide filters including manufacturing effects with fest 3d," *International Journal of RF and Microwave Computer-Aided Engineering*, vol. 22, no. 1, pp. 93–103, 2012.

[20] J. R. Aitken and J. Hong, "Tolerance considerations for wireless backhaul diplexer circuits," in *2014 44th European Microwave Conference (EuMC)*, Oct. 2014, pp. 620–623.

[21] E. Ofli, R. Vahldieck, and S. Amari, "Novel E-plane filters and diplexers with elliptic response for millimeter-wave applications," *IEEE Transactions on Microwave Theory and Techniques*, vol. 53, no. 3, pp. 843–851, Mar. 2005.

[22] Z. Xu, J. Guo, C. Qian, and W. Dou, "Broad-band E-plane filters with improved stop-band performance," *IEEE Microwave and Wireless Components Letters*, vol. 21, no. 7, pp. 350–352, Jul. 2011.

[23] R. Levy, "Tapered corrugated waveguide low-pass filters," *IEEE Transactions on Microwave Theory and Techniques*, vol. 21, no. 8, pp. 526–532, Aug. 1973.

[24] L. Young, "Stepped-impedance transformers and filter prototypes," *IRE Transactions on Microwave Theory and Techniques*, vol. 10, no. 5, pp. 339–359, Sep. 1962.

[25] G. Matthaei, L. Young, and E. M. T. Jones, *Microwave filters, impedance-matching networks and coupling structures*. Artech House, 1980.

[26] R. Cameron, C. Kudsia, and R. Mansour, *Microwave Filters for Communication Systems: Fundamentals, Design and Applications*. Wiley-Interscience, 2007.

[27] M. Simeoni, F. Cacchione, S. Vanin, J. Molina-Perez, and D. Schmitt, "Automatic dimensional synthesis without optimization for stepped impedance low-pass filters," *Microwave Optical and Technology Letters*, vol. 44, no. 1, pp. 190–193, Jan. 2005.

[28] N. Marcuvitz, *Waveguide Handbook*. McGraw-Hill, 1951.

CHAPTER 8

MEANDERED LPFs AND BPFs WITH FLEXIBLE ROUTING CAPABILITIES

In this Chapter, a new topology for rectangular waveguide band-pass and low-pass filters is presented [1], [2]. A simple, accurate and robust design technique for these novel meandered waveguide filters is provided. The proposed filters employ a concatenation of $\pm 90^{\circ}$ E-plane mitered bends ($\pm 90^{\circ}$ EMBs) with different heights and lengths whose dimensions are consecutively and independently calculated. Each $\pm 90^{\circ}$ EMB satisfies a local target reflection coefficient along the device so that they can be calculated separately. The novel structures allow to drastically reduce the total length of the filters and to embed bends if desired, or even to provide routing capabilities. Furthermore, the new meandered topology allows the introduction of transmission zeros above the passband of the low-pass filter, which can be controlled by the free parameters of the $\pm 90^{\circ}$ EMBs. A band-pass and a low-pass filter with meandered topology have been designed following the proposed novel technique. Measurements of the manufactured prototypes are also included to validate the novel topology and design technique, achieving excellent agreement with the simulated results.

It is important to note that the techniques developed in this Chapter have been done within the framework of a NPI activity with the European Space Agency [3].

New Filter Design Methods and Topologies for the Future Microwave and Millimeter-Wave High-Capacity Satellites, by Fernando Teberio. 2018 Public University of Navarre.

8.1 Background

Similarly, the industry is demanding reductions in manufacturing costs pursuing to eliminate tuning screws and guarantee successful first-shot fabrications. Finally, in such applications, waveguide bends can often be found after the filters [4], [5], misusing the available volume/mass budget and increasing the insertion loss. Moreover, when two different structures are used (screwed by their flanges), an additional negative impact is produced on the PIM parameter [6]–[8]. Therefore, the development of new BPFs and LPFs is in the spotlight, as well as accurate and robust design techniques to allow designers to obtain structures that: a) do not require post-manufacturing tuning, b) are compact, and c) provide routing capabilities.

To the author's knowledge, all efforts to fold waveguide filters have remained focused on BPFs. An early attempt to achieve curved filters was published in [9], where the design of curved inductively-coupled BPFs starts from the same in-line prototype and the deviations caused by the curvature of the cavities are afterwards compensated by means of a full-wave optimization procedure. Then, the folded topology was intensively utilized to miniaturize BPFs in the lower GHz frequency range with the development of waveguide combline filters [10], [11] and ridge waveguide filters [12]. After that, based also on the folded structures, design procedures for H-plane filters and diplexers were also proposed [13]–[16]. The common feature of all the above structures is that they all have a symmetry in the H-plane and, therefore, the main current lines are broken when they are manufactured following the standard procedure in two halves, which deteriorates the measured insertion loss and PIM [17]. Recently, folded BPFs with E-plane symmetry have been proposed [17]–[19]. In [17] and [18], a folded topology was presented as a flexible alternative to implement trisections. Then, the technique in [17] was extended to implement transmission zeros above and below the passband [19]. Although very high-performance structures can be obtained with the above methods, they might not be suitable for the design and manufacture of tuning-less inexpensive filters with stringent specifications for the emerging Q-V-bands (assuming standard milling as the fabrication technique) since they all use coupled resonant cavities to obtain the desired frequency response.

Although compact high-power LPFs have been obtained in [20]–[24] an E-plane bend cannot be embedded in these types of filters. Hence, if an E-plane bend is required before or after the LPF, two different structures will be needed (with their corresponding flanges, screws, etc.). This issue will have a negative impact on the insertion loss, volume/weight, and PIM products due to the mandatory presence of extra junctions.

Stepped-impedance waveguide structures have been widely used for LPFs [25]–[33], and also for BPFs [25], [26], [34], always featuring an in-line (straight) topology, and they still remain a very common solution for the implementation of waveguide LPFs. Fortunately, stepped-impedance BPFs are very good candidates as it was demonstrated in Chapter 7, [34], where a straight BPF with reduced sensitivity to manufacturing tolerances was proposed. However, although the manufacturing yield of the structure was clearly enhanced, the price to pay was the total size of the final device.

In this Chapter, a detailed modular methodology with a clear physical insight to LPFs and BPFs, allows us to design tuning-free compact filters, with the flexibility of embedding bends and providing routing capabilities in the filter structure. Furthermore, due to their modular design methodology, cascading $\pm 90^{\circ}$ E-plane mitered bends ($\pm 90^{\circ}$EMBs), the design procedure can be easily implemented in a software tool to directly obtain a bended filter with the required routing specifications. Last but not least, the novel meandered filters have E-plane symmetry, reducing the measured insertion loss and the PIM due to the fabrication assembly. The design method (Section 8.3) has been demonstrated with two examples: a meandered LPF of order 11, with transmission zeros for Ku-band applications, and a meandered BPF of order 13 (implemented with multiple topologies) with the same frequency specifications as in the example in Chapter 7.4, [34]. The LPF, and two BPF topologies, have been fabricated and measured, showing a very good agreement between simulated and measured results.

8.2 Objective

The main objective of this Chapter is to develop a modular synthesis technique for LPFs and BPFs which allows different layout configurations without further optimizations, accomplishing ad-hoc designs with routing capability. Additionally, more compact structures may be also obtained. These new filters will permit to design more complex and compact systems for the future high-capacity communication satellites.

8.3 Design Method

The novel meandered filters presented in this Chapter (of order N for both the band-pass and low-pass responses) consist of the concatenation of $N+1$ $\pm 90^{\circ}$ E-plane mitered bends ($\pm 90^{\circ}$EMBs) with the same width, a, but different heights (input b_{i-1} and output b_i), lengths (input $l_{i,1}$ and output $l_{i,2}$) and tilts of the chamfer (input $d_{i,1}$ and output $d_{i,2}$), where sub-index i identifies the ith-EMB, see Figure 8.1. The "$+$" or the "$-$" of the $\pm 90^{\circ}$EMB is in accordance with Figure 8.2.

The design method begins by calculating the stepped-impedance prototype (distributed transmission line model), see Figure 8.3, which consists of $N+2$ commensurate transmission lines with electrical lengths θ and characteristic impedances Z_i, (which produces the $N+1$ impedance steps) for a chosen all-pole frequency response of order N such as Butterworth, Chebyshev, Zolotarev, Chained Function, etc. As it is well known, the commensurate lines have the same frequency behavior, since they are commensurate and homogeneous. In fact, all lines ideally have ideally the same physical length l, and show the same wavelength λ_g at any frequency. These properties allow to define the frequency behavior of the prototype as a function of the electrical length of a line, θ:

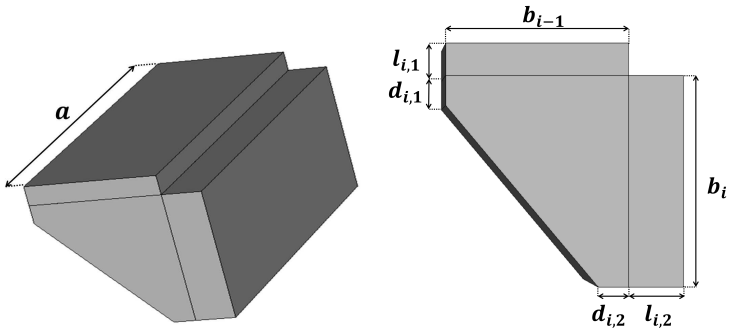

Figure 8.1: Sketch view of the ith $\pm 90^{\circ}$EMB (a) 3-D view (b) side view.

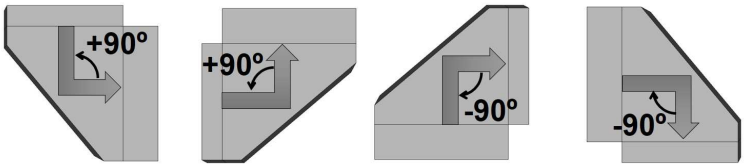

Figure 8.2: Orientation of the bend and sign notation.

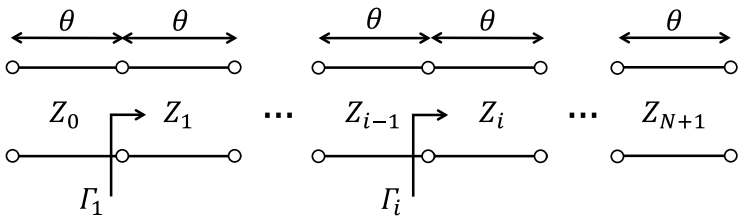

Figure 8.3: Stepped-impedance prototype with commensurate transmission lines with electrical length θ and characteristic impedances Z_i.

$$\theta = \beta \cdot l = \frac{2 \cdot \pi}{\lambda_g} \cdot l \tag{8.1}$$

Each commensurate line has a different characteristic impedance Z_i whose value can be calculated by applying the well-known *Richards' transformation* and the iterative extraction procedure fully detailed in Annex, A, [35]. Then, as it was explained in Chapters 2.3, 7.3, [33], a local reflection coefficient, Γ_i, is produced at each junction between two commensurate lines by the characteristic impedance mismatch, whose value is given by

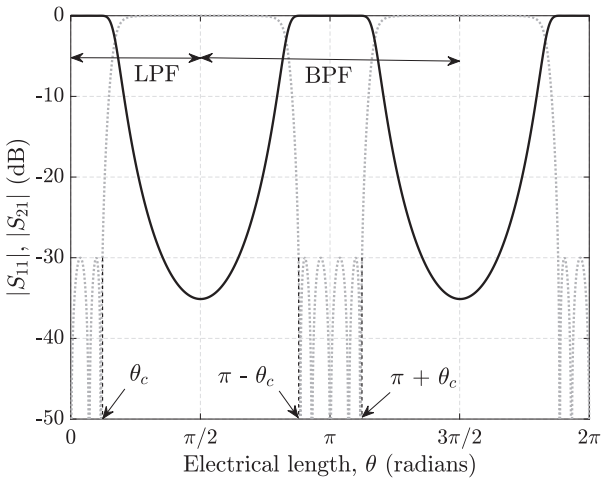

Figure 8.4: 5-th order commensurate-line stepped-impedance prototype response for the LPF and BPF. $|S_{11}|$ (grey line) and $|S_{21}|$ (black line) parameters.

$$\Gamma_i = \frac{Z_i - Z_{i-1}}{Z_i + Z_{i-1}} \tag{8.2}$$

The combination of all these local reflections placed θ rad apart produces the aimed frequency response of the filter (see Figure 8.4).

The synthesis technique proposed in this paper utilizes a modular design strategy. Thus, instead of paying attention to the final structure as a whole, each constituent $\pm 90^{\circ}$EMB (with its physical dimensions labeled in Figure 8.1) will be designed separately and consecutively to resemble the electrical behavior of the transmission line model in terms of its local reflection coefficients, Γ_i, and electrical separations, θ, to subsequently assemble the final structure. Thus, the ith-EMB will implement a $\theta/2$-transmission line subsection cascaded with another $\theta/2$-transmission line subsection and the reflection coefficient, Γ_i, that appears between them, see Figure 8.5. This Γ_i depends mainly on the contrast between the b_{i-1} and b_i dimensions, taking into account that $\Gamma_i > 0$ requires $b_{i-1} < b_i$ while $\Gamma_i < 0$ needs $b_{i-1} > b_i$. On the other hand, the electrical lengths $\theta/2$ implemented by the ith-EMB will be dominated by the physical lengths $l_{i,1}$ and $l_{i,2}$. To ensure the full equivalence between the transmission line model and the ith-EMB, the dimensions of the ith-EMB are adjusted in such a way that its S_{11}-parameter satisfies $|S_{11,i}| = |\Gamma_i|$ (see Figure 8.6) and its S-parameter phases (see Figure 8.6) verify equation (8.3) for a positive reflection coefficient ($\Gamma_i > 0$):

$$\phi_{i,S_{11}} = -\theta_c \quad \text{and} \quad \phi_{i,S_{21}} = -\theta_c \tag{8.3}$$

and equation (8.4) for a negative reflection coefficient ($\Gamma_i < 0$):

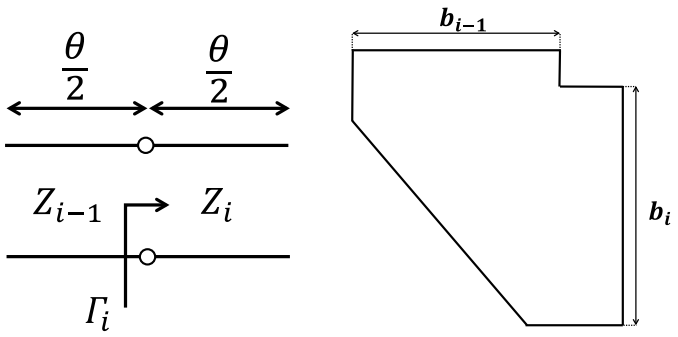

Figure 8.5: Section of the stepped-impedance prototype (a) implemented by the ith-EMB in (b).

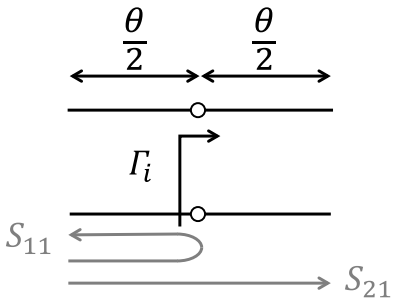

Figure 8.6: Sketch of the S_{11} and S_{21} parameters corresponding to the section of the stepped-impedance prototype implemented by the ith-EMB.

$$\phi_{i,S_{11}} = -\theta_c + \pi \quad \text{and} \quad \phi_{i,S_{21}} = -\theta_c \tag{8.4}$$

It is important to note that the dimensions that directly define the chamfer of the bend, $d_{i,1}$ and $d_{i,2}$, provide extra degrees of freedom in our design technique.

8.3.1 Meandered LPFs

The design method for the novel meandered LPF (see Figure 8.7) begins by fixing the maximum frequency of the passband, f_c, the required in-band return loss, the frequency of maximum rejection, f_0, and the order, N, of the all-pole filtering function that will be employed. From the guided wavelength, λ_g, corresponding to f_c and f_0, the value of θ_c will be obtained (see Figure 8.4):

$$\theta_c = \frac{\pi}{2} \cdot \frac{\lambda_{g,f_0}}{\lambda_{g,f_c}} \tag{8.5}$$

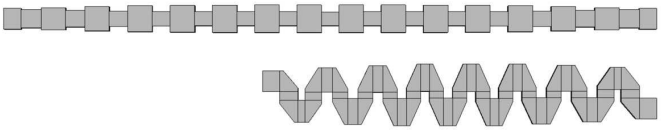

Figure 8.7: Side-view (same scale) of (a) the classical in-line waveguide LPF of order 29 and (b) the novel meandered topology applied to the same LPF.

Then the low-pass stepped-impedance prototype is computed by extracting the commensurate lines (Unit Elements) with their corresponding characteristic impedances, Z_i, which will satisfy the required frequency specifications. Next, the local reflection coefficients, Γ_i, are calculated using equation (8.2).

The design procedure continues by mapping each Γ_i with the physical dimensions corresponding to the ith-EMB (see Figure 8.1 and Figure 8.5). Initially, b_0 is set according to the desired stopband performance and the minimum mechanical gap allowed in the filter (related to the power handling capability of the filter). Then, b_1 is calculated to satisfy $|S_{11,1}(f_c)| = |\Gamma_1|$, where $|S_{11,1}(f_c)|$ is the magnitude of the S_{11}-parameter of the 1st-EMB at f_c, also taking into account that $b_0 < b_1$ for $\Gamma_1 > 0$ and $b_0 > b_1$ for $\Gamma_1 < 0$. After that, we proceed iteratively in such a way that once a certain b_{i-1} is known, b_i is computed to guarantee that:

$$|S_{11,i}(f_c)| = |\Gamma_i| \tag{8.6}$$

where $|S_{11,i}(f_c)|$ is the magnitude of the S_{11}-parameter of the ith-EMB at f_c. When $i = N + 1$, all b_i have been calculated. Although the effect of the b_i over the frequency response of the $\pm 90°$EMBs is dominant, the effect of $d_{i,1}$ and $d_{i,2}$ cannot be neglected. In the previous procedure for the separated calculation of b_i two different strategies can be followed with respect to $d_{i,1}$ and $d_{i,2}$. The first one is to *a priori* fix $d_{i,1}$ and $d_{i,2}$ in all the $\pm 90°$EMBs to a constant value. The second one is to use in each $\pm 90°$EMB $d_{i,1}$ and $d_{i,2}$ along with b_i (recalling that b_{i-1} is fixed in the previous $\pm 90°$EMB) to obtain the required $|\Gamma_i|$. The advantage of this second option is that it allows the designer to control the required excursion for the b_i.

Finally, it just remains to compute the lengths $l_{i,1}$ and $l_{i,2}$ of the $\pm 90°$EMBs (see Figure 8.1). For doing so, the phase response of the ith-EMB should be considered and, following equations (8.3) and (8.4), depending on the type of step that we have, i.e., either positive or negative Γ_i, the lengths $l_{i,1}$ and $l_{i,2}$ will be adjusted to satisfy equation (8.7) or equation (8.8) respectively:

$$\phi_{i,S_{11}}(f_c) = -\theta_c \quad \text{and} \quad \phi_{i,S_{21}}(f_c) = -\theta_c \tag{8.7}$$

$$\phi_{i,S_{11}}(f_c) = -\theta_c + \pi \quad \text{and} \quad \phi_{i,S_{21}}(f_c) = -\theta_c \tag{8.8}$$

being $\phi_{i,S_{11}}(f_c)$ and $\phi_{i,S_{21}}(f_c)$ the phase response of the S_{11}- and S_{21}-parameters, respectively, of the ith-EMB at f_c. Finally, the l_i are computed by means of (8.9), where the special cases for the global input and output lengths are calculated as $l_0 = 2 \cdot l_{1,1}$ and $l_{N+1} = 2 \cdot l_{N+1,2}$.

$$l_i = l_{i,2} + l_{i+1,1} \quad \text{for} \quad i = 1 : N \tag{8.9}$$

One remarkable property of the meandered LPFs proposed in this paper is the ability to introduce transmission zeros with this topology. It allows us to obtain very steep slopes between the pass- and the stop-band with a filter order reduction that will produce a substantial size reduction in comparison with the classical in-line structure Chapter 2, [33], as it will be shown in the design examples Section. These transmission zeros are obtained by the interference between the fundamental TE_{10} operation mode and evanescent higher order modes which are excited at the bends. When we have two consecutive $-90°$EMBs (or $+90°$EMBs), and the distance between the resulting input and output ports is small, see Figure 8.8(a), the evanescent higher order modes excited can provide an alternative *path* for the signal to go from the input to the output port. When the EM fields that propagate through the main *path* (fundamental TE_{10} mode) interfere with the fields propagating through the alternative *path* (higher-order modes) with the same strength but opposite phasing, then a cancellation occurs. This physical phenomenon produces a transmission zero at the cancellation frequency [14]. In order to obtain the transmission zero at a frequency close to the passband, the strength of the higher order mode fields that reach the output port must be high. To achieve it, the distance between the input and output ports must be small [14]. This can be accomplished by increasing f_0 (frequency of maximum rejection) to achieve a reduction in θ_c, see equation (8.5), since this variable is directly connected to the length of each line and finally to the distance between the ports l_i. As a general rule, if the distance between the ports l_i is decreased, the frequency of the transmission zero is also decreased, getting closer to the passband of the filter. Additionally, a fine tuning in the position of the zero can be achieved by changing the shape of the two bends through the adjustment of all their parameters, see Fig 9. To demonstrate the control that can be exerted over the position of the transmission zero, the two consecutive $-90°$EMBs structure of Figure 8.8(a) has been designed for three examples, to provide the same frequency response (magnitude and phase) for a passband up to 11 GHz approximately, while introducing a transmission zero at 13 GHz, 14 GHz and 15 GHz, respectively. The physical parameters of the three examples are given in Table 8.1 and the frequency responses obtained are shown in Figure 8.8. As it can be seen, the transmission zero can be shifted towards lower and higher frequencies around 2 GHz (for these examples), while keeping the frequency response unaltered for the lower frequencies of the passband. Unfortunately, these transmission zeros cannot be achieved in the meandered BPFs, since the distance between the input and the output ports of the two consecutive $-90°$EMBs structure of Figure 8.8 is around $l_i \approx \lambda_(g, f_\pi)/2$ for the BPFs that will be presented in the following Subsection, and cannot be reduced as in the novel meandered LPFs case.

Finally, it is important to note that the aim of the proposed meandered filters is to operate with the fundamental TE_{10} mode in the required passband and stopband. If the suppression of higher order modes is also desired in the stopband, a waveguide width modification (in the x-axis) following the method presented in Section 4.3.2.2 could be also included.

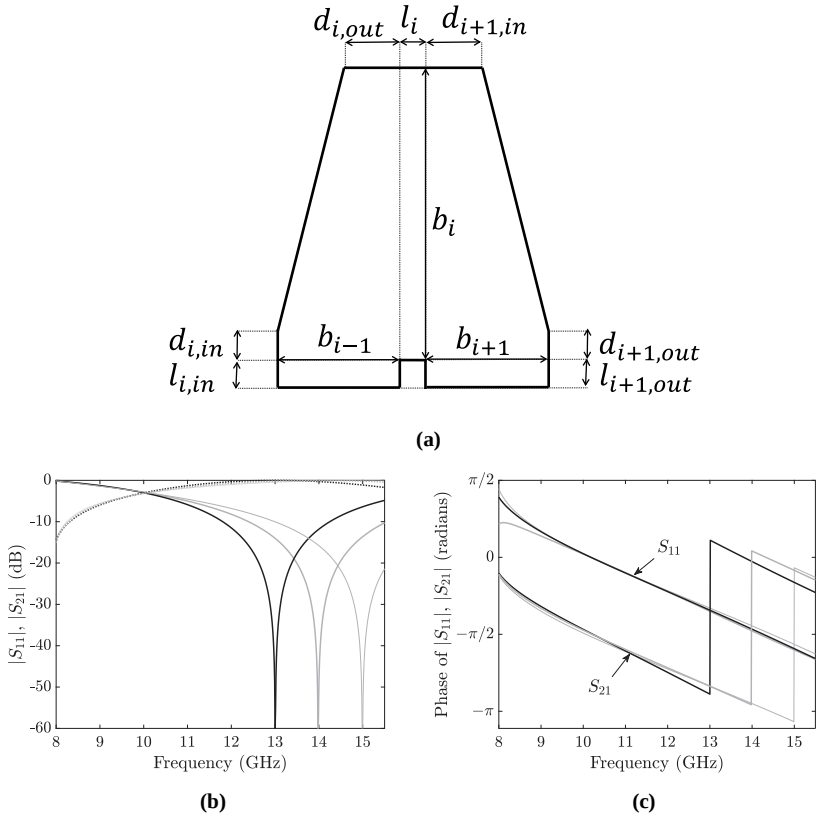

Figure 8.8: Structure formed by two consecutive $-90°$EMBs, responsible of the introduction of a transmission zero (a). Frequency response of the structure for the three examples with dimensions detailed in Table 8.1: Tx zero 13 GHz (black line), Tx zero 14 GHz (thick grey line), and Tx zero 15 GHz (thin grey line); magnitude (b) and phase (c).

Table 8.1: Dimensions for the 3 examples of two consecutive $-90°$EMBs structures with different transmission zeros designed in Section 8.3.1.

Design Parameters	Frequency of Tx zero: 13 GHz	Frequency of Tx zero: 14 GHz	Frequency of Tx zero: 15 GHz
b_{i-1}	4.229	4.229	4.229
b_i	10.940	10.046	9.576
b_{i+1}	5.253	4.229	3.936
$l_{i,1}$	0.074	0.2	0.003
l_i	0.150	0.818	1.458
$l_{i+1,2}$	0.404	0.2	0.443
$d_{i,1}$	1.380	1.547	1.466
$d_{i,2}$	1.145	1.025	0.693
$d_{i+1,1}$	1.814	1.947	2.246
$d_{i+1,2}$	0.719	1.025	1.794

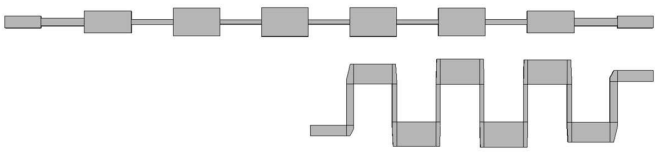

Figure 8.9: Side-view (same scale) of (a) the straight waveguide BPF of order 13 presented in Chapter 7 and (b) the novel meandered topology applied to the same filter.

8.3.2 Meandered BPFs

The novel meandered BPF (see Figure 8.9) is designed utilizing the first inherent passband replica of the classical stepped-impedance low-pass prototype, centered at $\theta = \pi$, Chapter 7, [34]. The synthesis procedure begins by fixing the order of the filter, N, the required in-band return loss, and its lower and upper frequencies, f_1 and f_2, corresponding to $\theta = \pi - \theta_c$ and $\theta = \pi + \theta_c$, respectively (see Figure 8.4), where θ_c is computed following equation (8.10).

$$\theta_c = \pi \cdot \frac{\lambda_{g,f_1} - \lambda_{g,f_2}}{\lambda_{g,f_1} + \lambda_{g,f_2}} \tag{8.10}$$

It is worth noting that the maximum rejection of the lower and upper stopbands takes place at $\theta = \pi/2$ and $\theta = 3\pi/2$, respectively. Then, we compute the transmission-line model for the selected all-pole filtering function, extracting the commensurate lines or Unit Elements following the procedure described in detail in Annex A, [35] (the collection of $N + 2$ characteristic impedances Z_i) which will satisfy the required frequency specification, see Figure 8.3. Now, the required local reflection coefficients, Γ_i, can be calculated using equation (8.2).

The procedure to obtain the dimensions of each $\pm 90^{\circ}$EMB starts by fixing the width, a. Typically, this parameter is fixed as the standard port width. However, it can be reduced to enhance the fabrication yield of the filter as it was introduced in Chapter 7, [34]. This is due to the fact that the electrical bandwidth of the filter will be wider for reduced widths. Thus, a higher value of θ_c will be needed, and impedance ratios required for the same frequency specifications will be reduced. Consequently, more relaxed fabrication tolerances are attained. This is particularly relevant for high frequency bands and for applications where narrow fractional bandwidths are required. However, it is important to note that this waveguide width reduction will produce a shifting towards the passband of the maximum rejection frequencies of the lower and upper stopbands.

The design method continues by mapping the ith local reflection coefficient, Γ_i, calculated by equation (8.2), with the physical dimensions of the ith-EMB, see Figure 8.1 and Figure 8.5. Initially, b_0 is fixed. Then b_1 is computed to satisfy that $|S_{11,1}(f_\pi)|$ provides the reflection value prescribed by $|\Gamma_1|$, where $|S_{11,1}(f_\pi)|$ is the magnitude of the S_{11}-parameter of the 1st-90°EMB at f_π, which is calculated following equation (8.11).

$$f_\pi = \sqrt{\left(\frac{c}{2\cdot a}\right)^2 + \left(\frac{c\cdot(\lambda_{g,f_1}+\lambda_{g,f_2})}{2\cdot\lambda_{g,f_1}\cdot\lambda_{g,f_2}}\right)^2} \tag{8.11}$$

The previous magnitude value mainly depends on the heights b_0 and b_1 and, since b_0 has been already fixed, b_1 can be easily obtained by means of an EM SW tool and taking into account that $\Gamma_i > 0$ requires $b_{i-1} < b_i$ while $\Gamma_i < 0$ needs $b_{i-1} > b_i$. There is also a slight, but appreciable, dependence on the shape of the chamfer through the $d_{1,1}$ and $d_{1,2}$. This extra degree of freedom is used to reduce the height excursion. Then, proceeding consecutively with the rest of the $\pm 90^{\circ}$EMBs, once a certain b_{i-1} is known, b_i is calculated to ensure that:

$$|S_{11,i}(f_\pi)| = |\Gamma_i| \tag{8.12}$$

taking advantage also of the $d_{i,1}$ and $d_{i,2}$. When $i = N+1$, all b_i ,$d_{i,1}$,and $d_{i,2}$ in the final structure have been calculated. It is important to note that the maximum height b_i of the structure must be equal or smaller than the maximum allowed height, b_{max}, calculated through equation (8.13) to avoid the resonance of the TE_{011} mode inside the structure up to a selected maximum frequency, f_{max}. This is fulfilled by selecting appropriately the starting b_0.

$$b_{max} = \frac{1}{\sqrt{\left(\frac{2\cdot f_{max}}{c}\right)^2 - \left(\frac{2}{\lambda_{g,f_\pi}}\right)^2}} \tag{8.13}$$

Next, we calculate the lengths $l_{i,1}$ and $l_{i,2}$ of the ith-EMB (see Figure 8.1). Following equations (8.3) and (8.4), depending on the type of step that we have in the transmission-line model, i.e., either positive or negative Γ_i, the lengths $l_{i,1}$ and $l_{i,2}$ will be adjusted to satisfy (9) or (10) respectively:

Depending on the type of step that we have in the electrical model, i.e., either negative or positive Γ_i, the lengths $l_{i,1}$ and $l_{i,2}$ will be adjusted to satisfy equation (8.14) or equation (8.15) respectively:

$$\phi_{i,S_{11}}(f_\pi) = -\pi \quad \text{and} \quad \phi_{i,S_{21}}(f_\pi) = -\pi \tag{8.14}$$

$$\phi_{i,S_{11}}(f_\pi) = -\pi + \pi = 0 \quad \text{and} \quad \phi_{i,S_{21}}(f_\pi) = -\pi \tag{8.15}$$

being $\phi_{i,S_{11}}(f_\pi)$ and $\phi_{i,S_{21}}(f_\pi)$ the phase of the S_{11}- and S_{21}-parameters, respectively, of the ith-EMB at f_π. Since the ith and the $(i+1)$th-EMB share the height of their output and input ports respectively, it is convenient to add the lengths $l_{i,2}$ and $l_{i+1,1}$ to obtain a single l_i value following equation (8.16).

$$l_i = l_{i,2} + l_{i+1,1} \quad \text{for} \quad i = 1 : N \tag{8.16}$$

where the special cases for the global input and output lengths are calculated as $l_0 = 2 \cdot l_{1,1}$ and $l_{N+1} = 2 \cdot l_{N+1,2}$.

Many possible topologies can be obtained depending on the sequence of $\pm 90°$EMBs employed without the need of redesigning from scratch. Thus, if the selected sequence is $90°$EMB, $-90°$EMB, $90°$EMB, $90°$EMB, and so on, the most compact structure is obtained. This example is presented in Figure 8.9(b) in comparison with the in-line classical topology that is depicted in Figure 8.9(a).

The design methods presented in this Chapter are based on a simple modular procedure which can be easily introduced in a software tool. In fact, the $\pm 90°$EMBs which compose the different structures are very simple, and the dimensions of each $\pm 90°$EMB are obtained in a negligible computing time. At this point, it is important to note that the same kind of optimizations are necessary in the classical design process of in-line corrugated waveguide LPFs due to the effect of higher-order mode excitation at the discontinuities between the adjacent waveguides of different heights [31]. Moreover, the routing of the structure can be easily achieved with the proposed meandered filters, avoiding the use of subsequent bends, reducing the insertion loss, mass, and PIM. Additionally, the proposed techniques open the door to more complex routing structures with different angles.

Design Examples

According to the design methodology proposed, two examples will be presented. In the first example (Section 8.4), the design methodology described in Section 8.3.1 will be applied to a validation Ku-band LPF [1], [2]. The second example (Section 8.5) will be a BPF for Q-band applications which exploits the freedom of the topology. It will be designed following the methodology described in Section 8.3.2, [2]. Two prototypes have been fabricated and measured to demonstrate the feasibility of designing LPF and BPF with the new meandered topology.

8.4 Design Example 1: Ku-band Meandered LPF

The proposed methodology in Section 8.3.1 is applied to the design of a compact LPF for Ku-band.

8.4.1 Specifications

The frequency specifications are: passband defined between 10.7 GHz and 11.7 GHz with in-band return loss better than 20 dB and an attenuation level higher than 60 dB in the required stopband, which is defined between 13.75 GHz and 14.5 GHz.

8.4.2 Design and Simulation

In order to fulfil the previous frequency specifications, a 11th-order Chebyshev will be synthesized. The maximum frequency of the passband, f_c, and the frequency of maximum rejection, f_0, have been set equal to f_c=11.85 GHz and f_0=17 GHz respectively. The in-band return loss will be 25 dB. The slope between the pass- and the stop-band will be reinforced by the introduction of 3 transmission zeros close to the pass-band. The width of the filter is fixed to a = 19.05 mm, and the input port height is b_0= 7 mm. Now, using equation (8.5), the electrical length results in θ_c= 0.9236 rad for our design. Next, applying the Unit Element extraction procedure (Annex A), the list of characteristic impedances for the stepped-impedance prototype is obtained: $Z_1 = Z_13 = 1$, $Z_2 = Z_12 = 0.75$, $Z_3 = Z_11 = 1.32$, $Z_4 = Z_10 = 0.60$, $Z_5 = Z_9 = 1.62$, $Z_6 = Z_8 = 0.53$, and $Z_7 = 1.69$. Then, the required local reflection coefficients Γ_i are calculated using equation (8.2). Now, as explained in Section 8.3.1, each $\pm 90°$EMB is sequentially computed. For the ith $\pm 90°$EMB, $d_{i,1}$, $d_{i,2}$, and b_i are computed to satisfy (8.6) (taking into account that b_{i-1} is fixed in the previous $\pm 90°$EMB), while $l_{i,1}$ and $l_{i,2}$ are computed to satisfy equations (8.7) and (8.8). Additionally, as explained in Section 8.3.1, each two consecutive $-90°$EMBs (or $+90°$EMBs) can produce a transmission zero, and it will be possible to generate 3 transmission zeros close to the passband in our design. FEST3D is used as electromagnetic simulator for the previous calculations and parameter adjustments. The dimensions obtained are listed in Table 8.2 (after applying (8.9)). The frequency response of the filter designed is plotted in Figure 8.10. Although a clear pass-band is achieved, its matching must be improved (obtained return loss better than 15 dB) and a frequency shift appears. To solve those problems, a fine adjustment over the d_i's and l_i's is run. The final dimensions of the filter are detailed in Table 8.3. The frequency response of the filter obtained after the adjustment fully satisfies the prescribed specifications and is also plotted in Figure 8.10. Unlike in the previous meandered BPFs, a final quick optimization over the d_i's and l_i's has been required. This is due to the interaction of the transmission zeros with the implemented Chebyshev frequency response. That interaction cannot be neglected in our case of transmission zeros close to the passband, but it is easily compensated with the final quick optimization over the d_i's and l_i's explained. The novel filter designed in our example has 3 transmission zeros in the required stopband. The first zero

Table 8.2: Final dimensions of the example in Section 8.4 following the technique in Section 8.3.1.

i-th EMB	Γ_i	$d_{i,1}$ (mm)	$d_{i,2}$ (mm)	b_i (mm)	l_i (mm)
				7.000	5
1, 12	-0.115	0.573	1.275	5.775	1.002
2, 11	0.249	3.358	0.558	7.965	0.858
3, 10	-0.378	2.414	0.365	3.561	0.944
4, 9	0.461	1.534	1.919	8.951	1.101
5, 8	-0.504	1.682	1.601	3.224	1.077
6, 7	0.521	2.316	0.960	8.843	0.608

Table 8.3: Final dimensions of the example in Section 8.4 following the technique in Section 8.3.1 after the adjustment over the d_i's and l_i's

i-th EMB	Γ_i	$d_{i,1}$ (mm)	$d_{i,2}$ (mm)	b_i (mm)	l_i (mm)
				7.000	5
1, 12	-0.115	1.000	1.001	5.775	1.002
2, 11	0.249	1.163	1.498	7.965	0.858
3, 10	-0.378	0.810	1.231	3.561	0.050
4, 9	0.461	1.676	1.997	8.951	1.101
5, 8	-0.504	1.652	1.564	3.224	0.050
6, 7	0.521	1.949	1.068	8.843	0.608

is located at 13.75 GHz (produced by the 6th-7th consecutive $-90°$EMBs), and a double zero is located at 15 GHz (produced by the 4th-5th consecutive $+90°$EMBs, and their symmetrical 8th-9th consecutive $+90°$EMBs). Additionally, 2 transmission zeros (a double zero) located at higher frequencies (not used in our design) are produced by the 2th-3th consecutive $-90°$EMBs, and their symmetrical 10th-11th consecutive $-90°$EMBs.

As a general rule, a filter of order N (odd for simplicity) will feature $N+1$ $\pm 90°$EMBs. Each two consecutive $-90°$EMBs (or $+90°$EMBs) can produce a transmission zero. Assuming that the topology selected is the most compact like in our example (i.e., +–++–++...–+), there will be $(N-1)/2$ two-consecutive $-90°$EMBs (or $+90°$EMBs) which can produce a transmission zero. Finally, assuming symmetry in the stepped-impedance prototype (as it happens for Butterworth or Chebyshev functions) the transmission zeros will be grouped in pairs except for a possible single transmission zero.

The novel meandered LPF with transmission zeros designed has been compared with the classical in-line LPF designed following the technique in Section 2.3, and the meandered LPF structure proposed in [1]. Their simulated frequency responses are compared in Figure 8.11, and a side-view of the filters is shown in Figure 8.12.

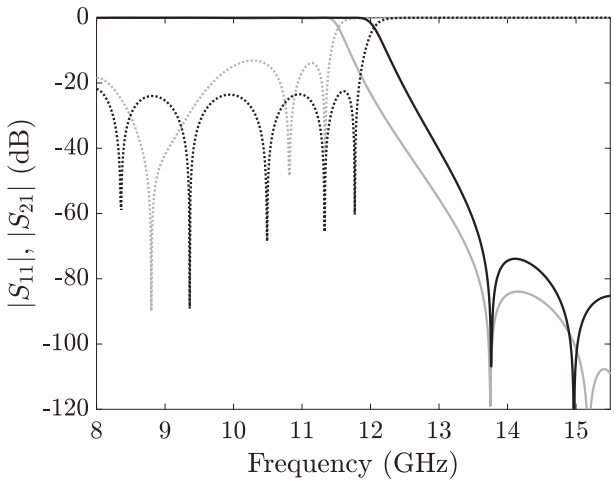

Figure 8.10: FEST3D simulated frequency response comparison between the novel LPF designed with the technique in Section 8.3.1 (grey line) and after the final adjustment of the filter parameters (black line). $|S_{11}|$ in dotted line and $|S_{21}|$ in solid line.

As it can be seen, all the filters fulfill the frequency specifications, but the novel filter proposed in this paper is more compact than its counterparts. Actually, the novel filter is only 29.3 mm-long while the filter in [1] is 104.5 mm-long and the in-line filter is 180.1 mm-long (more than 70% and 83% of length reduction respectively).

8.4.3 Fabrication and Measurement

The novel meandered LPF with transmission zeros has been fabricated in clam-shell configuration, in bare aluminum, by standard milling with a radius of the drill equal to 1 mm. A photograph of the prototype is shown in Figure 8.14. In order to reach the standard WR75 ports for the measurements, two impedance transformers of 1 step have been added to the input and output ports of the structure. The measurement results are also given in Figure 8.14. A remarkable agreement between the simulated (including the impedance transformers) and the measured results is obtained. A detail with the insertion loss of the filter at the passband is shown in Figure 8.15. As it can be seen, the measured insertion loss for the LPF is below 0.1 dB.

8.4.4 High-Power Behavior

It is worth noting that the minimum mechanical gap of the final structure obtained in our design example is larger than 3.5 mm, which will provide high-power handling capability as customarily needed. The high-power behavior of the novel filter has been estimated by means of SPARK3D, using the EM fields previously calculated with CST MWS. The high-power simulation has been performed at 11.7 GHz (upper

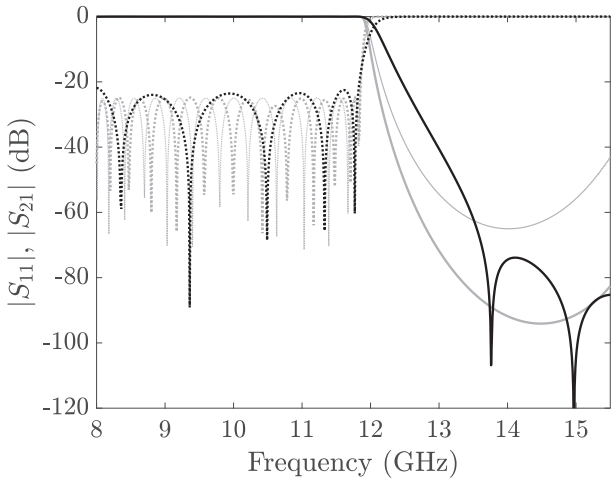

Figure 8.11: FEST3D simulated frequency response comparison between the classical straight LPF designed following the technique in Section 2.3, [33] (grey thin line), the LPF with meandered topology in [1] (grey thick line), and the LPF with transmission zeros designed in this Section (black line), all fulfilling the same frequency specifications. $|S_{11}|$ in dotted line and $|S_{21}|$ in solid line.

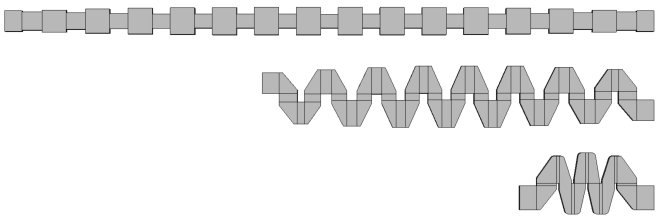

Figure 8.12: Side-view (same scale) of (a) the classical straight LPF designed following the technique in Section 2.3, [33], (b) the filter with meandered topology in [1], and (c) the filter with transmission zeros designed in this Section, all fulfilling the same frequency specifications.

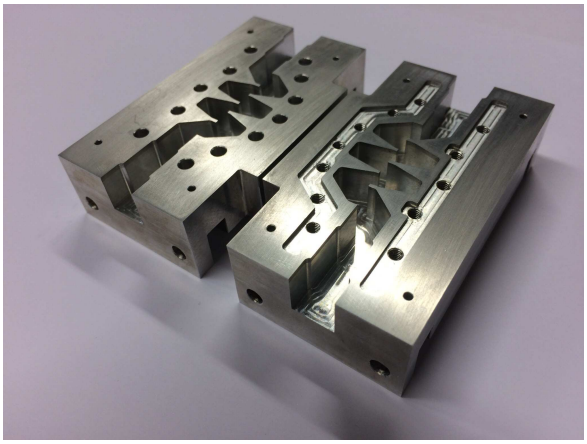

Figure 8.13: Photograph of the unassembled fabricated prototype.

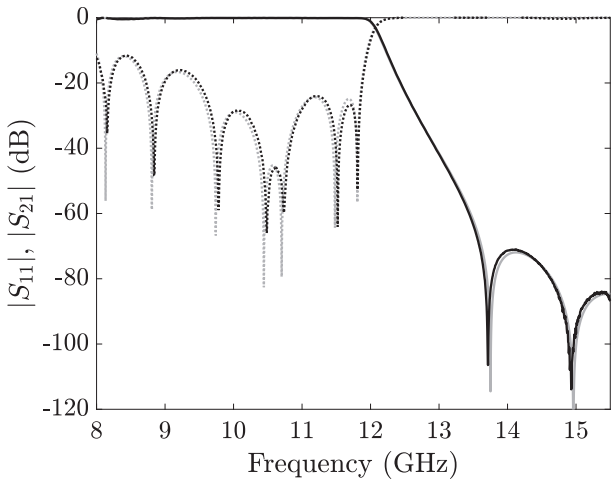

Figure 8.14: Comparison between the CST MWS simulated frequency response (grey line) of the proposed LPF and measurements of the fabricated prototype (black line). $|S_{11}|$ in dotted line and $|S_{21}|$ in solid line.

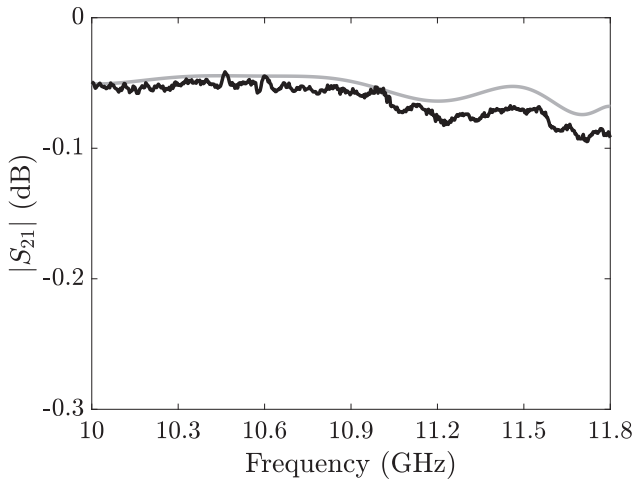

Figure 8.15: Comparison between the CST MWS simulated insertion loss (grey line) of the proposed LPF and measurements of the fabricated prototype (black line).

passband edge, where the EM fields are maximum and the input power threshold will be minimum), using the SEY of silver (ECSS, [36]). The input power threshold level of the proposed LPF is higher than 20 kW, which is a very high value comparable with those that can be found in the literature [24], [37].

8.5 Design Example 2: Q-band Meandered BPF

8.5.1 Specifications

The novel meandered topology for BPFs has been proved targeting the same frequency specifications given in Chapter 7.4. The meandered filter will have a passband between 37.5 and 42.5 GHz with in-band return loss better than 20 dB. The minimum attenuation required will be 65 dB between 47 and 50 GHz. Besides, we will also enforce at least a 65 dB rejection level between 34-35 GHz.

8.5.2 Design and Simulation

In order to fulfill the previous frequency specifications, a meandered band-pass will be synthesized using the novel design technique in Section 8.3.2. After including the usual design margin, a 13th order Chebyshev function is chosen with a return loss level of 25 dB on a passband range defined between f_1 = 37 GHz and f_2 = 43 GHz. The width of the structure is fixed to a = 4.65 mm. The input port height has been set to b_0=1.4 mm, to avoid the coupling to the resonant TE_{011} mode inside the structure up to f_{max}=50 GHz. Finally, the free parameters that adjust the shape of the bends

$d_{i,1}$ and $d_{i,2}$ (see Figure 8.1), have been fixed to 0.5 mm for all the $\pm 90°$EMBs, since they have no influence to obtain transmission zeros which are not possible in the BPF case.

Thus, using equation (8.10) the electrical length results in $\theta_c = 0.6938 rad$ for the proposed design, and applying the Unit Element extraction procedure the characteristic impedance list is obtained: Z_1 = Z_15 = 1, Z_2 = Z_14 = 0.67, Z_3 = Z_13 = 1.84, Z_4 = Z_12 = 0.41, Z_5 = Z_11 = 2.35, Z_6 = Z_10 = 0.37, Z_7 = Z_9 = 2.46, and Z_8 = 0.36. Next, using equation (8.2), the target reflection coefficients Γ_i are calculated, and then the physical dimensions of each $\pm 90°$EMB (b_i, $l_{i,1}$, and $l_{i,2}$) are computed to satisfy equations (8.12), (8.14), and (8.15). FEST3D is employed for the electromagnetic simulation and adjustment of each $\pm 90°$EMB. The final dimensions of the $\pm 90°$EMBs are given in Table 8.4 (after applying (8.16)). To demonstrate the equivalence between the designed $\pm 90°$EMBs and their corresponding sections of the stepped-impedance prototype (see Figure 8.5), their frequency responses are compared in Figure 8.16 for the 1st (initial) and the 7th (central) $\pm 90°$EMBs. A remarkable wideband agreement is achieved between the frequency responses and the theoretical required values: $|\Gamma_1|$=0.201, $|\Gamma_7|$=0.743, see Table 8.4, and $\phi_{1,S_{11}}(f_\pi) = \phi_{7,S_{11}}(f_\pi) = 0$ and $\phi_{1,S_{21}}(f_\pi) = \phi_{7,S_{21}}(f_\pi) = -\pi$, see (8.14) and (8.4).

If the $\pm 90°$EMBs are cascaded following a compact arrangement (-++–++...–+) in accordance with Figure 8.9(b), the frequency response of the resulting meandered BPF (with no final optimization) is shown in Figure 8.17. Its equivalent in-line BPF has been also designed following the design techique described in Section 7.3 (see Figure 8.18). As it can be seen in Figure 8.9, the total length of the structure has been significantly reduced. The length of the novel meandered BPF is only 37.6 mm vs. 81 mm for the in-line BPF (more than 50% length reduction).

One of the most remarkable features of the novel design method proposed in this paper is that, since it is a modular design procedure, once all the $\pm 90°$EMBs are calculated, they can be connected as the designer desires. In order to demonstrate the high versatility and great flexibility of the meandered structures proposed, different topologies have been simulated, fabricated, and measured. Using the $\pm 90°$EMBs designed for the example in Figure 8.17 without any final optimization in their physical parameters (the physical dimensions employed are exactly those given in Table 8.4), different ad-hoc layouts are proposed in Figure 8.19 and Figure 8.20. As it is shown in Figure 8.19 and Figure 8.20, the frequency response of both structures fulfills the specifications.

8.5.3 Fabrication and Measurement

In order to demonstrate the feasibility of designing BPF with meandered topology, two of the previous filters (see Figure 8.17(b) and Figure 8.20(b)) have been fabricated. Firstly, two transformers of two sections have been added to the input and output ports to reach the WR-22 standard ports. The prototypes have been fabricated by CCM in two halves cut by the E-plane in aluminum.

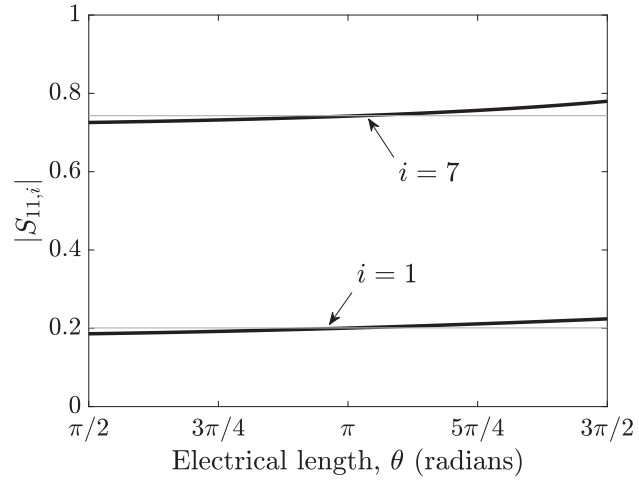

(a)

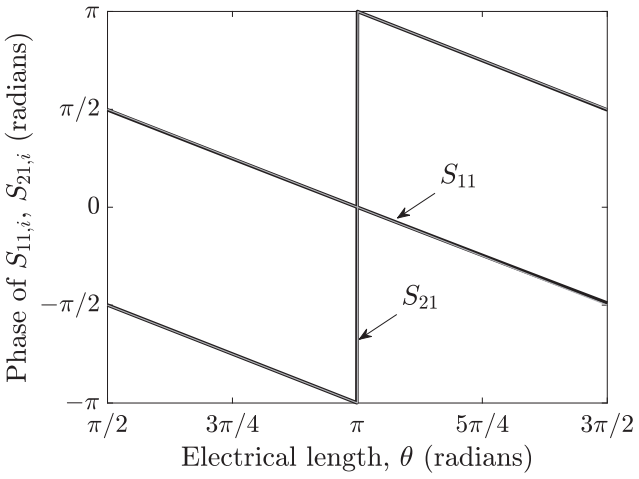

(b)

Figure 8.16: (a) Magnitude and (b) Phase of the frequency response of the 1st and 7th EMBs designed for the Q-band meandered BPF (black thick line) vs. the frequency response of their corresponding sections of the stepped-impedance prototype (grey thin line).

Table 8.4: Final dimensions of the example in Section 8.5 following the technique in Section 8.3.2.

i-th EMB	Γ_i	b_i (mm)	l_i (mm)
		1.400	5
1, 14	-0.201	0.971	5.835
2, 13	0.469	2.547	5.386
3, 12	-0.637	0.602	5.398
4, 11	0.704	3.191	5.531
5, 10	-0.729	0.546	5.326
6, 9	0.739	3.322	5.552
7, 8	0.743	0.540	5.312

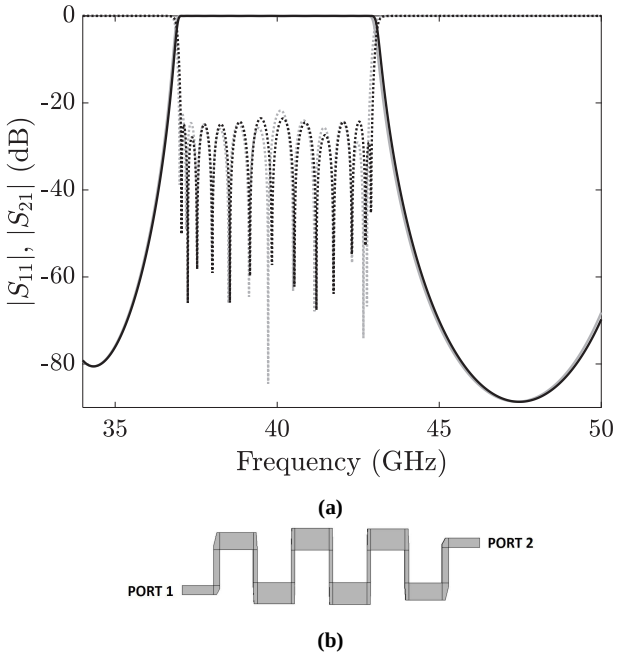

Figure 8.17: (a) Simulated frequency response of the novel meandered BPF designed with the technique in Section 8.3.2 FEST3D simulation in grey line and CST MWS in black line. $|S_{11}|$ in dotted line and $|S_{21}|$ in solid line. (b) Side view of the simulated BPF.

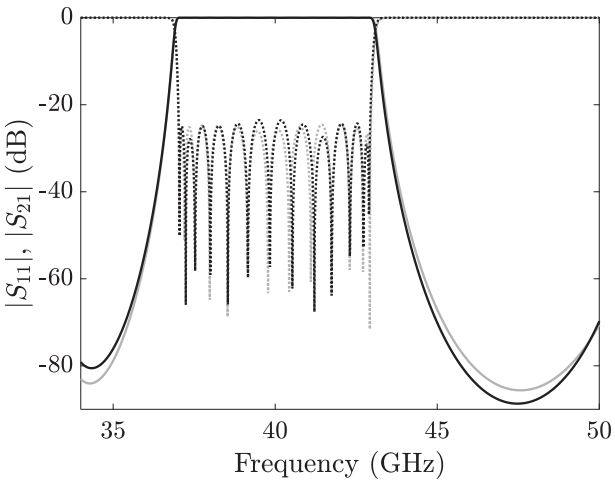

Figure 8.18: FEST3D simulated frequency response comparison between the novel meandered BPF (black line) and the in-line design as in Section 7.3 (grey line). $|S_{11}|$ in dotted line and $|S_{21}|$ in solid line.

The photograph of the first prototype is shown in Figure 8.21 and the measurement results are given in Figure 8.22. As it can be observed, an excellent agreement is attained. In the case of the second prototype (see Figure 8.23), a slight deviation in the return loss is observed in the measurement results of the device (see Figure 8.24 – worst value -18.4 dB).

8.6 Conclusions

In this Chapter, a new meandered topology for rectangular waveguide LPFs and BPFs is proposed. The novel filters cascade $\pm 90^{\circ}$EMBs whose physical dimensions are calculated in a simple modular manner, that can be easily integrated in an EM SW tool. Furthermore, due to its modular nature, different lay-out configurations can be achieved without further optimizations, allowing us to obtain ad-hoc designs with routing capabilities. Additionally, in the case of the novel meandered LPF, transmission zeros can be achieved, producing very steep slopes between the pass- and the stopband. Moreover, the novel meandered topology allows more compact structures in comparison with the state-of-the-art filters. Two different examples, a BPF and a LPF, have been designed and simulated to demonstrate the aforementioned characteristics. Both have been fabricated by CCM, and the measurements of the prototype show an excellent agreement with the simulated results, confirming the robustness of the novel filter topology.

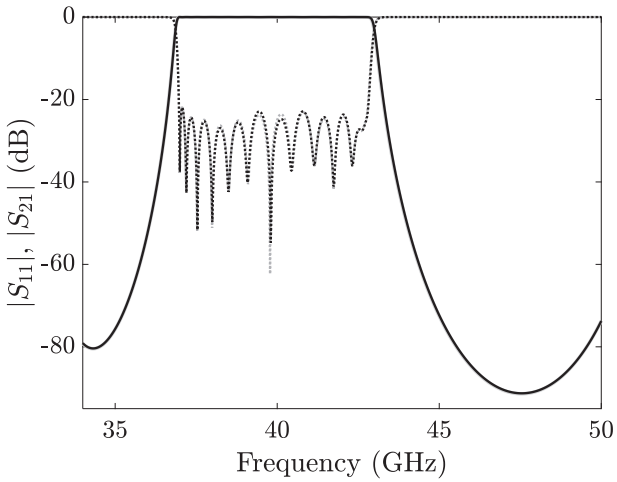

(a)

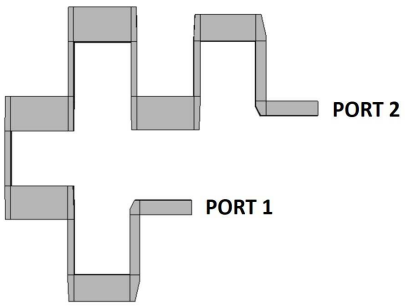

(b)

Figure 8.19: (a) Simulated frequency response of a different topology of meandered BPF designed with the technique in Section 8.3.2 FEST3D simulation in grey line and CST MWS in black line. $|S_{11}|$ in dotted line and $|S_{21}|$ in solid line. (b) Side view of the simulated BPF.

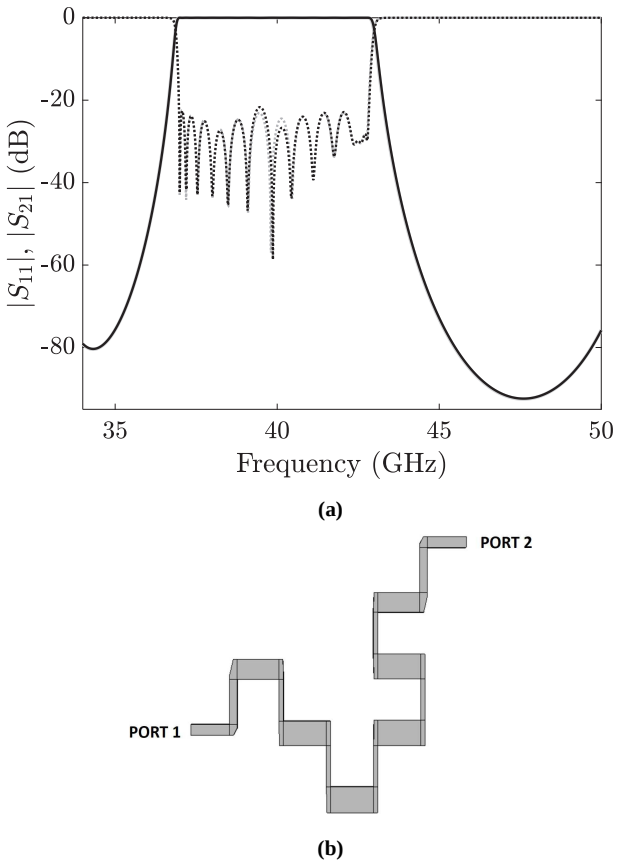

Figure 8.20: (a) Simulated frequency response of a different topology of meandered BPF designed with the technique in Section 8.3.2 FEST3D simulation in grey line and CST MWS in black line. $|S_{11}|$ in dotted line and $|S_{21}|$ in solid line. (b) Side view of the simulated BPF.

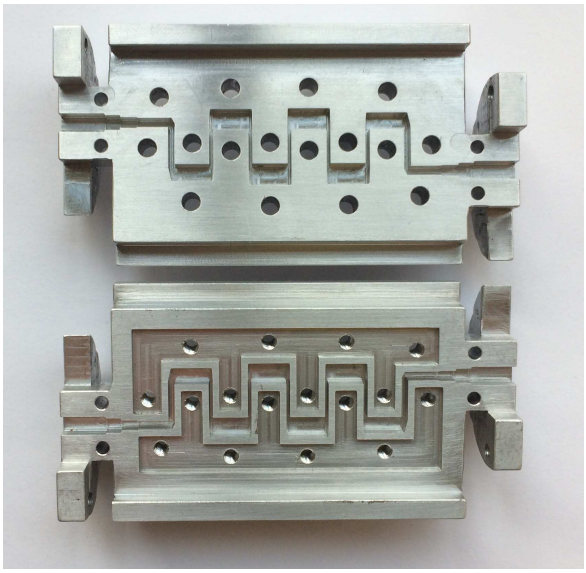

Figure 8.21: Photograph of the unassembled fabricated prototype.

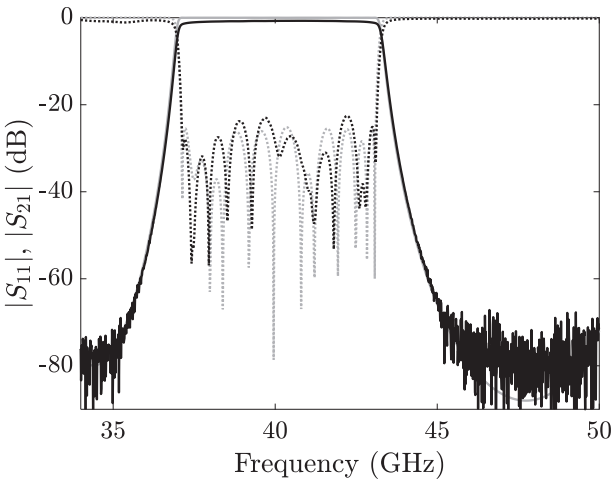

Figure 8.22: Comparison between the CST MWS simulated frequency response (grey line) of the proposed LPF and measurements of the fabricated prototype (black line). $|S_{11}|$ in dotted line and $|S_{21}|$ in solid line.

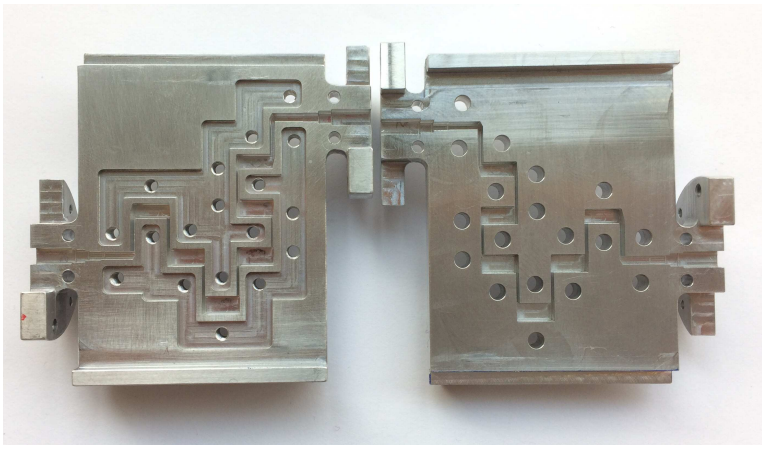

Figure 8.23: Photograph of the unassembled fabricated prototype.

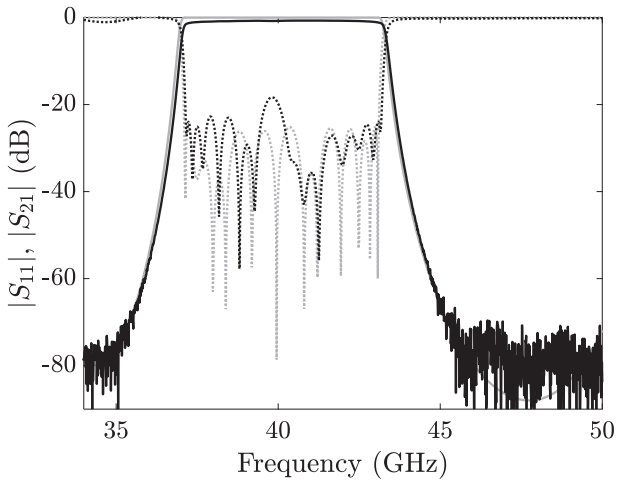

Figure 8.24: Comparison between the CST MWS simulated insertion loss (grey line) of the proposed LPF and measurements of the fabricated prototype (black line).

REFERENCES

[1] F. Teberio, I. Arnedo, J. M. Percaz, I. Arregui, P. Martin-Iglesias, T. Lopetegi, and M. A. G. Laso, "Meandered corrugated waveguide low-pass filter," in *IEEE MTT-S International Microwave Workshop Series on Advanced Materials and Processes (IMWS-AMP)*, Sep. 2017.

[2] F. Teberio, J. M. Percaz, I. Arregui, P. Martin-Iglesias, T. Lopetegi, M. A. G. Laso, and I. Arnedo, "Rectangular waveguide filters with meandered topology," *IEEE Transactions on Microwave Theory and Techniques*, vol. -, no. -, pp. -, 2018.

[3] UPNA, "Design techniques for low-cost filters with reduced sensitivity to fabrication tolerances at high-frequencies," ESA and Thales Alenia Space, NPI 4000114859/15/NL/HK, 2018.

[4] H. Wolf, M. Schneider, S. Stirland, and D. Scouarnec, "Satellite multibeam antennas at airbus defence and space: State of the art and trends," in *2014 8th European Conference on Antennas and Propagation (EuCAP)*, Apr. 2014, pp. 182–185.

[5] H. Moheb, C. Robinson, and J. Kijesky, "Design amp; development of co-polarized ku-band ground terminal system for very small aperture terminal (vsat) application," in *IEEE Antennas and Propagation Society International Symposium. 1999 Digest. Held in conjunction with: USNC/URSI National*

Radio Science Meeting (Cat. No.99CH37010), vol. 3, Jul. 1999, 2158–2161 vol.3.

[6] C. Vicente, D. Wolk, H. L. Hartnagel, and D. Raboso, "An experimental investigation on passive intermodulation at rectangular waveguide interfaces," in *2006 IEEE MTT-S International Microwave Symposium Digest (IMS)*, Jun. 2006, pp. 242–245.

[7] X. Zhao, Y. He, M. Ye, F. Gao, W. Peng, Y. Li, C. Bai, and W. Cui, "Analytic passive intermodulation model for flange connection based on metallic contact nonlinearity approximation," *IEEE Transactions on Microwave Theory and Techniques*, vol. 65, no. 7, pp. 2279–2287, Jul. 2017.

[8] D. Smacchia, P. Soto, V. E. Boria, M. Guglielmi, C. Carceller, J. R. Garnica, J. Galdeano, and D. Raboso, "Advanced compact setups for passive intermodulation measurements of satellite hardware," *IEEE Transactions on Microwave Theory and Techniques*, vol. 66, no. 2, pp. 700–710, Feb. 2018.

[9] A. Morini, T. Rozzi, and M. Mongiardo, "Curved filters in rectangular waveguide," in *1996 26th European Microwave Conference (EuMC)*, vol. 1, Sep. 1996, pp. 153–154.

[10] C. Wang, K. A. Zaki, A. E. Atia, and T. G. Dolan, "Dielectric combline resonators and filters," *IEEE Transactions on Microwave Theory and Techniques*, vol. 46, no. 12, pp. 2501–2506, Dec. 1998.

[11] M. Yu, W.-C. Tang, A. Malarky, V. Dokas, R. Cameron, and Y. Wang, "Predistortion technique for cross-coupled filters and its application to satellite communication systems," *IEEE Transactions on Microwave Theory and Techniques*, vol. 51, no. 12, pp. 2505–2515, Dec. 2003.

[12] T. Shen and K. A. Zaki, "Folded evanescent-mode ridge waveguide bandpass filters," in *2001 31st European Microwave Conference (EuMC)*, Sep. 2001, pp. 1–4.

[13] E. Ofli and R. Vahldieck, "A novel compact millimeter wave diplexer," in *2002 IEEE MTT-S International Microwave Symposium Digest (IMS)*, vol. 1, Jun. 2002, 377–380 vol.1.

[14] M. Guglielmi, F. Montauti, L. Pellegrini, and P. Arcioni, "Implementing transmission zeros in inductive-window bandpass filters," *IEEE Transactions on Microwave Theory and Techniques*, vol. 43, no. 8, pp. 1911–1915, Aug. 1995.

[15] C. Tomassoni, L. Marcaccioli, M. Dionigi, M. Mongiardo, R. V. Gatti, and R. Sorrentino, "CAD of folded filters and diplexers by the generalized scattering matrix of the single step discontinuity," in *2004 IEEE MTT-S International Microwave Symposium Digest (IMS)*, vol. 3, Jun. 2004, 1843–1846 Vol.3.

[16] J. Bornemann, S. Amari, and R. Vahldieck, "A flexible s-matrix algorithm for the design of folded waveguide filters," in *2005 European Microwave Conference (EuMC)*, vol. 1, Oct. 2005, 4 pp.-.

[17] C. Carceller, P. Soto, V. Boria, M. Guglielmi, and D. Raboso, "New folded configuration of rectangular waveguide filters with asymmetrical transmission zeros," in *2014 44th European Microwave Conference (EuMC)*, Oct. 2014, pp. 183–186.

[18] U. Rosenberg, M. Knipp, and S. Amari, "Compact diplexer design using different E-plane triplets to serve contiguous passbands with high interband selectivity," in *2006 36th European Microwave Conference (EuMC)*, Sep. 2006, pp. 133–136.

[19] C. Carceller, P. Soto, V. E. Boria, and M. Guglielmi, "Design of hybrid folded rectangular waveguide filters with transmission zeros below the passband," *IEEE Transactions on Microwave Theory and Techniques*, vol. 64, no. 2, pp. 475–485, Feb. 2016.

[20] F. Teberio, I. Arregui, A. Gomez-Torrent, I. Arnedo, M. Chudzik, M. Zedler, F. J. Görtz, R. Jost, T. Lopetegi, and M. A. G. Laso, "Chirping techniques to maximize the power-handling capability of harmonic waveguide low-pass filters," *IEEE Transactions on Microwave Theory and Techniques*, vol. 64, no. 9, pp. 2814–2823, Sep. 2016.

[21] F. Teberio, I. Arregui, A. Gomez-Torrent, E. Menargues, I. Arnedo, M. Chudzik, M. Zedler, F. J. Görtz, R. Jost, T. Lopetegi, and M. A. G. Laso, "Low-loss compact ku-band waveguide low-pass filter," in *2015 IEEE MTT-S International Microwave Symposium Digest (IMS)*, May 2015, pp. 1–4.

[22] ——, "High-power waveguide low-pass filter with all-higher-order mode suppression over a wide-band for ka-band satellite applications," *IEEE Microwave and Wireless Components Letters*, vol. 25, no. 8, pp. 511–513, Aug. 2015.

[23] I. Arregui, F. Teberio, I. Arnedo, A. Lujambio, M. Chudzik, D. Benito, T. Lopetegi, R. Jost, F.-J. Gortz, J. Gil, C. Vicente, B. Gimeno, V. Boria, D. Raboso, and M. Laso, "High-power low-pass harmonic filters with higher-order TEn0 and non-TEn0 mode suppression: Design method and multipactor characterization," *IEEE Transactions on Microwave Theory and Techniques*, vol. 61, no. 12, pp. 4376–4386, Dec. 2013.

[24] O. A. Peverini, G. Addamo, R. Tascone, G. Virone, P. Cecchini, R. Mizzoni, F. Calignano, E. P. Ambrosio, D. Manfredi, and P. Fino, "Enhanced topology of e-plane resonators for high-power satellite applications," *IEEE Transactions on Microwave Theory and Techniques*, vol. 63, no. 10, pp. 3361–3373, Oct. 2015.

[25] L. Young, "Stepped-impedance transformers and filter prototypes," *IRE Transactions on Microwave Theory and Techniques*, vol. 10, no. 5, pp. 339–359, Sep. 1962.

[26] G. Matthaei, L. Young, and E. M. T. Jones, *Microwave filters, impedance-matching networks and coupling structures*. Artech House, 1980.

[27] S. B. Cohn, "A theoretical and experimental study of a waveguide filter structure," *Office Naval Res.*, vol. 39, no. 11, Apr. 1948.

[28] R. Levy, “Tables of element values for the distributed low-pass prototype filter,” *IEEE Transactions on Microwave Theory and Techniques*, vol. 13, no. 5, pp. 514–536, Sep. 1965.

[29] ——, “A generalized design technique for practical distributed reciprocal ladder networks,” *IEEE Transactions on Microwave Theory and Techniques*, vol. 21, no. 8, pp. 518–526, Aug. 1973.

[30] ——, “Tapered corrugated waveguide low-pass filters,” *IEEE Transactions on Microwave Theory and Techniques*, vol. 21, no. 8, pp. 526–532, Aug. 1973.

[31] M. Simeoni, F. Cacchione, S. Vanin, J. Molina-Perez, and D. Schmitt, “Automatic dimensional synthesis without optimization for stepped impedance low-pass filters,” *Microwave Optical and Technology Letters*, vol. 44, no. 1, pp. 190–193, Jan. 2005.

[32] V. Boria, P. Soto, and S. Cogollos, “Distributed models for filter synthesis,” *Microwave Magazine, IEEE*, vol. 12, no. 6, pp. 87–100, Oct. 2011.

[33] F. Teberio, I. Arnedo, J. M. Percaz, I. Arregui, T. Lopetegi, and M. A. G. Laso, “Accurate design of corrugated waveguide low-pass filters using exclusively closed form expressions,” in *2017 47th European Microwave Conference (EuMC)*, Oct. 2017.

[34] F. Teberio, P. Soto, I. Arregui, T. Lopetegi, S. Cogollos, I. Arnedo, P. Martin-Iglesias, V. E. Boria, and M. A. G. Laso, “Waveguide band-pass filter with reduced sensitivity to fabrication tolerances for q-band payloads,” in *2017 IEEE MTT-S International Microwave Symposium Digest (IMS)*, Jun. 2017, pp. 1464–1467.

[35] R. Cameron, C. Kudsia, and R. Mansour, *Microwave Filters for Communication Systems: Fundamentals, Design and Applications*. Wiley-Interscience, 2007.

[36] ESA, *ECSS Space engineering, multipactor design, and test*. Noordwijk, The Neederlands: ESA Publications Division, Apr. 2000, vol. ECSS-E-20-01.

[37] P. Sarasa, A. González, H. Esteban, P. Mader, K. Tossou, and P. Lepeltier, “Comparative study of the power handling capability of space broadband antenna filters in ku-band,” in *2005 5th ESA International Workshop on Multipactor, Corona and Passive Intermodulation in Space RF Hardware (MULCOPIM)*, Sep. 2005.

CHAPTER 9

CONCLUSIONS AND FUTURE WORK

In this Thesis, the main goals have been successfully achieved. Firstly, a novel quasi-analytical synthesis procedure for stepped-impedance LPFs has been proposed. It allows the designers to obtain a final prototype whose frequency response is very close to the theoretical one. Actually, only closed-form expressions are utilized to obtain the final dimensions, reducing the costs associated with the design-times. Additionally, this technique has been extended to include the rounded corners if a CCM manufacturing is assumed. This technique can be easily integrated in a SW module obtaining excellent results in a negligible CPU time. Moreover, the possibility of embedding routing capabilities in this kind of structure is also presented, avoiding subsequent bending structures and reducing insertion loss, volume/weight, and PIM. Then, a novel accurate design procedure for classical waffle-iron filters has been proposed. The novel technique allows to design in a matter of minutes waffle-iron filters fulfilling any frequency specifications with or without transmission zeros. Up to now, the design of this kind of devices follows a hard and time-consuming process, since the existing design procedures are based on approximations and further optimizations. In this case, the proposed method gives directly a final design or a very approximate solution which can be slightly optimized in a very short time. Finally, a compact waffle-iron structure has been proposed. This novel filter achieves multi-

ple transmission zeros at multiple frequencies in a single structure. This permits to reduce the size of the filter more than 40% in comparison with the state-of-the-art.

After that, two novel design techniques to design high-power LPFs with very wide rejected bands have been proposed. The first is based on smooth-profile structures and the second utilizes step-shaped bandstop elements, which are easier to be fabricated by conventional CCM. Both structures are an excellent solution to reduce mass and volume for the output stage of a communication satellite payload. Moreover, very steep slopes between the passband and the rejection bands can be accomplished in a very compact size (this does not occur in classical implementations, where high orders are needed). Furthermore, it is also a tailored technique, being able to be utilized in different applications such as multi-beam payloads or diplexers. In all those different applications, the novel filters are a better solution in comparison with its classical counterparts. Indeed, for example in the case of the Ka-band LPF developed for multi-beam payloads, the novel filter is around 40%-length smaller, has almost half insertion loss and handles at least 10 dB more power than its classical counterpart the waffle-iron filter. Besides, the proposed filter can be easily fabricated by CCM, making it especially attractive to mass-production in multi-beam applications, where hundreds of filters must be manufactured. Additionally, a *multipactor-free* solution has been developed whose multipactor threshold level is higher than 100 kW. It allows to avoid cumbersome multipactor testing campaigns in multi-carrier systems. Last but not least, in order to demonstrate the great flexibility of the step-shaped LPF, they have been incorporated in the design of diplexer, obtaining excellent results in terms of foot-print reduction. This work has been extended to a novel BPF based on the previous low-pass filtering structure in combination with a high-power response, which has been proposed as part of high-performance compact diplexers for Ku- and K-band satellite applications. This technique allows to design and manufacture very practical compact BPFs with very wide rejection bands, low losses and high power-handling. The novel diplexers benefit from a very compact size, which makes them especially attractive for satellite applications, where compact hardware is needed to reduce mass and volume. Indeed, more than 50%-foot-print reduction is achieved for the two different examples presented. Similarly, they also benefit from an easy manufacturing, making them an excellent solution for multi-beam payloads.

Pursuing the goal of reducing the sensitivity to manufacturing tolerances, a novel BPFs intended for Q/V-band applications has been proposed. The new filters are based on the first inherent passband replica of the classical stepped-impedance low-pass filter and utilize a waveguide width reduction to improve dramatically the manufacturing yield of a BPF for Q-band applications. Indeed, the fabrication yield ($\pm$ 25μm) is highly enhanced, 92% in the novel filter vs. 8% in its classical counterpart (the classical inductive iris filter). With the second approach, moderate narrower bandwidths can be accomplished (that cannot be achieved with the first approach). Two clear future work-lines have been identified at this point: i) to embed the waveguide transformers and to suppress the low-pass intrinsic replica of these devices, allowing to obtain more compact structures and ii) to include transmission zeros to enhance the stopband of the BPFs, allowing us to reduce the required order and, hence, the size of the prototypes. Furthermore, the opportunity of utilizing this kind

of filters in higher frequency bands (such as E/W/F-bands) will be also studied due to their excellent resilience to the influence of the fabrication-technique tolerances.

Finally, a new meandered topology has been proposed to reduce further the size of the previous filters and the classical low-pass structures as well as to embed routing capabilities in these filters, allowing to obtain different ad-hoc designs. The novel meandered structures are based on the connection of 90° E-plane mitered bends whose physical dimensions are calculated in a simple modular manner, that can be easily integrated in an EM SW tool. Besides, in the case of the novel meandered LPF, transmission zeros can be achieved, producing very steep slopes between the pass- and the stopband. A further investigation on this kind of structures with different angles will be performed in the future since it might open the possibility of designing the best structure to be manufactured by additive manufacturing in metal (i.e. by selective laser sintering). Moreover, the meandered structures are potentially interesting in complex diplexers and feed-chains at high frequency bands.

It is important to note that all the filters developed in this Thesis are tuning-free solutions which have been applied to the different satellite operating bands.

Conclusiones (Spanish)

En esta Tesis se han conseguido los diferentes objetivos propuestos al inicio de la misma. En primer lugar, se ha desarrollado un nuevo tipo de síntesis para los filtros corrugados clásicos, cuyo procedimiento cuasi-analítico basado en expresiones cerradas permite obtener las dimensiones finales del filtro en tiempos de computación despreciables. Esta técnica se ha extendido para tener en cuenta los redondeos debidos a las fabricaciones por fresado clásico. El nuevo método ya no está basado en expresiones analíticas, pero gracias a su diseño modular y a la sencillez del procedimiento puede ser integrado de manera fácil en una herramienta de diseño EM como FEST3D o CST MWS. Igualmente, este último método puede modificarse ligeramente para poder incorporar capacidad de enrutado a estas estructuras, lo cual permite obtener filtros doblados tal y como desee el diseñador de manera que se puedan eliminar estructuras como codos etc. Esto supone un beneficio claro en cuestión de peso, pérdidas de inserción o PIM. Además de los filtros corrugados, se ha trabajado en un nuevo método de diseño para los filtros waffle-iron, que son la opción clásica cuando se requiere la supresión de modos de alto orden. Hasta hoy, las técnicas existentes están basadas en aproximaciones y optimización, cuestión que hace a estos filtros difíciles y costosos de diseñar. Con la nueva técnica propuesta, tanto los filtros clásicos sin ceros de transmisión como con múltiples ceros de transmisión localizados a una sola frecuencia se pueden diseñar en cuestión de unos pocos minutos. Asimismo, también se ha propuesto un nuevo tipo de waffle-iron con múltiples ceros de transmisión a múltiples frecuencias, con el que se consigue una reducción de tamaño de más de un 40% así como una disminución de las pérdidas de inserción.

Sin embargo, los filtros anteriores no sirven cuando se requieren, simultáneamente, niveles de potencia altos y un ancho de banda de rechazo amplio. Para ello, se han presentado dos tipos de filtros que son capaces de conseguirlo. El primero está

basado en perfiles suaves, muy aconsejables para manejar alta potencia, y el segundo en estructuras rectangulares con las que se reducen enormemente los costes asociados a su fabricación, teniendo siempre en cuenta CCM como estándar de la industria espacial. Con los filtros suaves se ha demostrado la posibilidad de reducir la masa y el volumen de la parte de salida de un satélite de comunicaciones. Aparte de esta aplicación, el método de diseño de los filtros con perfil rectangular es fácilmente personalizable, ya que la idea fundamental es que estos filtros se puedan utilizar en diferentes aplicaciones, como los satélites multi-haz o diplexores. Para corroborar la gran ventaja de estos filtros frente a sus alternativas clásicas se ha diseñado un filtro paso bajo para aplicaciones multi-haz en banda Ka donde se incorporan cientos de filtros iguales. Este nuevo filtro es un 40% más pequeño, tiene la mitad de pérdidas de inserción y, además, maneja 10 dB más de potencia que su alternativa clásica, el filtro waffle-iron. Asimismo, se ha diseñado un filtro que se podría denominar como libre de multipactor dado que se obtienen niveles de potencia mayores de 100 kW, lo cual permite evitar realizar medidas de multipactor de sistemas multi-portadora, que son difíciles y costosas. Por último, con el objetivo de certificar la gran flexibilidad de los nuevos filtros paso bajo con perfiles rectangulares, se han aplicado en el diseño de diplexores obteniendo excelentes resultados. Este trabajo se ha extendido con el diseño de nuevos filtros paso banda para diplexores de altas prestaciones, que están basados en la combinación de la respuesta paso bajo que dan los filtros con perfil rectangular unido a una respuesta tipo paso alto. Todo ello da lugar a unos filtros muy interesantes que permiten reducir notablemente el tamaño del diplexor consiguiendo estructuras muy pequeñas y fáciles de fabricar.

Con el fin de conseguir dispositivos muy robustos frente a las tolerancias de fabricación, se ha propuesto un nuevo tipo de filtro paso banda. En este caso, la idea esencial es que sea aplicable a las bandas de frecuencia Q y V, donde el tamaño de las cavidades de los dispositivos clásicos es del mismo orden que las herramientas que se utilizan para fabricarlos, produciendo muchas imprecisiones. El diseño del nuevo filtro está fundamentado en la primera réplica del filtro clásico basado en saltos de impedancia. Además de utilizar la primera réplica, se reduce la anchura de la guía de manera constante, lo que da lugar a una mejora muy importante en las tolerancias de fabricación. De hecho, el éxito de fabricación de la nueva estructura es de un 92% cuando para su alternativa clásica es de sólo un 8%. En este tipo de estructuras es en las que se continuará trabajando en el futuro más próximo. Concretamente, ya se han detectado claramente dos líneas de investigación. En primer lugar, se mejorararán algunas de las limitaciones del anterior diseño, como intentar eliminar la banda paso-bajo intrínseca a este tipo de filtros así como integrar los transformadores necesarios para conseguir los puertos estándar dentro del propio filtro. En segundo lugar, se estudiará la posibilidad de incluir ceros de transmisión en estas estructuras para dotarlas de mayor selectividad y mejorar su factor de calidad, ya que los órdenes de filtro necesarios para cumplir especificaciones con los filtros propuestos en esta tesis son altos.

Por último, se ha presentado una nueva topología y método de diseño para filtros con meandros. Este nuevo método se puede aplicar tanto a los filtros paso bajo como los paso banda (los desarrollados anteriormente) basados en saltos de impedancias.

La principal ventaja de estas estructuras es que se pueden obtener diseños totalmente personalizables desde el punto de vista de enrutabilidad, lo cual también le confiere una gran versatilidad si se quieren incorporar dentro de un sistema más complejo a la hora de acomodar más dispositivos. Además de todo lo anterior, en el caso del filtro paso bajo se pueden conseguir ceros de transmisión que permiten lograr pendientes muy abruptas entre la banda de paso y de rechazo, reduciendo en gran medida el orden de filtro necesario y, por consiguiente, su tamaño final. Por lo tanto, en este ámbito se abre también una nueva línea de investigación, dado que la gran flexibilidad de estas estructuras hace que puedan ser diseñadas con diferentes ángulos (en el ejemplo sólo se usan ángulos de $90°$). Esta característica las hace muy propicias para ser producidas en metal por fabricación aditiva, ya que se podría elegir el ángulo más adecuado para crear el mejor dispositivo en términos de tolerancias o rugosidad superficial.

Es importante resaltar que todos los filtros y las estructuras desarrollados en esta Tesis no necesitan ningún tipo de ajuste posterior, además de haber sido diseñados en diferentes bandas de frecuencia, demostrando su gran versatilidad

APPENDIX A

UNIT ELEMENT EXTRACTION PROCEDURE

A key procedure in the realization of stepped-impedance filters is the extraction procedure of the so-called Unit Elements (UEs). Although this procedure is fully detailed in [1], it is also included in this Annex for the sake of completeness.

The theory behind the synthesis of stepped-impedance filters is mainly due to Levy, which published several papers in the 1960s and 1970s related to this topic [2]–[5]. In these publications, the synthesis of the low-pass stepped-impedance prototype (see Figure A.1) is achieved by means of a class of polynomials that are suitable for representing the transfer function of the LPF performance. This includes any all-pole function, e.g. Butterworth, Chebyshev, Zolotarev, Chained function, etc.

On the basis of the element values $g_1, g_2, ..., g_N, g_{N+1}$ of the lumped-element low-pass prototype filter of order N ($\omega_c = 1$rad/s and $R_g = 1\Omega$) which can be found in [6] or can be obtained using several readily-available electrical filter SW tools, the LC ladder network can be utilized to calculate its $Z_{in}(s)$ in an analytical manner (see Figure A.2).

Then, the value of $S_{11}(s)$ is calculated following equation (A.1).

New Filter Design Methods and Topologies for the Future Microwave and Millimeter-Wave High-Capacity Satellites, by Fernando Teberio. 2018 Public University of Navarre.

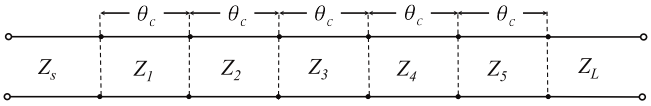

Figure A.1: Stepped-impedance prototype.

$$S_{11}(s) = \frac{Z_{in}(s) - 1}{Z_{in}(s) + 1} \tag{A.1}$$

Next, $S_{11}(s)$ is expressed as the ratio of the N-degree polynomials $F(s)$ and $E(s)$ as indicated in equation (A.2).

$$S_{11}(s) = \frac{F(s)}{E(s)} \tag{A.2}$$

After that, the roots of the polynomials $F(s)$ and $E(s)$ are calculated and mapped to the Richards' transformation plane (in order to use t as complex-frequency variable) following equation (A.3), where the variable a is given by equation (A.4). As it was demonstrated by Richards, microwave networks composed of commensurate transmission lines and lumped resistors, can be treated as lumped-element networks using a frequency transformation known as *Richards' transform*. In that way, the frequency response of the commensurate line network will be identical to that of its equivalent lumped-element network, but with a frequency dependence that varies as $t = j \cdot \tan\omega$ (*Richards' transform*) instead of $s = j\omega$, [7]. Moreover, all commensurate lines will have identical electrical length θ_c, which is the electrical length at the maximum frequency of the passband, f_c, which is related to the physical length of the final structure, l, through the phase constant, β_{f_c}, or the wavelength, λ_{g,f_c}, as it is defined in equation (A.5).

$$t = \frac{\pm s}{\sqrt{a^2 + s^2}} = \frac{\pm s \cdot \sin\theta_c}{\sqrt{1 + (s \cdot \sin\theta_c)^2}} \tag{A.3}$$

$$a = \frac{1}{\sin\theta_c} \tag{A.4}$$

$$\theta_c = \beta_{f_c} \cdot l = \frac{2\pi}{\lambda_{g,f_c}} \cdot l \tag{A.5}$$

The effect of applying this mapping function to the s-plane transfer function is that, as θ increases from zero, the corresponding frequency variable in the s-plane increases, reaching passband edge at $\theta = \theta_c$. The range $\theta_c \leq \theta \leq 90^\circ$ maps into the range $[1, a]$. As θ increases beyond 90° towards 180°, the rejection goes back to zero and then on to $-a$ as θ reaches 270°. Thus, the frequency of maximum rejection, f_0, is attained when $\theta = \pi/2 = \theta_0$ rad. Furthermore, the frequency response is repeated with π-rad periodicity.

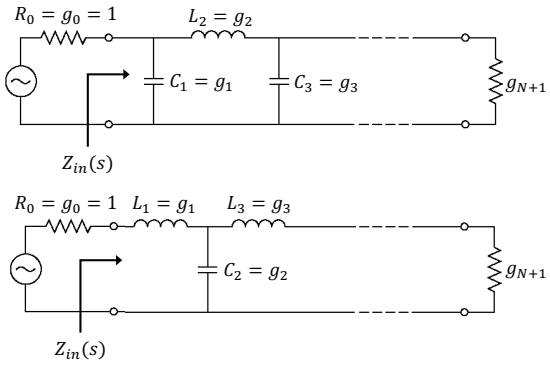

Figure A.2: Definition of the LC ladder network prototype filter parameters, [8]. There are two dual implementations with the same frequency response.

After that, the polynomials $F(t)$ and $E(t)$ in the t-plane are calculated by utilizing the mapped roots of the polynomials $F(s)$ and $E(s)$. Then, $S_{11}(t)$ is determined by equation (A.6).

$$S_{11}(t) = \frac{F(t)/\varepsilon_{Rt}}{E'(t)} \tag{A.6}$$

where $F(t)$ and $E'(t)$ are the reconstructed polynomials of order N in the t-plane (obtained by using the mapped roots) and ε_{Rt} is a constant defined by equation (A.7), which is non-unity but very close to unity for the higher-degrees . The most accurate method to determine $E'(t)$ is to transform the N s-plane roots of $E(s)$ to the t-plane by using equation (A.3), and then factorizing them to form the new polynomial in t.

$$\varepsilon_{Rt} = \frac{\varepsilon_t}{\sqrt{\varepsilon_t^2 - 1}} \tag{A.7}$$

$$\varepsilon_t = \left.\frac{\left(1-t^2\right)^{N/2}}{\left(\sqrt{1-10^{-RL/10}}\right)\cdot|E'(t)|}\right|_{t=t_c} \tag{A.8}$$

where $t_c = j \cdot \tan\theta_c$ and RL is the required return loss (+dB) and N is the order of the filter.

Now, we are going to calculate the different UEs (values of the different characteristic impedances, Z_i), using the ABCD matrix [1].

Starting from equation (A.6) and with the knowledge of the form of equations (A.9) and (A.10), the polynomials $A(t)$, $B(t)$, $C(t)$, and $D(t)$ are calculated using the numerator and denominator coefficients of $S_{11}(t)$ following equations (A.11) to (A.14). It is important to note that $A(t)$ and $D(t)$ will be even polynomials and $B(t)$ and $C(t)$ will be odd polynomials for N even, and vice versa for N odd (see equations (A.9) and (A.10).

$$[ABCD] = \left[\frac{1}{\sqrt{1-t^2}}\right]^N \cdot \begin{bmatrix} A_N(t) & B_{N-1}(t) \\ C_{N-1}(t) & D_N(t) \end{bmatrix} \quad (N \ \ even) \tag{A.9}$$

$$[ABCD] = \left[\frac{1}{\sqrt{1-t^2}}\right]^N \cdot \begin{bmatrix} A_{N-1}(t) & B_N(t) \\ C_N(t) & D_{N-1}(t) \end{bmatrix} \quad (N \ \ odd) \tag{A.10}$$

$$A(t) = (e_0 + f_0) + (e_2 + f_2) \cdot t^2 + (e_4 + f_4) \cdot t^4 + ... \tag{A.11}$$

$$B(t) = (e_1 + f_1) \cdot t + (e_3 + f_3) \cdot t^3 + (e_5 + f_5) \cdot t^5 + ... \tag{A.12}$$

$$C(t) = (e_1 + f_1) \cdot t + (e_3 + f_3) \cdot t^3 + (e_5 + f_5) \cdot t^5 + ... \tag{A.13}$$

$$D(t) = (e_0 + f_0) + (e_2 + f_2) \cdot t^2 + (e_4 + f_4) \cdot t^4 + ... \tag{A.14}$$

In the previous equations, e_i are the coefficients of $E'(t)$ and f_i (i=0...N) are the coefficients of $F(t)/\varepsilon_{Rt}$. By writing the polynomials in this way ensures that the form is correct, ant that the $S_{11}(t)$ and $S_{21}(t)$ are satisfied.

After that, the first impedance, Z_1, of the first UE is calculated following equation (A.15):

$$Z_1 = \left.\frac{A(t)}{C(t)}\right|_{t=1} = \left.\frac{B(t)}{D(t)}\right|_{t=1} \tag{A.15}$$

The residual network will be given by the following polynomials $A_{res}(t)$, $B_{res}(t)$, $C_{res}(t)$, and $D_{res}(t)$:

$$A_{res}(t) = \frac{A(t) - t \cdot Z_1 \cdot C(t)}{1 - t^2} \tag{A.16}$$

$$B_{res}(t) = \frac{B(t) - t \cdot Z_1 \cdot D(t)}{1 - t^2} \tag{A.17}$$

$$C_{res}(t) = \frac{C(t) - \dfrac{t}{Z_1} \cdot A(t)}{1 - t^2} \tag{A.18}$$

$$D_{res}(t) = \frac{D(t) - \dfrac{t}{Z_1} \cdot B(t)}{1 - t^2} \tag{A.19}$$

Then, proceeding iteratively, all the UEs (Z_i values) are calculated using the previous equations until the residual network contains only the output load of the filter, R_L.

REFERENCES

[1] R. Cameron, C. Kudsia, and R. Mansour, *Microwave Filters for Communication Systems: Fundamentals, Design and Applications*. Wiley-Interscience, 2007.

[2] R. Levy and S. B. Cohn, "A history of microwave filter research, design, and development," *IEEE Transactions on Microwave Theory and Techniques*, vol. 32, no. 9, pp. 1055–1067, Sep. 1984.

[3] R. Levy, "Tables of element values for the distributed low-pass prototype filter," *IEEE Transactions on Microwave Theory and Techniques*, vol. 13, no. 5, pp. 514–536, Sep. 1965.

[4] ——, "A new class of distributed prototype filters with applications to mixed lumped/distributed component design," *IEEE Transactions on Microwave Theory and Techniques*, vol. 18, no. 12, pp. 1064–1071, Dec. 1970.

[5] ——, "Tapered corrugated waveguide low-pass filters," *IEEE Transactions on Microwave Theory and Techniques*, vol. 21, no. 8, pp. 526–532, Aug. 1973.

[6] G. Matthaei, L. Young, and E. M. T. Jones, *Microwave filters, impedance-matching networks and coupling structures*. Artech House, 1980.

[7] P. Richards, “Resistor-transmission-line circuits,” *Proceedings of the IRE*, vol. 36, no. 2, pp. 217–220, Feb. 1948.

[8] D. M. Pozar, *Microwave Engineering Fourth Edition*. Wiley, 2011.

APPENDIX B

WAVEGUIDE BENT TRANSFORMERS

In this Annex, the meandered topology described in Chapter 8 for LPFs and BPFs is extended to the design of novel compact bent transformers embedding routing capability. The new design technique proposed in this Annex allows the designers to obtain a maximum of $N^3 - 1$ bent alternatives for a given N-order in-line transformer. It is accomplished by means of mimicking the local reflection coefficients in magnitude and phase of each discontinuity with the targeted one. The novel design procedure has been proved trough the design and simulation of a Ku-band $90°$-bent transformer between WR75 standard input port and a reduced-height output port. The novel structure achieves more than 50%-footprint reduction in comparison with its classical counterpart.

New Filter Design Methods and Topologies for the Future Microwave and Millimeter-Wave High-Capacity Satellites, by Fernando Teberio. 2018 Public University of Navarre.

B.1 Background

Transformers and bends are key components of multiple RF and microwave applications such as radar, ground stations, and satellite communication payloads [1]–[4]. Waveguide technology is extensively utilized in the previous applications where low insertion loss and a high-power handling are desired characteristics despite of its intrinsic trade-offs: mass and volume. Therefore, the reduction of both characteristics, for example in satellite applications, is seen as highly advantageous. Furthermore, in such of those applications (i.e., antenna feed-chains and multi-beam satellite payloads where hundreds of waveguide components must be accommodate making the best use of space), waveguide bends can be often found before and/or after waveguide devices [5]–[7]. When two different structures are utilized, it produces a negative impact in terms of insertion loss, volume/mass, and PIM. Hence, to develop new design procedures which allow designers to embed routing capabilities in waveguide structures is the spotlight.

Waveguide impedance transformers are a very common solution to connect properly all the components of a complex systems (i.e., the antenna feed network) and to match the standardized dimensions in such devices, maximizing the power transfer through the network by minimizing the deterioration of the return loss due to reflections in these discontinuities. Indeed, a large variety of waveguide structures which use matching networks can be found in the literature, such as: low-pass filters [8]–[14], band-pass filters [15], [16], diplexers [17], [18] or orthomode transducers [19]–[21]. The classical waveguide multi-section transformer was firstly proposed by Cohn [22], and then, other methods which utilize the *Richards' transformation* [23], optimizations to obtain multiband responses [24], [25], iterative methods for short-step transformers [3] and tapered lines [26] has been published. However, the common denominator of all the previous structures is that all of them have an in-line (straight) topology. Indeed, the different steps are implemented by cascading straight waveguide sections of rectangular shape of different heights/widths or by following a smooth tapering profile, but always in a straight manner. Then, as far as the authors' knowledge, the integration of bends in transformer sections in order to embed routing capability in waveguide structures has never been proposed before in waveguide technology.

The proposed design method (Section B.2) translates the impedance steps into E-plane mitered bends (in up or down configuration) or two waveguide sections cascaded in straight configuration with different input/output dimensions. This is possible by the consecutive calculation of the local magnitude and phase reflection coefficients of these structures. This approach allows to embed routing capability in the matching structures. Thus, an N-order in-line transformer can be converted into $N^3 - 1$ bent alternatives (depending on the selected up-straight-down for each discontinuity) (see Figure B.1). The one subtracted corresponds to the starting in-line combination. All those alternative gives the designer many degrees of freedom to accommodate other requirements related to volume constraints or routing capabilities demanded, avoiding subsequent bending structures and reducing insertion loss, volume/weight, and PIM. The novel topology has been validated in Section B.3

trough the design and simulation of a novel $90°$-bent transformer of order 3 which has 9.525 mm input-port height and 1 mm output-port height and covers the entire Ku-band (10.7 GHz – 12.7 GHz). The footprint of the novel bent transformer has been dramatically reduced and is only 14.3 mm x 15.66 mm while its classical counterpart (composed of an E-plane bend + straight transformer) is 49.42 mm x 9.525 mm. Therefore, our proposal achieves more than 50% footprint reduction.

B.2 Design Method

The design method proposed in this Annex utilizes a modular design strategy. Two different Design Building Blocks (DBBs) will be considered in the design method (see Figure B.2): the E-plane mitered bends (in up or down configuration) (see Figure B.2(a)) and the in-line (straight) structure (composed of the second half of the ith-waveguide section, the first half of the $(i+1)$th-section, and the junction between them) (see Figure B.2(b)). Then, a given N-order in-line transformer can be converted at most into N^3-1 bent alternatives (depending on the selected up/straight/down for each discontinuity, where the one subtracted corresponds to the baseline topology). Thus, their constituent DBBs will be calculated consecutively one by one to assemble the structure afterwards. It is important to note that the distances of the bend, $d_{i,1}$ and $d_{i,2}$, are free parameters in our design technique which can be adjusted or optimized to accomplish the best final structure in terms of return-loss and size.

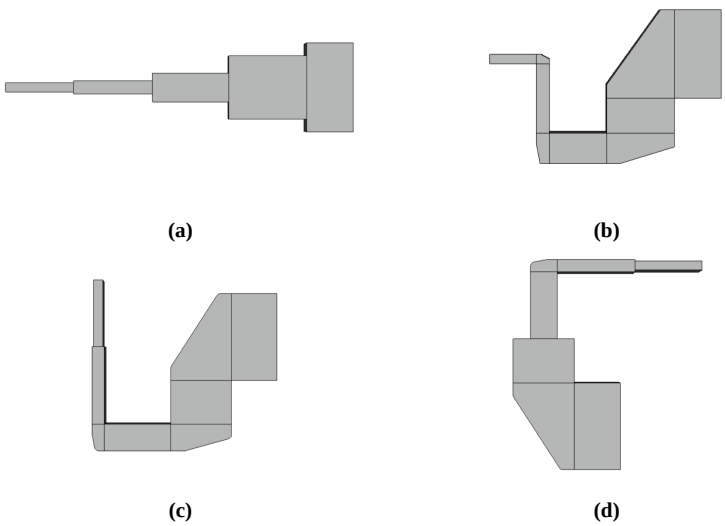

Figure B.1: Side-view (same scale) of the (a) baseline N-order in-line transformer and (b), (c), and (d) some examples of the N^3-1 bent alternatives for the novel bent transformer that can be accomplished with the design method proposed in this Annex (Section B.2).

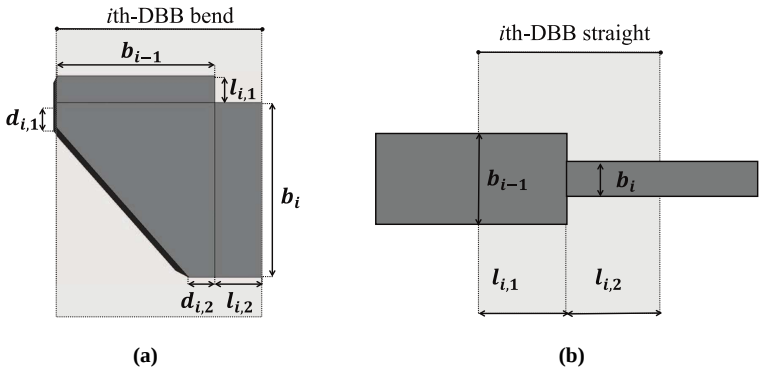

Figure B.2: Detailed notation of an ith-Design Building Block (DBB) and their associated constituent parameters: (a) Sketch of the bend topology (whose orientation could be upwards or downwards). (b) Sketch of the straight topology.

The synthesis procedure of the novel bent transformer begins by computing the magnitude and phase of the local reflection coefficients of the baseline in-line transformer. As it was aforementioned, the baseline in-line transformer will be predesigned with any of the design procedures which can be found in the literature (i.e., [22]–[26]). Thus, the order of the transformer, N, the obtained in-band return loss and the heights of the input and output ports, b_0 and b_{N+1} respectively, are predefined. Similarly, the lower and upper frequencies of the required passband, f_1 and f_2, are given. Then, we compute the value of the magnitude and phase of the local reflection coefficients, Γ_i, which correspond to the baseline structure.

The technique for obtaining the dimensions of each DBBs begins by mimicking the previously calculated ith local reflection coefficient of the baseline structure with the physical dimensions of the ith-DBB, Figure B.2. The design procedure starts with the calculation of the heights of the novel bent transformer. Depending on the final topology desired by the designer, the novel method can start with the design of the first or last DBB. Indeed, it is recommendable to finish with the design of a DBB-bend since we will have the free parameters $d_{i,1}$ and $d_{i,2}$. Hence, in this case if we assume that we finish with a DBB-straight (as it will occur in the proposed example in Section B.3), firstly b_{N+1} is set. Then, b_N, is computed to satisfy that $|S_{11,1}(f_\pi)| = \Gamma_N$, where $|S_{11,N}(f_\pi)|$ is the magnitude of the S_{11}-parameter of the Nth DBB at the central frequency of the passband, f_π (B.1).

$$f_\pi = \sqrt{\left(\frac{c}{2\cdot a}\right)^2 + \left(\frac{c\cdot(\lambda_{g,f_1}+\lambda_{g,f_2})}{2\cdot\lambda_{g,f_1}\cdot\lambda_{g,f_2}}\right)^2} \tag{B.1}$$

After that, proceeding iteratively with the rest of DBBs except for the last one, once a certain b_i is known, b_{i-1} is calculated to assure that $|S_{11,i}(f_\pi)| = \Gamma_i$. In the previous cases, the free parameters $d_{i,1}$ and $d_{i,2}$ are predefined (for example by manufacturing issues) or can be also utilized in the calculations. For the last DBB,

as b_1 has been previously calculated and b_0 is the height of the output port, $d_{1,1}$ and $d_{1,2}$ can be utilized to satisfy that $|S_{11,1}(f_\pi)| = \Gamma_1$.

At the same time that the heights are being calculated, the lengths $l_{i-1,1}$ and $l_{i,2}$ are calculated satisfying that the phase of the local reflection coefficients, $\phi_{i,S_{11}}(f_\pi)$ and $\phi_{i,S_{21}}(f_\pi)$, are the same in the baseline in-line and in the bent structure. For example, if a classical quarter-wave in-line transformer is assumed as starting point structure, the phases of the local reflection coefficients will be calculated following equation (B.2). It is important to note that $l_{i,1}$, $l_{i,2}$ b_i, and b_{i+1} can be calculated simultaneously since the lengths negligibly affect the heights and vice versa, having imperceptible impact in the targeted local reflection coefficient magnitude and phase respectively.

$$\phi_{i,S_{11}}(f_\pi) = 90^\circ \quad and \quad \phi_{i,S_{21}} = -90^\circ \tag{B.2}$$

being $\phi_{i,S_{11}}(f_\pi)$ and $\phi_{i,S_{21}}(f_\pi)$ the phase response of the S_{11}- and S_{21}-parameters, respectively, of the i-th DBB at f_π. Since the ith and the $(i+1)$th-EMB share the height of their output and input ports respectively, it is convenient to add the lengths $l_{i,2}$ and $l_{i+1,1}$ to obtain a single l_i value following equation (B.3).

$$l_i = l_{i,2} + l_{i+1,1} \quad for \quad i = 1 : N \tag{B.3}$$

where the special cases for the global input and output lengths are calculated as $l_0 = 2 \cdot l_{1,1}$ and $l_{N+1} = 2 \cdot l_{N+1,2}$.

It is important to note that many of the existing N^3topologies (including the in-line topology) can be obtained depending on the sequence of DBBs employed (see Fig 1) although there exist non-feasible structures as a result of an auto-collision trajectory when, for instance, all selected DBBs are upwards. Finally, a slight adjustment on the calculated physical parameters will be needed to obtain the final structure.

B.3 Design Example

In order to demonstrate the feasibility of the novel design technique proposed in this Annex, a novel compact bent transformer with routing capability has been designed. The proposed bent transformer performs a 90°-angle between the input and output ports and the starting-point structure is a classical quarter-wave in-line transformer (see Figure B.3) which matches the WR75 standard input port (a=19.05 mm and b_0=9.525 mm) with a reduced port height (a=19.05 mm and b_{N+1}=1 mm). Moreover, it covers the entire down-link Ku-band (10.7 GHz – 12.7 GHz) with return loss better than 35 dB.

Following the design method in this Annex with the design parameters given in Table B.1, the frequency response of the novel bent transformer (see Figure B.3) is shown in Figure B.4 (grey line). As can be seen, only a slight adjustment is needed to obtain the targeted frequency response also given in Figure B.4 (black line). The final dimensions of the novel bent transformer are detailed in Table B.2, with the

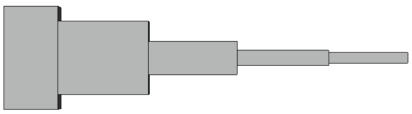

(a)

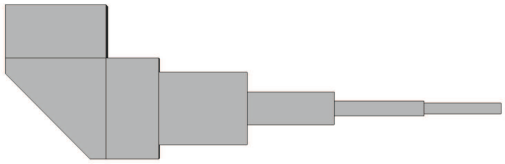

(b)

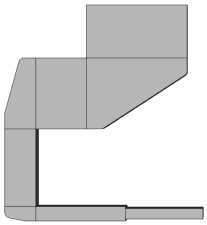

(c)

Figure B.3: Side-view (same scale) of (a) baseline quarter-wave in-line transformer, (b) the typical solution of bend + straight transformer and (c) the novel bent transformer of order 3.

Table B.1: Design parameters of the novel bent transformer designed in Section B.3.

Filtering function type	Chebyshev
Order, N	3
In-band return loss	25 dB
Lower frequency of the passband, f_1	10.6 GHz
Upper frequency of the passband, f_2	12.8 GHz
Input height, b_0	9.525 mm
Output height, b_4	1 mm
Waveguide width, a	19.05 mm

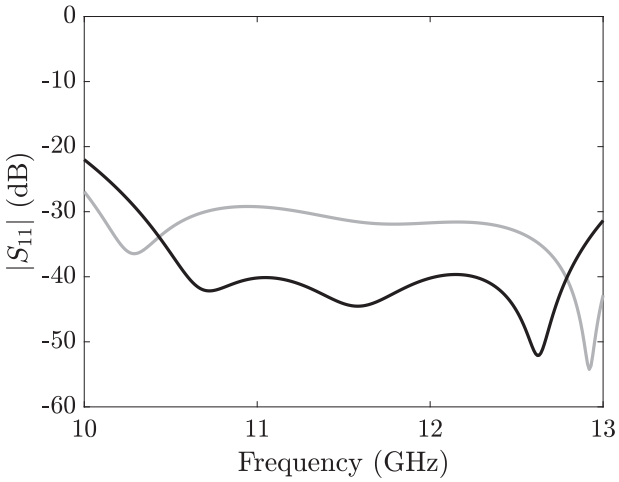

Figure B.4: FEST3D simulated frequency response comparison between the novel bent transformer designed with the technique in Section B.2 (grey line) and after a final slight adjustment of the physical parameters (black line).

targeted reflection coefficients for the sake of reproducibility. Finally, the frequency response of the final bent transformer using two different EM full-wave simulators (FEST3D in black line and CST MWS in grey line) is shown in Figure B.5. Both simulations show in-band return loss better than 35 dB. The proposed structure has been compared with the classical approach of cascading an $90°$E-plane bend with a straight transformer (see Figure B.3) designed fulfilling the same frequency specifications. As can be seen in Figure B.6, the novel and the classical solution fulfil the frequency specifications. If we compare the footprint of both alternatives, a dramatic footprint reduction (more than 50%) is achieved with the proposed structure in this Annex (14.3 mm x 15.66 mm vs. 49.42 mm x 9.525 mm) (see Figure B.3).

Table B.2: Final dimensions of the novel bent transformer designed in Section B.3.

i-th DBB	Γ_i	$d_{i,1}$ (mm)	$d_{i,2}$ (mm)	b_i (mm)	l_i (mm)
1 (bend down)	-0.151	2.187	0.15	9.525	5.06
2 (bend up)	-0.389	1.5	1.5	6.674	3.207
3 (bend up)	-0.389	1.0	1.0	2.993	6.298
4 (straight)	-0.151	-	-	1.327	8.414
				1.000	8.566

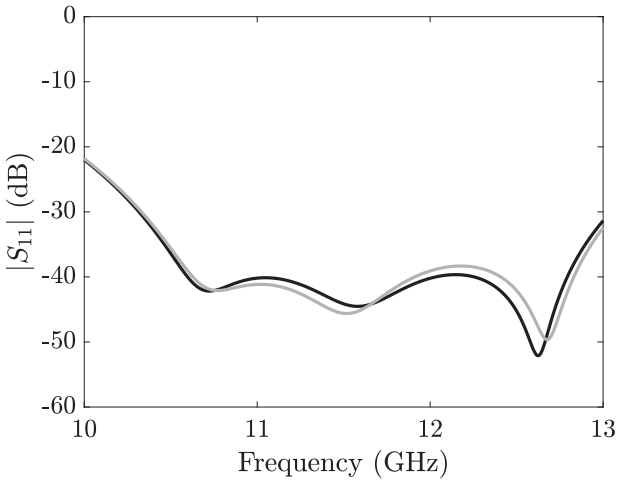

Figure B.5: FEST3D (black line) and CST MWS (grey line) simulated frequency response comparison of the final novel bent transformer proposed in this Annex.

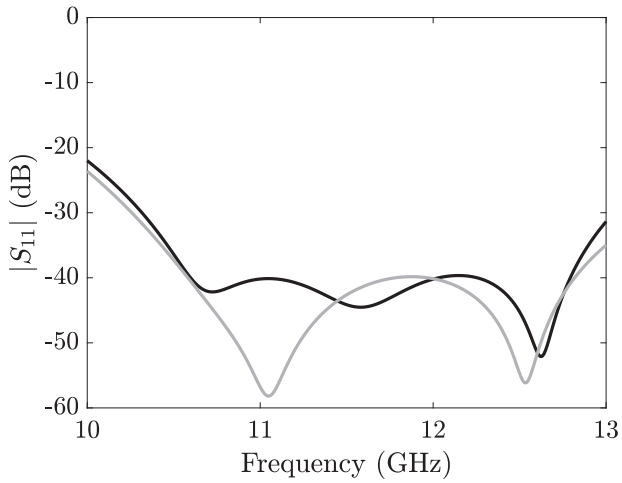

Figure B.6: FEST3D simulated frequency response comparison between the final novel bent transformer (black line) and its classical counterpart (grey line).

B.4 Conclusions

In this Annex, novel compact bent transformers embedding routing capabilities are proposed. The proposed design technique allows designers to obtain a large variety of bent structures depending on the different configuration of each discontinuity (bend up, bend down, or straight). This approach has been proved in the design of a compact $90°$bent transformer between WR75 standard input port and an output port with reduced height. In this particular case, more than 50% footprint reduction has been accomplished in comparison with its classical counterpart.

REFERENCES

[1] G. Matthaei, L. Young, and E. M. T. Jones, *Microwave filters, impedance-matching networks and coupling structures*. Artech House, 1980.

[2] J. Uher, J. Bornemann, and U. Rosenberg, *Waveguide Components for Antenna Feed Systems: Theory and CAD*. Artech House, 1993.

[3] R. Cameron, C. Kudsia, and R. Mansour, *Microwave Filters for Communication Systems: Fundamentals, Design and Applications*. Wiley-Interscience, 2007.

[4] M. Skolnik, *Radar Handbook*. McGraw-Hill, 2008.

[5] H. Moheb, C. Robinson, and J. Kijesky, "Design amp; development of co-polarized ku-band ground terminal system for very small aperture terminal (vsat) application," in *IEEE Antennas and Propagation Society International Symposium. 1999 Digest. Held in conjunction with: USNC/URSI National Radio Science Meeting (Cat. No.99CH37010)*, vol. 3, Jul. 1999, 2158–2161 vol.3.

[6] H. Wolf, M. Schneider, S. Stirland, and D. Scouarnec, "Satellite multibeam antennas at airbus defence and space: State of the art and trends," in *2014 8th European Conference on Antennas and Propagation (EuCAP)*, Apr. 2014, pp. 182–185.

[7] F. F. Manzillo, R. Sauleau, N. Capet, and M. Ettorre, "Mode matching analysis of an e-plane 90 bend with a square step in parallel-plate waveguide," *IEEE Antennas and Wireless Propagation Letters*, vol. 16, pp. 2187–2190, 2017.

[8] F. Teberio, I. Arnedo, J. M. Percaz, I. Arregui, T. Lopetegi, and M. A. G. Laso, "Accurate design of corrugated waveguide low-pass filters using exclusively closed form expressions," in *2017 47th European Microwave Conference (EuMC)*, Oct. 2017.

[9] M. Manuilov and K. Kobrin, "Field theory CAD of waffle-iron filters," in *2005 35th European Microwave Conference (EuMC)*, vol. 2, Oct. 2005, pp. 1–4.

[10] F. Teberio, I. Arnedo, J. M. Percaz, I. Arregui, P. Martin-Iglesias, T. Lopetegi, and M. A. G. Laso, "Accurate synthesis procedure for waffle-iron low-pass filter," in *2018 IEEE MTT-S International Microwave Symposium Digest (IMS)*, Jun. 2018.

[11] F. Teberio, J. M. Percaz, I. Arregui, P. Martin-Iglesias, T. Lopetegi, M. A. G. Laso, and I. Arnedo, "Design procedure for new compact waffle-iron filters with transmission zeros," *Submitted for consideration in IEEE Transactions on Microwave Theory and Techniques*, 2018.

[12] F. De Paolis, R. Goulouev, J. Zheng, and M. Yu, "CAD procedure for high-performance composite corrugated filters," *IEEE Transactions on Microwave Theory and Techniques*, vol. 61, no. 9, pp. 3216–3224, Sep. 2013.

[13] F. Teberio, I. Arnedo, J. M. Percaz, I. Arregui, P. Martin-Iglesias, T. Lopetegi, and M. A. G. Laso, "Meandered corrugated waveguide low-pass filter," in *IEEE MTT-S International Microwave Workshop Series on Advanced Materials and Processes (IMWS-AMP)*, Sep. 2017.

[14] F. Teberio, J. M. Percaz, I. Arregui, P. Martin-Iglesias, T. Lopetegi, M. A. G. Laso, and I. Arnedo, "Rectangular waveguide filters with meandered topology," *IEEE Transactions on Microwave Theory and Techniques*, vol. -, no. -, pp. -, 2018.

[15] A. Kirilenko, L. Rud', V. Tkachenko, and D. Kulik, "Design of bandpass and lowpass evanescent-mode filters on ridged waveguides," in *1999 29th European Microwave Conference (EuMC)*, vol. 3, Oct. 1999, pp. 239–242.

[16] F. Teberio, P. Soto, I. Arregui, T. Lopetegi, S. Cogollos, I. Arnedo, P. Martin-Iglesias, V. E. Boria, and M. A. G. Laso, "Waveguide band-pass filter with reduced sensitivity to fabrication tolerances for q-band payloads," in *2017 IEEE MTT-S International Microwave Symposium Digest (IMS)*, Jun. 2017, pp. 1464–1467.

[17] J. Esteban and J. M. Rebollar, "Design and optimization of a compact ka-band antenna diplexer," in *1995 IEEE Antennas and Propagation Society International Symposium Digest*, vol. 1, Jun. 1995, 148–151 vol.1.

[18] J. Bornemann, J. Uher, and K. N. Patel, "Efficient full-wave cad of waveguide diplexers," in *1996 Symposium on Antenna Technology and Applied Electromagnetics*, Aug. 1996, pp. 591–594.

[19] J. A. Ruiz-cruz, J. R. Montejo-garai, J. M. Rebollar, C. E. Montesano, M. J. Martin, and M. Naranjo-Masi, "Computer aided design of wideband orthomode transducers based on the boifot junction," in *2006 IEEE MTT-S International Microwave Symposium Digest (IMS)*, Jun. 2006, pp. 1173–1176.

[20] M. A. Abdelaal, S. I. Shams, and A. A. Kishk, "Asymmetric compact omt for x-band sar applications," *IEEE Transactions on Microwave Theory and Techniques*, vol. 66, no. 4, pp. 1856–1863, Apr. 2018.

[21] A. A. Sakr, W. Dyab, and K. Wu, "Design methodologies of compact orthomode transducers based on mechanism of polarization selectivity," *IEEE Transactions on Microwave Theory and Techniques*, vol. 66, no. 3, pp. 1279–1290, Mar. 2018.

[22] S. B. Cohn, "Optimum design of stepped transmission-line transformers," *IRE Transactions on Microwave Theory and Techniques*, vol. 3, no. 3, pp. 16–20, Apr. 1955.

[23] H. J. Riblet, "General synthesis of quarter-wave impedance transformers," *IRE Transactions on Microwave Theory and Techniques*, vol. 5, no. 1, pp. 36–43, Jan. 1957.

[24] U. Rosenberg, J. Bornemann, and S. Amari, "Design of dual-band waveguide transformers," in *2005 IEEE MTT-S International Microwave Symposium Digest (IMS)*, 2005, pp. 1215–1218.

[25] S. Cogollos, V. E. Boria, and J. D. Martinez, "Generalized short step transformers for multi-band impedance matching," in *2012 42nd European Microwave Conference (EuMC)*, Oct. 2012, pp. 380–383.

[26] S. Cogollos, J. Vague, V. E. Boria, and J. D. Martínez, "Novel planar and waveguide implementations of impedance matching networks based on tapered lines using generalized superellipses," *IEEE Transactions on Microwave Theory and Techniques*, vol. 66, no. 4, pp. 1874–1884, Apr. 2018.

APPENDIX C

FABRICATION PROCEDURES

The purpose of this Anex is to show, step by step, the different fabrication processes utilized in this Thesis.

C.1 Electroforming process

Electroforming process has been explained in detail in Chapter 1, Section 1.6.3. The steps of the electroforming process used in the different fabrications of this Thesis are the following:

- **Drawing.** The drawing has been developed for the *negative* structure.
- **Material for the mandrel.** Aluminium alloy EN-AW6082 has been used to manufacture the mandrel.
- **Mandrel manufacturing - EDM process.** The fastest and cheapest way to produce the mandrel in aluminium is by using EDM (see Chapter 1, Section 1.6.2) with a very thin wire (∅ 0.1 mm). However, sometimes the effect of electro dis-

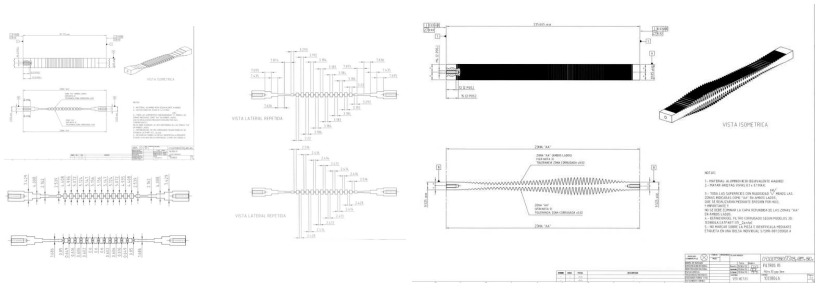

Figure C.1: Examples of drawings.

charges on the surface of the material, on thin walls might deform permanently the component. In this case, if it is possible, CCM is recommended.

- **Mandrel manufacturing - Milling.** The use of other techniques such as CCM (see Chapter 1, Section 1.6.1) can be also employed if the geometry of the mandrel cannot be achieved with EDM.

Figure C.2: Photograph of the mandrel of the corrugated E-plane low-pass filter.

- **Visual inspection.** Binoculars of 20X and 40X have been used to assure the absence of superficial marks or chips to be removed, assuring that the final surface is perfect since it will affect to the final electroformed device.
- **Dimensional measurement.** Dimensional measurement has been performed for each prototype. A coordinate measuring machine (Mitutoyo Super BNH) and a two dimensions measurement process have been used.
- **Electrodeposition.** Once the mandrel is manufactured, the electrodeposition (see Chapter 1 Section 1.6.3) of the filter is performed. In the prototypes of Chapter 2 Example 4.4, firstly, 15-micron-thick layer of silver and then 1-mm-thick layer of copper was deposited onto the mandrel.
- **Mandrel removal**. Finally, the aluminium mandrel is dissolved with a chemical solution leaving behind the finished filter.

C.2 CCM process

- **Drawing.** Typically, each prototype is manufactured in two identical pieces cutting by the H-plane or E-plane (depending on the prototype). E-plane cut is

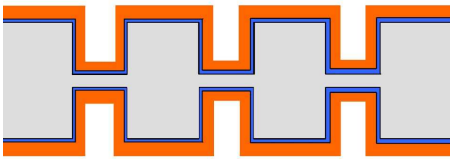

Figure C.3: Detail of the electroforming process showing the different materials. Grey: Aluminium, Blue: Silver (15 μm thickness), Orange: Copper (1 mm thickness)..

better for the insertion loss (since the currents are not interrupted). The thickness of the subsequent silver plating is taken into account and it is subtracted for the final dimension of each prototype.

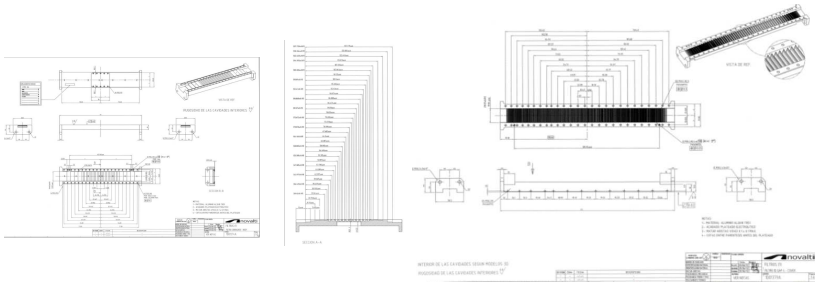

Figure C.4: Examples of drawings.

- **Materials.** Aluminium alloy 6082 and 7075 have been typically used.
- **Manufacturing.** Five axis machine has been used.

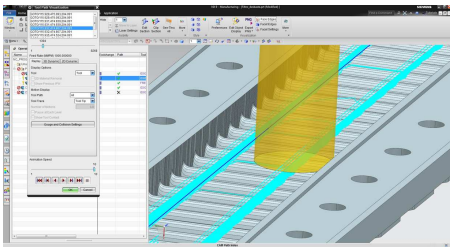

Figure C.5: CATIA image of the manufacturing process.

- **Visual inspection.**
  Binoculars of 20X and 40X were used to assure the absence of superficial marks or chips to be removed, as well as the perfect finishing of the blind holes.
- **Dimensional measurement.** The dimensional measurements were performed for each prototype using a coordinate measuring machine.

- **Silver plating.**

  - **Etching.** First, a controlled chemical etching is done in order to remove any dirty trace, to adequate the roughness and to improve the adherence.
  - **Zinc amalgam.** Then, a thin layer of zinc is deposited to improve the adherence of the nickel over the aluminium.
  - **Chemical nickel.** 10-microns nickel layer allows the adherence of the silver. As this is a chemical process, the uniformity of the layer is assured.
  - **Electrolytic silver.** Finally, a silver layer between 5 and 10 microns is deposited.

- **Visual inspection.**
  Binoculars of 20X and 40X were used to assure the perfect finishing of the silver plated.

- **Dimensional measurement.**
  The dimensional measurements were performed for each prototype using a coordinate measuring machine.

APPENDIX D

USEFUL INFORMATION

Table D.1: Physical constants.

Speed of light in free-space	$c = 2.998 \times 10^{8}\ m/s$
Permittivity of free-space	$\varepsilon_0 = 8.854 \times 10^{-12}\ F/m$
Permeability of free-space	$\mu_0 = 4\pi \times 10^{-7}\ H/m$
Impedance of free-space	$\eta_0 = 376.7\ \Omega$

Table D.2: Waveguide-standard dimensions.

Waveguide Standard	Standard frequency range (GHz)	Inside dimensions $a_0 \times b_0$ (mm)
WR-90	8.2–12.4	22.86 × 10.16
WR-75	10–15	19.05 × 9.525
WR-62	12.4–18	15.799 × 7.899
WR-51	15–22	12.954 × 6.477
WR-42	18–26.5	10.668 × 4.318
WR-28	26.5–40	7.112 × 3.556
WR-22	33–50	5.690 × 2.845

Table D.3: Conductivity.

Aluminium	$3.56 \times 10^7\ S/m$
Silver	$6.3012 \times 10^7\ S/m$
Copper	$5.8 \times 10^7\ S/m$

APPENDIX E

RESEARCH MERITS OF THE AUTHOR

E.1 Journal Papers (18)

E.1.1 IEEE Microwave Magazine

- I. Arnedo, I. Arregui, M. Chudzik, **F. Teberio**, A. Lujambio, D. Benito, T. Lopetegi, and M. A. G. Laso, "Direct and Exact Synthesis: Controlling the Microwaves by Means of Synthesized Passive Components with Smooth Profiles," *IEEE Microwave Magazine*, vol.16, no.4, pp.114,128, May 2015.

E.1.2 IEEE Transactions on Microwave Theory and Techniques

- **F. Teberio**, J. M. Percaz, I. Arregui, P. Martin-Iglesias, T. Lopetegi, M. A. G. Laso, and I. Arnedo, "Design procedure for compact waffle-iron filters with transmission zeros," *IEEE Transactions on Microwave Theory and Techniques*, Submitted.

- **F. Teberio**, J. M. Percaz, I. Arregui, P. Martin-Iglesias, T. Lopetegi, M. A. G. Laso, and I. Arnedo, "Rectangular waveguide filters with meandered topology," *IEEE Transactions on Microwave Theory and Techniques*.

- I. Arnedo, M. Chudzik, J. M. Percaz, I. Arregui, **F. Teberio**, D. Benito, T. Lopetegi, and M. A. G. Laso, "Synthesis of one dimensional electromagnetic bandgap structures with fully controlled parameters," *IEEE Transactions on Microwave Theory and Techniques*, vol. 65, no. 9, pp. 3123-3134, Jul. 2017.

- **F. Teberio**, I. Arregui, P. Soto, M. A. G. Laso, V. E. Boria, and M. Guglielmi, "High-performance compact diplexers for Ku/K-band satellite applications," *IEEE Transactions on Microwave Theory and Techniques*, vol. 65, no. 10, pp. 3866-3876, Apr. 2017.

- **F. Teberio**, I. Arregui, A. Gomez-Torrent, I. Arnedo, M. Chudzik, M. Zedler, F. -J. Görtz, R. Jost, T. Lopetegi, and M. A. G. Laso, "Chirping techniques to maximize the power-handling capability of harmonic waveguide low-pass filters ," *IEEE Transactions on Microwave Theory and Techniques*, vol. 24, no. 9, pp. 2814-2823, Sept. 2016.

- I. Arregui, **F. Teberio**, I. Arnedo, A. Lujambio, M. Chudzik, D. Benito, T. Lopetegi, R. Jost, F. -J. Görtz, J. Gil, C. Vicente, B. Gimeno, V. E. Boria, D. Raboso, and M. A. G. Laso, "High-power low-pass harmonic filters with higher-order TEn0 and Non-TEn0 mode suppression: design method and multipactor characterization," *IEEE Transactions on Microwave Theory and Techniques*, vol. 61, no. 12, pp. 4376-4386, Dec. 2013.

- M. Chudzik, I. Arnedo, A. Lujambio, I. Arregui, I. Gardeta, **F. Teberio**, J. Azana, D. Benito, M. A. G. Laso, and T. Lopetegi, "Design of transmission-type Nth-order differentiators in planar microwave technology," *IEEE Transactions on Microwave Theory and Techniques*, vol. 60 no. 11, pp. 3384-3394, Nov. 2012.

E.1.3 IEEE Microwave Wireless Components Letters

- **F. Teberio**, I. Arregui, A. Gomez-Torrent, E. Menargues, I. Arnedo, M. Chudzik, M. Zedler, F. -J. Görtz, R. Jost, T. Lopetegi, and M. A. G. Laso, "High-power waveguide low-pass filter with all-higher-order mode suppression over a wide-band for Ka-band satellite applications," *IEEE Microwave Wireless Components Letters*, vol. 25, no. 8, pp. 511-513, Aug. 2015.

- I. Arregui, **F. Teberio**, I. Arnedo, A. Lujambio, M. Chudzik, D. Benito, R. Jost, F. -J. Görtz, T. Lopetegi, and M. A. G. Laso, "High-Power Low-Pass Harmonic Waveguide Filter with TEn0-Mode Suppression," *IEEE Microwave and Wireless Components Letters*, vol. 22, no. 7, pp. 339-341, Jul. 2012.

E.1.4 IEEE Antennas and Wireless Propagation Letters

- J. M. Percaz, M. Chudzik, I. Arnedo, I. Arregui, **F. Teberio**, M. A. G. Laso, and T. Lopetegi, "Producing and exploiting simultaneously the forward and backward coupling in EBG-assisted microstrip coupled lines," *IEEE Antennas and Wireless Propagation Letters*, vol. 15, pp. 873-876, 2016

E.1.5 Radio Science

- **F. Teberio**, J. M. Percaz, I. Arregui, P. Martin-Iglesias, T. Lopetegi, M. A. G. Laso, and I. Arnedo, "Automated synthesis for stepped-impedance waveguide filters," *Radio Science*, Submitted.

E.1.6 Progress In Electromagnetic Research (PIER)

- **F. Teberio**, J. Percaz, I. Arregui, P. Martin-Iglesias, T. Lopetegi, M. A. G. Laso, and I. Arnedo,, "Routing with classical corrugated low-pass filters with embedded bends," *Progress In Electromagnetic Research Letters (PIER-L)*, vol. 75, pp. 1-6, Apr. 2018.

- I. Arregui, **F. Teberio**, I. Arnedo, J. Percaz, A. Gomez-Torrent, M. Chudzik, M. A. G. Laso, and T. Lopetegi, "Resonant Quasi-Periodic Structure for Rectangular Waveguide Technology with Wide Stopband and Band-Pass Behavior," *Progress In Electromagnetic Research C (PIER-C)*, vol. 69, pp. 97-104, Nov. 2016.

E.1.7 Microwave and Optical Technology Letters

- **F. Teberio**, I. Arregui, I. Arnedo, M. Chudzik, R. Jost, F. -J. Görtz, T. Lopetegi, and M. A. G. Laso, "Tailoring of higher-order mode suppression in a high-power alternative to classical waffle-iron filters", *Microwave and Optical Technology Letters*, vol. 56, no. 12, pp. 2967-2974, Dec. 2013.

- I. Arnedo, M. Chudzik, J. Schwartz, I. Arregui, A. Lujambio, **F. Teberio**, D. Benito, M. A. G. Laso, D. Plant, J. Azana, and T. Lopetegi, "Analytical solution for the design of planar electromagnetic bandgap structures with spurious-free frequency response", *Microwave and Optical Technology Letters*, vol. 54, no. 4, pp. 956-960, Feb. 2012.

E.1.8 International Journal of Antennas and Propagation

- I. Arnedo, I. Arregui, Chudzik, **F. Teberio**, A. Lujambio, D. Benito, T. Lopetegi, and M. A. G. Laso, "Passive microwave component design using inverse scattering: Theory and applications," *International Journal of Antennas and Propagation*, pp. 1-10, May 2013.

E.1.9 IET Electronic Letters

- M. Chudzik, I. Arnedo, A. Lujambio, I. Arregui, **F. Teberio**, M. A. G. Laso, and T. Lopetegi, "Microstrip coupled-line directional coupler with enhanced coupling based on EBG concept," *Electronics Letters*, vol. 47, no. 23, pp. 1284-1286, Nov. 2011.

E.2 International Conferences (39)

E.2.1 IEEE MTT-S International Microwave Symposium Digest (IMS)

- **F. Teberio**, I. Arnedo, J. M. Percaz, I. Arregui, P. Martin-Iglesias, T. Lopetegi, and M. A. G. Laso, "Accurate design procedure for waffle-iron low-pass filter," *Proc. IEEE MTT-S International Microwave Symposium Digest (IMS)*, Philadelphia, USA, Jun. 2018.
- A. Cordon, I. Arregui, I. Arnedo, **F. Teberio**, I. Arnedo, C. Arnold, M. A. G. Laso, and J. Lorente, "Design technique for integration of manifold multiplexers considering constraints on inter-channel spacings," *Proc. IEEE MTT-S International Microwave Symposium Digest (IMS)*, Philadelphia, USA, Jun. 2018.
- **F. Teberio**, P. Soto, I. Arregui, T. Lopetegi, S. Cogollos, I. Arnedo, P. Martin-Iglesias, V. E. Boria, and M. A. G. Laso, "Waveguide band-pass filter with reduced sensitivity to fabrication tolerances for Q-band payloads," *Proc. IEEE MTT-S International Microwave Symposium Digest (IMS)*, Honolulu, USA, Jun. 2017.
- **F. Teberio**, I. Arregui, M. Guglielmi, A. Gomez-Torrent, P. Soto, M. A. G. Laso, and V. E. Boria, "Compact broadband waveguide diplexer for satellite applications," *Proc. IEEE MTT-S International Microwave Symposium Digest (IMS)*, San Francisco, USA, May 2016.
- **F. Teberio**, I. Arregui, A. Gomez-Torrent, E. Menargues, I. Arnedo, M. Chudzik, M. Zedler, F. -J. Görtz, R. Jost, T. Lopetegi, and M. A. G. Laso, "Low-loss compact Ku-band waveguide low-pass filter," *Proc. IEEE MTT-S International Microwave Symposium Digest (IMS)*, Phoenix, USA, May 2015.
- I. Arregui, **F. Teberio**, I. Arnedo, A. Lujambio, M. Chudzik, D. Benito, T. Lopetegi, R. Jost, F. -J. Görtz, J. Gil, C. Vicente, B. Gimeno, V. E. Boria, D. Raboso, and M. A. G. Laso, "Multipactor-resistant low-pass harmonic filters with wide-band higher-order mode suppression," *Proc. IEEE MTT-S International Microwave Symposium Digest (IMS)*, Seattle, USA, Jun. 2013.

E.2.2 European Microwave Conference (EuMC)

- **F. Teberio**, J. M. Percaz, I. Arregui, P. Martin-Iglesias, T. Lopetegi, M. A. G. Laso, and I. Arnedo "Novel compact bent transformers embedding rout-

ing capability in waveguide structures," *48th European Microwave Conference*, Madrid, Spain, Sept. 2018.

- J. M. Percaz, M. Chudzik, I. Calero, **F. Teberio**, I. Arregui, T. Lopetegi, and M. A. G. Laso, "Analog signal processing: a time-domain demonstration of microwave differentiation," *48th European Microwave Conference*, Madrid, Spain, Sept. 2018.

- **F. Teberio**, I. Arnedo, J. M. Percaz, I. Arregui, T. Lopetegi, and M. A. G. Laso, "Accurate design of corrugated waveguide low-pass filters using exclusively closed form expressions," *47th European Microwave Conference (EuMC)*, Nuremberg, Germany, Oct. 2017.

- **F. Teberio**, A. Gomez-Torrent, I. Arregui, J.M. Percaz, I. Arnedo, M. Chudzik, T. Lopetegi, and M.A.G. Laso, "Sensitivity analysis of a 3-D printed low-cost compact waveguide low-pass filter," *46th European Microwave Conference (EuMC)*, London, UK, Oct. 2016.

- A. Gomez-Torrent, I. Arregui, J. D. Martinez, **F. Teberio**, J. V. M. Sanchez de Rojas, V. E. Boria, and M. A. G. Laso "A low-loss compact stripline low-pass filter for millimeter-wave applications," *46th European Microwave Conference (EuMC)*, London, UK, Oct. 2016.

- E. Menargues, M. Chudzik, I. Arnedo, S. Cogollos, I. Arregui, **F. Teberio**, A. Lujambio, D. Benito, C. Vicente, J. Gil, T. Lopetegi, and M. A. G. Laso, "Fast synthesis of microwave devices with arbitrary frequency responses and smooth profiles," *44th European Microwave Conference (EuMC)*, Rome, Italy, Oct. 2014.

- M. Chudzik, I. Arnedo, I. Arregui, **F. Teberio**, A. Lujambio, T. Lopetegi, M. A. G. Laso, Q. Yu, N. S. Barker, A. Ghaddar, A. Chahadih, G. Ducournau, J. F. Lampin, and T. Akalin, T. "Pulse shaping for millimeter-wave and terahertz applications in coplanar technology," *44th European Microwave Conference (EuMC)*, Rome, Italy, Oct. 2014.

- M. Chudzik, I. Arnedo, A. Lujambio, I. Arregui, **F. Teberio**, D. Benito, T. Lopetegi, and M. A. G. Laso, "Design of EBG microstrip directional coupler with high directivity and coupling," *42nd European Microwave Conference (EuMC)*, Amsterdam, The Netherlands, Oct. 2012.

E.2.3 European Conference on Antennas and Propagation (EuCAP)

- A. Gomez-Torrent, **F. Teberio**, A. Martinez, J. M. Percaz, I. Arnedo, I. Maestrojuán, I. Arregui, G. Crespo, T. Lopetegi, M.A.G. Laso, and J. Teniente "A Study of the Additive Manufacturing Technology for RF/Microwave Components," *Proc. 11th European Conference on Antennas and Propagation (EuCAP)*, Paris, France, Mar. 2017.

E.2.4 2018 IEEE MTT-S International Conference on Numerical Electromagnetic and Multiphysics Modeling and Optimization

- **F. Teberio**, P. Martin-Iglesias, I. Arregui, J. M. Percaz, T. Lopetegi, M. A. G. Laso, and I. Arnedo, "Quasi-Analytical Design of Commensurate-Line Waveguide Band-Pass Filters," *IEEE MTT-S International Conference on Numerical Electromagnetic and Multiphysics Modeling and Optimization (NEMO)*, Reykjavik, Iceland, Aug. 2018.

- P. Martin-Iglesias and **F. Teberio**, "Analysis of multipactor effect with linear frequency modulated signals," *IEEE MTT-S International Conference on Numerical Electromagnetic and Multiphysics Modeling and Optimization (NEMO)*, Reykjavik, Iceland, Aug. 2018.

E.2.5 IEEE MTT-S International Microwave Workshop Series on Advanced Materials and Processes (IMWS-AMP)

- **F. Teberio**, I. Arnedo, J. M. Percaz, I. Arregui, P. Martin-Iglesias, T. Lopetegi, and M. A. G. Laso, "Meandered corrugated waveguide low-pass filter," *IEEE MTT-S International Microwave Workshop Series on Advanced Materials and Processes (IMWS-AMP)*, Pavia, Italy, Sept. 2017.

- P. Martin-Iglesias, I. Montero, **F. Teberio**, I. Arregui, J. M. Percaz, T. Lopetegi, I. Arnedo, L. Olano, and M. A. G. Laso, "Enhanced multipactor performance in 3D printed microwave parts," *IEEE MTT-S International Microwave Workshop Series on Advanced Materials and Processes (IMWS-AMP)*, Pavia, Italy, Sept. 2017.

E.2.6 IEEE MTT-S Latin America Microwave Conference (LAMC)

- I. Arnedo, I. Arregui, **F. Teberio**, M. Chudzik, A. Lujambio, D. Benito, J. M. Percaz, A. Gomez-Torrent, T. Lopetegi, and M. A. G. Laso, "Microwave periodic structures and synthesized structures with smooth profiles and their application," *IEEE MTT-S Latin America Microwave Conference (LAMC)*, Puerto Vallarta, Mexico, Dec. 2016.

E.2.7 International Workshop on Microwave Filters (IWMF)

- **F. Teberio**, I. Arregui, C. Vicente, J. Gil, P. Martin-Iglesias, M. Zedler, J. A. Lorente, D. Raboso, and M. A. G. Laso, "High-power low-pass filter for Ka-band multibeam payload," *International Workshop on Microwave Filters (IWMF)*, ESA/ESTEC, The Netherlands, Apr. 2018.

- **F. Teberio**, J. M. Percaz, I. Arregui, P. Martin-Iglesias, T. Lopetegi, M. A. G. Laso, and I. Arnedo, "Matlab accurate synthesis of classical stepped-impedance

rectangular waveguide filters," *International Workshop on Microwave Filters (IWMF)*, ESA/ESTEC, The Netherlands, Apr. 2018.

- P. Martin-Iglesias, **F. Teberio**, S. Martin-Iglesias, I. Arregui, M. A. G. Laso, I. Arnedo, and L. Accatino, "Thermal stability variation for AlSi (40)," *International Workshop on Microwave Filters (IWMF)*, ESA/ESTEC, The Netherlands, Apr. 2018.

- P. Martin-Iglesias, I. Montero, **F. Teberio**, I. Arregui, J. M. Percaz, T. Lopetegi, I. Arnedo, L. Olano, and M. A. G. Laso, "Enhanced multipactor performance in 3D printed microwave parts," *International Workshop on Microwave Filters (IWMF)*, ESA/ESTEC, The Netherlands, Apr. 2018.

- **F. Teberio**, I. Arregui, A. Gomez-Torrent, E. Menargues, M. A. G. Laso, C. Vicente, J. Gil, A. Alonso, N. Sidiropoulos, P. Martin-Iglesias and M. Diaz Martin, "Assessment of electroforming for complex RF/Microwave components," *Proc. International Workshop on Microwave Filters*, Toulouse, France, Mar. 2015.

- I. Arregui, A. Gomez-Torrent, I. Arnedo, A. Lujambio, J. D. Martínez, M. Chudzik, **F. Teberio**,E. Menargues, V. Boria, T. Lopetegi, and M. A. G. Laso, "Filter design by an inverse scattering method based on poles and zeros decomposition," *Proc. International Workshop on Microwave Filters*, Toulouse, France, Mar. 2015.

- **F. Teberio**, I. Arregui, I. Arnedo, A. Lujambio, M. Chudzik, D. Benito, R. Jost, F.-J. Görtz, T. Lopetegi and M.A.G. Laso, "High-power alternative to the design of wide-band spurious-free waffle-iron filters and prediction of multipacting breakdown," *Proc.International Workshop on Microwave Filters*, Toulouse, France, Oct. 2012.

E.2.8 International Workshop on Multipactor, Corona and Passive Intermodulation (MULCOPIM)

- **F. Teberio**, I. Arregui, C. Vicente, J. Gil, P. Martin-Iglesias, M. Zedler, J. A. Lorente, and M. A. G. Laso, "Fully-Customized Waveguide Harmonic Low-Pass Filters for High-Power Satellite Applications," *Proc. 9th International Workshop on Multipactor, Corona and Passive Intermodulation in Space RF Hardware (MULCOPIM 2017)*, Noordwiijk, The Netherlands, Apr. 2017.

- P. Martin-Iglesias, I. Montero, L. Olano, M. A. G. Laso, **F. Teberio**, I. Arregui, M. A. Garcia, A. Doblado, and V. Cabrera, "SEY in additively manufactured surfaces," *Proc. 9th International Workshop on Multipactor, Corona and Passive Intermodulation in Space RF Hardware (MULCOPIM 2017)*, Noordwiijk, The Netherlands, Apr. 2017.

- I. Arregui, **F. Teberio**, I. Arnedo, M. Chudzik, A. Lujambio, T. Lopetegi, R. Jost, F. J. Görtz, J. Gil, C. Vicente, B. Gimeno, V. E. Boria, P. Martin Iglesias,

D. Raboso, and M. A. G. Laso, "Multipactor characterization with a ring resonator of low-pass harmonic filters designed for high-power operation," *Proc. 8th International Workshop on Multipactor, Corona and Passive Intermodulation in Space RF Hardware (MULCOPIM 2014)*, Valencia, Spain, Sept. 2014.

- I. Arregui, S. Anza, **F. Teberio**, C. Vicente, I. Arnedo, J. Gil, A. Lujambio, M. Chudzik, R. Jost, F. -J. Görtz, B. Gimeno, D. Benito, T. Lopetegi, M. A. G. Laso, D. Raboso, and V. E. Boria, "Multipactor prediction in novel high-power low-pass filters with wide rejection band," *Proc. 7th International Workshop on Multipactor, Corona and Passive Intermodulation in Space RF Hardware (MULCOPIM 2011)*, Valencia, Spain, Sept. 2011.

E.2.9 ESA Satcom Final Presentation Days

- **F. Teberio**, I. Arregui, M. A. G. Laso, C. Vicente, J. Gil, A. Alonso, P. Martin-Iglesias, M. Zedler, "Compact high-power Ka-band low-pass filters for multi-beam S/L payloads (ITI-B project)," *ESA Satcom Final Presentation Days*, ESA/ESTEC, The Netherlands, Jan. 2018.

E.2.10 ESA Industry Days on Additive Manufacturing for RF/Microwave Hardware

- A. Gomez-Torrent, **F. Teberio**, A. Martinez, J. M. Percaz, I. Arnedo, I. Maestrojuán, I. Arregui, G. Crespo, T. Lopetegi, M. A. G. Laso, and J. Teniente "Assessment of Additive Manufacturing for RF/Microwave components," *Proc. ESA Industry Days on Additive Manufacturing for RF/Microwave Hardware*, ESA/ESTEC, The Netherlands, Nov. 2016.

E.2.11 Ka and Broadband Communications Conference

- **F. Teberio**, I. Arregui, M. A. G. Laso, C. Vicente, J. Gil, A. Alonso, P. Martin-Iglesias, M. Zedler, "Compact high-power Ka-band low-pass filters for multi-beam satellite payloads," *Proc. 22nd Ka and Broadband Communications Conference*, Cleveland, USA, Oct. 2016.

E.2.12 CST European User Conference (CST - EUC)

- I. Arnedo, **F. Teberio**, I. Arregui, J. M. Percaz, C. Martinez-de-Morentin, T. Lopetegi, and M. A. G. Laso "Advances in passive microwave components at MCG-UPNA," *CST European User Conference (CST - EUC)*, Darmstadt, Germany, Apr. 2017.

E.2.13 Microwave Technology and Techniques Workshop (MTT)

- J. M. Percaz. I. Arnedo, M. Chudzik, I. Arregui, **F. Teberio**, C. Briso-Rodriguez, J. Moreno, T. Lopetegi, and M. A. G. Laso, "Synthesis and Applications of Smooth-Profiled Planar Coupled-Lines," *Microwave Technology and Techniques Workshop (MTT'17)*, ESA/ESTEC, The Netherlands, Apr. 2017.

E.2.14 International Conference on Infrared, Millimeter and Terahertz Waves (IRMMW-THz)

- A. Chahadih, M. Chudzik, I. Arnedo, A. Ghaddar, I. Arregui, **F. Teberio**, A. Lujambio, M. A. G. Laso, T. Lopetegi, and T. Akalin, "Low loss microstrip transmission-lines using cyclic olefin copolymer COC-substrate for sub-Thz and Thz applications," *Proc. 38th International Conference on Infrared, Millimeter and Terahertz Waves (IRMMW-THz)*, Mainz, Germany, Sept. 2013.

E.2.15 Mediterranean Microwave Symposium (MMS)

- A. Chahadih, S. Keya, A. Ghaddar, T. Akalin, M. Chudzik, I. Arnedo, I. Arregui, **F. Teberio**, A. Lujambio, and T. Lopetegi, "Low loss transitions and microstrip lines on cyclo-olefin co-polymer substrate for terahertz applications," *Proc. Mediterranean Microwave Symposium (MMS)*, Saida, Algeria, Sept. 2013.

E.2.16 International Workshop on Optical Terahertz Science and Technology (OTST 2013)

- M. Chudzik, A. Chahadih, I. Arnedo, A. Ghaddar, A. Lujambio, **F. Teberio**, I. Arregui, G. Ducournau, J.-F. Lampin, D. Benito, T. Lopetegi, M. A. G. Laso and T. Akalin, "Synthesis of passive terahertz devices in coplanar technology," *Proc. International Workshop on Optical Terahertz Science and Technology (OTST 2013)*, Kyoto, Japan, Apr. 2013.

E.3 Invited Presentation in International Workshops (3)

- Workshop Title:Recent Advances in RF Microwave filters for space applications. Presentation Title: Advanced design techniques for waveguide filters for satellite applications. Location: European Microwave Conference (EuMC), Madrid, Spain. Dates: Sept. 2018.

- Workshop Title:Additive-Manufacturing of Radio-Frequency Components. Presentation Title: Additive manufacturing for RF/microwave components: RF and high-power considerations Location: IEEE MTT-S International Microwave Symposium Digest (IMS), Honolulu, USA. Dates: Jun. 2017.

- CST Aerospace Workshop. Presentation Title: Filters and multiplexers for satellite payloads using FEST3D and CST MWS. Location: CST European User Conference, Darmstadt, Germany. Dates: Apr. 2017.

E.4 Awards

- 2017 CST University Publication Award